1-1-1999

Template-directed synthesis of inorganic heterogeneities and the development of ultrasonic spectroscopy for the analysis of polymers.

Gregory Thomas Schueneman
University of Massachusetts Amherst

TEMPLATE - DIRECTED SYNTHESIS OF INORGANIC HETEROGENEITIES AND THE DEVELOPMENT OF ULTRASONIC SPECTROSCOPY FOR THE ANALYSIS OF POLYMERS

A Dissertation Presented

by

GREGORY THOMAS SCHUENEMAN

Submitted to the Graduate School of the
University of Massachusetts Amherst in partial fulfillment
of the requirements for the degree of

DOCTOR OF PHILOSOPHY

September 1999

Polymer Science and Engineering

TEMPLATE - DIRECTED SYNTHESIS OF INORGANIC HETEROGENEITIES AND THE DEVELOPMENT OF ULTRASONIC SPECTROSCOPY FOR THE ANALYSIS OF POLYMERS

A Dissertation Presented

by

GREGORY THOMAS SCHUENEMAN

Approved as to style and content by;

Alan J. Lesser, Co-Chair

Bruce M. Novak, Co-Chair

David J. McClements, Member

Richard J. Farris, Department Head
Polymer Science and Engineering

Dedicated to my family and loving wife to be Susan

ACKNOWLEDGEMENTS

This time at UMass has been a profoundly enriching experience. I would like to begin by expressing my gratitude to Prof. Alan Lesser and Prof. Bruce Novak. You have provided support, guidance, and most importantly freedom to follow my scientific instincts and curiosity. I feel that I have learned a great deal about polymer science, research, and life though our direct and sometimes indirect interactions. Prof. Lesser you have gone above and beyond my expectations as an advisor, teacher, and friend.

I am indebted to Prof. McClements for actively participating in my committee. Much of the nature and scope of this dissertation is the result of our many interactions and discussions on ultrasound. Special thanks go to Prof. Thomas McCarthy for his willingness to sit in for Prof. Novak during my final defense.

The Polymer Science and Engineering Department has provided me a unique environment where cooperation between labs removed the bounds of individual research groups. The department's secretaries and support staff have been life savers on many occasions.

Having one foot in synthesis and one in fracture mechanics has been extremely challenging and rewarding. One of the best rewards was the interaction with two diverse groups of motivated and enthusiastic scientists. Many classmates have given me the gift of their friendship during my time here. Our interactions have enriched my graduate school experience. I would like especially like to thank Buddy, Elif, Felix, Heather, Jenny, Lisa, Matt, Naveen, Sam, Xin, and Yuan for making this an enjoyable experience.

My family has been an unending source of support and encouragement even in the face of your obvious curiosity on why I am still in school. The Newman Center has acted as my home away from home for these many years and will I miss it dearly. The Newman Center will always be a special place for this is where I met my wife to be. Susan your unconditional love, acceptance, and trust has made even the most difficult times smoothly flow by. I look forward with much anticipation to enjoying the rest of our lives together.

ABSTRACT

TEMPLATE - DIRECTED SYNTHESIS OF INORGANIC HETEROGENEITIES AND THE DEVELOPMENT OF ULTRASONIC SPECTROSCOPY FOR THE ANALYSIS OF POLYMERS

SEPTEMBER 1999

GREGORY THOMAS SCHUENEMAN

B.S., UNIVERSITY OF FLORIDA

M.S., UNIVERSITY OF FLORIDA

Ph.D., UNIVERSITY OF MASSACHUSETTS AMHERST

Directed by: Professors Alan J. Lesser and Bruce M. Novak

As polymers are utilized in new applications they encounter environments that push them to their limits. In response to this demand, materials are being engineered on the molecular, meso, and macro levels such that their properties match those required of them. One of the most effective methods of modifying physical and mechanical properties is the incorporation of an inorganic heterogeneity. Recent advances in controlled SiO_2 sol – gel synthesis have made it possible to created unique heterogeneities of desired dimensions. A detailed investigation of the mechanism of the room temperature sol – gel synthesis of rectangular cross section silica tubes is presented. It is elucidated that tubes are formed by simultaneous template formation and coating with rapidly condensing SiO_2. The templates are subsequently dissolved out from within the SiO_2 coating yielding tubes whose size and geometry match those of the templates.

Knowledge gained in examining the mechanism is utilized to create tubes of desired length and diameter. The process shows promise for fabricating hollow silica shapes of controlled dimension and geometry.

The morphology and damage states of complex multicomponent polymeric materials and composites are extremely difficult to characterize by current methods. Traditionally, morphology is characterized via gross differences in electron density (via electron microscopy), chemical nature (staining enhanced electron microscopy) and optical density (via optical microscopy). Ultrasonic spectroscopy is a new technique that utilizes high frequency (10-100 MHz) transducers to transmit and receive sound waves through materials. Sound waves translate via successive perturbations of the medium and consequently the rate and manner in which they are transmitted is a function of the medium's physical and mechanical properties. Hence, morphology is imaged through density or modulus differences regardless of optical clarity. Ultrasonic spectroscopy was applied to the morphological analysis of model polymers containing phase separated spherical heterogeneities, characterization of model reacting systems, and the elucidation of residual strengths in graphite fiber reinforced epoxy laminates exposed to thermal loads. This research resulted in the development of analysis methods that successfully characterized morphology on several levels, monitored gelation and phase separation *in situ*, and detected thermally induced incipient damage in polymer matrix composites.

TABLE OF CONTENTS

LIST OF TABLES

Table

LIST OF FIGURES

Figure

Page

CHAPTER 1

SYNTHESIS OF INORGANIC HETEROGENEITIES

1.1 Introduction

Synergistic effects can be obtained by combining materials with different mechanical and physical characteristics. Two such classes of materials with vastly different characteristics are polymers and ceramics. Polymers being viscoelastic exhibit mechanical behavior that depends greatly on the rate of load application and the temperature. Ceramics behave as elastic solids which principally fail in a brittle mode. Polymers degrade at relatively low temperatures, whereas ceramics are stable to high temperatures and maintain their structural integrity at these high temperatures. A polymer - ceramic composite would hopefully have a combination of the best of these properties. Inorganic fibers and particles are widely used to fabricate polymer matrix composites with superior hardness, shrinkage resistance, fire retardency, and thermal stability.[1] However, toughness is generally sacrificed depending upon the geometry of the reinforcing phase and its interaction with the matrix.

Inorganic fibers are very effective at improving the fracture resistance of polymers as the long axis impedes crack propagation. Particles are not as effective at increasing fracture toughness except when they promote localized deformation of a brittle matrix. Particles increase stiffness but not typically the strength of the composite as they tend to act as stress concentrators.[1] Fibers are commonly added to polymers to increase their strength, fracture toughness and stiffness.[2] Properties of several reinforcing fibers are shown in Table 1.[1]

Table 1.1: Properties of fibers used for reinforcement.

Material	Tensile Modulus (GPa)	Tensile Strength (GPa)	Density (g/cm3)	Specific Modulus (E/ρ)	Specific Strength (σu/ρ)
E-Glass	72.4	3.5*	2.54	28.5	1.38
S-Glass	85.5	4.6*	2.48	34.5	1.85
Silica	72.4	5.8	2.19	33.0	2.65
Graphite	390.0	2.1	1.90	205.0	1.1
Kevlar 49	130.0	2.8	1.50	87.0	1.87

* Values are for virgin non - treated fibers. Strengths prior to making composite are about 2.1 GPa.

The high strength of non-treated glass fibers is attributed to their defect free surfaces. Their principle advantages are low cost and high strength. Disadvantages of glass fibers are their poor abrasion resistance, low modulus of elasticity, and poor adhesion to polymer matrices. E-glass is the most widely used inorganic fiber due to its low cost.[1]

Sol-gel chemistry is widely used for the fabrication of fibers, films, and monoliths at low temperatures and higher purities.[3-7] Sol-gel chemistry utilizes low molecular weight ceramic precursors that under acid or base catalysis and careful drying form three dimensional networks analogous to those produced by high temperature sintering of powders. Although more expensive, the success of sol-gel chemistry can be attributed to its versatility and robustness that allows for the synthesis of high purity glasses.[3-7] The formation of inorganic structures capable of reinforcing polymeric matrixes under such

mild conditions enables the tailoring of heterogeneities and perhaps the simultaneous synthesis of reinforcing phase and polymeric matrix.

Sol-gel synthetic methods are beginning to play a major parts as directed inorganic building blocks in the synthesis of highly ordered meso and nano structures. Direction has been achieved via templates, spatial restriction, or a mixture of these approaches.[8] The directing phase dictates the dimension and shape of the final inorganic structure. Thus, precise control of the director expedites the creation of complex structures or domains of desired size and geometry. Several researchers have successfully employed directed sol – gel synthesis to create heterogeneities of significant aspect ratio. Davis *et al.* constructed macroporous arrays of SiO_2 channels via sol-gel condensation within preformed bacterial templates and then heated to remove organic constituents.[9] The dimensions of the silica macrostructure obtained were up to 3.5 mm long, and 0.2 mm thick with pores of 0.5 μm diameter and 200 nm wall thickness. Upon fracturing the silica macrostructures along the length it was discovered that hollow channels emanated from the pores. Schnur used preformed lipid tubules to form silica tubes after sol-gel coating and nickel tubes after metallization that had dimensions of up to 0.4 μm in diameter and 70 μm long.[10] Both of theses examples illustrate the use of preformed templates in the construction of inorganic heterogeneities.

Nakamura and Matsui, reported the synthesis of SiO_2 tubes with rectangular cross section via a room temperature sol-gel process.[11] The rectangular tubes had lengths of 200-300 μm, widths of 0.5-1 μm and shell thickness of 0.05-0.1 μm. However, no clear director – builder relationship was identified for this unique synthesis. Nakamura and Matsui state that the mechanism is unknown and propose that SiO_2 sol particles are the

starting point of the tubes and their growth may be directed by hydrogen bonded complexes of the *d,l*-tartaric acid (*d,l*-TTA) used in the reaction as a catalyst. It would be remarkable for a hydrogen bonded complex 10 Å across, as estimated by Nakamura and Matsui, to direct the synthesis of 1 μm x 300 μm structures. The generation of high aspect ratio (300) inorganic heterogeneities in the absence of a preformed director at room temperature is unprecedented and could yield *in situ* synthetic routes of generating inorganic heterogeneities.

Here and elsewhere[12] the results of a systematic study of the SiO_2 rectangular tube synthesis is presented, an alternate mechanism is proposed, three critical mechanistic stages of the reaction are identified, and the significance of these stages to the structures obtained is discussed. With the knowledge gained from this investigation, the mechanisms involved are exploited to obtain structures of controlled dimension.

1.2 Experimental

1.2.1 Mesotube synthesis

Tetraethyl orthosilicate (TEOS) and *d,l*-TTA were obtained from Aldrich Chemical. Spectroscopic grade water and reagent grade ammonium hydroxide (NH_4OH) (30% NH_3), sodium metasilicate, hydrochloric acid, tetrahydrofurane, sodium chloride, and sodium sulfate were obtained form Fisher Scientific, in the reagent grade form and used without further purification. Pharmaco brand absolute ethanol was obtained from the University of Massachusetts chemical stockroom. All reagents were used without further purification. Preliminary synthesis of the mesotubes was carried out as previously described.[11] This synthesis is summarized in Figure 1.1. The precipitate was

subsequently washed with water, collected via vacuum filtration on a 0.45 μm filter, and dried in an oven at 50°C for 24 hr.

1.2.2 Poly(silicic acid) (PSA) synthesis

PSA was synthesized by dissolving 8.5g (70 mmol) of sodium metasilicate in 50 mL of spectroscopic grade water and then adding this drop wise to 50 mL of 3M HCl at 0°C. After complete addition the solution was allowed to stir for 1 hr at 0 °C. The PSA was extracted via the addition of 30 g of NaCl dissolved in 100 mL of THF. This synthesis is summarized in Figure 1.2. The THF/PSA solution was dried over sodium sulfate and filtered to yield a clear non-viscous solution. The concentration of PSA was 0.0486 g/ml.

1.2.3 Scanning electron microscopy (SEM) analysis

SEM was conducted using a Joel 35 CF and a Joel field emission 6530FXV. Samples were placed on carbon tape affixed to a one inch diameter aluminum disk and coated with gold using a Polaron Instruments Inc. SEM Unit, model E51000. All images were taken in the secondary electron imaging mode and x-ray spectra were obtained with the electron dispersive spectroscopy mode on the Joel FSEM 6530FXV.

1.2.4 Nuclear magnetic resonance spectroscopy (NMR)

^{29}Si NMR was conducted using a Bruker 500 MHz instrument. Small amounts of deuterated methanol (Cambridge Isotope Laboratory) and tetramethylsilane (Aldrich) were added to the solution for locking and shift calibration respectively.

1.2.5 Mechanical behavior

Reaction products of the synthesis described in section 1.3.1 were hand blended into a stochiometric mixture of diglycidyl ether of bisphenol A and amine curing agent at 0 to 10 weight percent. The diglycidyl ether of bisphenol A was Epon 828 obtained from Shell Chemical Co. and the amine curing agent was Jeffamine D230 obtained from Huntsman Chemical Company. The mixture was placed into rectangular molds constructed of glass plates and a poly(tetrafluoroethylene) spacer, allowed to gel at room temperature for 24 hr, and then cured at 150 °C for 7 hr. The 0.32 cm thick composite plaques were cut into three point bend specimens for fracture toughness evaluation according to ASTM D5045[13] with a span to width ratio of four. Specimens were prenotched with a diamond saw and then sharp cracks were propagated a short distance with a razor blade. Mechanical testing was conducted on an Instron Model 1123 with a cross head speed of two millimeters per minute.

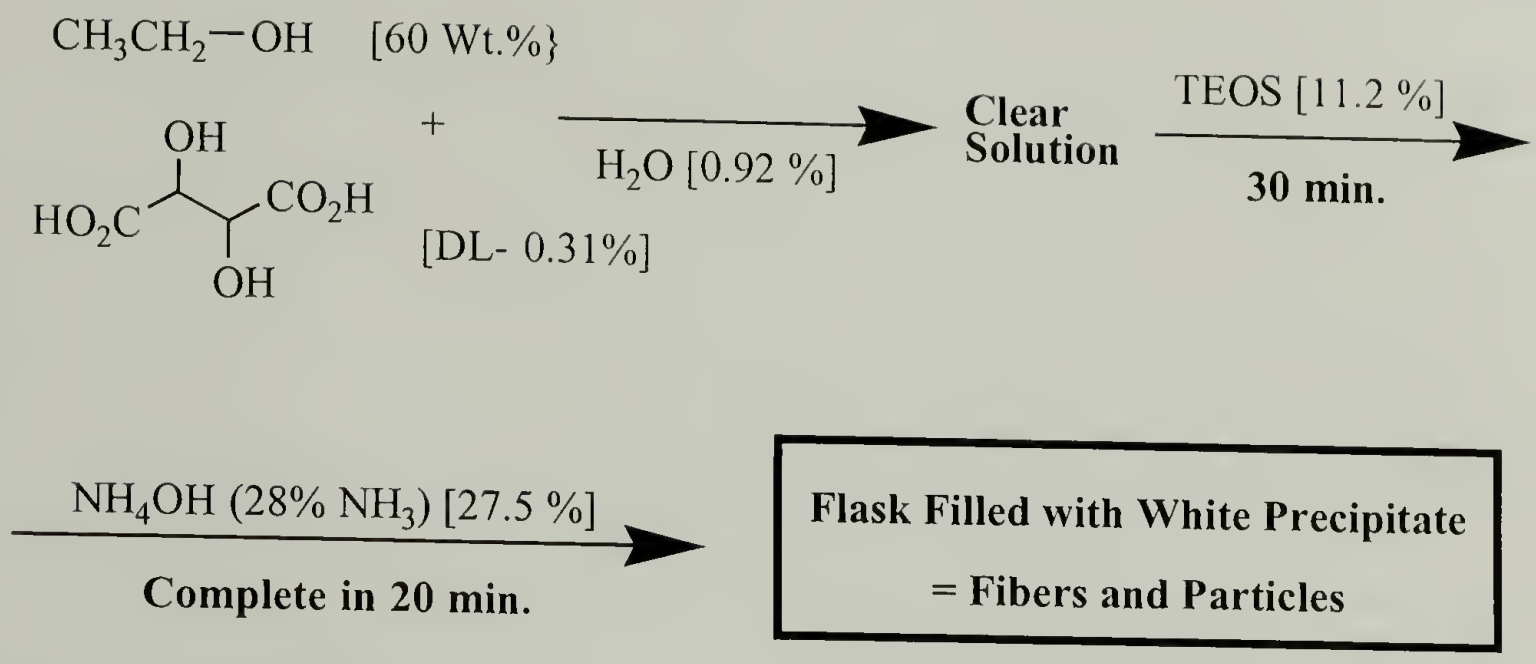

Figure 1.1: Mesotube synthesis.

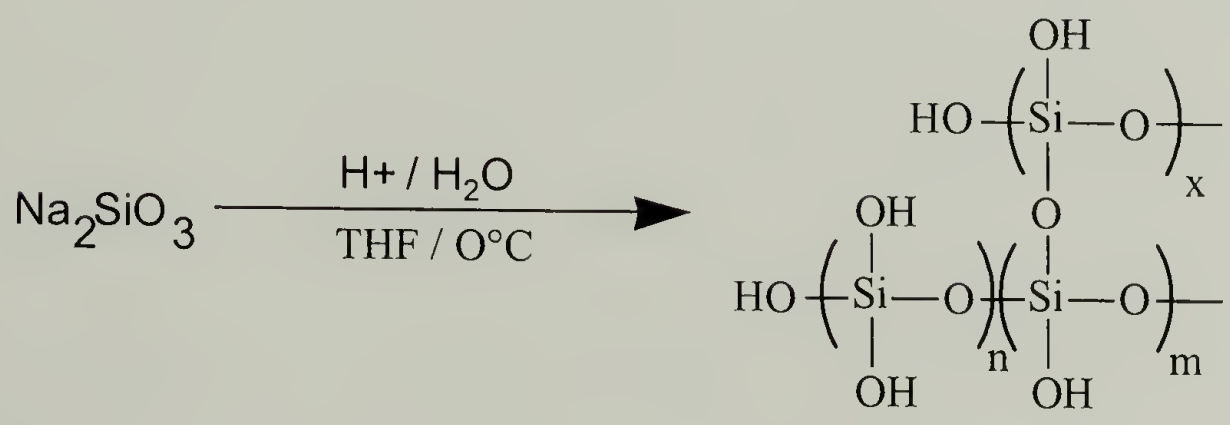

Figure 1.2: PSA synthesis.

1.3 Results and Discussion

The silica tube synthesis described by Nakamura and Matsui specifies the addition of NH_4OH to a solution of TEOS, ethanol, water and *d,l*-TTA that had been allowed to stand for 30 minutes after addition of TEOS. Twenty minutes after the addition of NH_4OH, the reaction vessel is filled with a white precipitate which upon washing with water yielded rectangular SiO_2 tubes and solid spheres. Stober *et al.* found that addition of NH_4OH to an alcoholic solution of TEOS yielded only spherical particles.[14] Thus, obtaining tubes from this reaction is unique and unexpected. Nakamura and Matsui made the following observations about this reaction; i) upon omission of the initial 30 minute waiting period no tubes formed, ii) the diameter of the tubes decreased with decreasing reaction temperature, and iii) no tubes were formed when the *l*, *d*, or meso isomers of tartaric acid were used. They used molecular modeling to show that a mixture of the *d*- and *l*- isomers are the only isomers that can form a ladder type hydrogen bonded complex in solution. Although Nakamura and Matsui clearly state that the mechanism is unknown, they propose that initial SiO_2 sol particles are the starting point of the tubes and their growth is directed by *d,l*-TTA hydrogen bonded complexes.

Repeating the reaction described by Nakamura and Matsui, we found that the TEOS/ethanol/H_2O/*d,l*-TTA solution remained clear with no noticeable change in viscosity during the 30 minute waiting period. Upon addition of NH_4OH, the solution became increasingly cloudy and viscous until it was completely opaque and non-flowing after 15-20 minutes. Washing the products with water yielded tubes, spherical particles, and particle aggregates, as shown in the SEM micrographs that make up Figure 1.3.

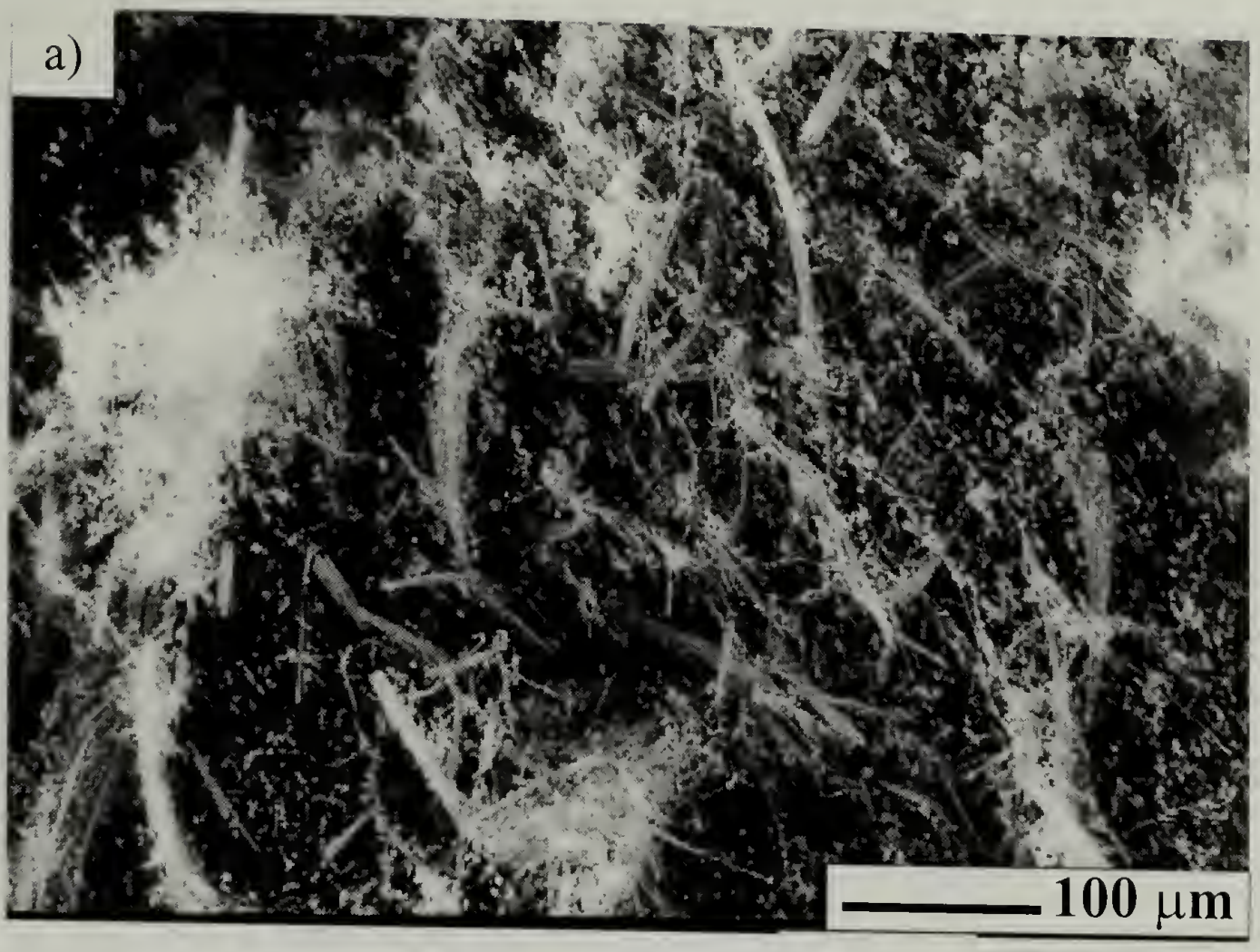

Figure 1.3: Products of SiO_2 mesotube synthesis; a) bulk products, b) bundle of tubes, c) tube ends, and d) close of tube end.

Continued on next page.

Figure 1.3 continued

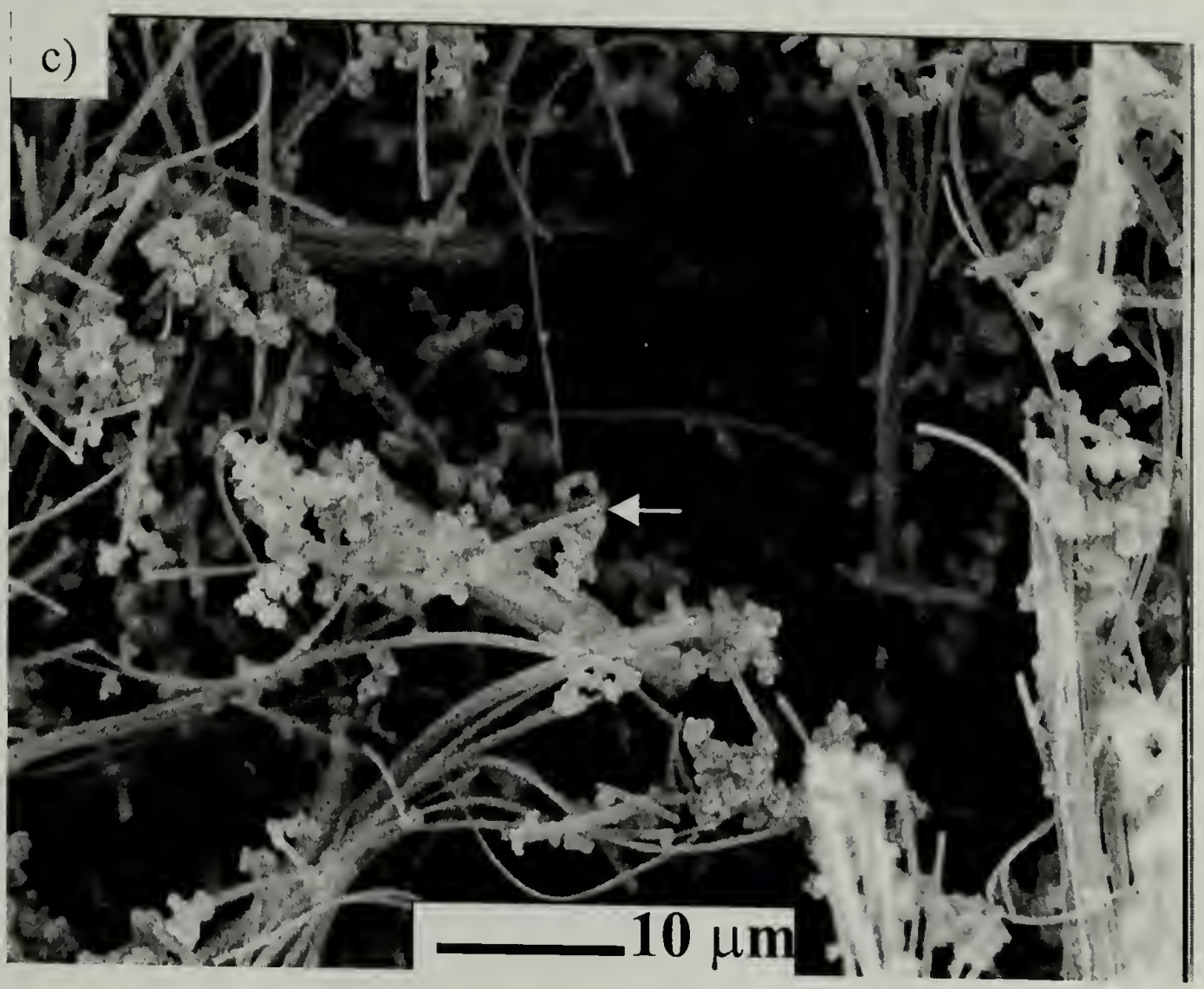

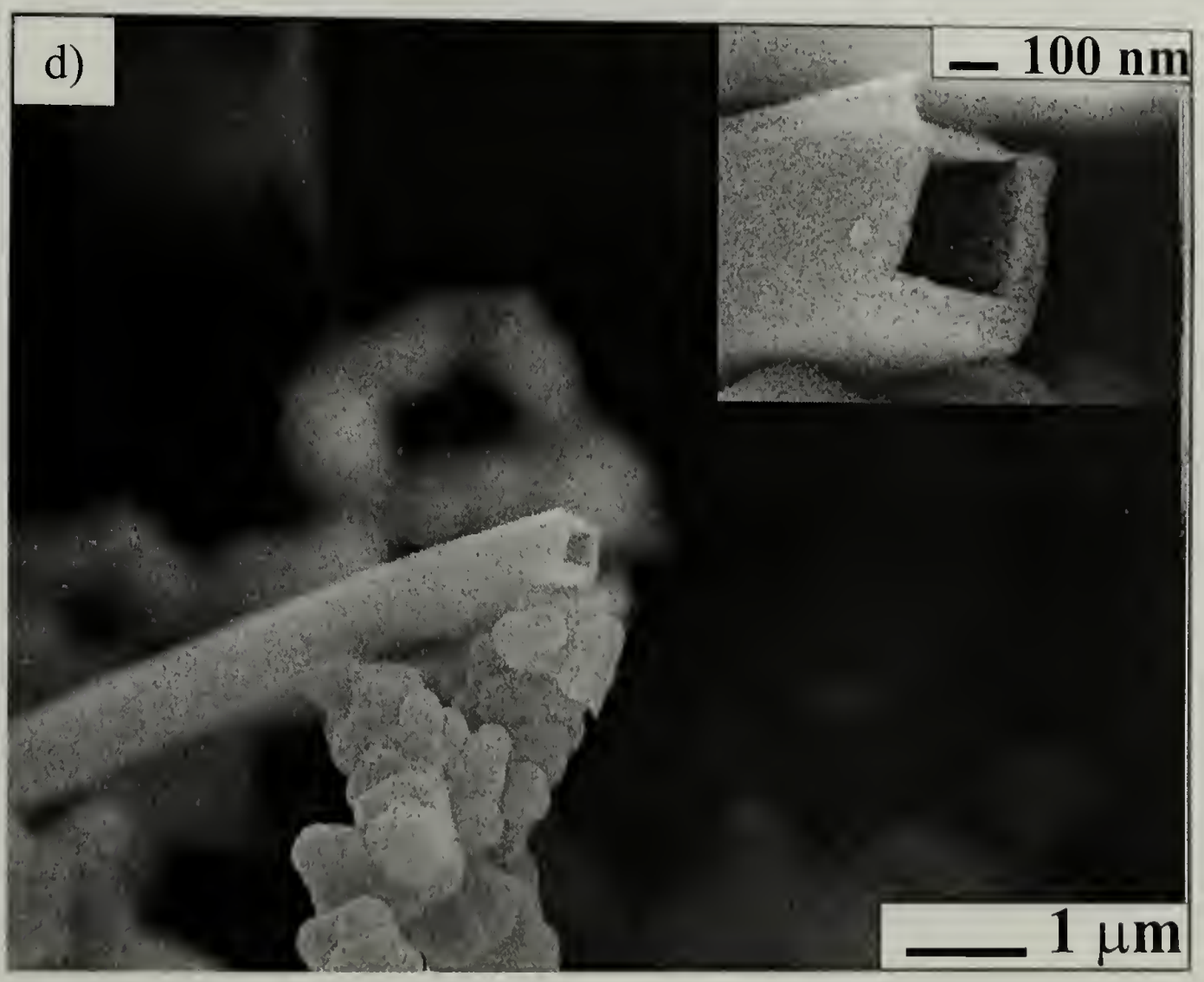

Figure 1.3a shows the bulk products and Figure 1.3b is a close up of these products showing a bundle of 1 μm outer dimension tubes. Figure 1.3c is a close up of a group of tube ends and Figure 1.3d is a close up of one end showing that it is rectangular in cross section with wall thickness of approximately 80 nm. Examination of the tube formation mechanism took place by identifying and studying three stages of the reaction. These stages are identified as 1) TEOS/ethanol solution, 2) NH_4OH addition/SiO_2 precipitation, and 3) precipitate washing and collection.

1.3.1 Stage 1: TEOS/ethanol solution

Nakamura and Matsui commented that the omission of the 30 minute waiting period prohibits tubes formation.[11] Monitoring the TEOS/ethanol/H_2O/*d,l*-TTA solution during the initial 30 minute waiting period via ^{29}Si NMR yielded the spectra shown in Figure 1.4. ^{29}Si NMR has been widely used to study the kinetics and mechanisms of sol - gel chemistry.[4,15-27] Pouxviel *et al.* studied the acid catalyzed reaction of TEOS with water.[20] Using the spectral assignments from their work the following peaks may be assigned; -81.9245 ppm is monomer (TEOS) and -78.9501 ppm is HO-Si-$(OEt)_3$. The other two peaks observed at longer reaction times are similar in position to peaks that were found for $(HO)_2$-Si-$(OEt)_2$ at -77.9802 ppm and $(HO)_3$-Si-O-Si-$(OH)_3$ at -81.0193 ppm. Therefore, hydrolysis of TEOS certainly occurs during the prescribed 30 minutes, followed by condensation of the resultant silanols at longer times. The 30 minute waiting period appears to be a priming stage necessary for effective tube formation.

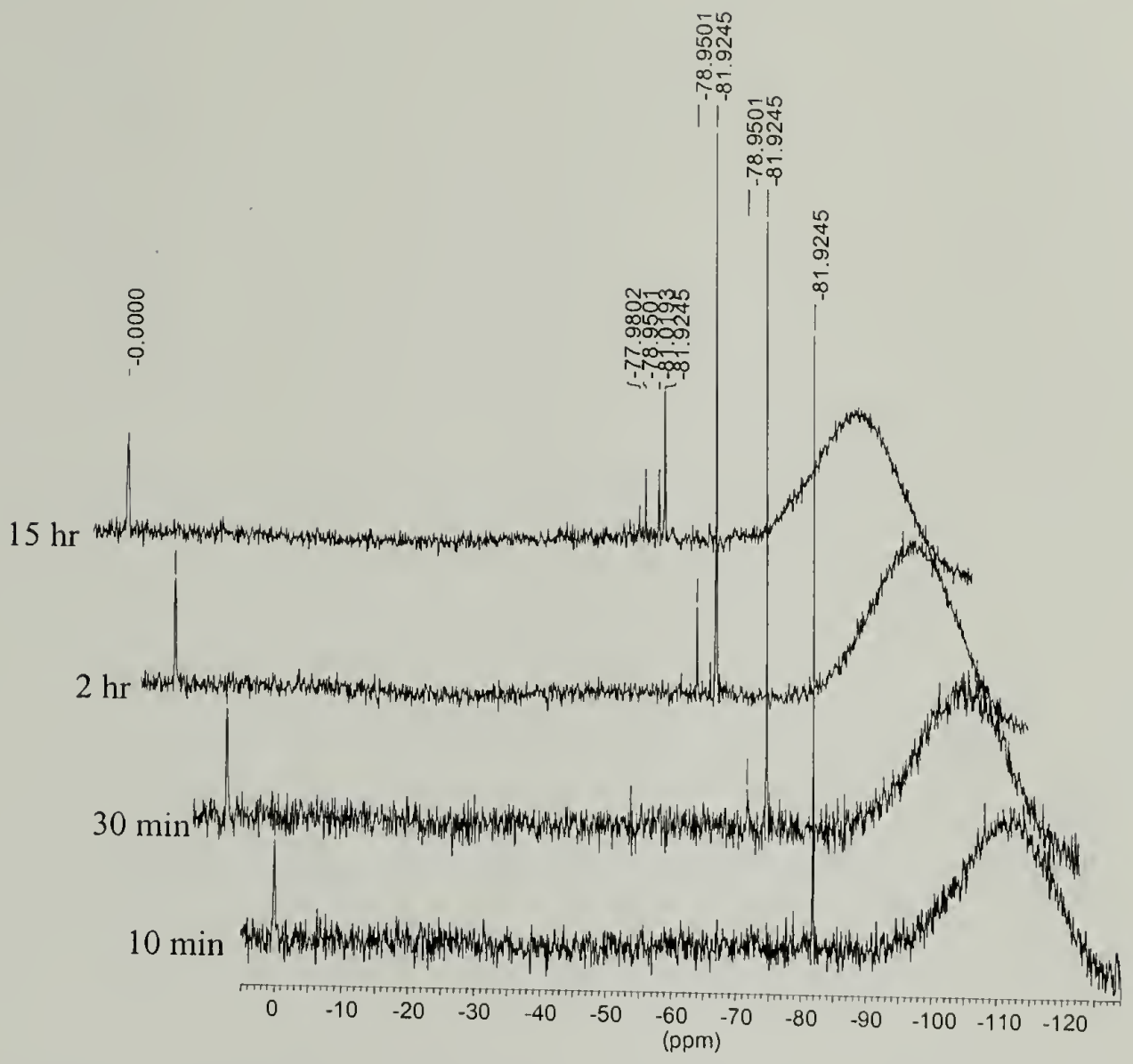

Figure 1.4: ^{29}Si of ethanol, water, *d,l*-tartaric acid solution at various times after adding TEOS.

1.3.2 Stage 2: NH_4OH addition/SiO_2 precipitation

Addition of NH_4OH and precipitation of products, occurs very rapidly and the opacity of the solution inhibits direct observation of this reaction. The pH of the solution turns from acidic (pH 3) to basic (pH 13) after the addition of NH_4OH. The rate of SiO_2 condensation greatly increases under basic conditions.[28] We hypothesized that the rapidly condensing SiO_2 encounters a director of some type causing it to grow or deposit in a manner such that a tube is formed.

Upon omission of TEOS, prismatic crystals precipitated from solution as the only product. Crystals began forming immediately upon addition of NH_4OH and continued to

them to immediately dissolve. Washing the products with ethanol yielded prismatic crystals (L: 75-2000 μm, OD: 0.5-10 μm), shown in Figure 1.5. Filtering the solution at various times after addition of NH_4OH controlled the dimensions of the crystals obtained. Table 1.2 shows the dimensions achieved after various filtration times. The cross-section and prismatic nature of the crystals are remarkably similar to the shape of the inside of the SiO_2 tubes. Fourier transform infrared (FTIR) analysis of the crystals indicates that they are composed of ammonium tartrate (ATT).

Table 1.2: Dimensions of ATT crystal obtained after various filtration times.

Crystallization Time (min)	**Crystal Width (μm)**	**Crystal Length (μm)**
0.5	0.5 - 1	50 - 100
1	0.5 - 10	100 - 400
2	0.5 - 10	100 - 400
4	0.5 - 10	100 - 800
Long Times	0.5 - 10	100 - 2000

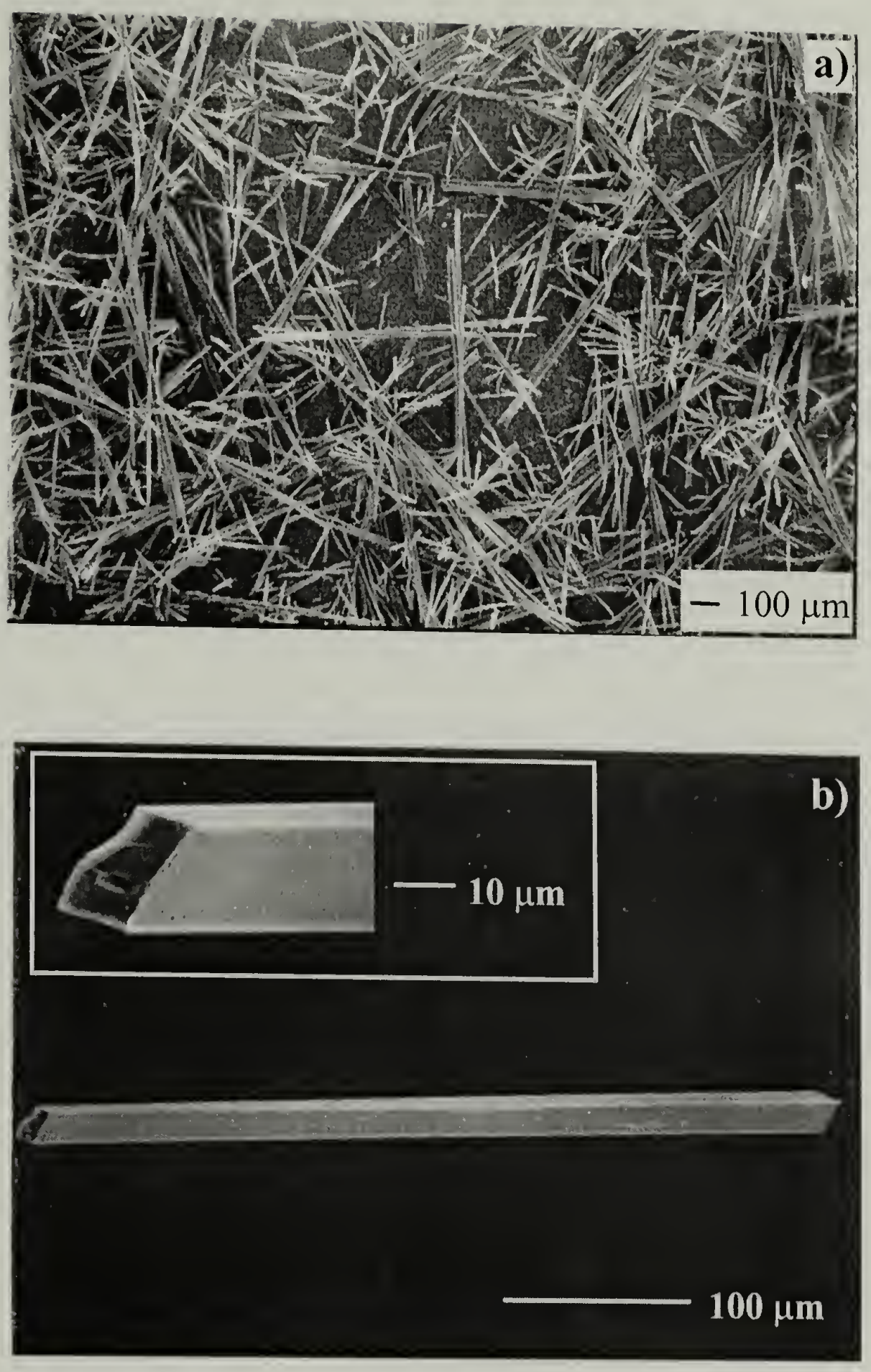

Figure 1.5: Crystals obtained after omission of TEOS from mesotube synthesis (a). Isolated crystal with close up of its end (inset) (b).

The ATT crystals isolated are of the correct length scale to act as templates to direct the deposition of SiO_2 into the observed tubes. Conducting similar experiments with the pure *l*- isomer of TTA yielded very few prismatic crystals even at times greater than one hour after the addition of NH_4OH. Thus, it appears that the racemate crystallizes under these conditions at a much greater rate than either pure enantiomer. The growth rate of ATT crystals derived from *d,l*-TTA fortuitously matches or is near the rapid rate of SiO_2 condensation and precipitation.

1.3.3 Stage 3: Precipitate washing and collection

To understand how ATT crystals act as templates, we conducted experiments to catch them in action. As noted above, ATT crystals immediately dissolve in water. Thus, our initial hypothesis for ATT action is that of water soluble templates upon which SiO_2 is deposited. Conducting the same synthesis as described in the original publication and then washing the products with ethanol should leave the ATT crystals in place. The products of this experiment are solid fibers, spherical particles and aggregates. The fibers have similar dimensions as the tubes. Figure 1.6 shows a SEM micrograph of the end of one of these fibers (Figure 1.6a) where the end appears to have fractured off exposing the interior. There is a sharp transition from fractured tip surface to that of the remainder of the smooth fiber surface below it. X-ray spectra show that the shaft (Figure 1.6b) is composed primarily of silicon and oxygen and the tip (Figure 1.6c) is carbon. Gold appears in the spectra because it was applied as a conduction layer prior to imaging.

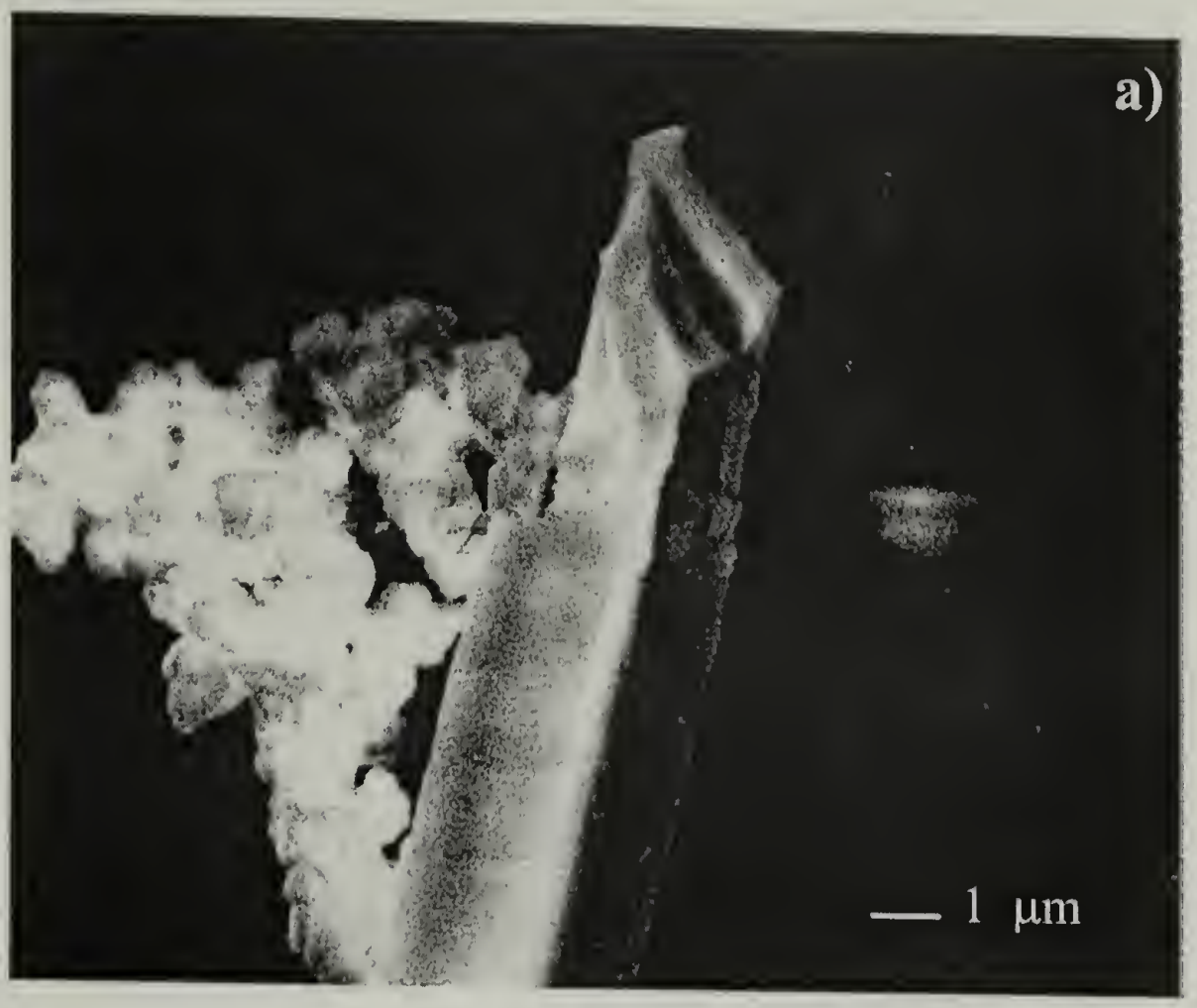

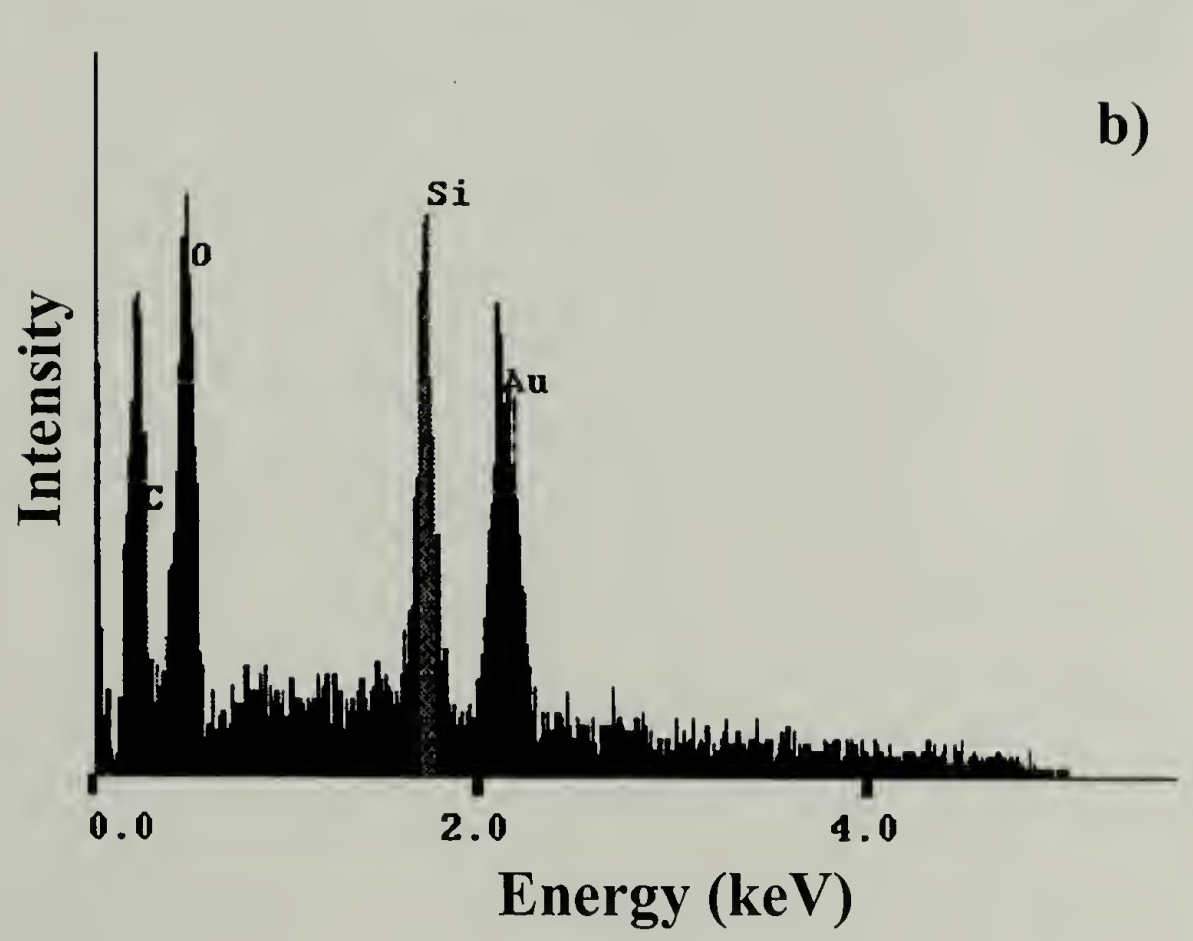

Figure 1.6: SEM picture of SiO_2 coated crystal (a), X-ray spectra from shaft (b), and X-ray spectra of the end of the fiber (c).

Continued next page

Figure 1.6 continued

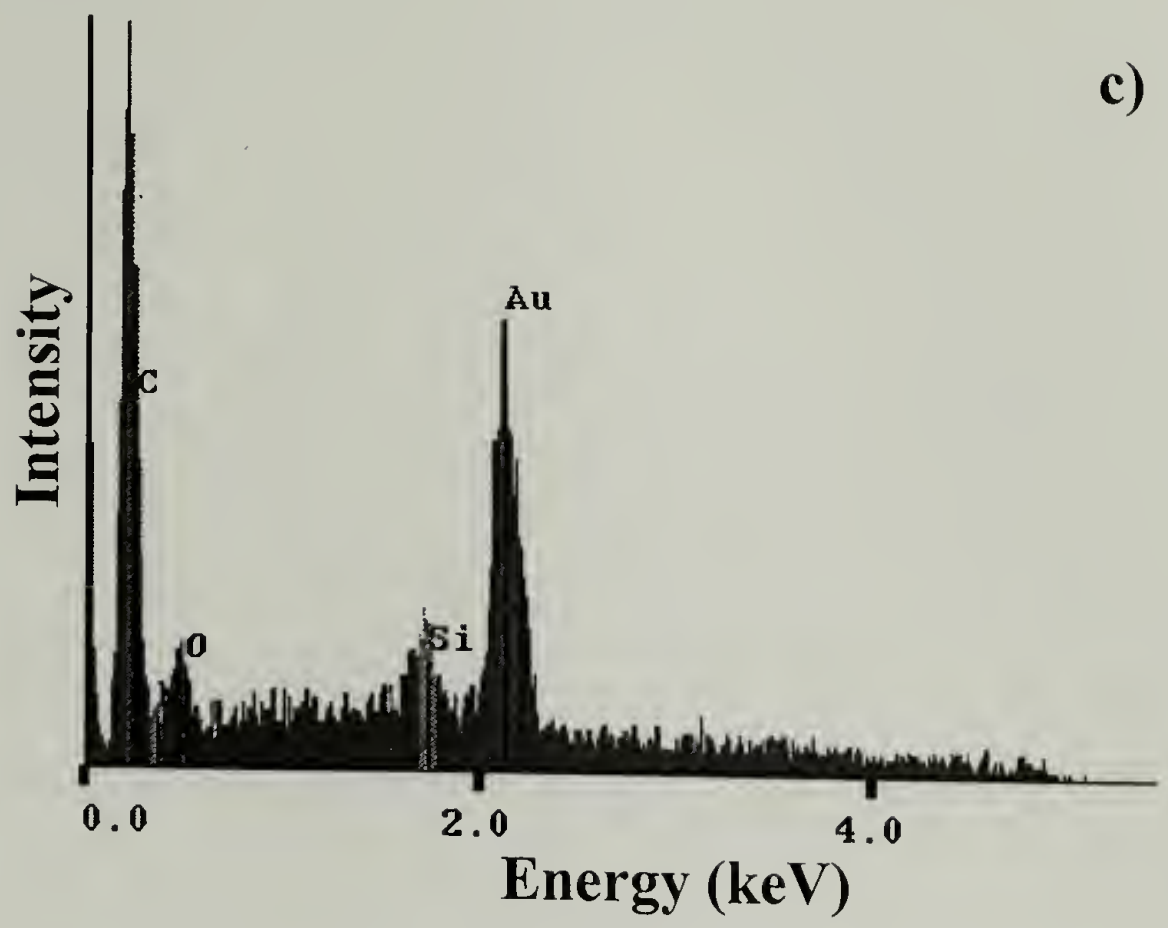

Thus, it is concluded from this analysis that washing the reaction products with ethanol yields ATT crystals coated with SiO_2. The sharp transition between shaft and tip marks the end of the SiO_2 coating. The coating appears to be 80-100 nm thick, which is similar to the shell thickness of the SiO_2 fibers shown in Figure 1.1.

1.3.4 Proposed mechanism

Bases on these observations, we propose that the following mechanism is responsible for rectangular tube formation. During the initial 30 minutes, hydrolysis of TEOS takes place priming the solution for rapid condensation. Upon addition of NH_4OH the solution becomes strongly basic causing ATT salt crystallization to begin. Simultaneously, the SiO_2 precursors begin to condense and precipitate from solution. The result is, ATT crystallizes in the form of long prisms and is coated with the

precipitating SiO_2. Washing the products with water dissolves the ATT templates out from within the SiO_2 coating leaving a tube. Condensing SiO_2 that does not encounter an ATT crystal most likely forms the spherical particles present in the reaction produces. This process is summarized in Figure 1.7.

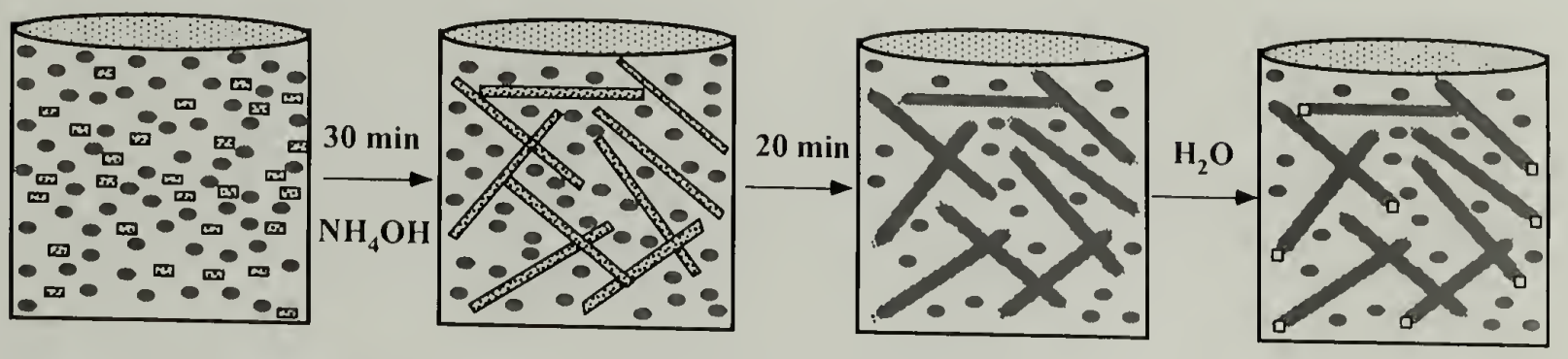

Figure 1.7: Schematic of SiO_2 – ATT templating process.

1.3.5 Controlled heterogeneities via preformed ATT crystals

Examination of the three stages of this reaction yields a detailed understanding of the mechanisms responsible for SiO_2 tube formation. With this knowledge, we examined methods to control this synthesis towards the formation of inorganic structures of controlled dimension and geometry. Addition of preformed ATT crystals of desired dimension to a TEOS/ethanol/H_2O solution yields ATT crystals with small surface deposits of SiO_2 after addition of NH_4OH and washing with ethanol. Thus, consideration must be made for the surface area of the template with respect to the coating ability, size, of the silicate. It is necessary to increase the molecular weight of the SiO_2 phase in an analogous manner as the increase in template surface area. Poly(silicic acid) (PSA), a highly branched – low molecular weight polymer, was synthesized to act as larger building blocks in conjunction with the larger surface area of the preformed ATT crystals. Addition of preformed ATT crystals (OD: 10 μm, L: 0.3 – 1 mm) to a PSA/THF solution resulted in the condensation of PSA onto the crystal surfaces.

Filtering this solution at various times after addition of the crystals, we found that the SiO_2 coatings became thicker and more uniform with longer exposure times. Below in Figure 1.8 are SEM micrographs that show ATT crystals coated with PSA. The PSA/THF solution, usually stable for weeks, became increasingly viscous until it is unfilterable at times greater than four hours. For reasons yet to be fully elucidated, the surface of the ATT crystals appears to accelerate the rates of silanol condensation (*vide infra*). Thus, with proper understanding of the mechanisms responsible for tube formation we can create structures with controlled dimension and complex geometries such as the sea urchin like structures we have recently obtained. These structures can lead to complex reinforcing phases.

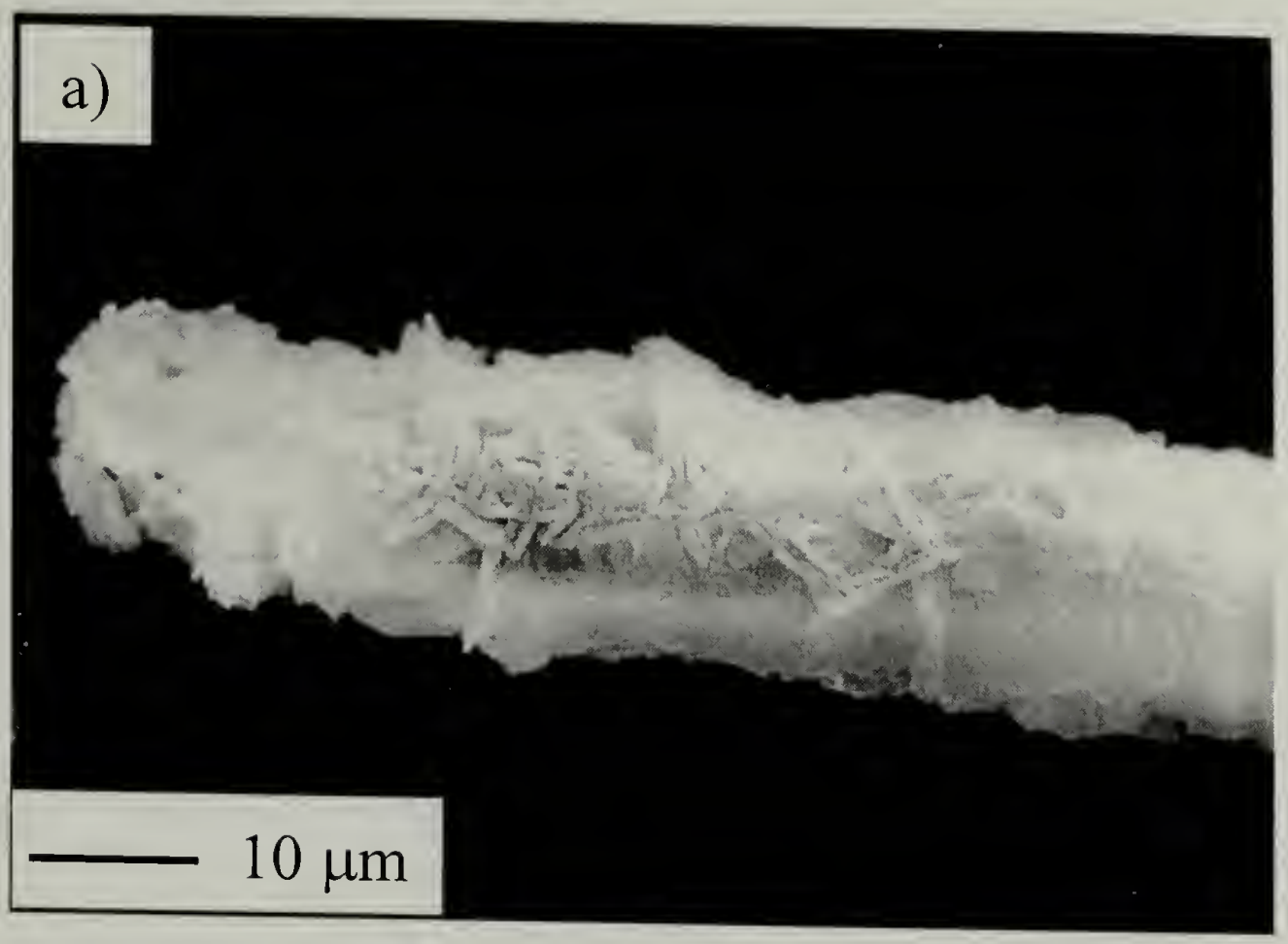

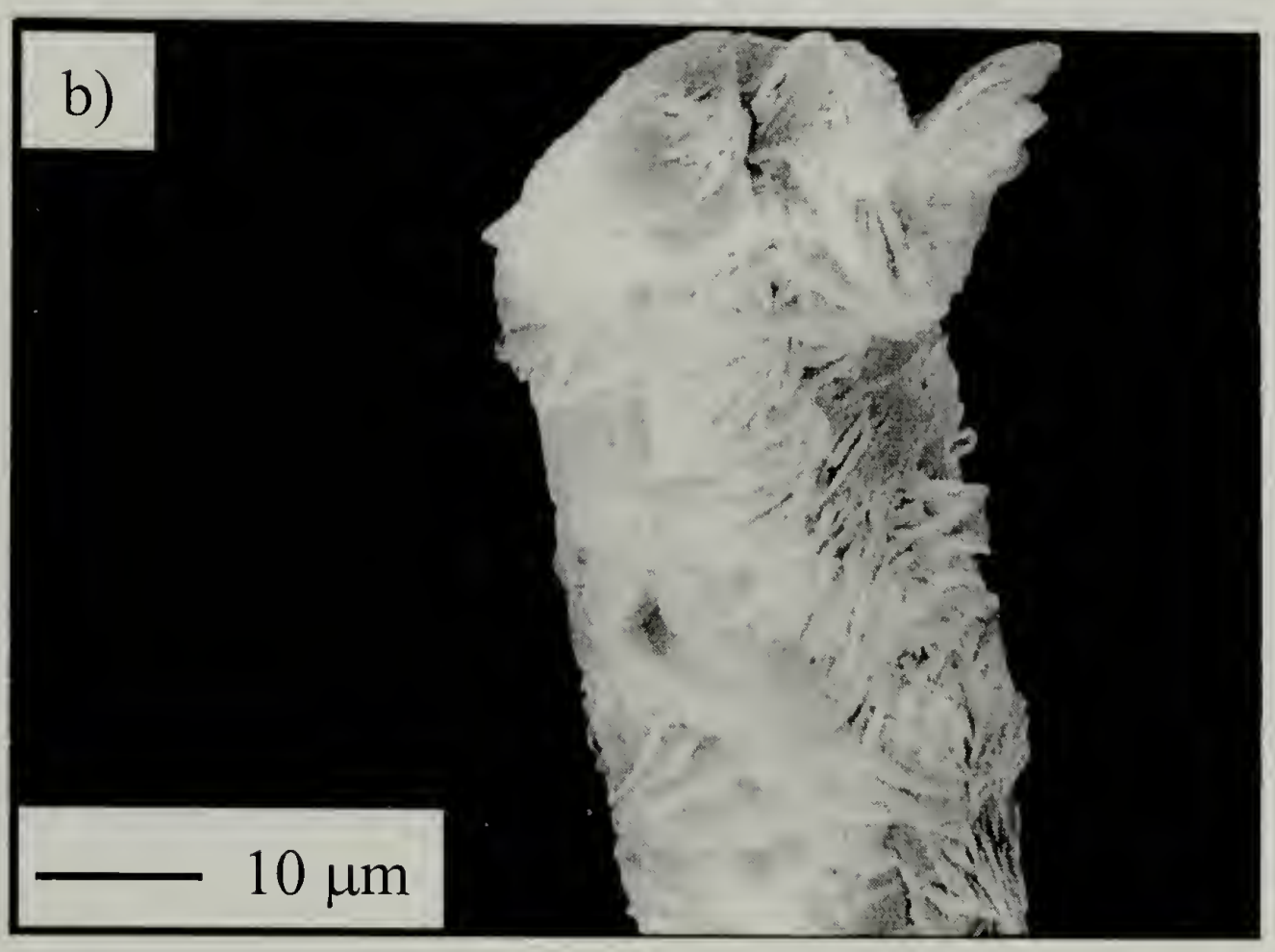

Figure 1.8: Ammonium tartrate crystals coated with PSA after one half (a), two (b), three (c) and four (d) hours of exposure.

Continued next page

Figure 1.8 continued

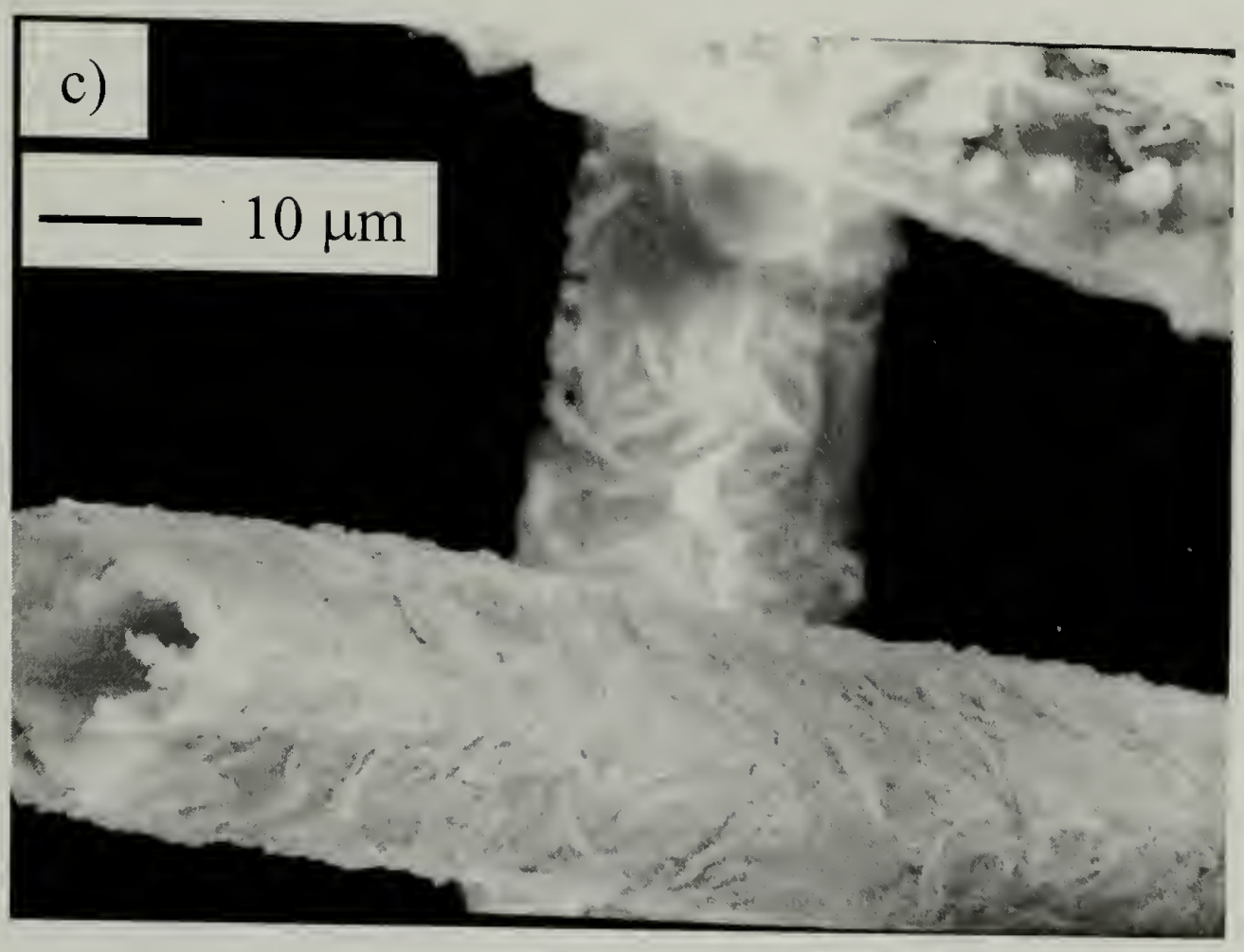

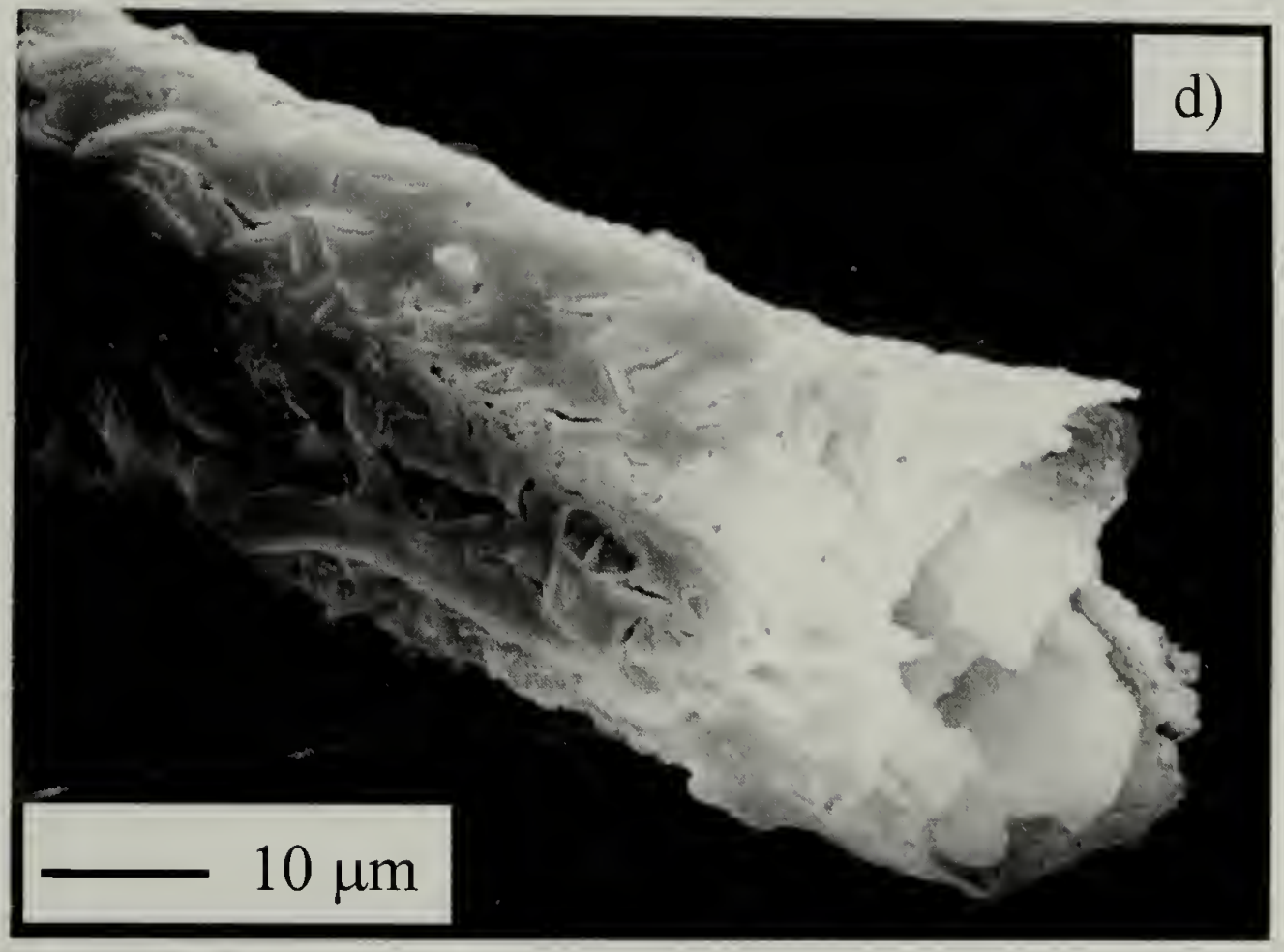

1.3.6 Polymer matrix composites with mesotube reaction products

Epoxy/mesotube polymer matrix composites were fabricated as described in section 1.34. Three point bend fracture toughness tests were conducted on pure epoxy and composites containing 2.5, 5 and 10 weight percent of mesotube synthesis reaction products. The stress intensity factor ($\mathbf{K_q}$) necessary for crack propagation was calculated using equation 1.1, where **M** is the bending moment given by equation 1.2, **Y** is a geometrical factor given by equation 1.3, **a** is the crack length, **W** is the specimen width, $\mathbf{P_c}$ is the applied load at failure, **B** is the specimen thickness and **S** is the distance between specimen support pins.

$$K_q = Y\left(\frac{6M}{BW^2}\right)\sqrt{a} \quad (1.1) \qquad M = \frac{Pc(S)}{4} \quad (1.2)$$

$$Y = \left(for\ \frac{S}{W} = 4\right) = 1.93 - 3.07\left(\frac{a}{W}\right) + 14.53\left(\frac{a}{W}\right)^2 - 25.11\left(\frac{a}{W}\right)^3 + 25.8\left(\frac{a}{W}\right)^4 \quad (1.3)$$

The stress intensity factor calculated using equation 1.1 is termed the conditional fracture toughness value and is only defined as the critical stress intensity factor ($\mathbf{K_{IC}}$) once it is established that fracture occurred in a state of plane strain. These initial tests are for comparison only and thus no experiments were conducted to evaluate if the specimens failed predominately in plane strain. However it is expected from others tests on epoxy systems that the specimen dimensions used do produce failures in plane strain.[29]

Figure 1.9 plots the compliance versus crack length data for pure epoxy and mesotube product composites. The compliance was taken from the slopes of the three point bend load versus displacement curves. It is clear that incorporation of the reaction products increases the stiffness of the composite. However, this increase in stiffness appears to be independent of concentration and is probably due to the broad availability

of reinforcement shapes obtained from this synthesis. It should be noted that a stick – slip phenomena was observed at 10 wt.% added reaction products. This is typically observed in neat resins under conditions which are quasi elastic. However, the toughness of the filled systems do not support this response (Figure 1.10).

Figure 1.10 shows the conditional fracture toughness values obtained from equation 1.1 normalized against that of pure epoxy (1.13 $MPa*m^{0.5}$). The error bars shown in Figure 1.10 are the standard deviation from a minimum of seven specimens per composite formulation. Fracture toughness decreases initially at low concentrations until at 10 wt.% the fracture toughness approaches that of the matrix and crack arresting occurs during testing. Thus, there is promise for heterogeneities of this length scale to act as the reinforcing phase in polymer matrix composites. However, this system clearly needs further optimization to reach its full potential. Reinforcing properties would be significantly improved upon removal of the particles in the reaction products.

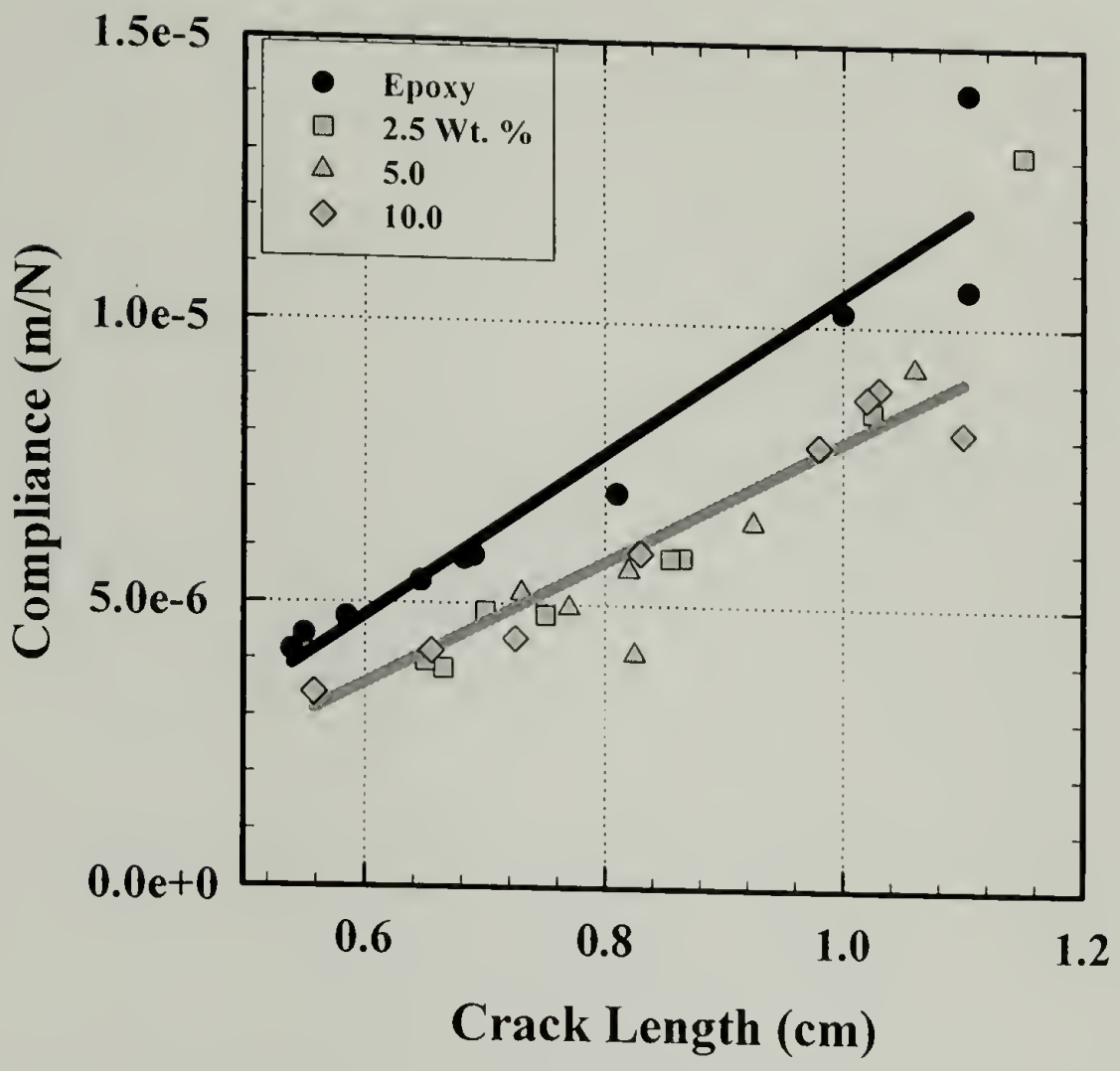

Figure 1.9: Compliance versus crack length for epoxy reinforced with mesotube reaction products.

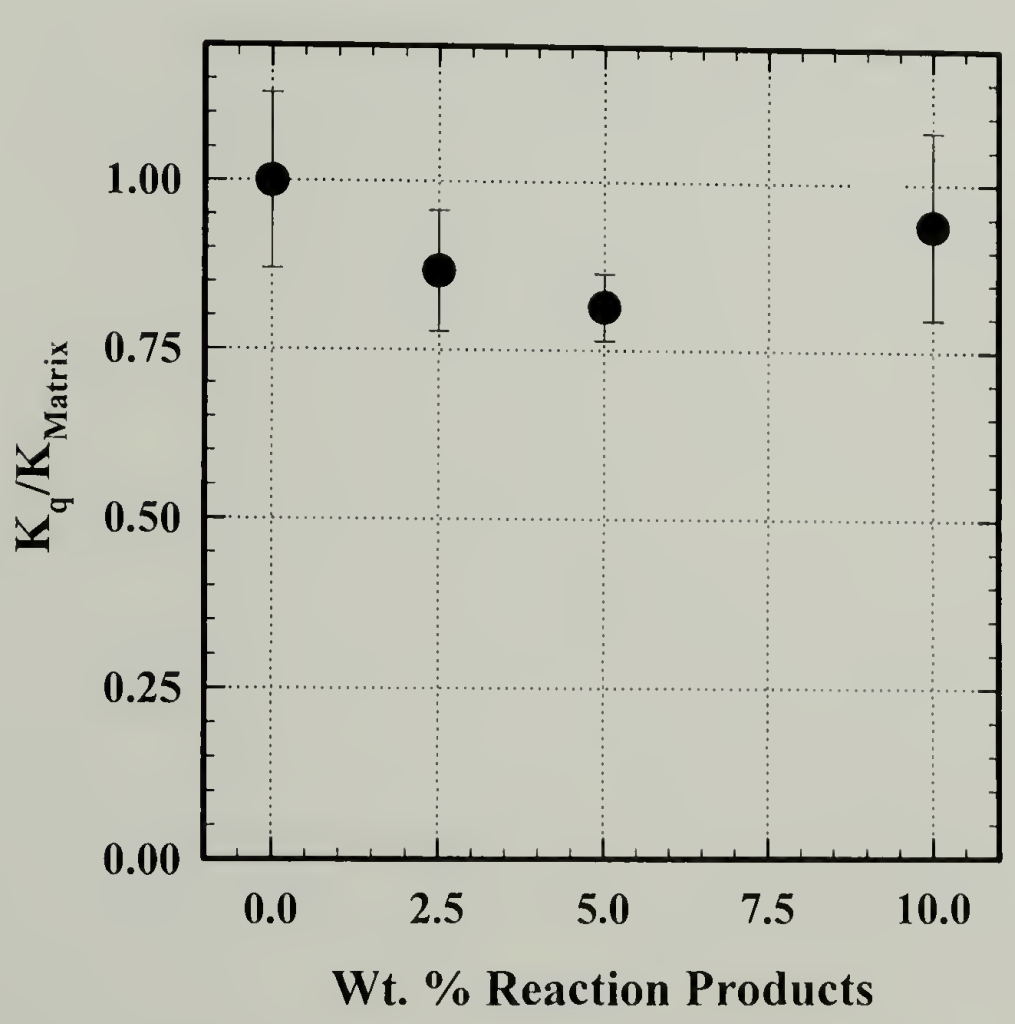

Figure 1.10: Conditional fracture toughness for epoxy reinforced with mesotube products.

1.4 Conclusions

The mechanism of rectangular SiO_2 tube is now elucidated. Upon addition of NH_4OH, TEOS rapidly condenses and precipitates from solution. Simultaneous with SiO_2 condensation, ATT crystallizes in the form of long prisms and is coated with SiO_2. Washing the products with water dissolves the ammonium tartrate templates out from within the SiO_2 coating leaving a tube having rectangular cross section. Addition of preformed ATT crystals to a PSA/THF solution caused PSA to condense on to the crystal surfaces. This indicates that the crystal surfaces are catalytic towards SiO_2 condensation. Thus, the coating of the ATT crystals during rectangular tube formation may not be merely serendipitous. ATT crystals may actively direct the deposition of SiO_2 onto their surfaces. Therefore, hollow SiO_2 structures of precisely controlled dimension and geometry may be formed via preformed ATT templates. Initial evaluation of the mesotube reaction products as a reinforcing phase of polymers indicates that as expected gains in stiffness occur. Fracture toughness decreases at low concentrations until at 10 wt.% the fracture toughness approaches that of the matrix with crack arrest occurring during testing. Thus, there is promise for heterogeneities of this length scale to act as the reinforcing phase in polymer matrix composites. However, this system clearly needs further optimization to reach its full potential. Properties would be significantly improved upon removal of the particles in the reaction products.

1.5 References

1) Agarwal, B. D.; Broutman, L. J. *Analysis and Performance of Fiber Composites*; 2 ed.; John Wiley and Son's, Inc.: New York, 1990.

2) Galli, E. *Plast. Compounding* **1991**, *May/June*, 73-82.s

3) Zelinski, B. J. J.; Uhlmann, D. R. *J. Phys. Chem. Solids* **1984**, *45*, 1069-1090.

4) Haruvy, Y.; Webber, S. E. *The Fast Sol-Gel Synthetic Route to Supported Glass Films: Synthetic Features, Scope, Applications and Mechanistic Studies*; Materials Research Society, 1992; Vol. 271, pp 297-302.

5) Pope, E. J. A. *Monolithic Optical Materials*; Pope, E. J. A., Ed.; Plenum Press: New York, 1994, pp 119-140.

6) Klein, L. C. *Sol-Gel Technology for Thin Films, Fibers, Preforms, Electronics, and Specialty Shapes*; Klein, L. C., Ed.; Noyes Publications: Park Ridge, 1988, pp 407.

7) Corriu, R. J. P.; Leclercq, D.; Vioux, A.; Pauthe, M.; Phalippou, J. *Some New Possibilities for the Preparation of Silica Gels*;John Wiley and Sons, Inc.: New York, 1987, pp 119-126.

8) Mann, S.; Burkett, S. L.; Davis, S. A.; Fowler, C. E.; Mendelson, N. H.; Sims, S. D.; Walsh, D.; Wilton, N. T. *Chem. Mater.* **1997**, *9*, 2300-2310.

9) Davis, S. A.; Burkett, S. L.; Mendelson, N. H.; Mann, S. *Nature* **1997**, *385*, 420.

10) Schnur, J. M. *Science* **1993**, *262*, 1669-1676.

11) Nakamura, H.; Matsui, Y. *J. Am. Chem. Soc.* **1995**, *117*, 2651-2652.

12) Schueneman, G. T.; Novak, B. M.; Lesser, A. J. *Chem. Mater.* **1999**, *submitted.*

13) ASTM *Standard Test Methods for Plane-Strain Fracture Toughness and Strain Energy Release Rate of Plastic Materials*; ASTM, Ed.; ASTM: New York, 1993; Vol. 2.1 D5045 - 93.

14) Stober, W.; Fink, A.; Bohn, E. *J. Colloid Interface Sci.* **1968**, *26*, 62.

15) Engelhart, G.; Michel, D. *High-Resolution Solid-State NMR of Silicates and Zeolites*; John Wiley and Sons: New York, 1987.

16) Damrau, U.; Marsmann, H. C. *J. of Non-C ryst. Solids* **1994**, *168*, 42-48.

17) Beek, J. J. v.; Seykens, D.; Jansen, J. B. H. *J. Non-Cryst. Solids* **1992**, *146*, 111-120.

18) Sanchez, J.; McCormick, A. V. *J. Non-Cryst. Solids* **1994**, *167*, 289-294.

19) Grimmerj, A. R.; Rosenberger, H.; Burger, H.; Vogel, W. *J. Non-Cryst. Solids* **1988**, *99*, 371-378.

20) Pouxviel, J. C.; Boilot, J. P.; Beloeil, J. C.; Lallemand, J. Y. *J. Non-Cryst. Solids* **1987**, *89*, 345-360.

21) Pouxviel, J. C.; Boilot, J. P. *J. Non-Cryst. Solids* **1987**, *94*.

22) Turner, C. W.; Franklin, K. J. *J. Non-Cryst. Solids* **1987**, *91*, 402-415.

23) Sugahara, Y.; Tanaka, Y.; Sato, S.; Kuroda, K.; Kato, C. *Silicon-29 NMR Study of the Initial Stage fo the CO-Hydrolysis of Tetraethoxysilane and Methyltriethoxysilane*; Vol. 271, pp 231-236.

24) McGrath, J. E.; Pullockaren, J. P.; Riffle, J. S.; Kilic, S.; Elsbernd, C. S. *Sol-Gel Networks: Fundamental Chemical Studies of Hydrolysis, Condensation, and Polysiloxane Toughening of Tetraethylothosilicate (TEOS) Systems*; John Wiley and Sons, Inc.: New York, 1987, pp 55-75.

25) Brinker, C. J.; Keefer, K. D.; Schaefer, D. W.; Assink, R. A.; Kay, B. D.; Ashley, C. S. *J. Non-Cryst. Solids* **1984**, *63*, 45-59.

26) Jonas, J. *Molecular-Level Understanding of the Sol-Gel Process*; Jonas, J., Ed.; John Wiley and Sons, Inc.: New York, 1987, pp 13-22.

27) Glasser, L. S. D.; Smith, D. N. *J. C. S. Chem. Comm* **1980**, 727-728.

28) Keefer, K. D.; Keefer, K. D., Ed.; MRS, 1986; Vol. II, pp 245.

29) Crawford, D.; University of Massachusets: Amherst, 1999, pp 168.

CHAPTER 2

ULTRASONIC SPECTROSCOPY ANALYSIS OF HETEROGENEOUS POLYMERS

2.1 Introduction

Nondestructive testing (NDT) methods are commonly used for quality control and safety certification.[1-3] One of the most commonly used methods of inspection is to employ ultrasonic sound waves to probe for defects.[1-3] Ultrasonics describes mechanical waves propagating in materials at frequencies above the upper limit of human hearing (f>20,000 Hz). Ultrasonic waves cause the medium to vibrate. The vibrations depend on the density and elasticity of the medium in which they travel and thus may be used to investigate their properties. The vibrational energy of the wave is transferred from one particle (element of volume) of the material to a neighboring particle and then to each particle in the medium as the sound wave moves through it. Each particle moves at slightly later times than the one before. Thus the vibrational motion travels with a finite velocity. Longitudinal and transverse sound waves are commonly used for ultrasonic inspection of materials. The particle motions associated with these waves are shown in Figure 2.1.

Figure 2.1: Particle motion induce by transmission of longitudinal (top) and transverse (below) waves.

Longitudinal waves move by localized compression and expansion of the medium and will travel though any material with longitudinal elasticity (all materials). The velocity of longitudinal waves is given in equation 2.1, where **E** is the elastic modulus and ρ is the density of the medium through which the waves are transmitting. Transverse waves move by localized shearing motions of the medium creating shear waves. This type of wave travels only in materials with shear elasticity (solids). The velocity of transverse waves is given in equation 2.2 where **G** is the shear modulus of the material in which the wave is traveling.

$$c_L = \sqrt{\frac{E}{\rho}} \qquad (2.1) \qquad\qquad c_T = \sqrt{\frac{G}{\rho}} \qquad (2.2)$$

Ultrasonic image (flaw) analysis involves sending high frequency pulses of electricity to a transducer containing a piezoelectric element. The piezoelectric element then vibrates imparting a pulsed mechanical deformation into any material it is in direct contact with. Sound waves are transmitted through materials until an interface is encountered and consequently the waves are reflected. The intensity of the reflected wave is dependent upon the density or elasticity mismatch of the two materials, this is known as the reflection coefficient. Characterization of the material occurs by detecting the reflections of the pulsed waves (pulse echo mode) or by using a second transducer to receive the transmitted pulses that penetrate the material (through transmission mode). As these reflected or transmitted mechanical pulses enter the transducer they induce vibrations within the piezoelectric element and it emits electrical pulses to a monitoring computer system. The computer generates a three dimensional map of the depth of the reflection or intensity of the transmitted sound as a function of the exact position on the sample. These techniques are commonly used to detect defects such as cracks and

impurities that can not be seen by visually inspection. An example is the detection of delaminations between layers in a multi-laminate composite. This type of defect may show no visual surface damage, but the integrity of the material is greatly compromised. The resolution of this method is dependent on how tightly the sound waves are focused and the geometry and orientation of the defect. This is depicted in Figure 2.2.[3]

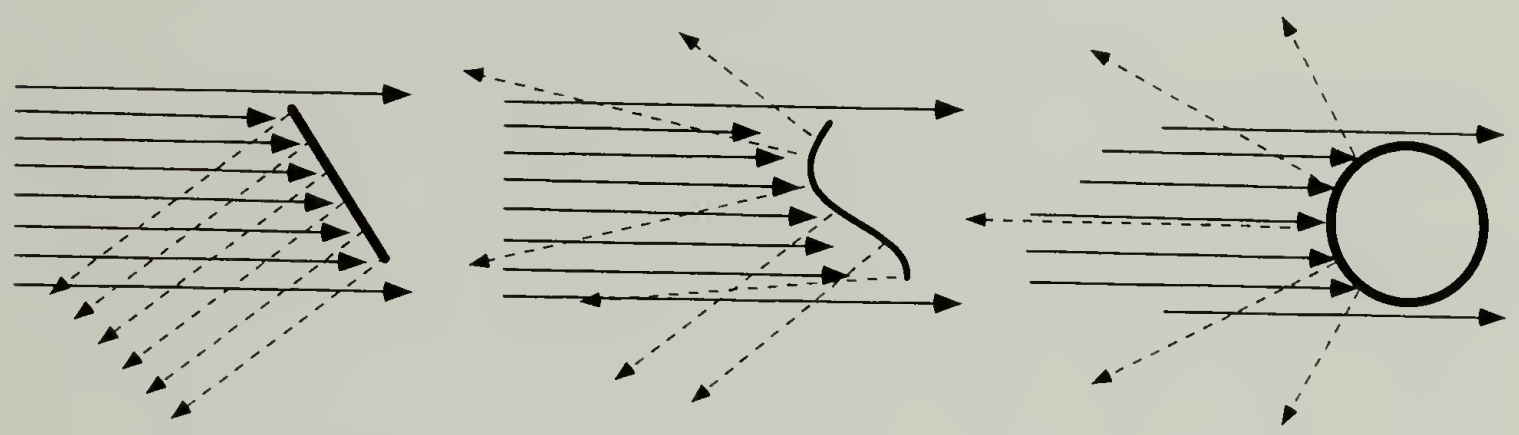

Figure 2.2: Reflection of sound waves by defects.

Higher resolutions of detection are achieved by discerning which frequencies of sound are transmitted and which are reflected by defects. As depicted in Figure 10, sound waves will begin to be scattered by defects that approach the wavelength of the sound and complete reflection will occur at defects that are larger than the wavelength of sound. Defects that are much smaller than the incident wavelength will not significantly interfere with the waves path.

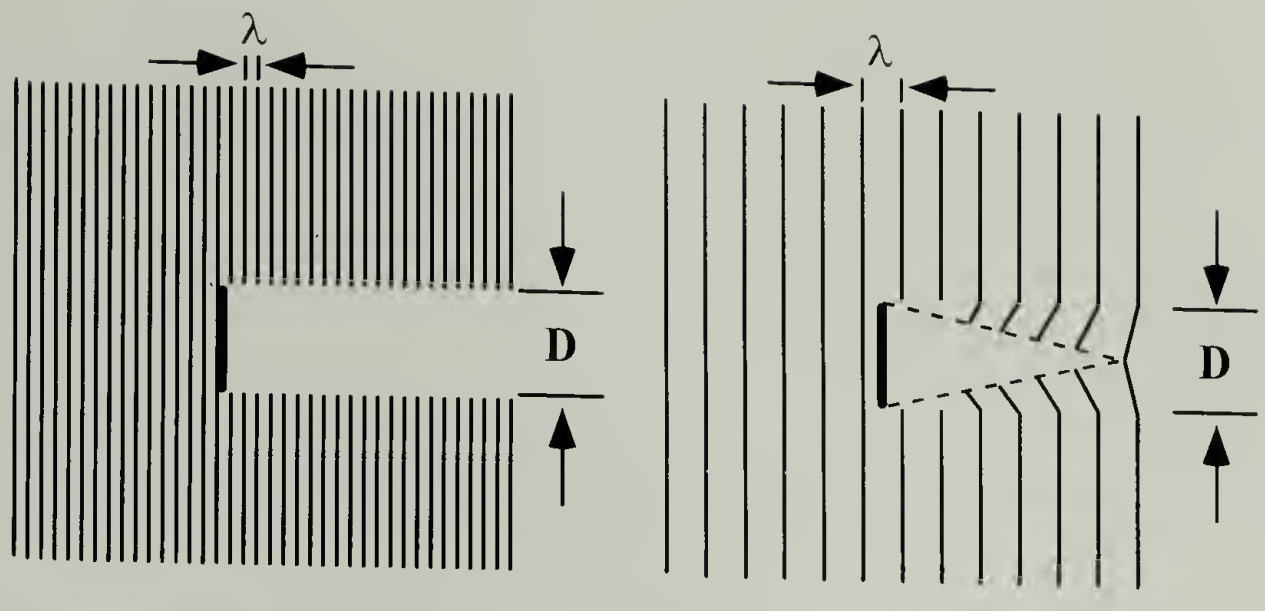

Figure 2.3: Scattering of sound waves by a defect.[3]

Thus, the resolution will be dependent upon the wavelength and the band width of the ultrasonic waves used. Also, because the wavelength is dependent upon the frequency and speed of the sound, resolution will depend upon the density and elasticity of the medium. This is shown in equation 2, where **c** is the speed of longitudinal or transverse waves as calculated using equation 2.1 and 2.2 and ω is the angular frequency ($\omega=2\pi f$). Using equation 2.3 the wavelength of sound waves of a given frequency can be determined for a given medium. This is shown in Figure 2.4 for aluminum, epoxy, and water. Note that water and aluminum represent the upper and lower bounds of resolution respectively where most polymers are within these bounds.

However, the above discussion is specifically for the case where the wavelength approaches the size of the heterogeneity. In general there are three regions; 1) long wavelength regime (LWR) where $\mathbf{r} << \lambda$ characterized by Rayleigh scattering, 2) intermediate regime (IMR) where $\mathbf{r} \sim \lambda$, and short wavelength regime (SWR) (a.k.a. Geometrical zone) where $\mathbf{r} >> \lambda$.[4,5] The size of the majority of heterogeneities introduced into polymers fall with in the LWR or the IMR. The IMR is limited by the

necessity to use high frequency sound waves that are strongly attenuated by polymers. Thus, ultrasonic characterization in the LWR would be the most powerful analysis method.

$$\lambda = \frac{c}{\omega} \qquad (2.3)$$

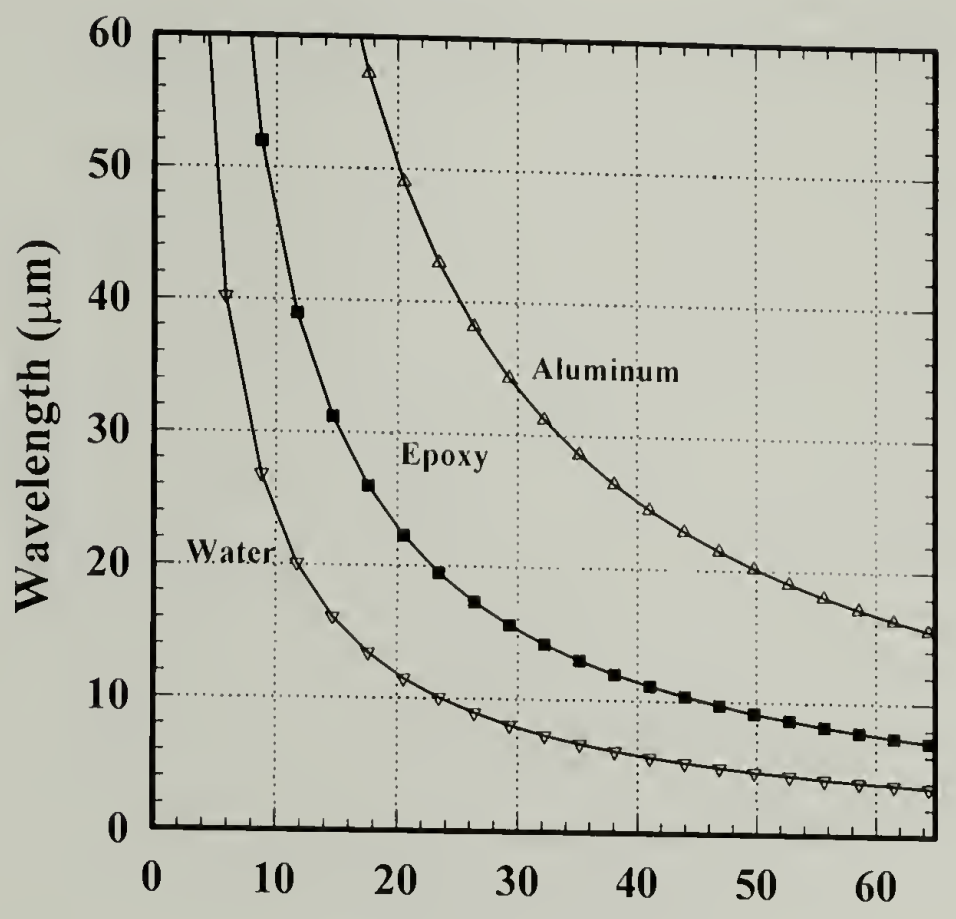

Figure 2.4: Wavelength of sound waves traveling in aluminum, epoxy, and water

2.2 Ultrasonic spectroscopy for the analysis of heterogeneous polymers

Methods of Investigating the structure of materials with ultrasound are being rapidly developed and utilized. Common methods are to examine the velocity and attenuation of ultrasonic waves and to correlate this with specific material properties and structure. Attenuation is the result of attenuation and scattering and can give unique results for a specific material in a given condition. A summary of some of the this research is listed below in Table 2.1.

Table 2.1: Summary of research efforts in ultrasonic analysis of polymers.

Research	Reference
Polymer property dependent velocity and attenuation	6-8
Identifying polymeric materials	9
Characterizing polymer solutions	10-14
Polymer blends	15-17
Polymer morphology	18,19

The complexity of the blends, alloys, and composite materials under development today make it difficult to characterize their morphology through conventional techniques. Ultrasonic spectroscopy is a new technique that utilizes high frequency (10-100 MHz) transducers to transmit and receive broad band ultrasonic signals through materials. Traditionally, morphology is characterized via gross differences in electron density (via electron microscopy), chemical nature (staining enhanced electron microscopy) and optical density (via optical microscopy). Ultrasonic spectroscopy images morphology through density and modulus differences and can do this regardless of optical clarity. This method is being developing to examine morphology via excess attenuation due to heterogeneities or changes in material condition. Ultrasonic spectroscopy utilizes traditional longitudinal sound waves that are transmitted through materials and converted into the frequency domain via fast Fourier transformation. Thus, we obtain a frequency spectrum that is specific to the morphology present.

Similar techniques were used to record characteristic frequency spectra were recorded for PE, PTFE, PMMA, and PC in the mid 1980's.[20] Also, the authors used a 5

MHz transducer to observe changes in the frequency spectra from 0.3 - 0.5 mm bubbles in PC and to observe changes in liquid crystalline phases.[20] Average pore sizes down to 100 μm have been detected in aluminum castings using the 1-20 MHz frequency range.[21]

Ying and Truell examined the scattering of a plane longitudinal wave by a single spherical obstacle in an isotropic - elastic solid.[22] Specifically they examined the case for Rayleigh scattering where the radius (**a**) of the obstacle is much smaller than the wavelength (λ) of sound used ($\mathbf{a} << \lambda$). They derived an expression for the rate that energy is transported away from a concentric surface enclosing the obstacle per unit time. This expression is then evaluated for a given obstacle by applying the boundary conditions of the resultant displacements and stresses imposed on the surface. A brief description of their derivation is presented here.

When a plane longitudinal wave encounters an obstacle scattering occurs. As a result, three separate waves exist: 1) the incident wave (I), 2) wave scattered by obstacle consisting of a longitudinal and transverse component, and 3) a transmitted wave also with having longitudinal and transverse components. The scattered and transmitted waves have transverse components due to mode conversion at the interface. The equation of motion for the incident wave is shown below in equation 3.

$$\rho_1 \ddot{\mathbf{S}} = (\lambda_1 + \mu_1)\nabla\nabla \bullet \mathbf{S} + \mu_1 \nabla^2 \mathbf{S} \qquad (2.4)$$

In equation 2.4, **S** is the displacement ($\mathbf{S} = \mathbf{s}e^{i\omega t}$), λ_1 and μ_1 are Lame's constants for the matrix (1), ρ_1 is the density of the matrix, and **s** is a function of space variables only. By choosing spherical coordinates and placing the origin at the center of the obstacle, **s** can be derived from the equation of motion of a wave with spherical symmetry.[23]

$$s = -\nabla\Psi + \nabla\times\left[\nabla\times\left(r_1 r\Pi\right)\right] \qquad (2.5)$$

where $\left(\nabla^2 + k^2\right)\Psi = 0$, $\left(\nabla^2 + \kappa^2\right)\Pi = 0$

$$k_n = \frac{2\pi}{\lambda_L} = \frac{\omega}{\sqrt{\frac{\lambda_n + 2\mu_n}{\rho_n}}} = \frac{\omega}{c_L} \qquad \kappa_n = \frac{2\pi}{\lambda_T} = \frac{\omega}{\sqrt{\frac{\mu_n}{\rho_n}}} = \frac{\omega}{c_T}$$

Ψ and Π represent the longitudinal and transverse components of the waves. $\mathbf{k_n}$ and κ_n are the acoustic wave number for the longitudinal and transverse waves respectively, where n denotes the medium the wave is traveling through. The incident wave has Π=0. Ψ and Π are functions of **r** and θ but not **z**. $\mathbf{r}_1$ is a unit vector in the direction of increasing **r**. Equation 2.5 was solved for the incident, scattered and transmitted wave, yielding expressions for Ψ and Π. The solutions contain undetermined coefficients that must be solved for by imposing the boundary conditions specific to the obstacle encountered. This was accomplished by obtaining expressions for the stresses and displacements in terms of Ψ and Π.

The energy scattered per unit time from a concentric surface enclosing the obstacle with radius **b** where **b>a** was derived in terms of the stresses and displacements acting on the surface. The relations between the stresses and displacements and the longitudinal and transverse components of the wave (Ψ and Π) allow the rate of energy transport to be expressed in terms of the undetermined coefficients. The scattering cross section (γ) is defined as the ratio of the total energy scattered per unit time to the energy per unit area carried per unit time by the incident wave. Combining this definition with the relation for the rate of energy transport yield an equation for the scattering cross section in terms of the undetermined coefficients.

$$\gamma = 4\pi \sum_{m=0}^{\infty} \frac{1}{2m+1} \left[|A_m|^2 + m(m+1) \frac{k_1}{\kappa_1} |B_m|^2 \right] \qquad (2.6)$$

$\mathbf{A_m}$ and $\mathbf{B_m}$ are the undetermined coefficients that must be solved for by imposing the appropriate boundary conditions for the specific obstacle. Ying and Truell solved this equation for a spherical elastic obstacle and a spherical cavity. Later Einspruch and Truell solved the equation for the case of a fluid filled cavity in an elastic medium.[24] The equations are similar in form and can be represented in general by equation 2.7 where $\mathbf{g_X}$ is a function of the elastic properties of the matrix and the scattering obstacle. Thus, there are three contributions to the scattering cross section; 1) elastic properties of the materials present, 2) the wavelength of the sound used, and 3) the size of the scattering obstacle. Equations yielding $\mathbf{g_X}$ for the various heterogeneities are given by equations 2.8 (elastic solid, $\mathbf{g_S}$), 2.9 (cavity, $\mathbf{g_C}$), and 2.10 (fluid, $\mathbf{g_F}$).

$$\gamma = \frac{4\pi}{9} k_1^4 a^6 g_X \qquad (2.7)$$

$$g_S = \left[\frac{3\frac{\kappa_1^2}{k_1^2}}{\left(3\frac{\kappa_2^2}{k_2^2} - 4\right)\frac{\mu_2}{\mu_1} + 4} - 1 \right]^2 + \frac{1}{3}\left[1 + 2\left(\frac{\kappa_1}{k_1}\right)^2\right] * \left[\left(\frac{\kappa_2}{\kappa_1}\right)\frac{\mu_2}{\mu_1} - 1\right]^2 + 40\left[2 + 3\left(\frac{\kappa_1}{k_1}\right)^5\right]$$
$$* \left[\frac{\frac{\mu_2}{\mu_1} - 1}{2\left(3\frac{\kappa_1^2}{k_1^2} + 2\right)\frac{\mu_2}{\mu_1} + \left(9\frac{\kappa_1^2}{k_1^2} - 4\right)} \right]^4 \qquad (2.8)$$

$$g_C = \frac{4}{3} + 40\frac{2 + 3\left(\frac{\kappa_1}{k_1}\right)^5}{\left[4 - 9\left(\frac{\kappa_1}{k_1}\right)^2\right]^2} - \frac{3}{2}\left(\frac{\kappa_1}{k_1}\right)^2 + \frac{2}{3}\left(\frac{\kappa_1}{k_1}\right)^3 + \frac{9}{16}\left(\frac{\kappa_1}{k_1}\right)^4 \qquad (2.9)$$

$$g_F = \left\{ \left(\frac{1}{4(k_f^2/\kappa_1) + 3(\rho_f/\rho_1)} \right)^2 + \frac{1}{3}\left(\frac{\rho_f}{\rho_1} - 1 \right)^2 \left(2\frac{\kappa_1^3}{k_1^3} - 1 \right) + 10 \frac{\left[8\frac{k_1^2}{\kappa_1^2} + 3\frac{\kappa_1}{k_1} \right]}{\left[\frac{1}{9 - 4(k_1^2/\kappa_1^2)} \right]^2} \right\} \qquad (2.10)$$

The scattering cross section can be expressed as a unitless quantity by dividing by the cross sectional area of the scatterer.

$$\gamma_N = \frac{\gamma}{\pi a^2} \qquad (2.11)$$

The scattering cross section has the same form for both obstacle with dependence on $\mathbf{k}_1$ to the fourth power and **a** to the sixth power. All **g** terms are dependent upon the ratio of the wave numbers. The $\mathbf{g}_S$ term also has a dependence on the ratio of the shear moduli. The ratio of the wave numbers equates to the ratio of the longitudinal wave velocity to that of the transverse velocity, as shown in equation 2.12 where σ is Poisson's ratio. The ratio of velocities is greater than then $\sqrt{2}$ for an isotropic elastic medium.[22,25]

$$\frac{\kappa}{k} = \sqrt{\frac{\lambda + 2\mu}{\mu}} = \sqrt{\frac{2(1-\sigma)}{(1-2\sigma)}} = \frac{c_L}{c_T} \qquad (2.12)$$

The scattering cross section is more commonly calculated from the ratio of the incident beam intensity ($\mathbf{I}_o$) to that of the reflected or transmitted intensity (**I(x)**) and represents the decay of the intensity or energy flux, as shown in equation 2.13, where **x** is the distance the beam has traveled. The attenuation coefficient is generally defined as the ratio of the incident amplitude ($\mathbf{A}_o$) to that of the reflected or transmitted wave (**A(x)**) and describes the amplitude decay, equation 2.14. The decay of the intensity is twice that of the amplitude and this relation ship is shown in equation 2.15.[26]

$$\gamma = -\frac{n_O}{x} \mathrm{Ln} \frac{I(x)}{I_O} \qquad (2.13)$$

$$\alpha = -\frac{n_o}{x} \mathrm{Ln} \frac{A(x)}{A_o} \qquad (2.14) \qquad\qquad \alpha = \frac{1}{2} n_o \gamma \qquad (2.15)$$

$$\text{where } n_o = \frac{\#\,\text{Scatters}}{\text{Volume}} = \text{number density of scatters}^{27}$$

Franzblau and Kraft measured attenuation of longitudinal waves in porous tungsten filaments.[28] The pores were introduced into tungsten by heating to 3000 °C. The pores consisted of randomly distributed spherical cavities with a mean diameter of 8.2 ± 0.2 μm and number density of (1.3±0.5)x10^7 cm^{-3} as determined via metallographic counting procedures. The attenuation versus frequency data was fitted with equation 2.15 until the root mean square deviation reached a minimum. This approach yielded values of 8.2 for the mean radius and 3.3x10^6 cm^{-3} for the number density. Which shows good agreement between measurement and theory.

Sayers examined the case of a plane longitudinal wave traveling in an elastic medium with a distribution of spherical cavities.[25] He used the same approach as Ying and Truell[22], and Waterman and Truell[29], except after obtaining expressions for the undetermined coefficients he used the complex propagation constant (β). equation 2.16, and related the amplitude of the wave scattered in the forward direction (**f**) to obtain expressions for the undetermined coefficients. This was accomplished using the relation Foldy derived for the scattering of waves by randomly distributed elastic obstacles, equation 2.17.[30]

$$\beta = \frac{\omega}{c_L} + i\alpha \qquad (2.16) \qquad\qquad \left(\frac{\beta^2}{k}\right) = 1 + \frac{4\pi n_o}{k^2} f \qquad (2.17)$$

Waterman and Truell extended the work of Ying and Truell to derive equations describing a wave propagating in a medium containing an array of finite scatters.[29] They

used the average exciting incident on a medium containing a uniform random distribution of identical scatterers. The result of their derivation is an equation for the complex propagation constant describing the propagation in the scattering medium.[29] They state that their equation appear to be valid for all regimes of scattering.[29] Restrictions are imposed upon the density and scattering amplitude of the obstacles to obtain the broad applicability of their equation. When the case of isotropic scatterers is considered Foldy's result is also obtained which is shown above in equation 2.17.

Continuing with Sayers' derivation, the undetermined coefficients are solved and equation 2.17 can be written as;

$$\left(\frac{\beta}{k}\right)^2 = 1 - \frac{4}{3}\pi a^3 n_o \left(A + Bk^2a^2 - iCk^3a^3\right) \quad (2.18)$$

Where A, B, and C are functions of $\kappa/\mathbf{k}$ which is equal to $\mathbf{c_L/c_T}$. The functions A, B, and C are similar to the $\mathbf{g_X}$ constant derived by Truell *et al.* except they are only functions of $\mathbf{c_L/c_T}$ as measured for the heterogeneous material in question.

The imaginary and real components of equation 2.18 can be separated yielding the velocity dispersion and the attenuation coefficient, equations 2.19 and 2.20 Velocity dispersion can be determine from the phase as a function of frequency as described by McClements and Fairley.[31]

$$\frac{c_L'}{c_L} = 1 + \frac{1}{2}\frac{\Delta V}{V}\left(A + Bk^2a^2\right) \quad (2.19) \qquad \text{where } \frac{\Delta V}{V} = \frac{4}{3}\pi a^3 n_o$$

$$\alpha = \frac{2\pi n_o}{3} k^4 a^6 C \quad (2.20)$$

The above discussion illustrates the potential for ultrasonic spectroscopy to provide information about the length scale and nature of phase separated materials.

However, no comprehensive study exists that explores the capabilities or limitations of this method. This chapter presents the results of employing ultrasonic spectroscopy to characterize heterogeneous polymers with a range heterogeneity sizes and natures.

2.3 Experimental

2.3.1 Porous epoxy

Specimens were synthesized by Dr. Emmett Crawford as describe in his dissertation.[32] The synthesis will be briefly discussed here. Epon 825 (Shell Chemical Co.), a diglycidyl of bisphenlol A, was stored under vacuum at 80 °C for 24 hr before being mixed with a stochiometric quantity of aminoethylpiperazine (AEP) (Aldrich Chemical Co.) and 10 weight percent of reagent grade hexane (VWR scientific). A heterogeneous mixture resulted where the continuous phase was a mixture of epoxy, curing agent, and hexane and the dispersed phase was hexane. This was allowed to gel at room temperature (20 °C) for 8 hr, heated at 60 °C for 3 hr and then completely cured after 3 hr at 150 °C.

2.3.2 Foamed polystyrene

Specimens were provided by Dr. Keyln Arora and fabricated as detailed in her dissertation.[33] Briefly, polystyrene (PS) (density: 1.04 g/cm^3, weight average molecular weight 190,000 g/mol) was obtained from Scientific Polymer Products, Inc., compression molded into 0.32 cm thick plaques, and sections of the plaques were saturated with supercritical carbon dioxide at 40 °C and 240 atm. Saturation with CO_2 markedly decreases polystyrene's glass transition temperature such that 40 °C is above this

temperature. Thus, releasing the pressure causes CO_2 to precipitate within the polystyrene forming domains that continue to grow until enough CO_2 is removed such that PS is no longer abovc its T_g. The specimens analyzed via ultrasonic spectroscopy were produced in this manner by releasing the CO_2 pressure instantly, over 3 minutes, and over 25 minutes.

2.3.3 Acrylic based blends

Specimens were provided by Dr. Naveen Agarwal and fabricated as detailed in his disscrtation.[34] Briefly, latex blends of poly(methyl methacrylate-*co*-ethyl acrylate) having a Tg of 45 °C and poly(methyl methacrylate-*co*-butyl acrylate) having a T_g of –5 °C were cast from solution on to glass platcs, dried at 70 °C for 3 to 4 hr and annealed at 130 °C for 20 minutes. The copolymer with a Tg of 45 °C is labeled the hard phase and that having a T_g of –5 °C is labeled soft for discussion purposes.

2.3.4 Rubber modified epoxy

Epon 828 (Shell Chemical Co.), a diglycidyl ether of bisphenol A, was stored under vacuum at 80 °C for 24 hr before being mixed with a stochiometric quantity of Jeffamine D230 (Huntsman Chemical Co.), an aliphatic tertiary amine curing agent and a desired weight percent of carboxyl terminated butadiene-*co*- acrylonitrile (CTBN) rubber modifier (BFGoodrich Performance Materials, Inc.). The mixture was allowed to degas at 50 °C for 30 minutes before being poured in to a reaction vessel and then gelled at the desired temperature. Gelation was roughly determined by tapping the specimen with a

pipette and ensuring that it was hard and no longer tacky. After gelation the specimens were placed in an oven at 150 °C for 15 hr to complete the cure.

2.3.5 Ultrasonic spectroscopy analysis

Specimens were analyzed by placing them between two ultrasonic transducers submerged in a water bath. An aluminum fixture held the transducers in place and allowed for accurate alignment. Also, the fixture held a removable polycarbonate specimen holder such that specimens could be accurately placed in the beam path. Specimens were obtained or machined such that they had a thickness of 0.6 mm or less with a variation of ± 3 μm. Three pairs of Panametrics, Inc. transducers were used to obtain a broad bandwidth. The transducers were driven by a Panametrics, Inc. model 5900 pulser/receiver. The transducer pairs and pulser/receiver settings are given in Table 2.2, where P and R denote the pulsing and receiving transducer respectively. Signals transmitted thought the specimen were conditioned by the pulser/receiver and digitized at a rate of 1 GHz with a Sonix STR81G PC based digitizer. Panametrics Inc. Multiscan software was used to set the trigger threshold and gate the received signals. A schematic of the setup is shown in Figure 2.5. The gated signal was averaged fifty times, baseline set to zero (mean subtracted), zero filled (band pass filtered), and transformed into the frequency spectrum via fast Fourier transformation. This process is demonstrated with the waveform and resultant frequency spectrum for 50 MHz through transmission of water in Figure 2.6.

Table 2.2: Transducer pairs used and pulser/receiver settings.

Transducer Pair (model, element diameter, focal length)	**Pulser Receiver Settings (Attenuation, Energy, Damping, Gain)**
P) 20 MHz V316, 0.32 cm, 1.9 cm R) 20 MHz V3287, 0.635 cm, unfocused	36 dB, 32 μJ, 7 Ohm, 40 dB
P) 50 MHz V390, 0.635 cm, 1.3 cm R) 50 MHz V3409, 0.635 cm, 4.45 cm	12.5 dB, 4 μJ, 7 Ohm, 40 dB
P/R) 100 MHz V3193, 0.635 cm, 1.3 cm	4.5 dB, 16 μJ, 7 Ohm, 54 dB

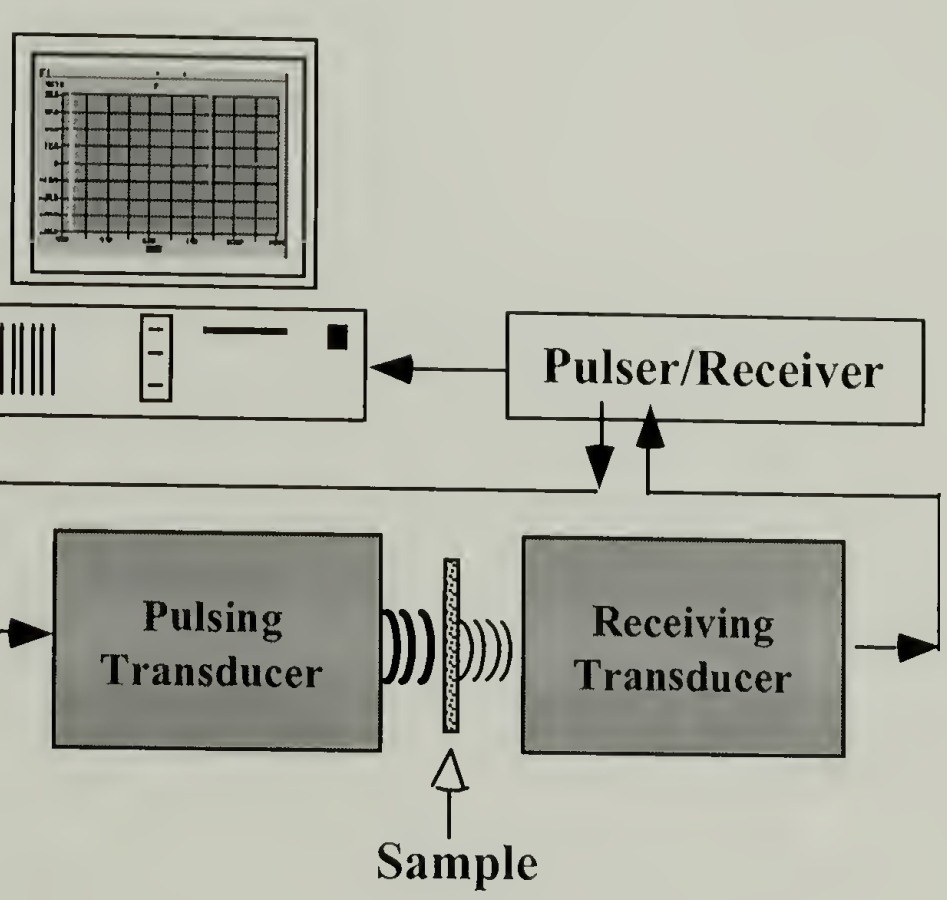

Figure 2.5: Experimental setup for ultrasonic spectroscopy of heterogeneous polymers.

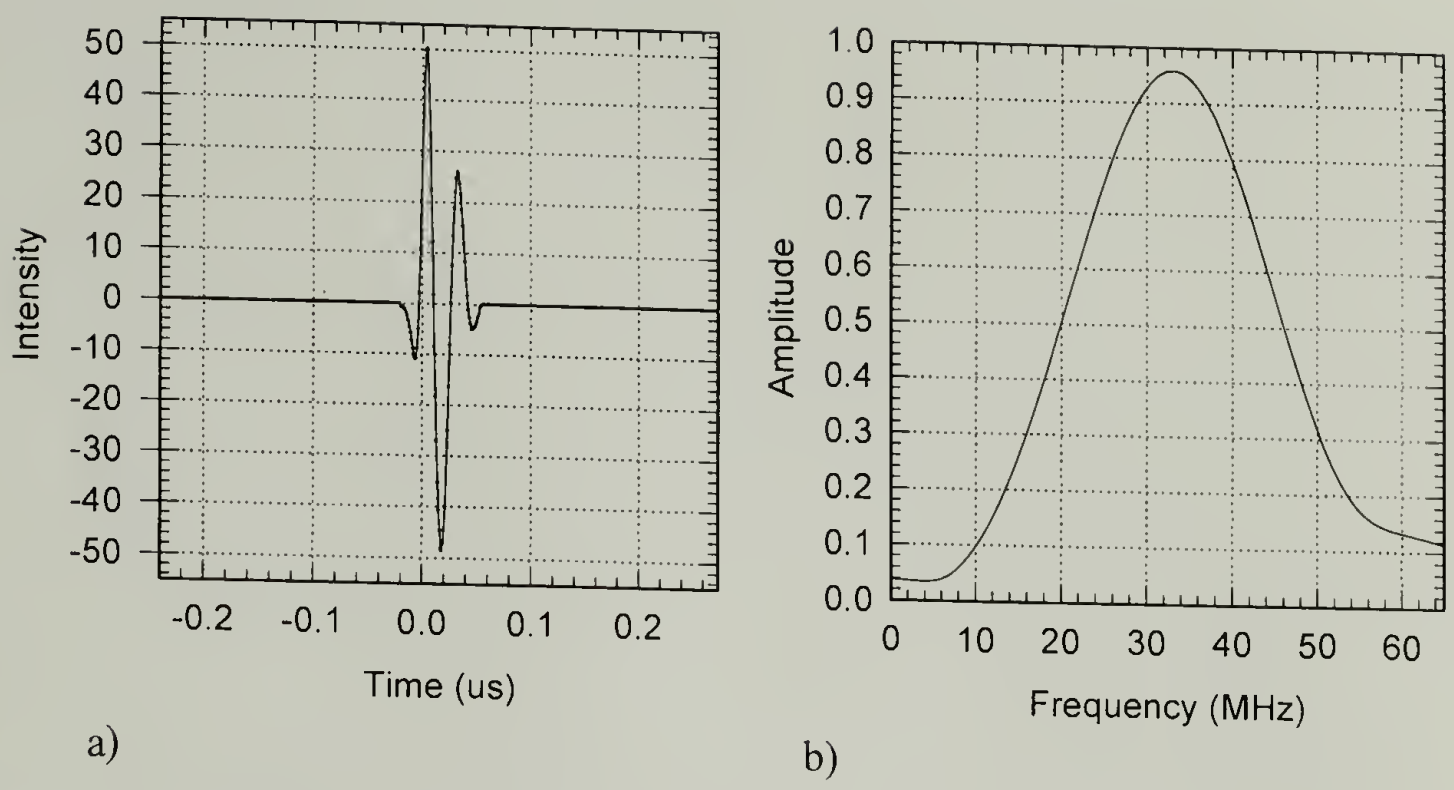

Figure 2.6: Waveform (a) and frequency spectrum (b) for through transmission of water.

2.3.6 Ultrasonic sound velocity

2.3.6.1 Longitudinal wave velocity

The 20 MHz Panametrics model V316 focused transducer was configured in a pulse/echo mode such that reflections from the front face and back wall of all specimens could be captured and recorded. The velocity was calculated as the ratio of twice the specimen thickness to that of the time between the front face and back wall reflection.

2.3.6.2 Shear wave velocity

Specimens were placed in direct contact with a 10 MHz Panametrics model V271BA unfocused shear wave transducer with honey (ρ=1.421g/cm^3) as a coupling medium. The velocity was calculated in a similar manner as that for the longitudinal waves. The thickness of the honey layer was 6 μm and thus will not greatly effect the values from the 0.5 mm thick specimens.

2.3.7 Differential scanning calorimetry (DSC)

Glass transition temperatures were measured on 5-15 mg samples sealed in TA Instruments aluminum hermetic pans and scanned at 10 °C per minute using a TA Instruments DSC Model 5910. Also, DSC was used to ensure the cure of the epoxies was complete. This is evidenced by an unchanged Tg after further heating at 150 °C. SEM.

2.3.8 Density

Density measurements were conducted by placing small quantities of each specimen into a density gradient column and recording the resting height of the specimens. The specimen density was then determined from a calibration plot of the density of glass spheres versus their resting position in the gradient column. The density gradient column was constructed by filling a jacketed cylinder with a mixture of heptane and carbon tetrachloride such that a density range of 1.03 to 1.24 g/cm^3 was obtained. The column was filled with Hewlett Packard Model 1050 gradient high performance liquid chromatography pump which input the desired ratio of each solvent as a function of column height. Polystyrene is soluble in carbon tetrachloride and thus its density and that of the PS foams were determined by volume displacement in ethanol. Although the volume is not as accurate as the gradient column with these small samples good agreement was obtained between the measured value (1.0 g/cm^3) and that reported by Scientific Polymer Products, Inc. (1.04 g/cm^3).

2.3.9 Scanning Electron Microscopy (SEM)

SEM images were taken using a Joel model 35CF SEM in secondary electron image mode. All specimens were frozen in liquid nitrogen and then fractured with the aid of a razor blade. The specimen fracture surfaces were mounted on 2.54 cm diameter aluminum disks using carbon tape and then coated with gold using a Polaron Instruments Inc. SEM Unit, model E51000.

2.3.10 Image analysis

SEM images were scanned into computer memory using a Hewlett Packard Scanjet 4c scanner and Deskscan II V2.3 software. Images brought into Ziess image analysis software version 3.0 as TIF files and the heterogeneities were identified and measured allowing the determination of the average diameter and the number density.

2.4 Results and Discussion

2.4.1 Ultrasonic spectrometer resolution

The resolution of this technique is dependent upon the bandwidth of the transducers and the material properties of the material under examination. Specifically, it is entirely dependent upon which scattering regime in being utilized. The resolution for Rayleigh scattering ($\mathbf{r} << \lambda$) is dependent the scattering efficiency of the discrete phase which is directly related to the property mismatch between the continuous and discrete phases. In the intermediate regime ($\mathbf{r} \sim \lambda$), resolution is still dependent upon property mismatch but is dominated by the wavelength of sound transmitted through the specimen. In order to maximize the bandwidth and hence intermediate regime resolution, three pairs

of transducers were utilized. The frequency spectra obtained using thesc transducers upon through transmission of water at 20 °C are shown in Figure 2.7. By setting a cutoff spectrum amplitude of 0.25 the available resolution regimc can be determined. The obtained bandwidths are shown in Table 2.3. The resolution lines calculated using equation 2.3 for epoxy (828/D230), polystyrene, and water are plotted in Figure 2.8 The wavelengths of sound that correspond to the available frequencies are shown in Table 2.3 for epoxy (828/D230).

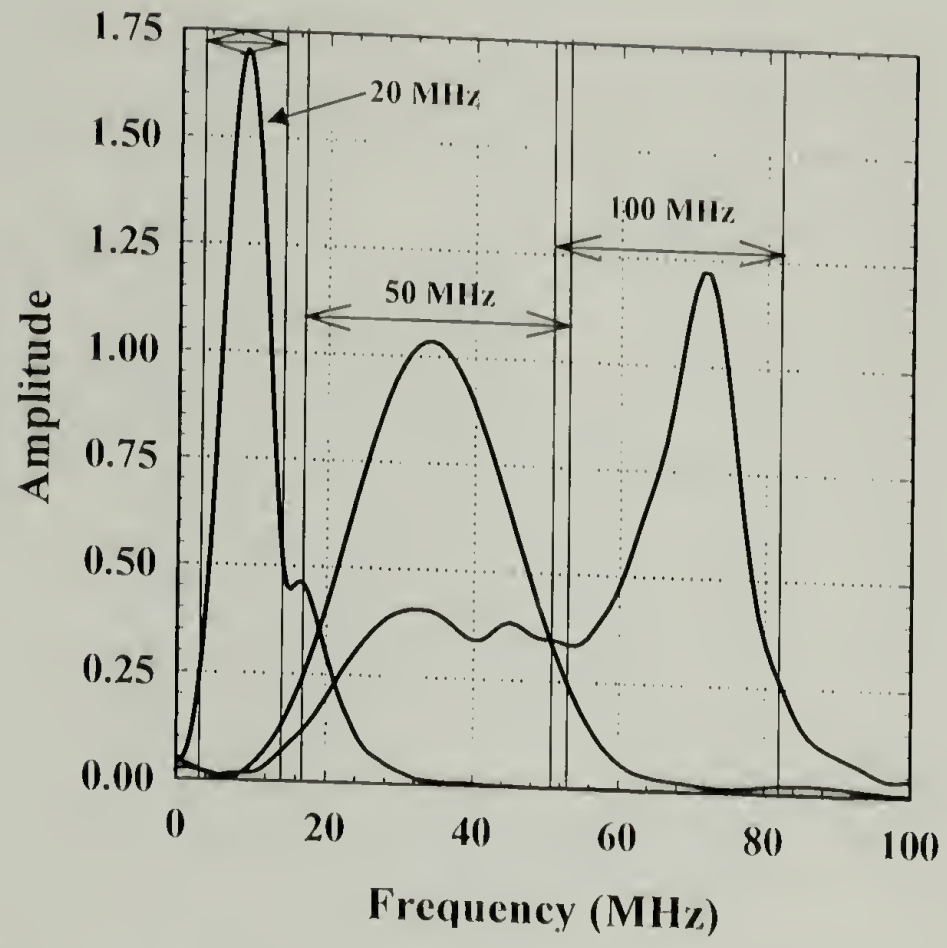

Figure 2.7: Frequency spectra from 20, 50, and 100 MHz transducer pairs.

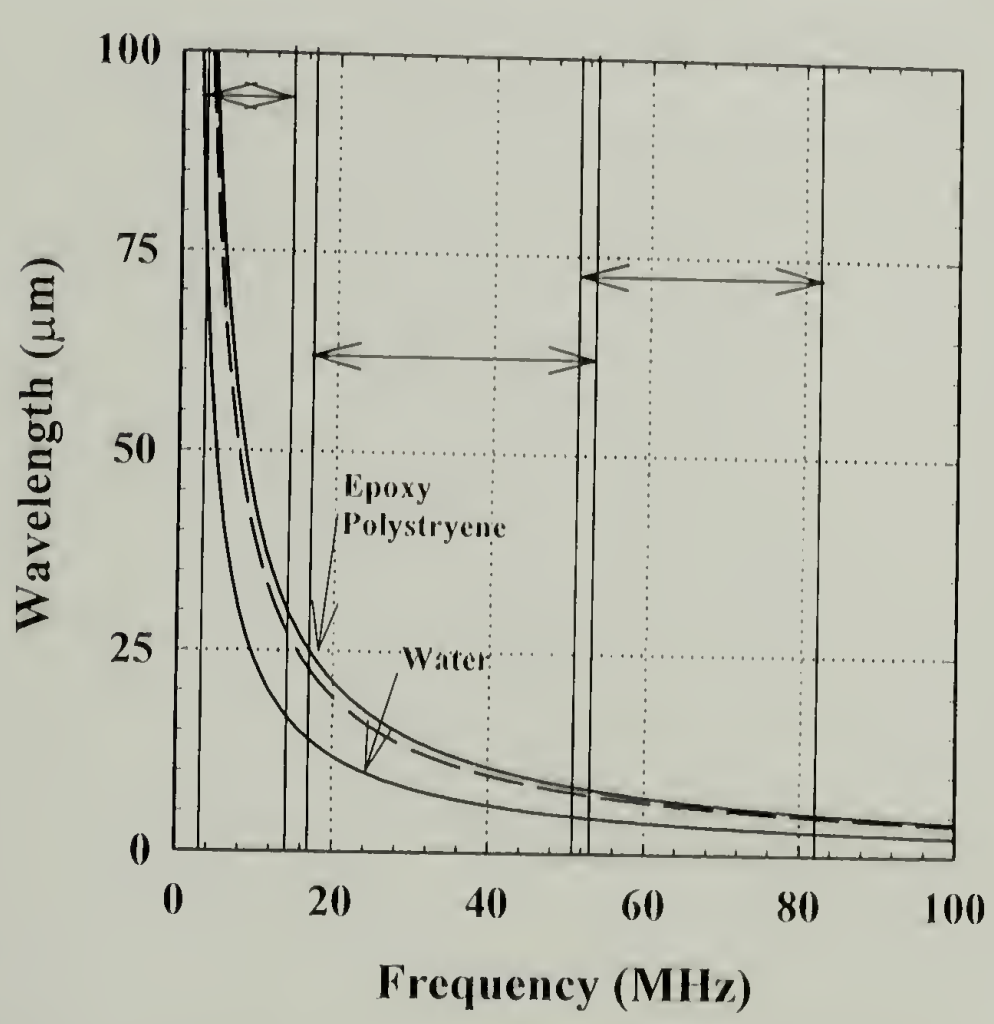

Figure 2.8: Resolution lines for epoxy (828/D230 – Ave), polystyrene, and water.

Table 2.3: Frequency bandwidth and wavelength for transducer pairs.

Transducers (MHz)	**Frequency Band Width (MHz)**	**Wavelength (μm) for Epoxy (828/D230 – Ave)**
20	3 – 14	30 – 144
50	17 – 54	8 - 25
100	51 - 82	5 - 8

Attenuation due entirely to interaction with the sample must be separated from the attenuation of the water path and that of the transmitting and receiving transducers. The amplitude of the experimentally measured frequency spectra represent frequency transfer functions which have contributions from the water path, transducers, and signal conditioning equipment. This is shown in Figure 2.9 where **y(t)** is the observed time domain transfer function given by equation 2.21 and **Y(w)** is the frequency transfer function obtained by fast Fourier transformation of **y(t)**, see equation 2.22.

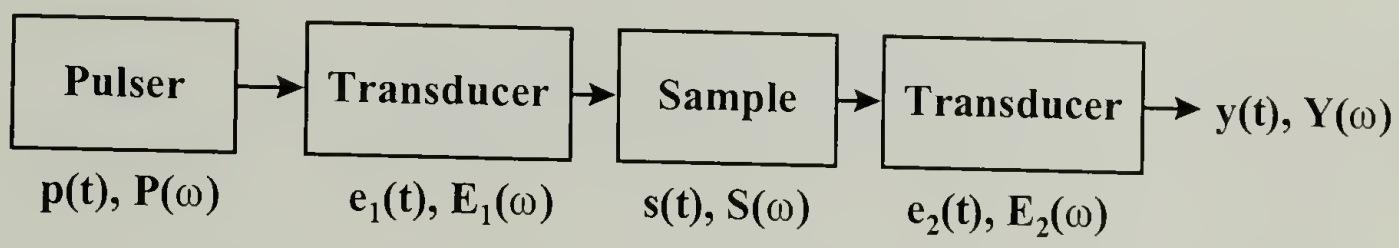

Figure 2.9: Time and frequency functions for individual components of ultrasonic spectroscopy apparatus.

$$y(t) = \int e_2(t_3)dt_3 * \int s(t_2)dt_2 * \int e_1(t_1) * p(t - t_1 - t_2)dt_1 \qquad (2.21)$$

$$Y(\omega) = \int y(t) - e^{-i\omega t}dt \qquad (2.22)$$

Also shown in Figure 2.9, are the time domain and frequency functions for each component of the ultrasonic spectroscopy apparatus. This approach is similar to the single pulse excitation method proposed by Matsushige and coworkers.[35] **Y(w)** is the

frequency transfer function when a sample is placed in the beam path and is related to the frequency functions of the all the components of ultrasonic apparatus, equation 2.23.

$$Y(\omega) = P(\omega) * E_1(\omega) * S(\omega) * E_2(\omega) * R(\omega) \quad (2.23)$$

In the absence of a sample (**Y'(ω)**) the frequency transfer function is given by equation 2.24.

$$Y'(\omega) = P(\omega) * E_1(\omega) * E_2(\omega) * R(\omega) \quad (2.24)$$

Thus, the frequency response of the sample (**S(ω)**) is obtained by the ratio of equation 2.23 and equation 2.24, equation 2.25.

$$S(\omega) = \frac{Y(\omega)}{Y'(\omega)} \quad (2.25)$$

In practice, absolute values of specimen attenuation (α_S) are obtained by considering the attenuation of the signal due to water (α_W) present as a coupling medium, the distance the beam travels in this water (**d**), the thickness of the specimen (**x**), and the transmission coefficients at the water/specimen ($\mathbf{T}_{W,S}$) and specimen/water ($\mathbf{T}_{S,W}$) interfaces[31]. These contributions produce a different relation for the specimen frequency transfer function, equation 2.26.

$$Y(\omega) = Y'(\omega) * e^{-\alpha_w (d-x)} * e^{-\alpha_s x} * T_{ws} * T_{sw} \quad (2.26)$$

The transmission coefficient relates the efficiency of energy transfer at an interface and is a function of the acoustic impedance (**Z**) mismatch between the two interface materials. The acoustic impedance is defined as the product of the density and longitudinal velocity ($\mathbf{c}_L$) of a given material. The transmission coefficient for transmission from material 1 to material 2 is given by equation 2.27.[36] A related quantity is the amount of energy reflected at an interface termed the reflection coefficient and is given in equation 2.28.

$$T_{1,2} = \frac{2Z_1}{Z_1 + Z_2} \quad (2.27) \qquad R_{1,2} = \frac{Z_1 - Z_2}{Z_1 + Z_2} = \left(1 - T_{1,2}\right) \quad (2.28)$$

However, $\mathbf{Y'(\omega)}$ can not be directly measured. Instead, the frequency transfer function from the through transmission of water ($\mathbf{Y_W(\omega)}$) is measured. $\mathbf{Y_W(\omega)}$ for the three transducer pairs is plotted in Figure 2.7. It is related to $\mathbf{Y'(\omega)}$ through equation 2.29.

$$Y_W(\omega) = Y'(\omega) * e^{-\alpha_w d} \quad (2.29)$$

$\mathbf{Y(\omega)}$ is obtained by taking the ratio of equations 2.26 and 2.29, shown in equation 2.30. This equation can be rearranged to yield α_S, equation 2.31. Lee *et al.* derived a similar expression.[37]

$$\frac{Y(\omega)}{Y_W(\omega)} = e^{\alpha_w x} * e^{-\alpha_s x} * T_{w,s} * T_{s,w} \quad (2.30)$$

$$\boxed{\alpha_s = \alpha_W + \frac{1}{x} Ln\left(\frac{Y(\omega)/Y_W(\omega)}{(1 - R_{w,s}^2)}\right)} \quad (2.31)$$

The α_S values obtained from equation 2.31 have units of Np/cm, where 1 Np = 8.686 dB. In equation 2.31, $\mathbf{R_{W,S}}$ is the reflection coefficient at the water/specimen interface. It is easily shown that $1\text{-}\mathbf{R^2_{W,S}}$ is equal to $\mathbf{T_{W,S}}*\mathbf{T_{S,W}}$. α_W at 20 °C is 0.025 Np/cm (0.22 dB/cm).[38] Equation 2.31 will be used thought the remainder of this results and discussion section to calculate absolute α_S values for the specimens examined.

2.4.2 Porous Epoxy

2.4.2.1 Morphology and properties

Hexane modification of epoxy was first utilized by Kiefer *et al.* as a method of obtaining closed cell epoxy foams.[39] They found that narrow void size distributions were

obtained in cured epoxy upon addition of hexane or cyclohexane to epoxy/curing agent mixtures. The fracture behavior of porous epoxies created by hexane phase separation were evaluated by Crawford.[32] It is important to note that Crawford found that even after extensive heating under vacuum the specimens still contain sufficient quantities of hexane to cause the suppression of the T_g. The T_g's, densities, and longitudinal velocities of epoxy (825/AEP) and epoxy modified with 10 wt.% hexane are shown in Table 2.4. The T_g of the hexane modified epoxy is significantly suppressed by 33 °C. The density of the hexane modified epoxy is 1.12 g/cm^3 which indicates a void content of 6.5 volume percent based upon a parallel rule of mixture model, see equation 2.32. In equation 2.32, **X** is the property being modeled, 1 and 2 are the respective phases, and ϕ_2 is the volume fraction of phase 2. However, the density calculation assumes that density of the epoxy matrix is the same as homogeneous epoxy. Thus, this calculated void volume is most likely overestimated.

$$X_{1,2} = X_1(1-\phi_2) + X_2\phi_2 \qquad (2.32)$$

Morphology was characterized via SEM and computer aided image analysis. Figure 2.10 is a SEM image of a freeze fractured surface of porous epoxy and Fig.2.11 is the histogram from the image analysis. The histogram indicates that a normal distribution of voids exists within the hexane modified epoxy. Image analysis resulted in the determination of the average void diameter ($\overline{\mathbf{D}}$) (7.42±1.72 μm) and the number of voids per cm^3 ($\mathbf{n_O}$) (1.25x10^8). The volume fraction of voids can be calculated using the average void diameter to determine the average volume per void, multiplying this by the number of voids present in a cm^3, and then dividing this number by the one cm^3. The void volume fraction calculated using this method yields a value of 2.67%. This

calculation assumes that none of the voids are filled with hexane. Comparing the measured densities the void volume is determined to be 6.8%, obviously the calculation is an under estimation most probably due to the presence of many voids larger than $\overline{D}$.

Table 2.4: Measure properties of epoxy (825/AEP) and hexane modified epoxy.

	T_g (°C)	Density (g/cm^3)	C_L (m/s)	Acoustic Impedance	Reflection Coefficient
Epoxy (825/AEP)	126	1.198	2870.0	343982	0.398
Porous Epoxy (10 wt.% hexane)	93	1.120	2569.1	287788	0.321

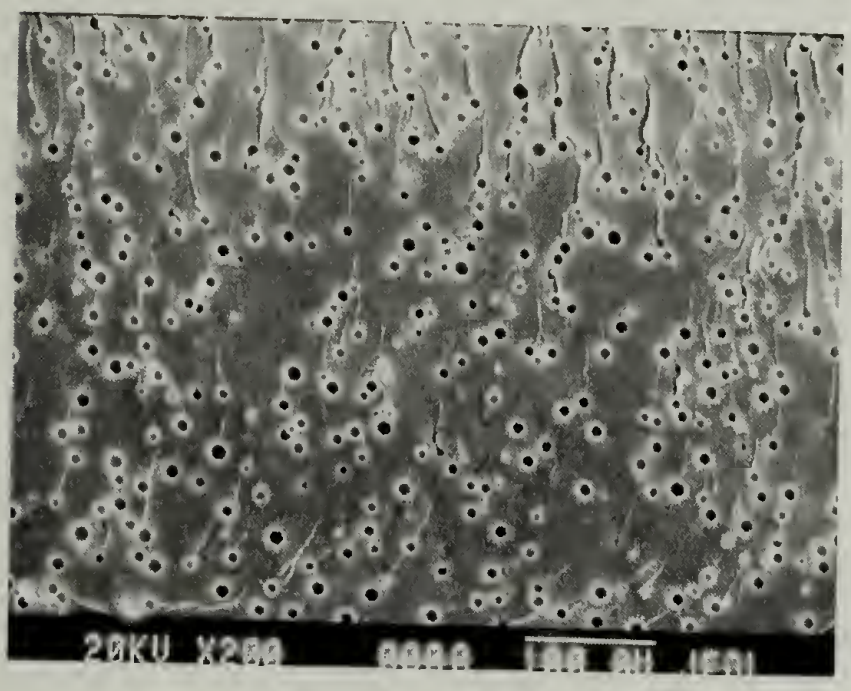

Figure 2.10: SEM image of freeze fractured surface of porous epoxy

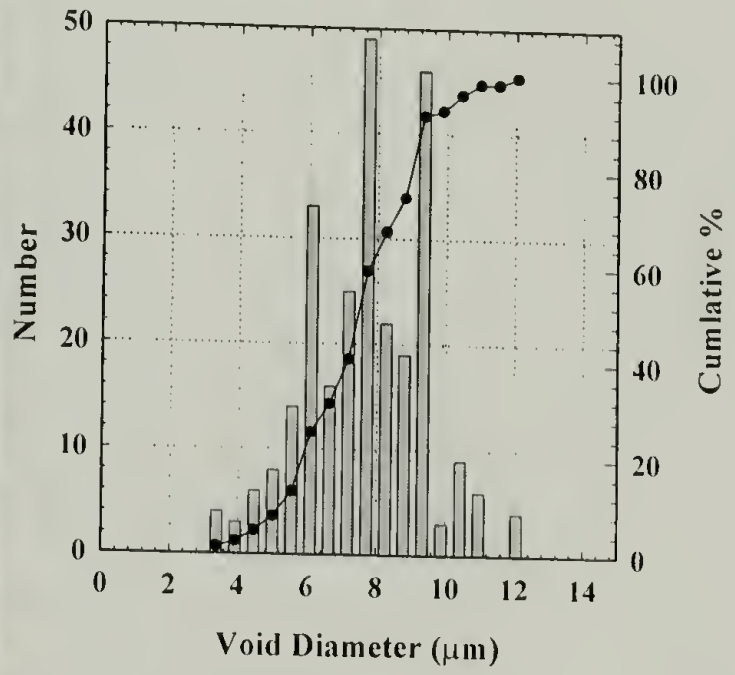

Figure 2.11: Porous epoxy void size histogram and cumulative percentage

2.4.2.2 Ultrasonic spectroscopy

The frequency spectra obtained from through transmission of water, epoxy, and porous epoxy are shown in Figure 2.12. The amplitude the epoxy frequency spectra is uniformly decreased over the entire bandwidth, which is expected for a homogeneous material. The amplitude for porous epoxy is uniformly decreased for the 20 MHz

bandwidth. However, the 50 MHz bandwidth shows an asymmetric decrease. The 100 MHz data is omitted because all of the signal intensity was absorbed by the porous epoxy. These spectra can be directly compared by calculating the specimen's attenuation coefficient (α_S) using the plots shown in Figure 2.12 and the properties in Table 2.4. Figures 2.13 and 2.14 plot the product of α_S versus λ for the 50 – 20 and 50 MHz bandwidths respectively. α_S is plotted versus λ so direct correlation can be made between discontinuities in the plots and the associated length scale over which they take place.

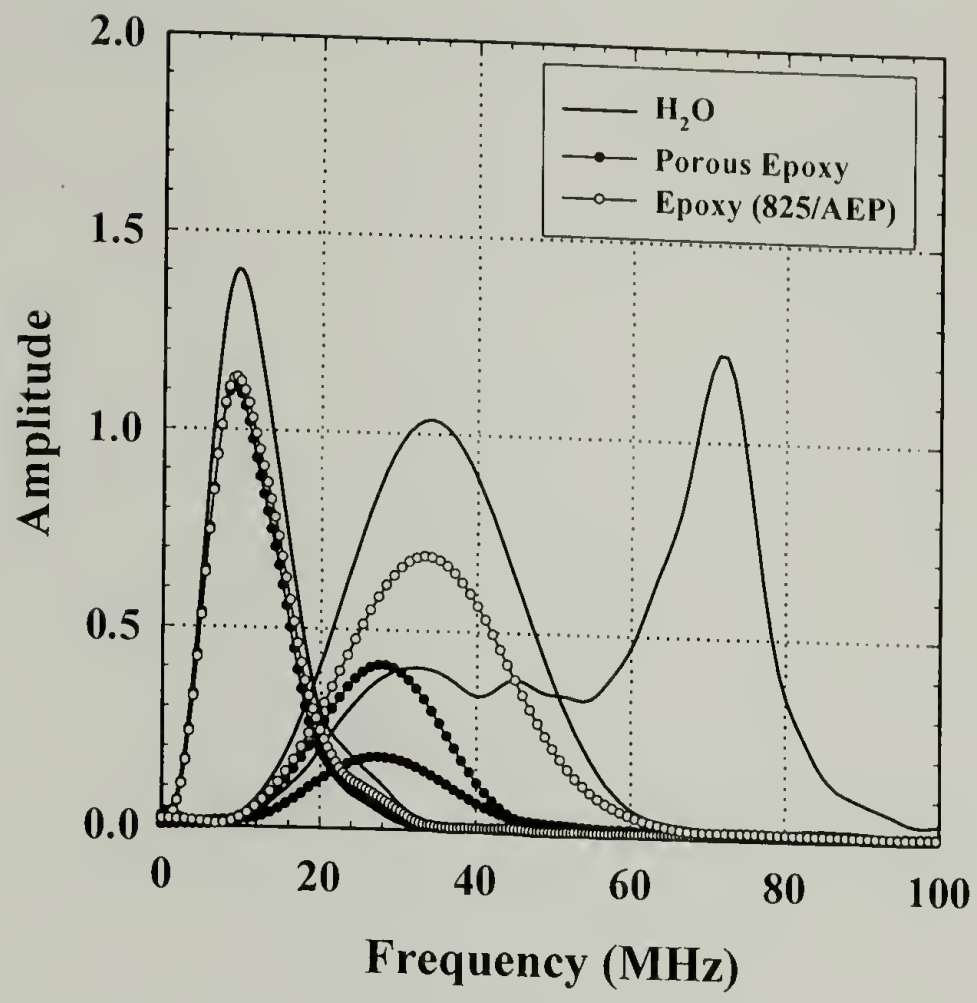

Figure 2.12: Frequency spectra from water, epoxy and porous epoxy.

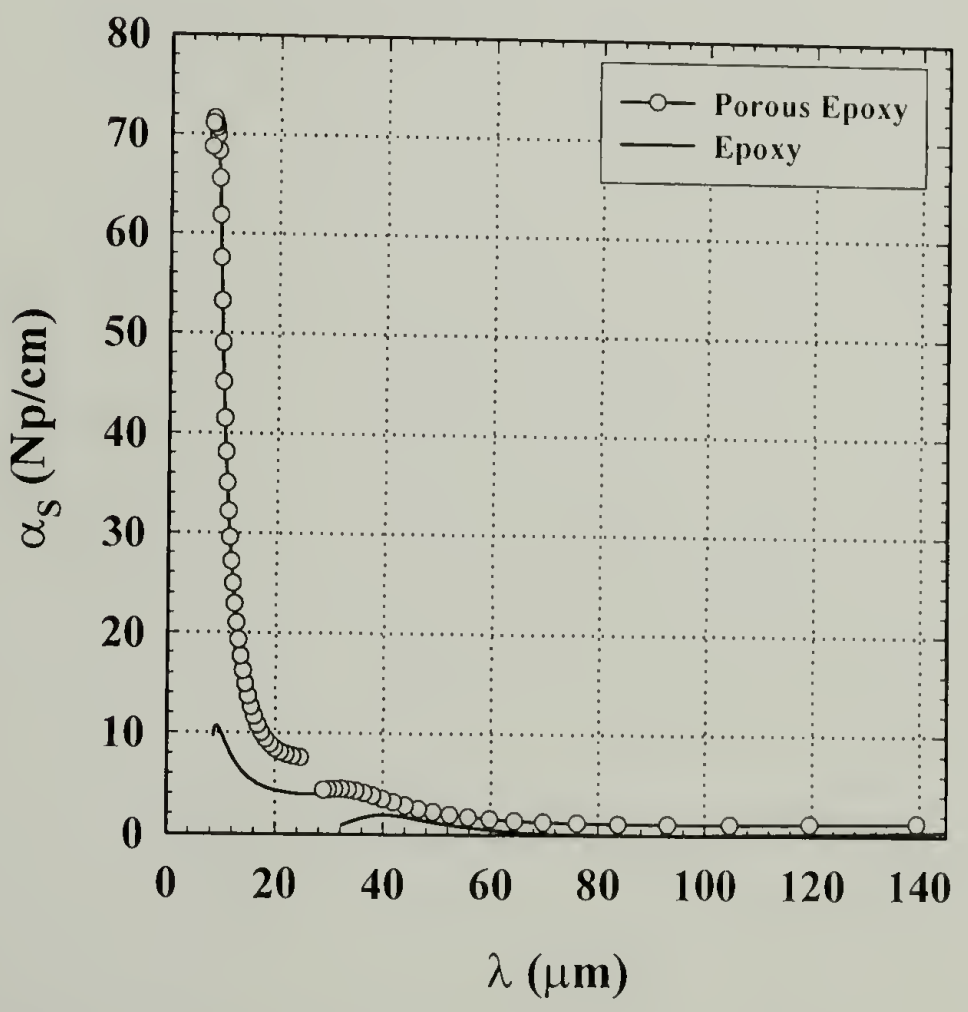

Figure 2.13: α_S versus λ for epoxy (825/AEP) and porous epoxy.

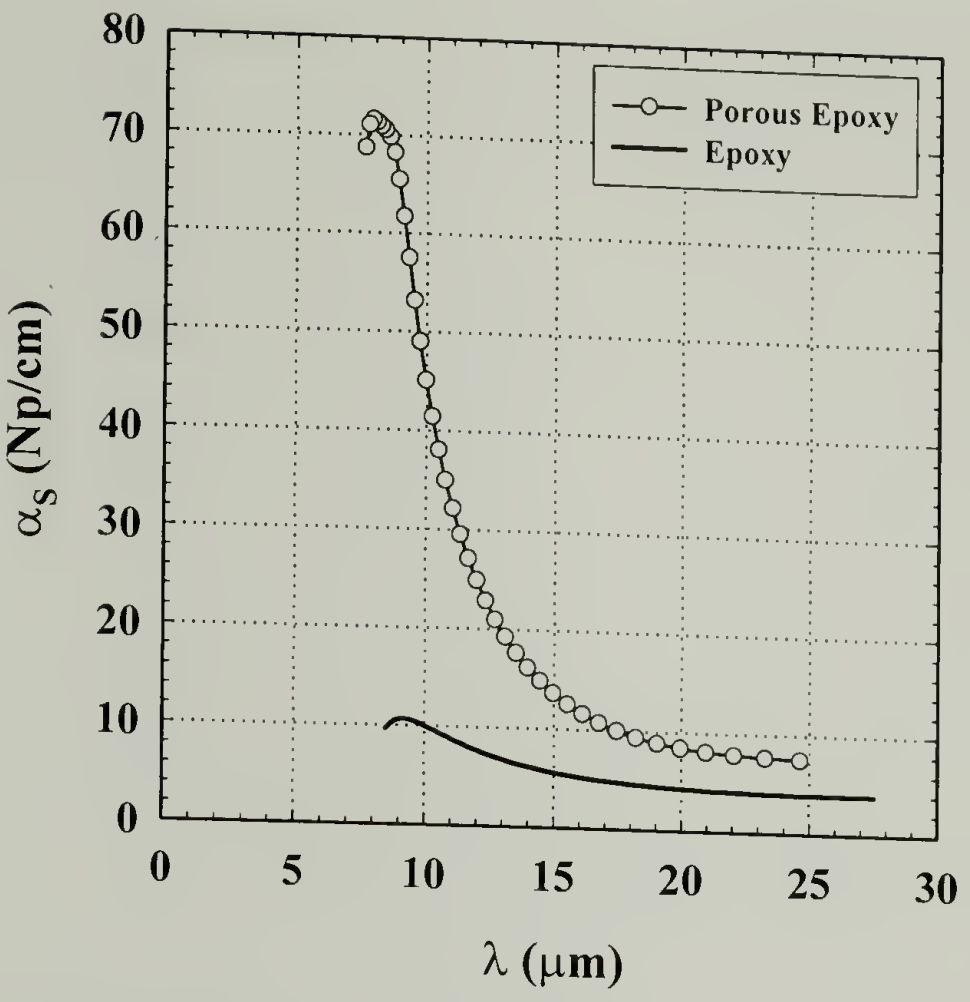

Figure 2.14: α_S versus λ for epoxy (825/AEP) and porous epoxy in the 50 MHz bandwidth

It is expected that a plot of α_S versus λ for a through transmission of a homogeneous material should yield an exponentially increasing attenuation with decreasing wavelength. This behavior is seen in polystyrene and other epoxies presented in latter sections. Heterogeneous materials will produce a sharply discontinuous α_S versus λ plot in wavelength regions that correlate with the length scale of the heterogeneity for scattering in the intermediate regime ($\mathbf{r} \sim \lambda$). This behavior is observed for the porous epoxy in the 50 MHz bandwidth where α_S is observed to begin to sharply increase at 15 μm and peak at a value of 8.5 μm. The peak value corresponds closely with the measured $\overline{\mathbf{D}}$ of 7.42 ± 1.72 μm. The 20 MHz bandwidth plot for porous epoxy is increased over that of epoxy, but does not exhibit discontinuities that are distinct from those of epoxy. The increase in attenuation here is due primarily to a concentration

dependence of the number of voids. However, there is also a dependence on the size of the void present for Rayleigh regime scattering ($\mathbf{r} << \lambda$). Rayleigh scattering of sound will be utilized in later sections. Here the intermediate wavelength regime ($\mathbf{r} \sim \lambda$) is extremely successful for detecting the $\overline{\mathbf{D}}$.

2.4.3 Foamed polystyrene

2.4.3.1 Morphology and properties

The foaming of PS with supercritical CO_2 was extensively studied by Dr. Keyln Arora and a detailed description is given in her Ph.D. dissertation.[33] Predominately, the foams produced were closed cell with the cells completely impinged upon one another. However, under specific conditions closed cell foams with isolated cells were produced. Some of these had relatively uniform size distributions and were selected for ultrasonic evaluation. SEM images and void size histograms for the foams are shown in Figure 2.15. The morphology and property data for these foams are listed in Table 2.5. The specimens selected had $\overline{\mathbf{D}}$ of approximately 1, 12 and 31 μm with a standard deviation of 30% for PS foams 1, 2, and 3 respectively. Comparing void volume percent calculated from the measured $\overline{\mathbf{D}}$ and $\mathbf{n_o}$ with the measured densities one finds discrepancies for all but foam 3. Foam 1 has a void volume percent almost three times higher than expected and foam 2 is about half the expected value. These large errors may arise from the roughness of the fracture surfaces and/or the polydispersity of void sizes present (Figures 2.15 b, d, and f). The histogram for PS foam 2 shows a significant number of large voids present in the sample. Cryomicrotombing of the PS foams in an attempt to eliminate surface roughness resulted in collapsed cells rending morphology analysis impossible.

Table 2.5: Morphology and property data for PS and PS foams.

	$\overline{D}$ (μm)	n_o (voids/cm^3)	Void Volume %	ρ (g/cm^3)	c_L (m/s)	R
Polystyrene	-	-	-	1.0	2412.6	0.241
PS Foam 1	1.02 ± 0.33	2.93×10^{11}	16.28	0.94	1794.9	0.064
PS Foam 2	11.72 ± 4.64	5.043×10^{7}	4.25	0.88	1806.0	0.0379
PS Foam 3	30.94 ± 7.56	2.105×10^{7}	32.64	0.62	1982.4	0.0918

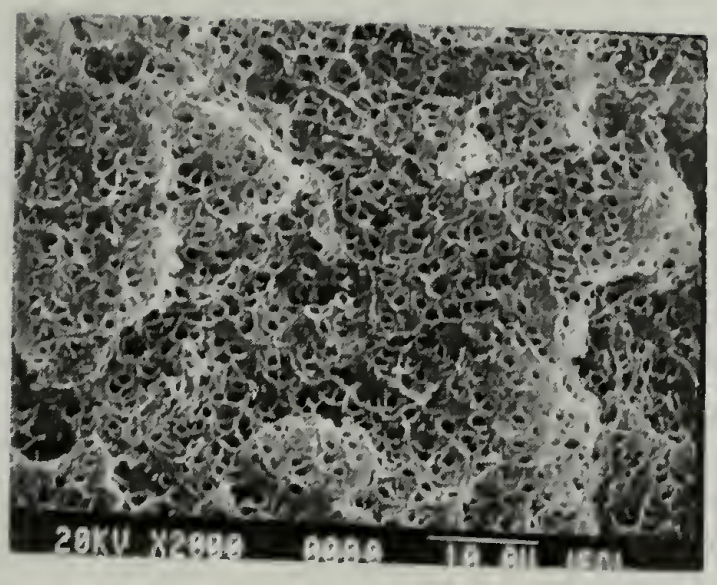

a)

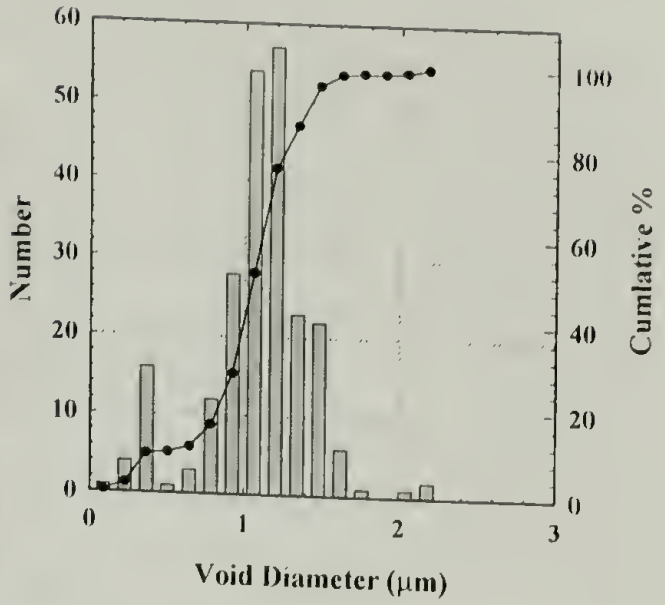

b)

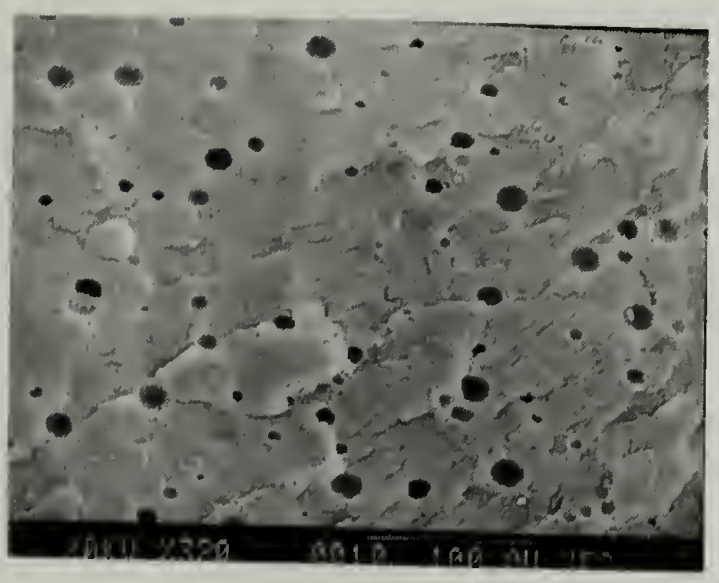

c)

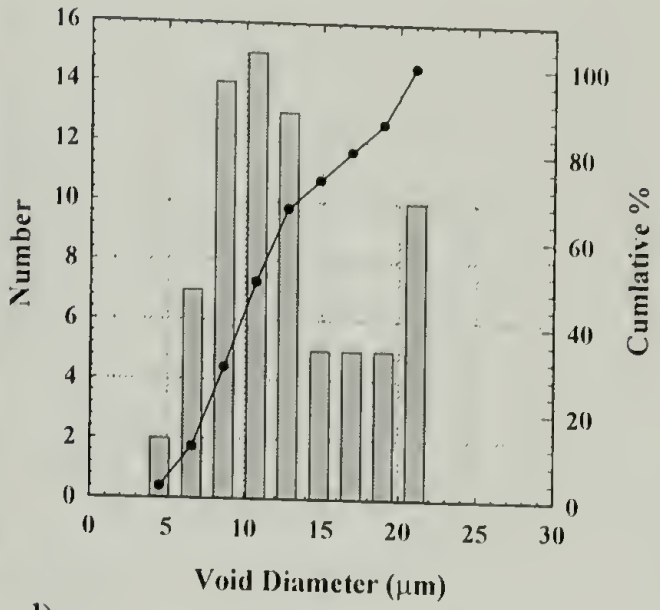

d)

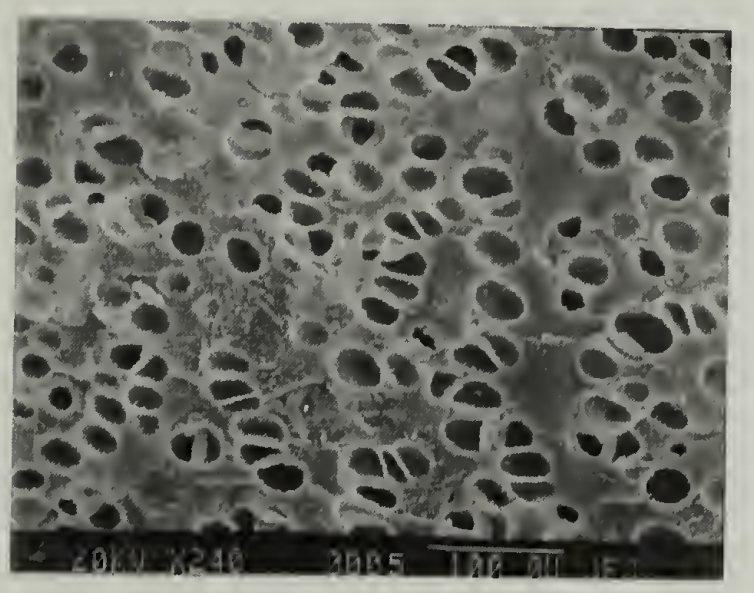

e)

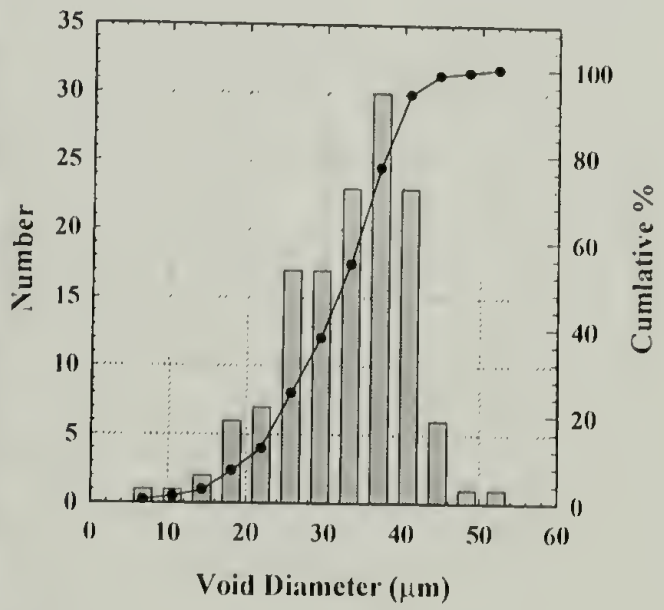

f)

Figure 2.15: SEM images (a, c, e) and void size histograms (b, d, f) for PS Foams 1, 2, and 3 respectively.

2.4.3.2 Ultrasonic spectroscopy

The void volumes are quite high and thus it was surprising to find that sound does transmit through the specimens at the high frequencies employed here. The frequency spectra are shown in Figure 2.16. A significant amount of sound is transmitted through foam 1 even within the 100 MHz bandwidth. However, foams 2 and 3 strongly absorb sound in the 50 and 100 MHz bandwidths. α_S versus λ is plotted for all bandwidths in Figure 2.17. Here is observed the expected exponential increase in attenuation with decreasing frequencies. In general, the curves are complex in nature and difficult to interpret. This is a direct result of the high void content and the dispersity of void sizes with in the specimens. Looking closely at the 50 and 100 MHz band widths (Figure 2.18) one observes a distinct increase in overall α_S with increasing $\overline{\mathbf{D}}$. This appears to occur irregardless of void volume percent or number density. Scattering of sound in foam 2 and 3 is occurring in the LWR and hence some indication of the length scale of the voids should be evident from the plots. Thus, examining Figure 2.18 it is observed that a shoulder appears in the 50 MHz bandwidth line of foam 2. This begins at 11 μm and ends at 7.5 μm where the curve resumes a sharp upward climb. This shoulder correlates well with the $\overline{\mathbf{D}}$ measured in this specimen. Figure 2.19 shows the 20 MHz bandwidth data for the foams. Here again a distinct increase in α_S with increasing $\overline{\mathbf{D}}$ is observed. A shoulder occurs in the foam 3 plot which begins at 32 μm and remains level until 28 μm where a sharp jump occurs. The line appears to join the data from the 50 MHz band width shown in Figures 2.17 and 2.18. It is anticipated that the sharpness of the increase in α_S and the resultant plateaus will increase in length and uniformity as $\overline{\mathbf{D}}$ becomes more monodisperse.

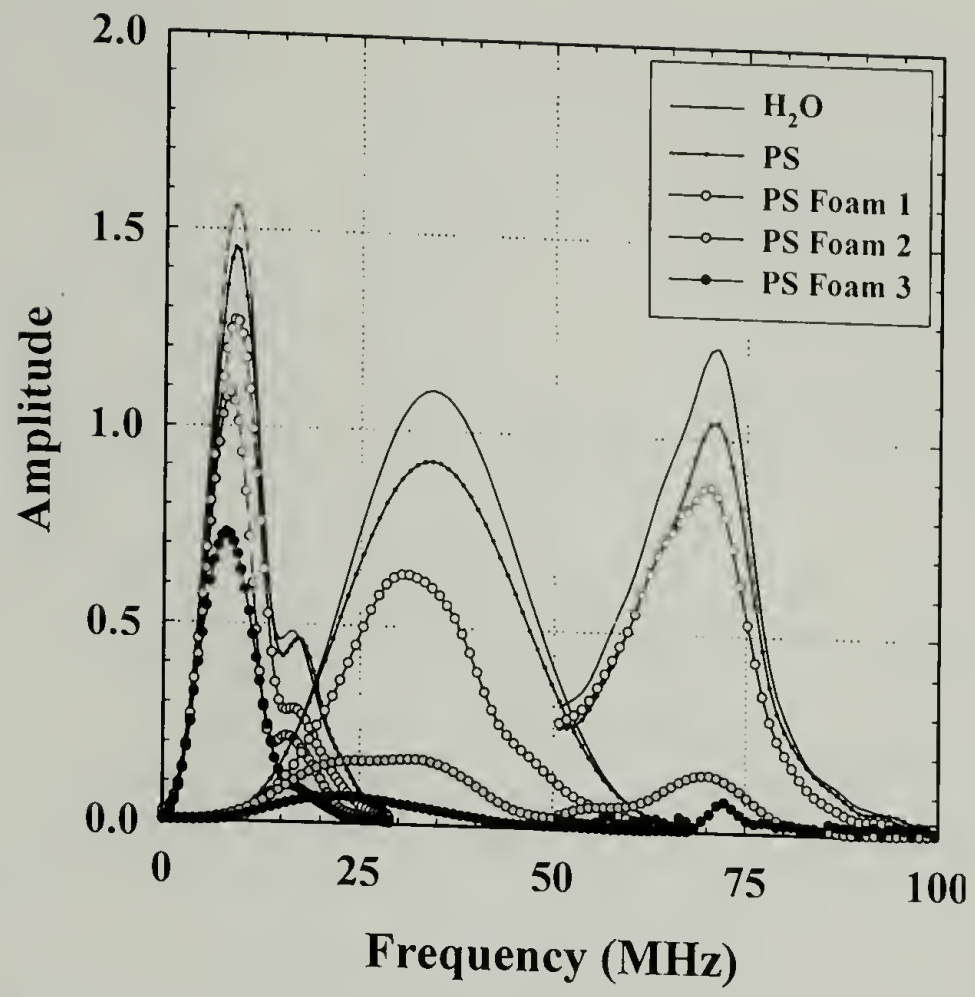

Figure 2.16: Frequency spectra from through transmission of water, PS, and PS foams.

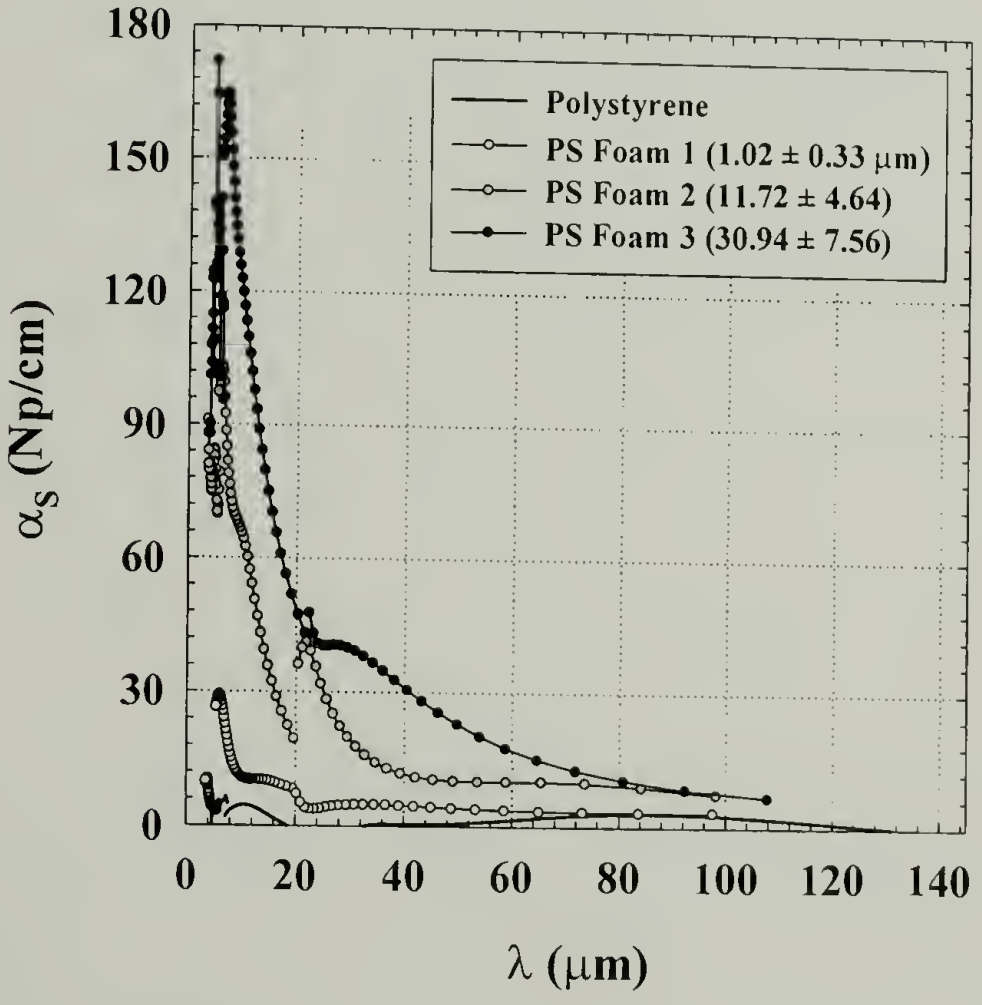

Figure 2.17: α_S versus λ for PS and PS foams in the 20, 50, and 100 MHz bandwidths.

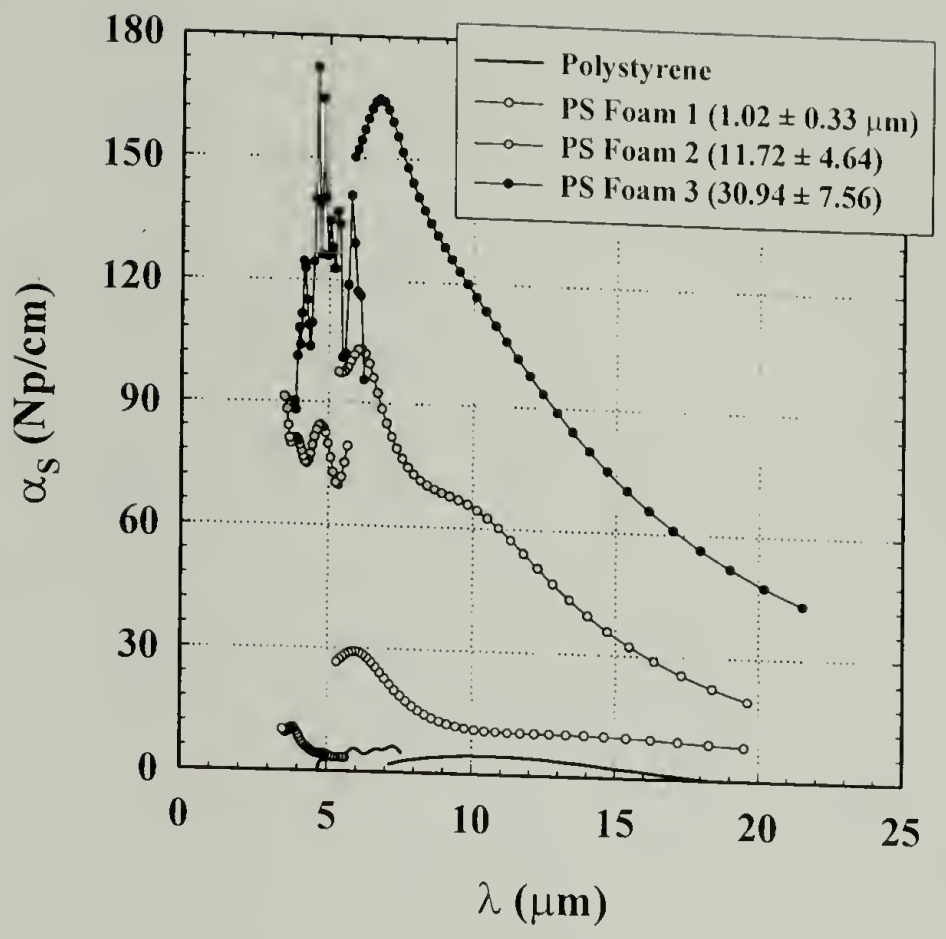

Figure 2.18: α_S versus λ for PS and PS foams in the 50, and 100 MHz bandwidths.

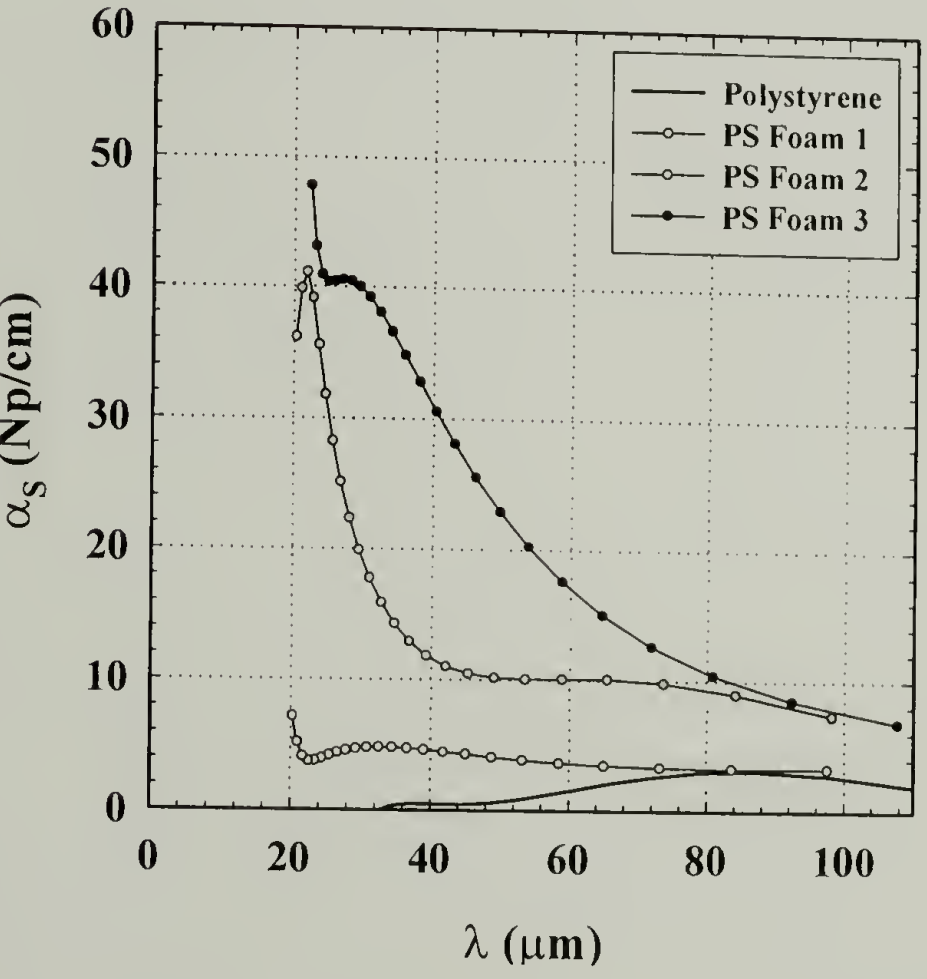

Figure 2.19: α_S versus λ for PS and PS foams in the 20 MHz bandwidth.

2.4.4 Acrylic based blends

2.4.4.1 Morphology and properties

The specimens under consideration here are films fabricated from blends of poly(methyl methacrylate-*co*-ethyl acrylate) and poly(methyl methacrylate-*co*-butyl acrylate) acrylic latices. The poly(methyl methacrylate-*co*-ethyl acrylate) latex has a Tg of 45 °C, behaves as a rigid material at room temperature, and will hence forth is referred to as the "hard phase". The poly(methyl methacrylate-*co*-butyl acrylate) latex having a Tg of –5 °C behaves an elastomer at room temperature and thus will be referred to a the "soft phase". These materials were studied by Dr. Naveen Agarwal and the thermodynamics associated with their deformation is presented in detail in his Ph.D. dissertation.[34] The blends are particularly interesting for ultrasonic analysis because the constituents are similar in refractive index and chemical structure. Consequently, they are transparent to electromagnetic radiation although they exhibit distinct T_gs for each phase indicating that they are indeed phase separated. Thus, they are ideal candidates for evaluating the effectiveness of ultrasonic spectroscopy in elucidating their morphology. The densities as determined by Agarwal and the velocities and reflection coefficients are shown in Table 2.6.

Light scattering experiments conducted on the original aqueous latices revealed that the particles are on the order of 100 nm.[34] However, Agarwal found that SEM images of fracture surfaces revealed domains as large as 1 μm exist. Thus, some coalescence occurs during the film formation process. Agarwal's research also revealed that phase inversions occur from continuous soft to bicontinuous to continuous hard at 40, 50 and 60 volume percent hard phase respectively. Accompanying this phase

inversion is a similar change in the percent elongation to break. Blends of 40, 50, and 60 volume percent hard have intermediate values (300-500% elongation) which are bracketed by lower values at 80% hard and above (200%), and much higher values for blends with 20% hard and below (800-900%).

Table 2.6: Morphology and property data for acrylic based blends

% Soft Phase	ρ^{34} (g/cm^3)	C_L (m/s)	R
100	1.093	2106	0.045
80	1.1002	2221	0.06
70	1.1103	2221	0.062
60	1.1053	2225	0.062
50	1.1208	2345	0.078
40	1.1264	2370	0.082
20	1.1439	2610	0.114
0	1.1584	2727	0.131

2.4.4.2 Ultrasonic analysis

The 50 MHz bandwidth only was used to characterize the acrylic blends. The frequency spectra are shown in Figure 2.20. The frequency spectra of the copolymers and blends shown a relatively uniform attenuation over the entire bandwidth. α_S was calculated using the data in Table 2.6 and the frequency spectra shown in Figure 2.20. This is plotted versus λ in Figure 2.21. α_S increases progressively with increasing volume percent soft phase until 80% soft phase and above where there is a dramatic change in slope of the α_S versus λ plots. Increased α_S with percent soft phase is expected

as the soft phase being a more ductile material is less efficient at transmitting mechanical force and thus acts to absorb more of the sound due to increased dampening. However, the dramatic change in slope is intriguing. Figure 2.22 is a plot of the slope of the α_S versus λ lines versus the percent soft phase. Three regimes are present in this plot. The first for the hard copolymer and 20% soft blend has a relatively low slope and hence small change in dampening with wavelength. An intermediate regime exits for the 40 – 70% soft blends with the slope being relatively unchanged among the blends. A regime of sharply increasing slope, increasing dampening with λ, occurs for the 80% soft blend and the soft copolymer. This trend matches that observed for the measured percent elongation. This result is confirmed by the observed transformation from continuous hard to continuous soft phase and the resulting brittle to ductile failure modes at 40 and 60% soft phase respectively. In summary, ultrasonic spectroscopy successfully identified phase inversions in acrylic latex blends that correlate with those measure by mechanical and electron microscopic methods.

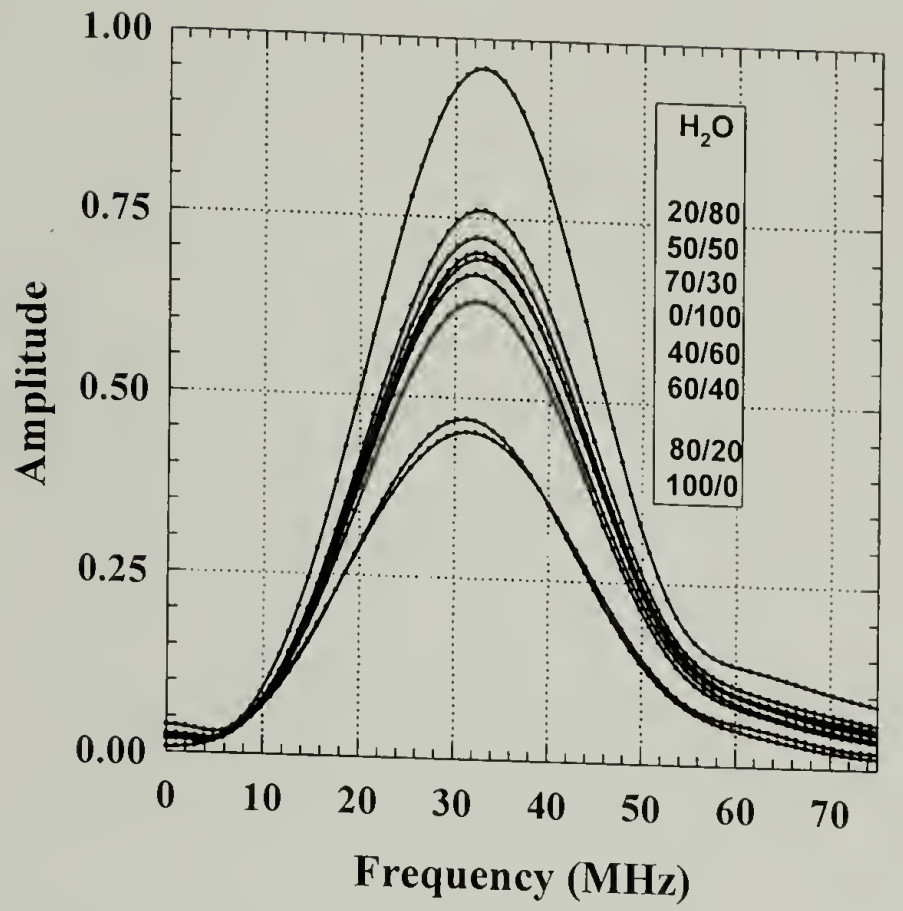

Figure 2.20: Frequency spectra from acrylic blends.

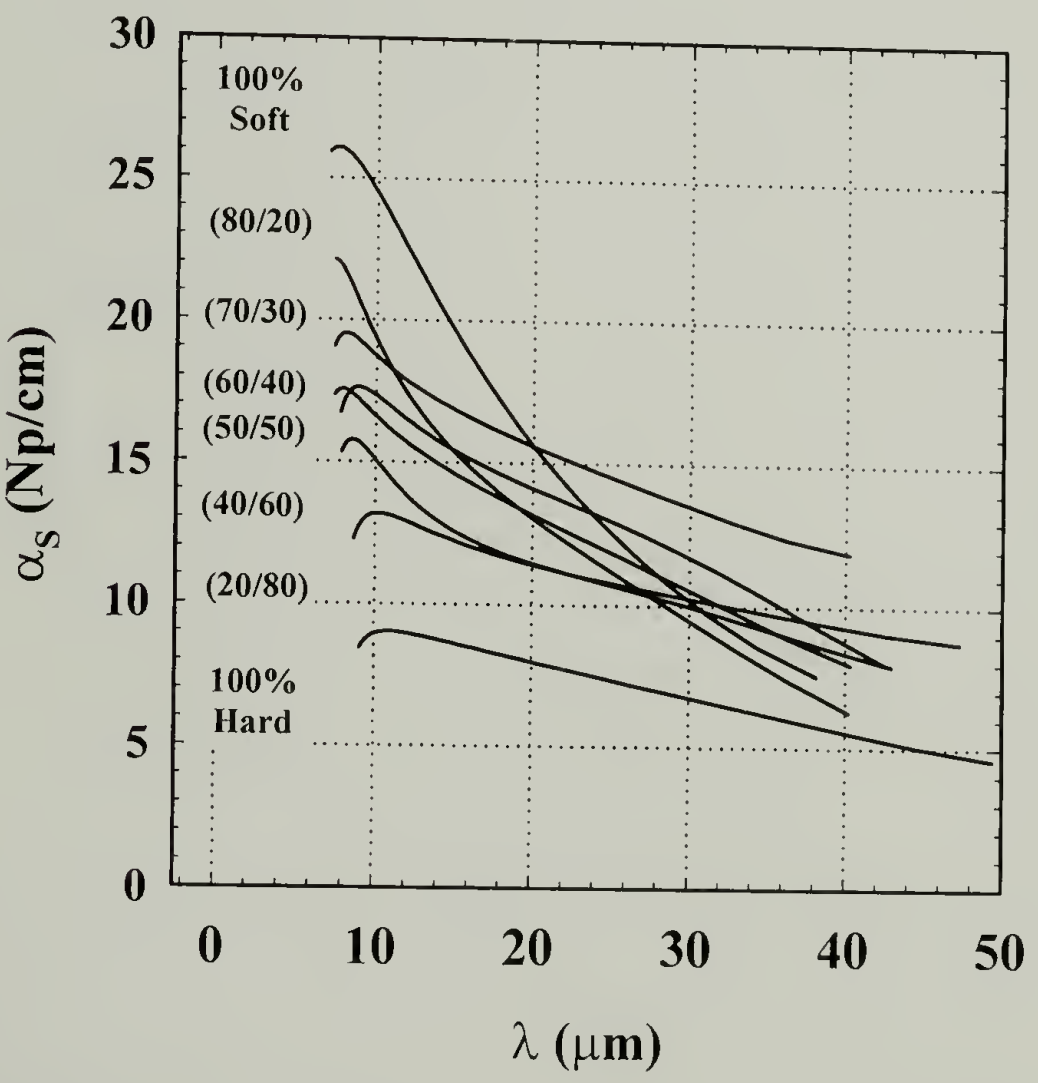

Figure 2.21: α_S versus λ for acrylic blends.

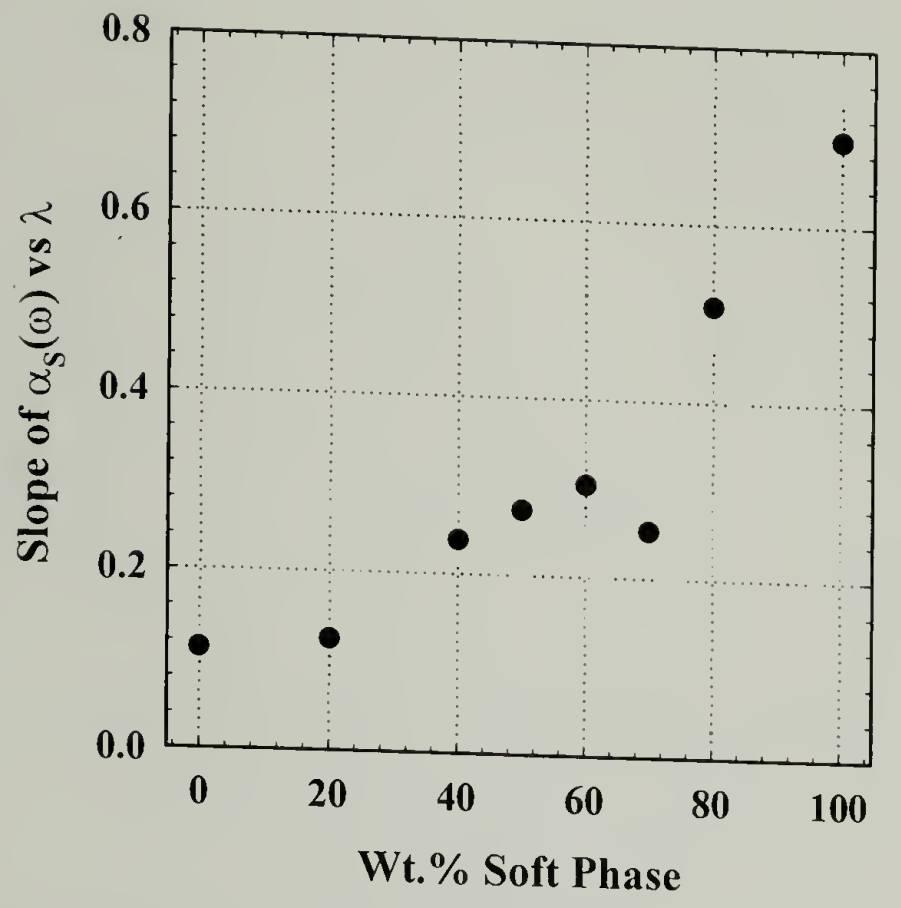

Figure 2.22: Slope of α_S versus λ plots shown in Figure 2.21 for acrylic blends.

2.4.5 Rubber modified epoxy

2.4.5.1 Morphology and properties

Rubber modification of epoxies and other polymers is widely used to increase their fracture toughness.[40-44] In epoxies, this is typically accomplished by the addition of a liquid rubber, most commonly a carboxyl terminated random co-oligomer of butadiene and acrylonitrile (CTBN) shown in Figure 2.23.

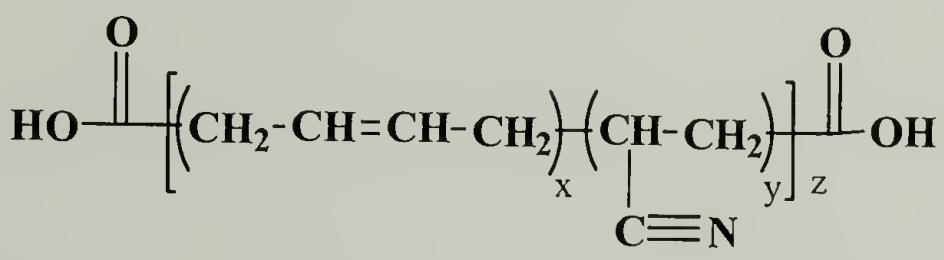

Figure 2.23: Chemical structure of CTBN rubber.

The liquid rubber is usually added directly to the mixture of epoxy prepolymer and curing agent and during cure the rubber phase separates forming spherical domains of liquid rubber. The degree of bonding at the interface can be controlled by addition of epoxy or

amine terminated co-oligomers of butadiene and acrylonitrile. The size of the rubber domains has been shown to be a function of the curing temperature,[45-48] gelation time,[48-50] amount of added rubber,[47,51,52] and the solubility parameter of the liquid rubber.[53-57] Temperature decreases the viscosity thus increasing the rate of phase separation. However, it also increases the solubility of the rubber in the epoxy. The gelation time, also a function of temperature but dominated by the reactivity of the curing agent, determines when the evolving morphology will be "locked in". The amount of added rubber dramatically affects the resultant morphology with the morphology tending to larger and larger diameter domains with added rubber. A similar trend occurs upon increasing the molecular weight of the rubber.[55,58]

Resultant toughening effects of rubber modified systems are a function of the morphology obtained. Generally, improved impact and crack propagation resistance is observed for rubber domain sizes only in the range of 0.1 – 10 μm. Bucknall has proposed that when the domain diameter is greater then 10 μm they act as Griffith[59] flaws.[60] However, Wu argues that the interparticle distance determines at what size the brittle to ductile transition occurs and that toughening effects are lost when the domains are too far apart no longer promoting the local yielding of the ligament.[61] Dompas and Groeninckx addressed the observed minimum domain size by developing a criterion for cavitation bases on the strain energy released by cavitation and the surface energy necessary to create the resultant new surface.[62] When the strain energy stored in the rubber is less than the surface energy required for cavity formation no toughening occurs. Thus, small particles require volume strains for cavitation that are greater than the failure

values of the matrix. Control and characterization of the rubber domain size is consequently of paramount importance for obtaining toughening effects.

The predominate method for morphology analysis is electron microscopy of freeze fractured specimens after cure. Researchers have used other methods such as dielectric spectroscopy,[52] laser light scattering,[46] optical microscopy,[46,49] and Rayleigh-Brillouin laser light scattering[56] to characterize morphology during phase separation and cure. Nigam and coworkers used wide angle x-ray scattering to study the effects of added rubber on the average molecular interchain spacing but did not obtain information about the rubber domain size.[63] A nondestructive means of determining the $\overline{\mathbf{D}}$ of phase separated rubber particle in solid polymers would be extremely useful for property prediction and quality control in these materials. Thus, ultrasonic spectroscopy analysis was conducted on a series of rubber modified epoxies made with varying weight percent rubber, rubber solubility parameter, and gelation temperature. A series of CTBN liquid rubber available from BFGoodrich Performance Materials, Inc. with varying acrylonitrile (AN) contents and hence solubility parameters, see Table 2.7, was used for this study. CTBN solubility in epoxy increases with increasing AN content.

Table 2.7: CTBN liquid rubbers used for rubber modification.

CTBN – Rubber Modifier	**Acrylonitrile Content (%)**	**Solubility Parameter $(kJ/m^3)^{1/2}$**
1300x31	10	547.4
1300x8	18	570.7
1300x13	26	592.0

Rubber modified epoxies fabricated with the CTBN containing 10% AN resulted in an extremely broad range of domain sizes (estimated D = 1-300 μm) upon varying the gelation temperature or weight percent rubber. Unfortunately, the majority of these morphologies appear to be multimodal and thus extremely difficult to analyze via scattering. Several authors have found that bimodal morphologies are common in these materials and that they provided the best toughening effects.[64,65] The CTBN rubber with 26% AN created rubber modified epoxy with relatively invariant domain size (estimated D = 0.1 – 0.3 μm) and at high gelation temperatures (150 °C) no phase separated rubber domains are observable. Rubber modified epoxies with CTBN containing 18% AN produced morphologies with $\overline{\mathbf{D}}$ varying from 0.2 - 1.4 μm that are predominately unimodal. The SEM images and rubber domain diameter histograms for rubber modified epoxies containing 5-15 weight percent rubber and gelled at 20 – 150 °C are shown in Figures 2.26 – 2.9. The $\overline{\mathbf{D}}$ and standard deviations obtained from the histogram data are summarized in Table 2.8, where **B** denotes those systems with bimodal distributions. The second mode observed in the bimodal systems has a $\overline{\mathbf{D}}$ of 0.4 μm. The average standard deviation for the non – bimodal morphologies is 26%. This clearly indicates that the morphologies are not monodisperse and thus not ideal for scattering studies. However, they are "real" systems and any morphology information obtained for this nondestructive technique is potentially valuable due to the increasingly wide application of rubber toughened polymers.

Table 2.8: Average rubber domain diameter of 18% AN CTBN in epoxy.

Weight % CTBNx8	**$\overline{D}$ (μm) Gelled at 20 °C**	**$\overline{D}$ (μm) Gelled at 50 °C**	**$\overline{D}$ (μm) Gelled at 100 °C**	**$\overline{D}$ (μm) Gelled at 150 °C**
5	0.71 ± 0.43 **(B)**	0.84 ± 0.47 **(B)**	0.39 ± 0.09	0.23 ± 0.06
10	1.12 ± 0.55 **(B)**	1.38 ± 0.32	0.69 ± 0.20	0.57 ± 0.15
15	1.29 ± 0.35	1.24 ± 0.34	1.02 ± 0.29	0.67 ± 0.16

The number densities are summarized in Table 2.9. The number density generally increases at gel temperature increases ($\overline{D}$ decreases), except for the 5 wt.% rubber specimens. Bimodal distribution occur at 20 and 50 °C and a great number of small domains exist causing the increased number density over that of the 10 wt.% rubber specimens gelled at these temperatures.

Table 2.9: Number density of rubber domains.

Weight % CTBNx8	**n_o (#/cm^3) Gelled at 20 °C**	**n_o (#/cm^3) Gelled at 50 °C**	**n_o (#/cm^3) Gelled at 100 °C**	**n_o (#/cm^3) Gelled at 150 °C**
5	7.8×10^{11}	7.4×10^{11}	4.1×10^{12}	1.9×10^{12}
10	7.0×10^{11}	4.2×10^{11}	2.2×10^{12}	3.8×10^{12}
15	9.0×10^{11}	9.6×10^{11}	1.5×10^{12}	4.2×10^{12}

Another factor which effects the measured number density is the amount of rubber which was unable to phase separate before gelation. An indication of the amount of rubber trapped within the matrix is the T_g. Immiscible blends exhibit distinct T_gs for

each blend component, but miscible blends have a single T_g usually in the temperature range between the constituent's T_gs. The T_gs of the rubber modified systems and the pure epoxies gelled at various temperatures are shown in Table 2.10. According to BFGoodrich the T_g of the CTBN containing 18% AN is –52 °C. This T_g was not observed in any of the specimens. The average T_g for the epoxy matrix gelled at various temperatures is 90.47 ± 0.98 °C it is significant depressed upon addition of CTBN. T_g with depression increasing as the amount of CTBN and the gelation temperature increase. Thus indicating an increasing amount of rubber trapped within the epoxy.

Table 2.10: Glass transition temperatures of epoxy and rubber modified epoxy.

Weight % CTBNx8	**T_g (°C) Gelled at 20 °C**	**T_g (°C) Gelled at 50 °C**	**T_g (°C) Gelled at 100 °C**	**T_g (°C) Gelled at 150 °C**
0	90.6	91.74	89.38	90.16
5	81.95	80.15	78.95	79.09
10	81.48	80.33	75.91	77.12
15	77.13	77.41	75.04	73.59

Incorporating CTBN rubber into epoxies also affects the ρ and $\mathbf{c_L}$, Tables 2.11 and 2.12. These effects typically follow a rule of mixtures model such as the one shown in equation 2.32. The ρ and $\mathbf{c_L}$ are plotted versus weight percent CTBN in Figures 2.24 and 2.25 along with the rule of mixtures (equation 2.32) predictions. The calculations used the CTBN ρ value of 0.948 g/cm^3, according to BFGoodrich, and $\mathbf{c_L}$ measured as 1698.2 m/s. Measured ρ values fall increasingly below the rule of mixtures line with

increasing rubber content again indicating that indeed an increasing amount of rubber is trapped within the epoxy matrix. The measured $\mathbf{c_L}$ data has a similar trend as the ρ except with more scatter in the data. The $\mathbf{c_L}$ scatter results partially from the variation in the specimen thickness. Specimen surfaces were sanded smooth with an approximate thickness deviation of $\pm$ 2 μm. This for example produces a variation in $\mathbf{c_L}$ for the epoxy gelled at 20 °C of $\pm$ 9.2 m/s. The ρ and $\mathbf{c_L}$ data are used to calculate the reflection coefficients shown in Table 2.13,

Table 2.11: Densities of epoxies and rubber modified epoxies.

Weight % CTBNx8	**ρ (g/cm^3) Gelled at 20 °C**	**ρ (g/cm^3) Gelled at 50 °C**	**ρ (g/cm^3) Gelled at 100 °C**	**ρ (g/cm^3) Gelled at 150 °C**
0	1.1500	1.1500	1.1530	1.1561
5	1.1434	1.1439	1.1409	1.1409
10	1.1318	1.1313	1.1318	1.1343
15	1.1192	1.1202	1.1207	1.1247

Table 2.12: Longitudinal wave speeds of epoxies and rubber modified epoxies.

Weight % CTBNx8	**c_L (m/s) Gelled at 20 °C**	**c_L (m/s) Gelled at 50 °C**	**c_L (m/s) Gelled at 100 °C**	**c_L (m/s) Gelled at 150 °C**
0	2640.4	2674.5	2672.8	2643.1
5	2596.7	2590	2610.07	2675.3
10	2561.2	2513.5	2531.6	2577.1
15	2475.9	2465.8	2477.8	2487.7

Table 2.13: Reflection coefficients of epoxy and rubber modified epoxy.

Weight % CTBNx8	**R Gelled at 20 °C**	**R Gelled at 50 °C**	**R Gelled at 100 °C**	**R Gelled at 150 °C**
0	0.345	0.350	0.351	0.347
5	0.335	0.334	0.336	0.347
10	0.324	0.315	0.319	0.328
15	0.304	0.302	0.305	0.308

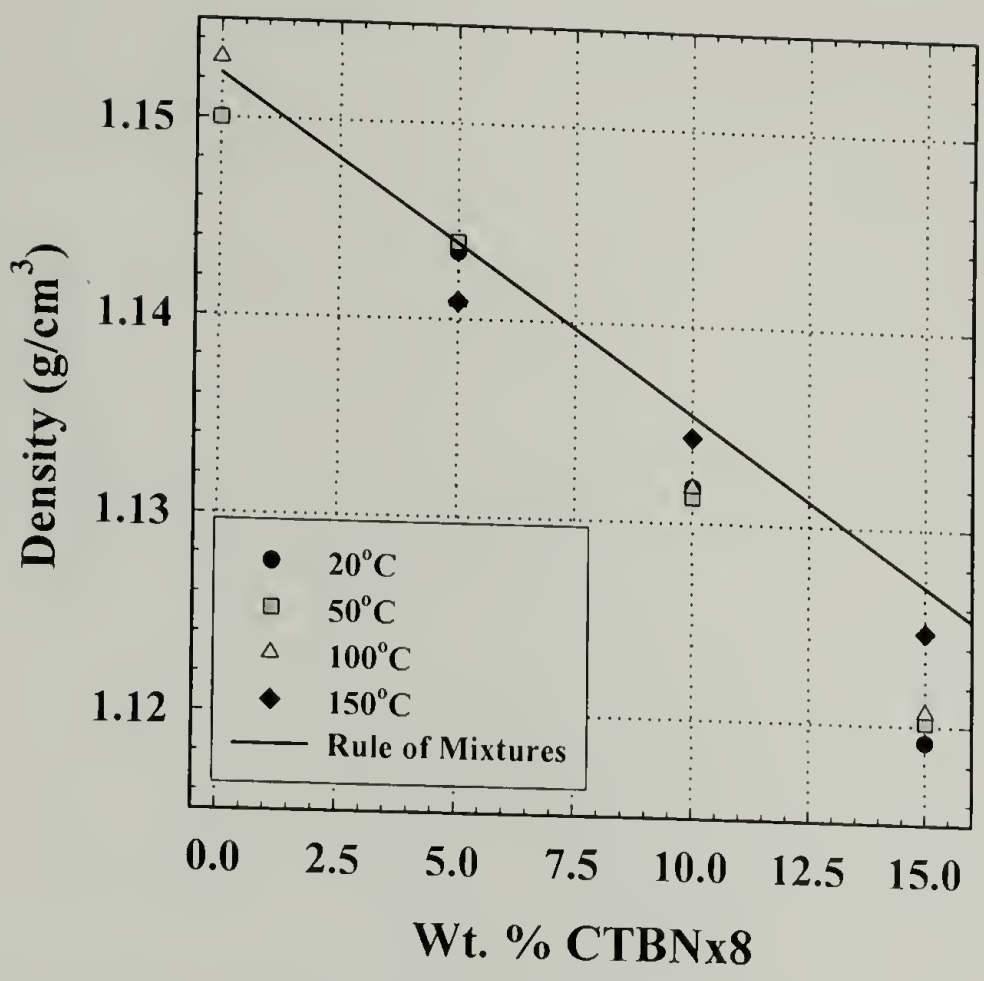

Figure 2.24: Density of epoxies, rubber modified epoxies, and rule of mixtures plot.

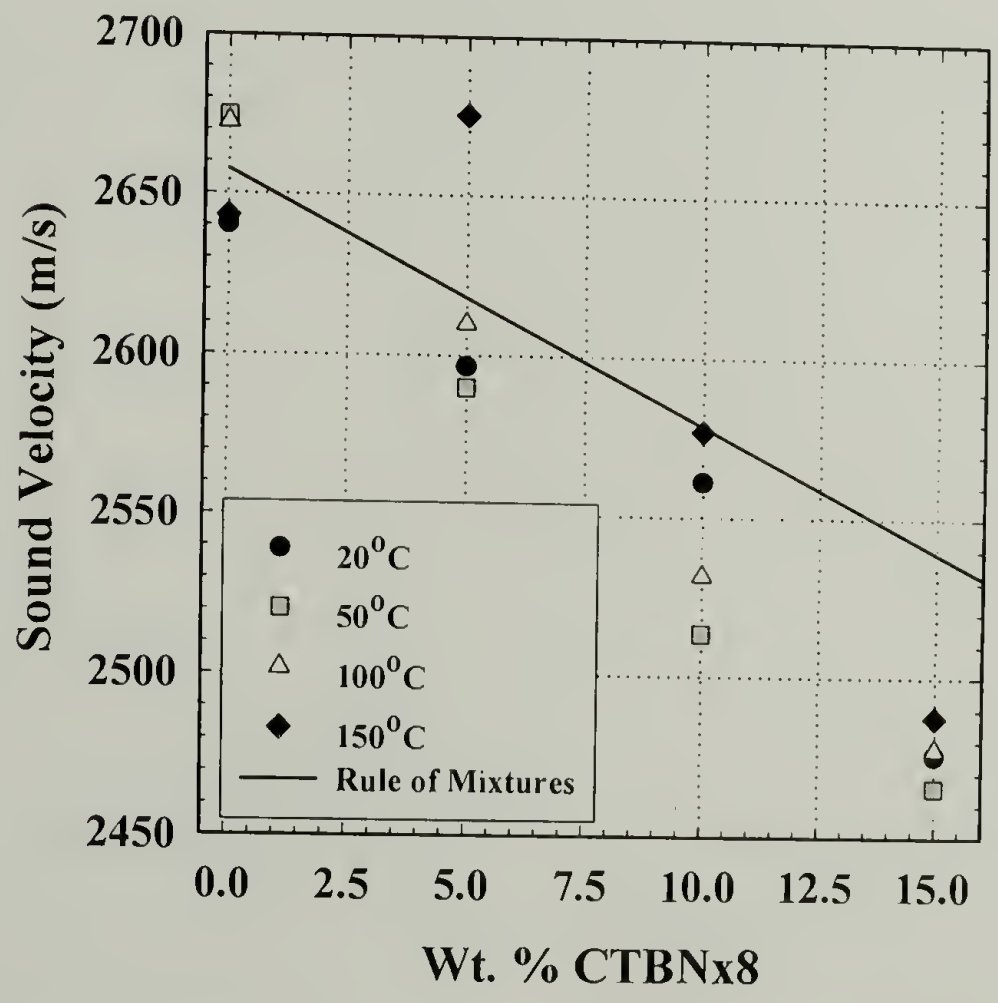

Figure 2.25: Longitudinal velocity of epoxies, rubber modified epoxies, and rule of mixtures plot.

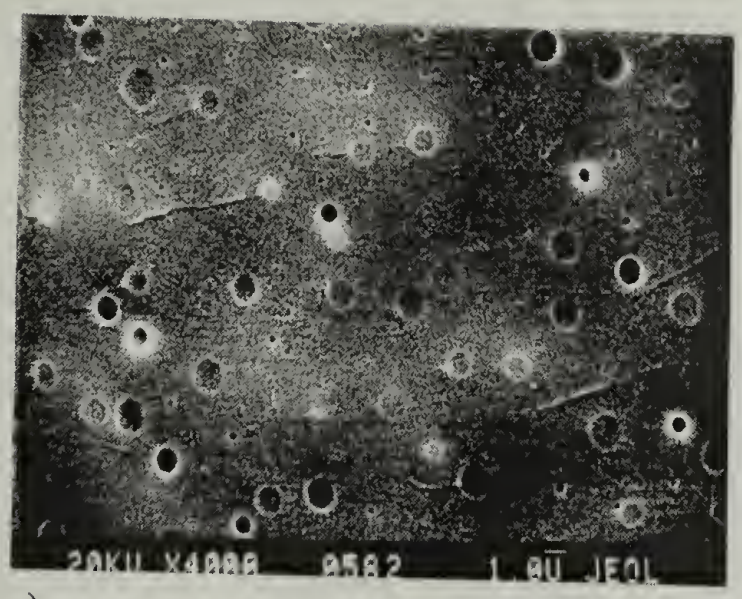

a)

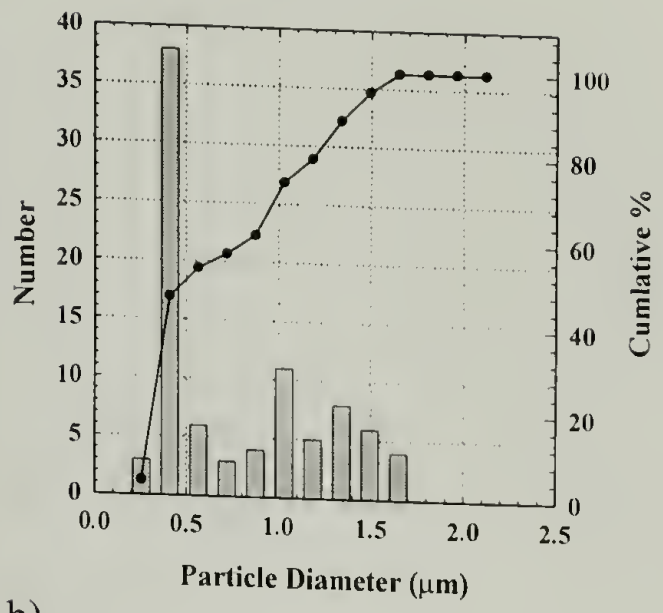

b)

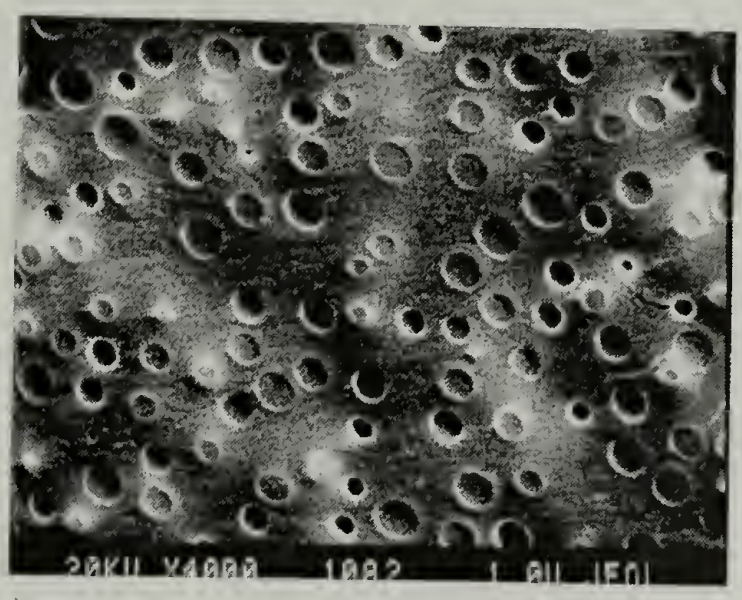

c)

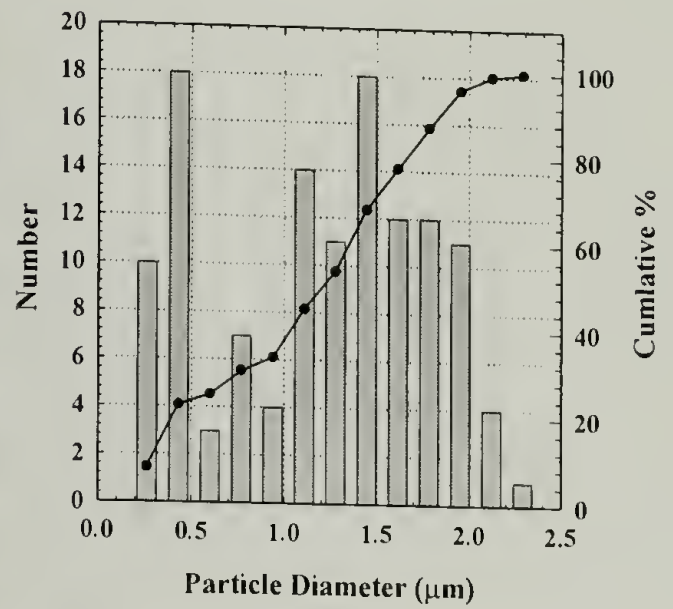

d)

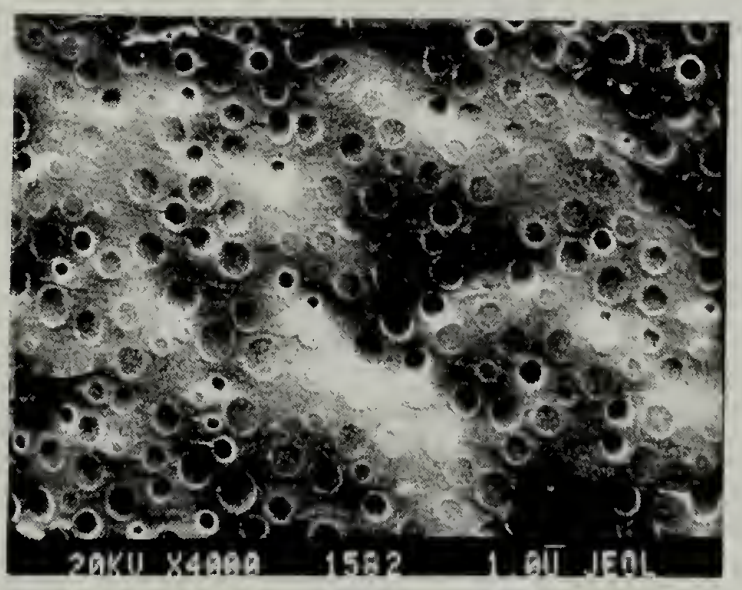

e)

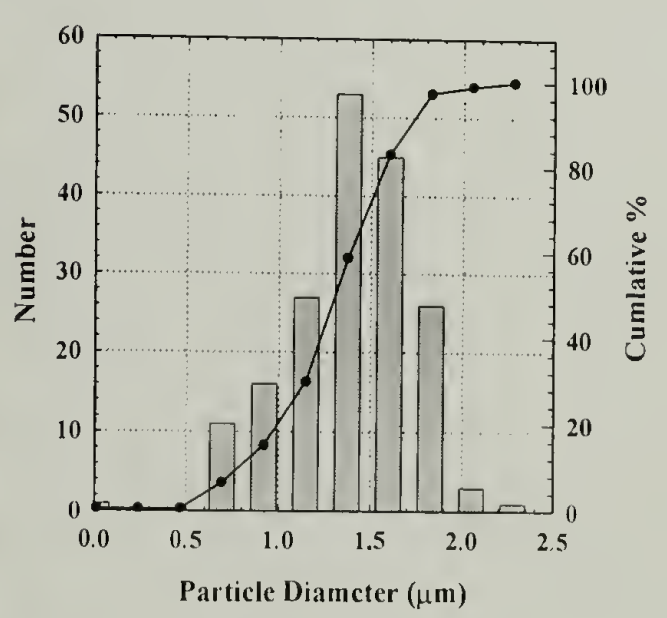

f)

Figure 2.26: SEM images from freeze fractured surfaces and domain size histogram and cumulative percentages of 5 (a, b), 10 (c, d) and 15 (e,f) wt.% CTBN-epoxy gelled at 20 ^{o}C.

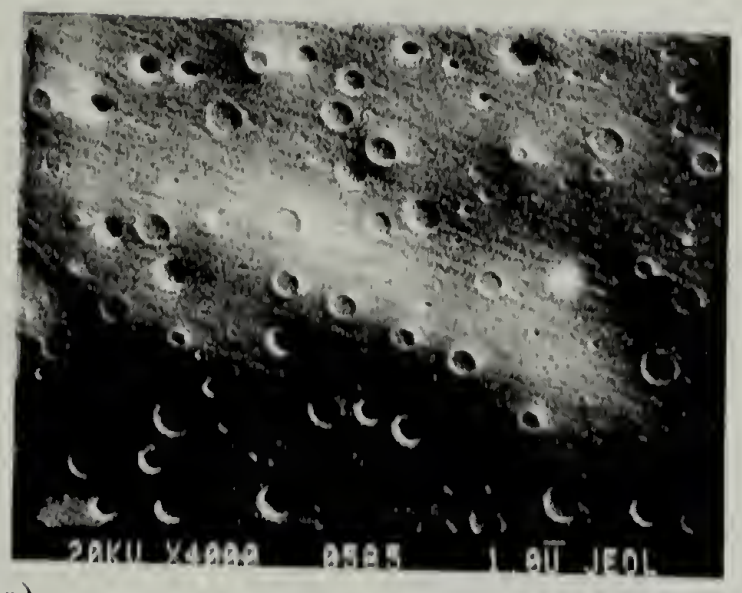

a)

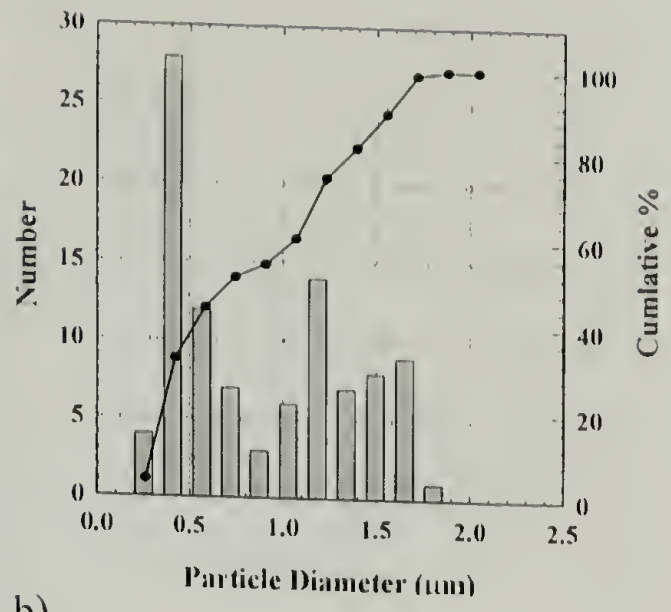

b)

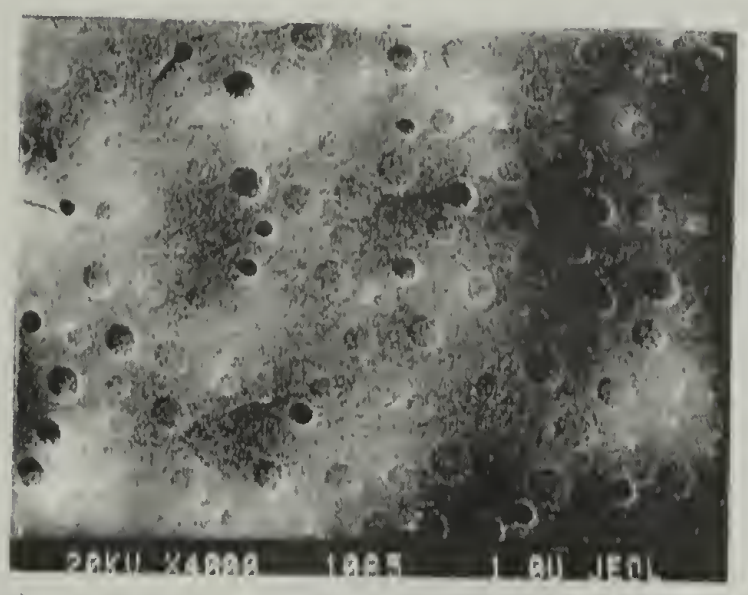

c)

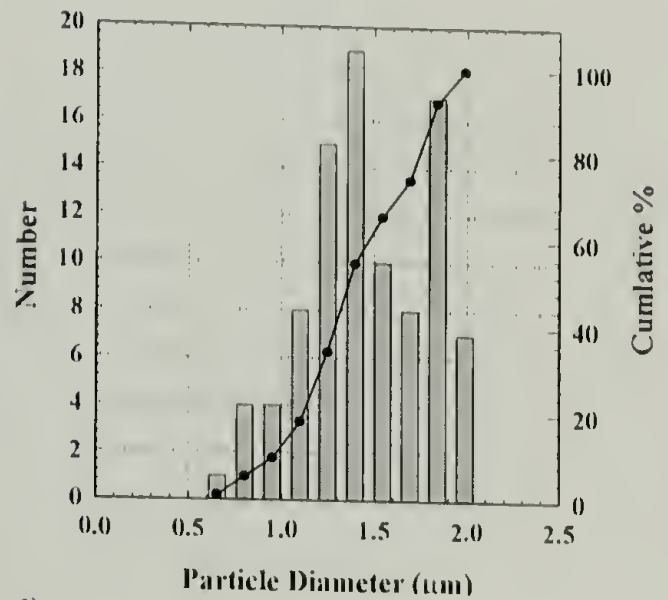

d)

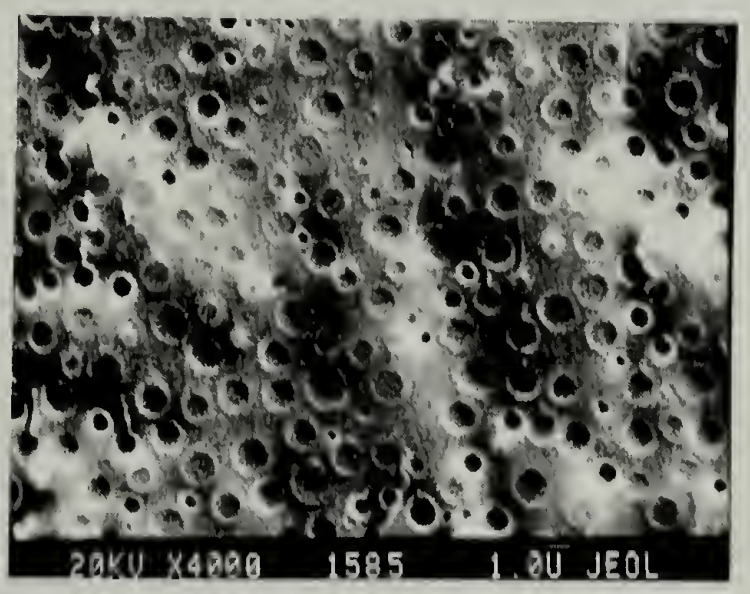

c)

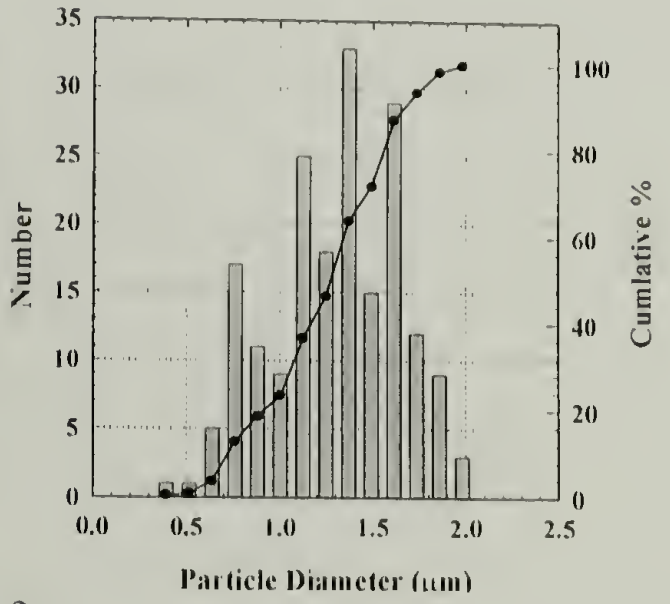

f)

Figure 2.27: SEM images from freeze fractured surfaces and domain size histogram and cumulative percentages of 5 (a, b), 10 (c, d) and 15 (e,f) wt.% CTBN-epoxy gelled at 50 ^{o}C.

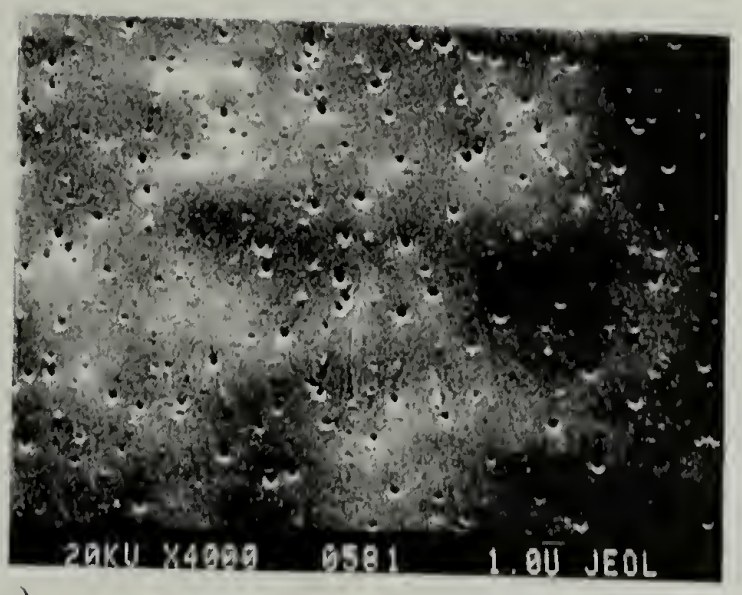

a)

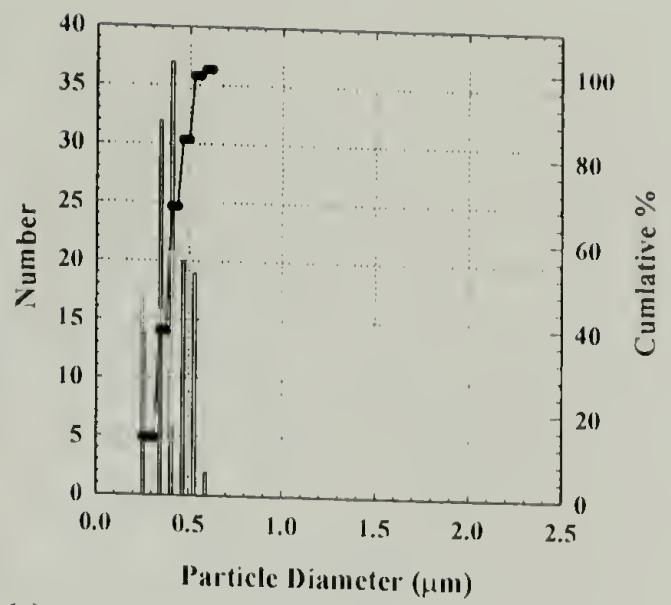

b)

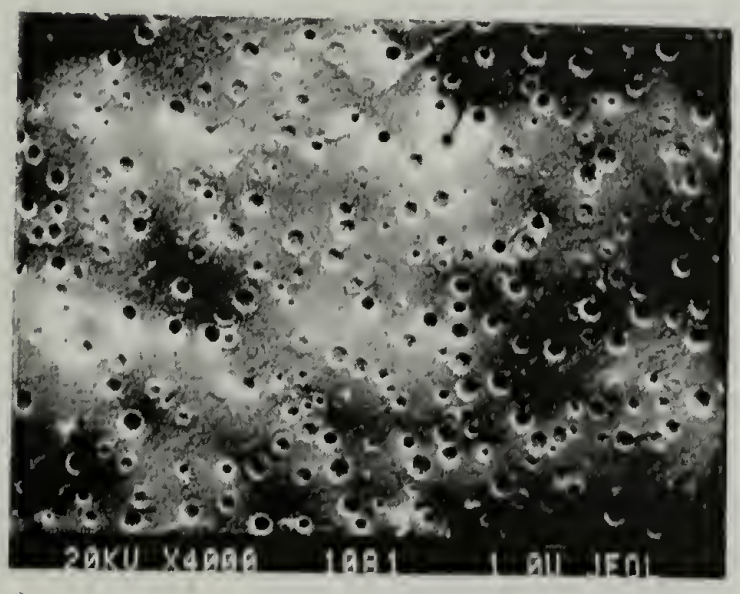

c)

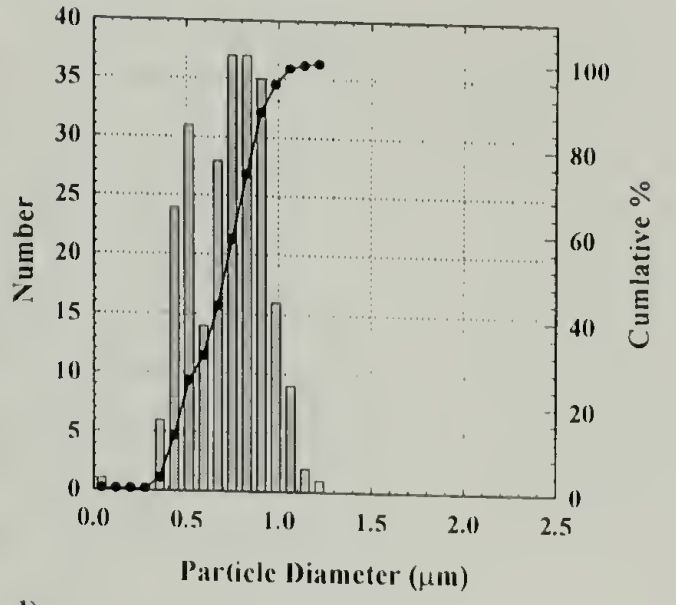

d)

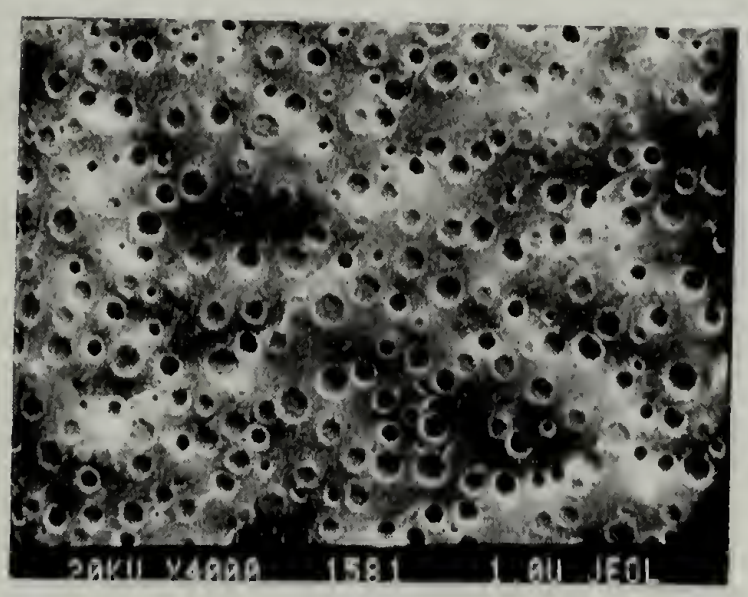

e)

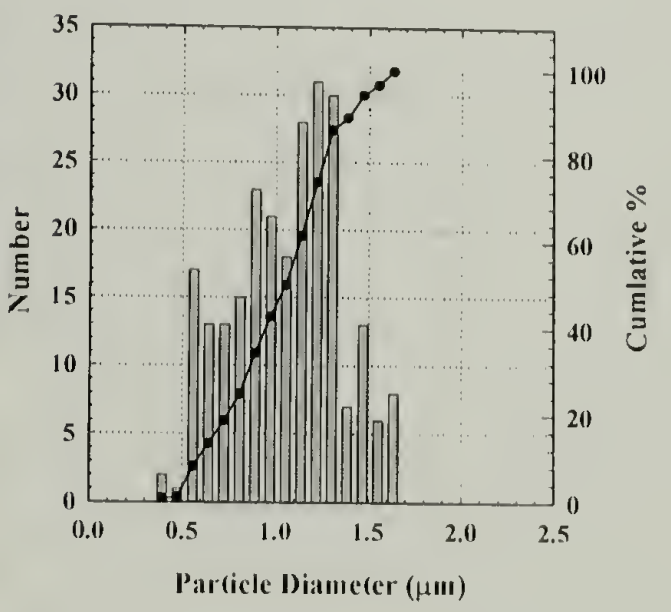

f)

Figure 2.28: SEM images from freeze fractured surfaces and domain size histogram and cumulative percentages of 5 (a, b), 10 (c, d) and 15 (e,f) wt.% CTBN-epoxy gelled at 100 ^{o}C.

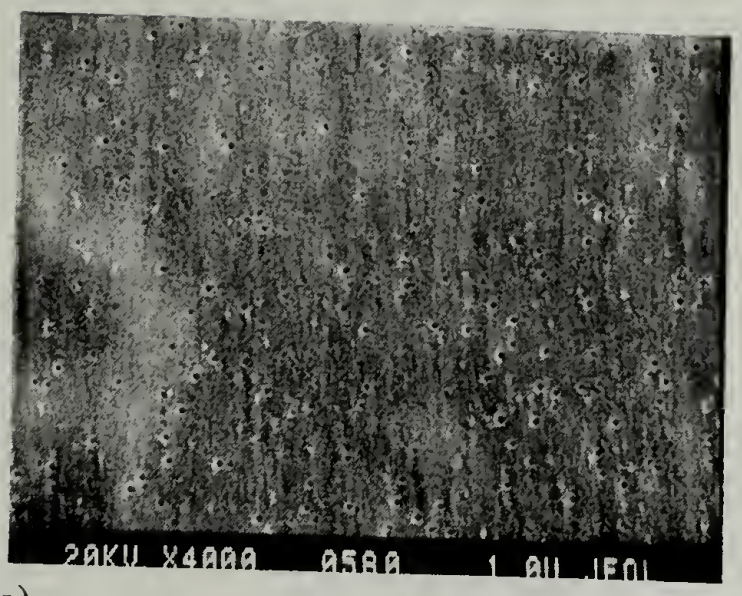

a)

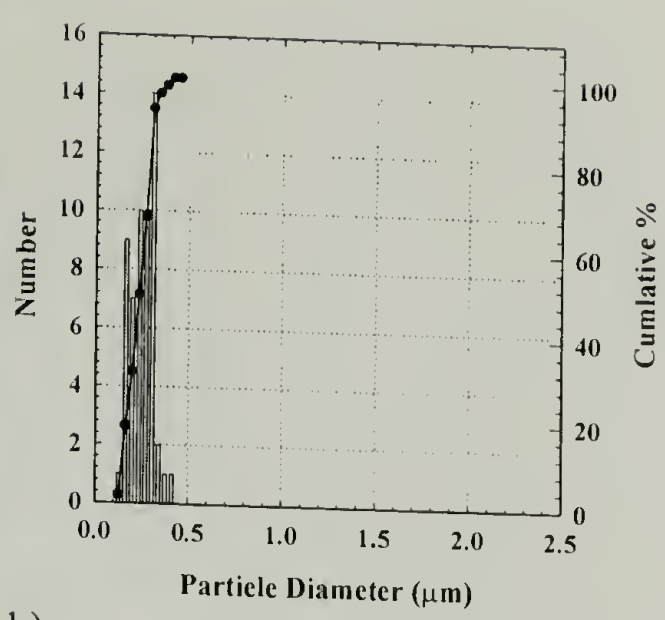

b)

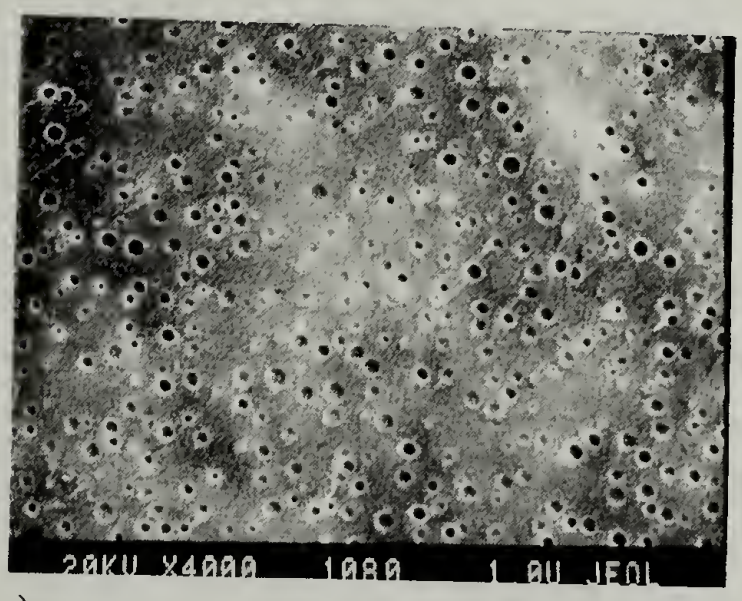

c)

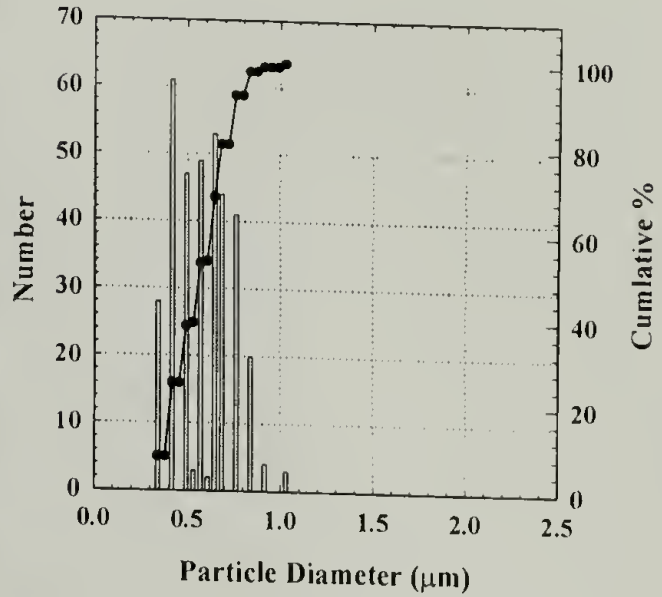

d)

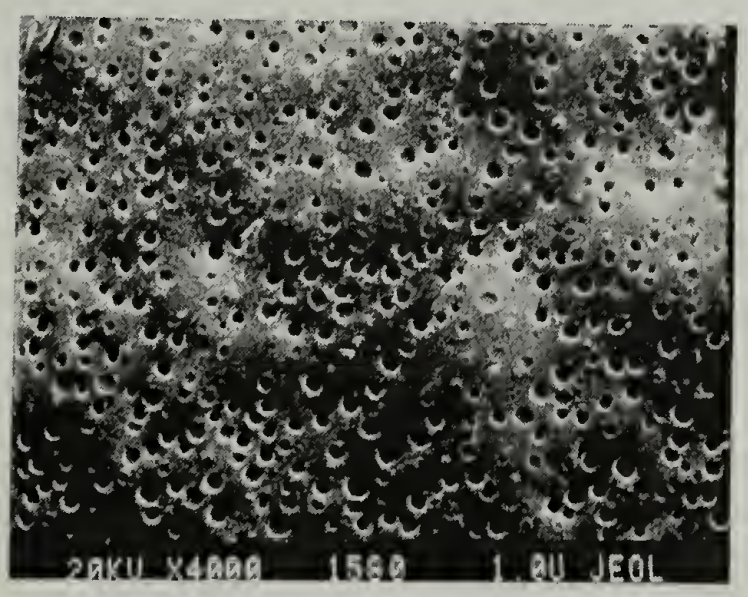

e)

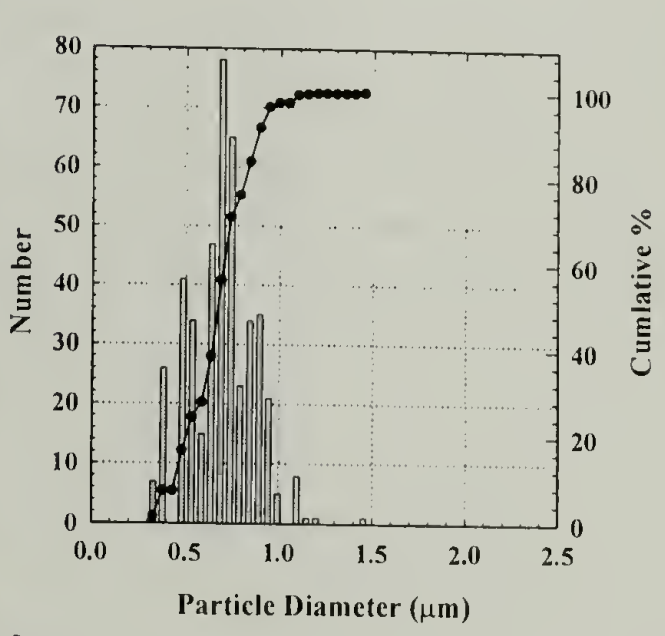

f)

Figure 2.29: SEM images from freeze fractured surfaces and domain size histogram and cumulative percentages of 5 (a, b), 10 (c, d) and 15 (e,f) wt.% CTBN-epoxy gelled at 150 ^{o}C.

2.4.5.2 Ultrasonic analysis

The ultrasonic amplitude spectra are shown for through transmission of water, the epoxies and the rubber modified epoxies in Figure 2.30. Amplitude appears to be uniformly decreased for all specimens. Fortunately, a significant amplitude was measured in the 100 MHz bandwidth that it may be used for analysis. α_S is calculated for all specimens using the data in Table 2.13 and the frequency spectra shown in Figure 2.30. Figure 2.31 is a plot of α_S versus λ for all pure epoxy specimens and has an exponential increase in α_S with decreasing λ. The data is uniform with each epoxy α_S overlapping one another until 20 μm where there is a deviation of the epoxy gelled at 150 °C followed by varying α_S with increasing λ in the data from the 20 MHz bandwidth. Figure 2.32 plots the α_S versus λ for 5, 10, and 15 wt.% CTBN – epoxies gelled at 20 °C. Again there is an exponential increase in α_S with decreasing λ. However, there is observed some degree of separation within the data that can be more closely examined by plotting the 100-50 MHz and 20 MHz bandwidths separately, Figures 2.33 and 2.34 respectively. An incremental increase in α_S with wt.% CTBN and domain size is observed in both the 100 and 50 MHz bandwidths, Figure 2.33, except for the 5 wt.% specimen in the 50 MHz bandwidth. Here α_S deviates to higher rather than expected lower vales with increasing λ . This specimen's morphology is bimodal with a large quantity of 0.4 μm domains dispersed around 1-1.5 μm domains. Thus, the smaller domains may be acting collectively to scatter longer λ in a similar manner as single large domains. The 20 MHz bandwidth is shown in Figure 2.34, where a similar trend of increasing α_S with wt.% CTBN occurs except for the 10 wt.% specimen. Here the data follows the trend only in the 50 to 77 μm range with it falling below all curves beyond

this range. Examining the 20 MHz bandwidth data for specimens gelled at 50, 100, and 150 °C similar irregularities are observed with no clear trends existing.

The 50 and 100 MHz bandwidth data for the specimens gelled at 50, 100, and 150 °C are plotted in Figures 2.35 through 2.37. All have an increasing α_S with *wt.*% CTBN and domain size. However there continue to be some irregularities in the data with non uniform steps between wt.% CTBN and line shapes. The specimens gelled at 50 °C, Figure 2.35, has irregularities in the 5 wt.% specimen in the 20 – 25 μm range and the 15 wt.% specimen in the 9 – 17 μm range. The 5 wt.% specimen has a bimodal morphology and the smaller domains may be acting as a single large domain or producing a higher overall concentration of scattering centers. This is similar to the 20 °C – 5 wt.% specimen yet not as dramatic of a deviation occurs in the data nor are there as many small domains in 50 °C specimen.

The 100 °C specimens, Figure 2.36, have a uniform increase in α_S with wt.% CTBN and domain size in the 100 MHz bandwidth, but in the 50 MHz bandwidth the step is not of the same magnitude nor does the 5 wt.% CTBN specimen follow the trend of the 10 and 15 wt.% specimens. These specimens are monomodal with standard deviations typical of these specimens. What is unusual about this series of specimens is that the $\mathbf{n_o}$ decreases with increasing wt.% CTBN and domain size. This would be expected if CTBN content is held constant while the domain size increases. Here it is the only series in which this occurs, not including the 5 wt.% bimodal specimens. How this impacts the α_S versus λ data is unclear. However, it does lead towards a conclusion that as one employs a smaller and smaller λ the α_S becomes more sensitive to domain size rather than number. This increased sensitivity is most likely the result of the increased

number of compression and rarefaction cycles that occur for a given sample thickness as wavelength decreases.

α_S in the 50 and 100 MHz bandwidths for the specimens gelled at 150 °C is plotted in Figure 2.37. This data is perhaps the most uniform of all CTBN specimens. There is a relatively uniform step increase in α_S with increasing wt.% CTBN and domain size. Also, the line shapes are similar among different samples in a given bandwidth. This series of specimens also has the smallest change in domains size with increased wt.% CTBN while the $\mathbf{n_o}$ increases significantly.

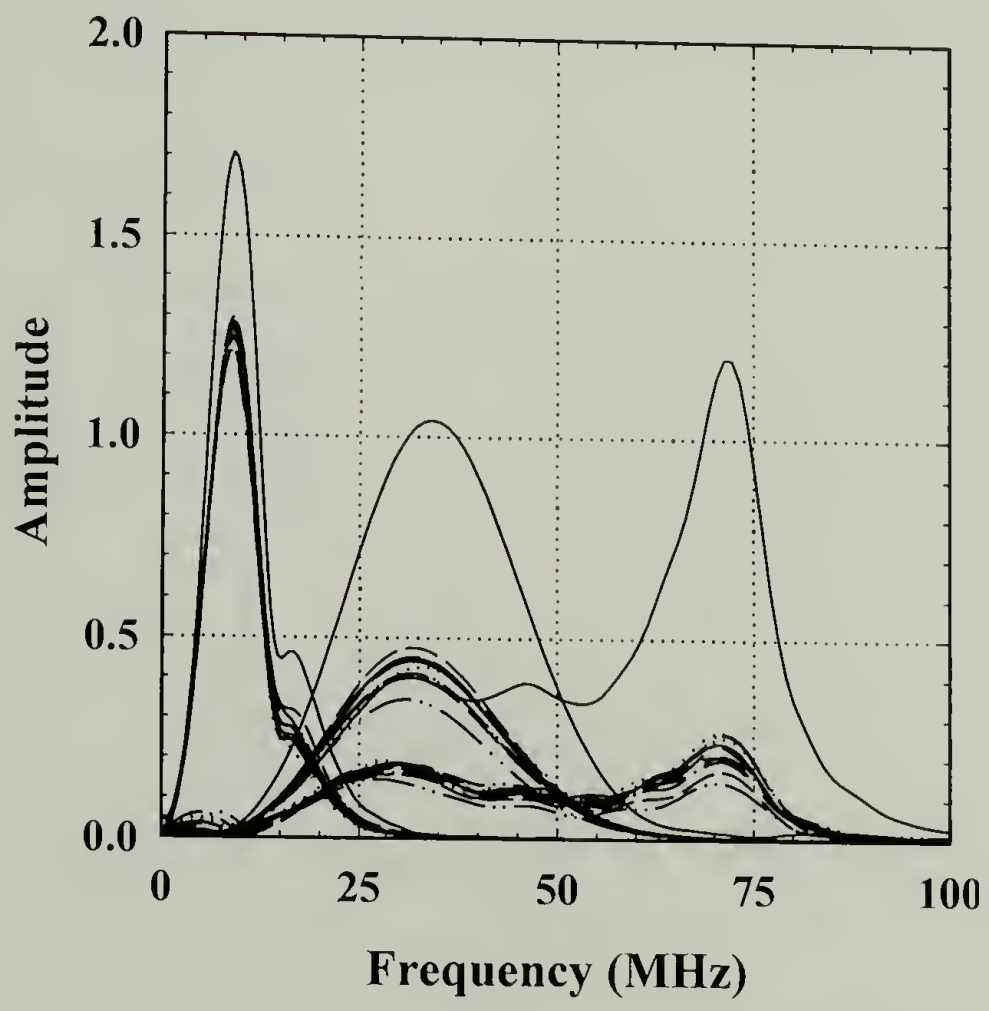

Figure 2.30: Frequency spectra over all bandwidths for water, epoxies and rubber modified epoxies gelled at 20, 50, 100 and 150 °C.

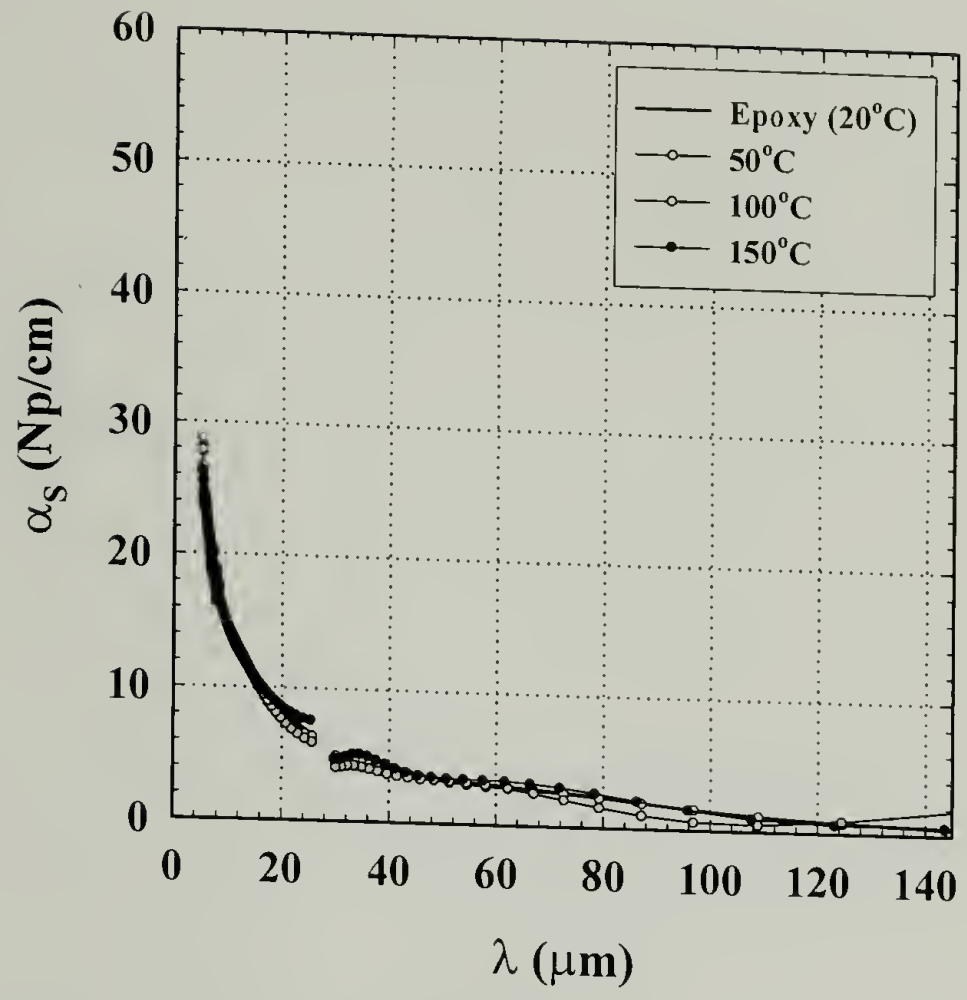

Figure 2.31: α_S versus λ over all bandwidths for epoxies gelled at 20, 50, 100 and 150 °C.

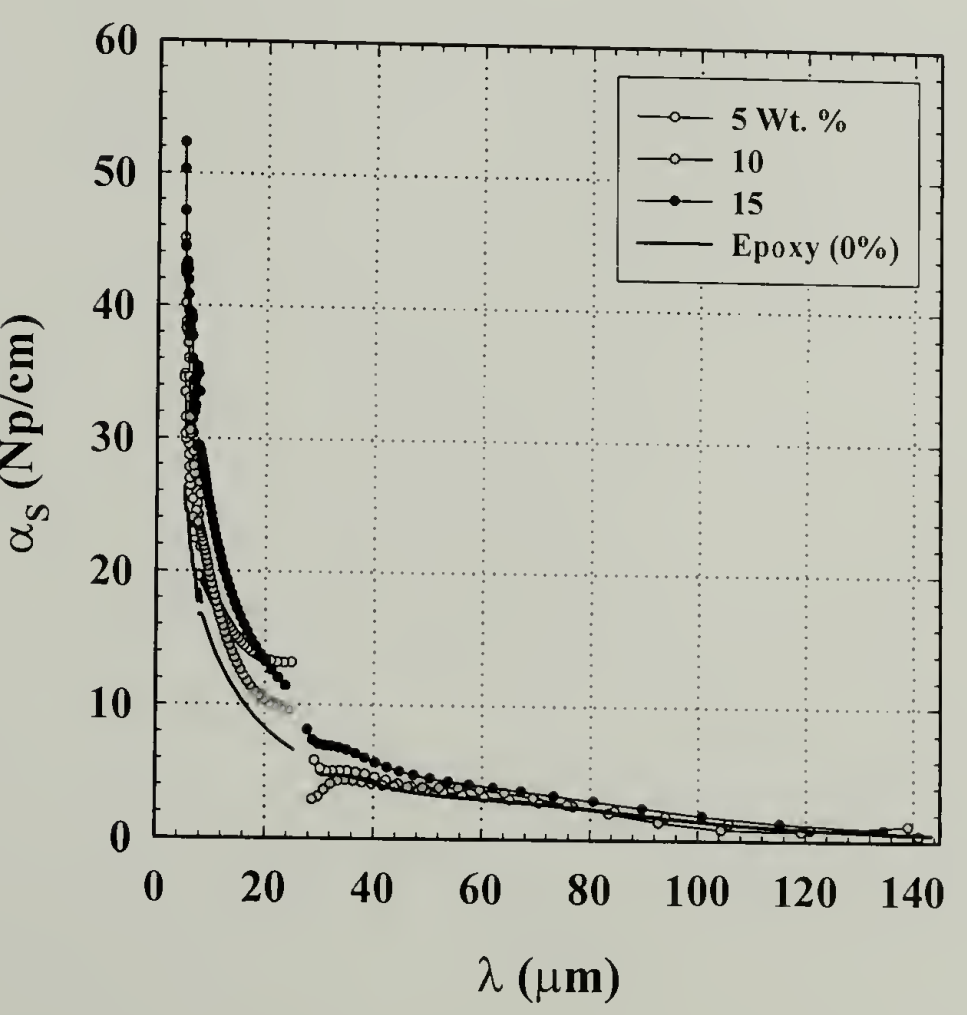

Figure 2.32: α_S versus λ over all bandwidths for 5,10, 15 wt.% CTBN – epoxy and epoxy gelled at 20 °C.

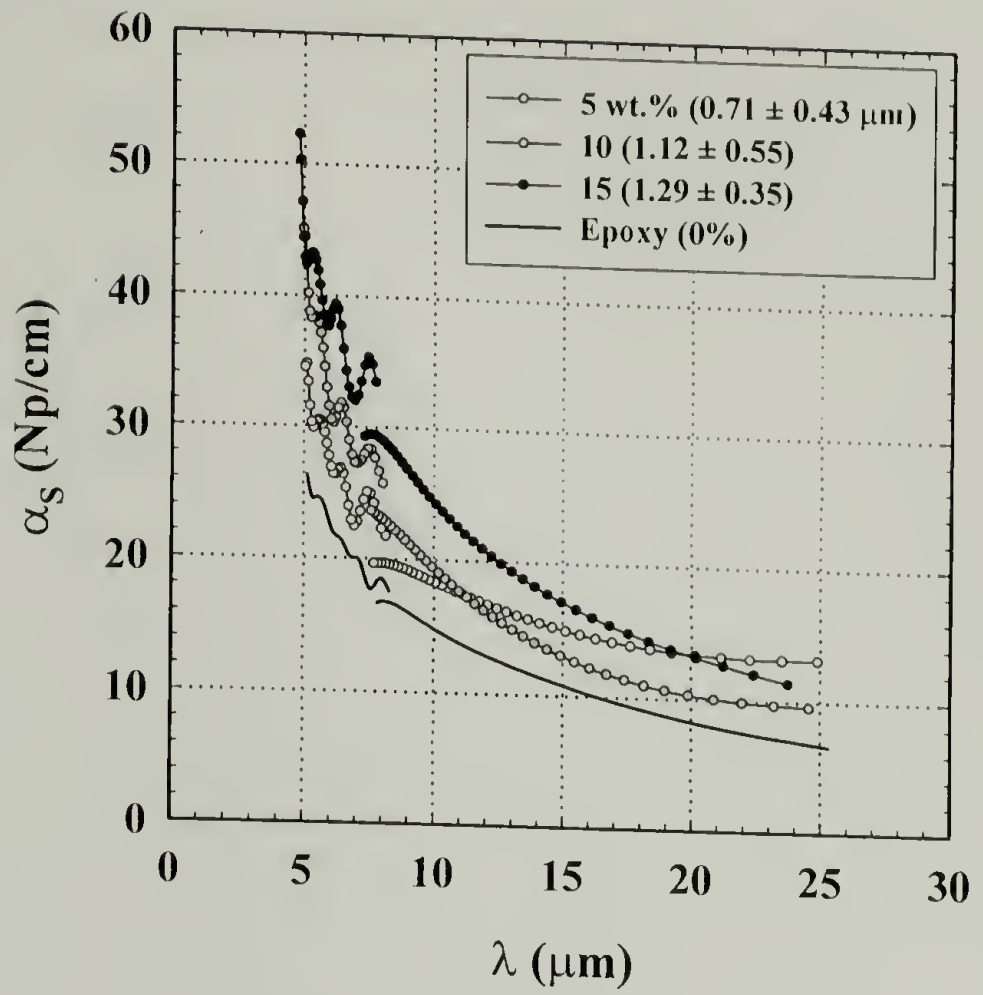

Figure 2.33: α_S versus λ over the 50 and 100 MHz bandwidths for 5,10, 15 wt.% CTBN – epoxy and epoxy gelled at 20 °C.

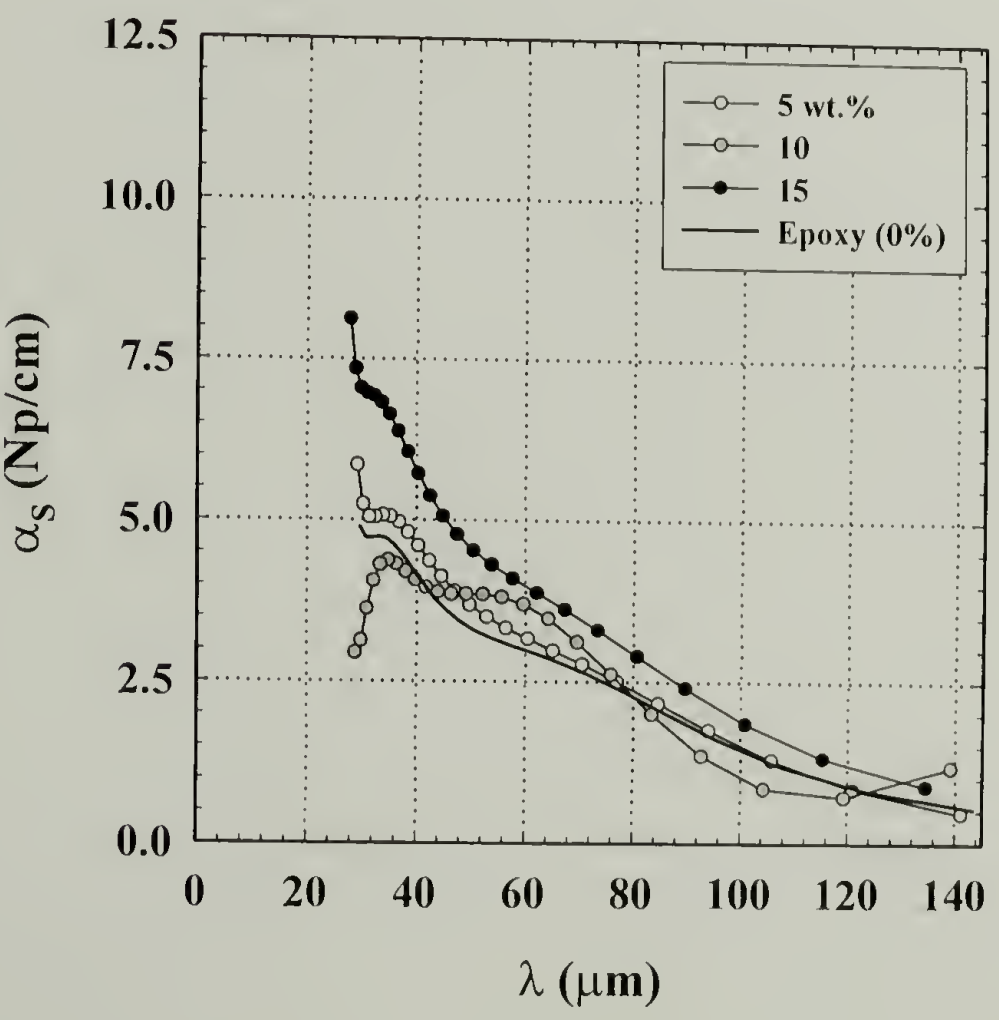

Figure 2.34: α_S versus λ over the 20 MHz bandwidth for 5,10, 15 wt.% CTBN – epoxy and epoxy gelled at 20 °C.

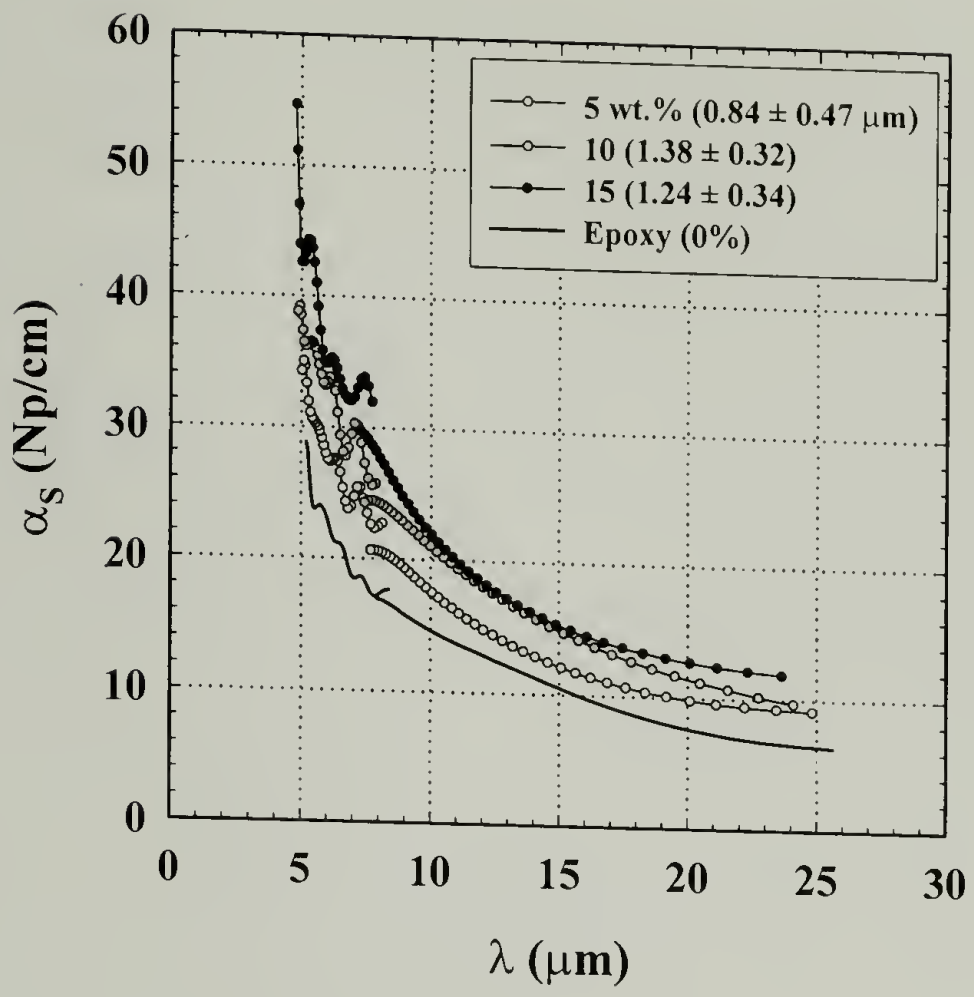

Figure 2.35: α_S versus λ over the 50 and 100 MHz bandwidth for 5,10, 15 wt.% CTBN – epoxy and epoxy gelled at 50 °C.

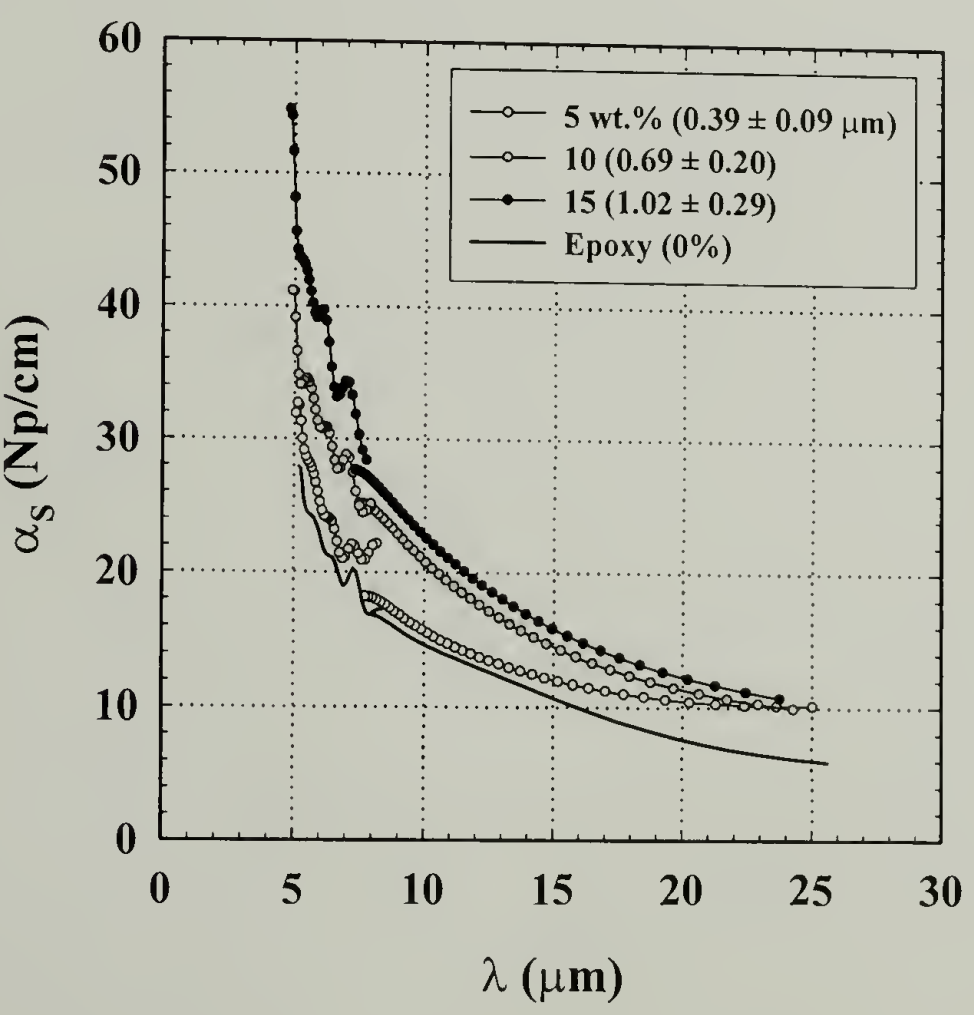

Figure 2.36: α_S versus λ over the 50 and 100 MHz bandwidth for 5,10, 15 wt.% CTBN – epoxy and epoxy gelled at 100 °C.

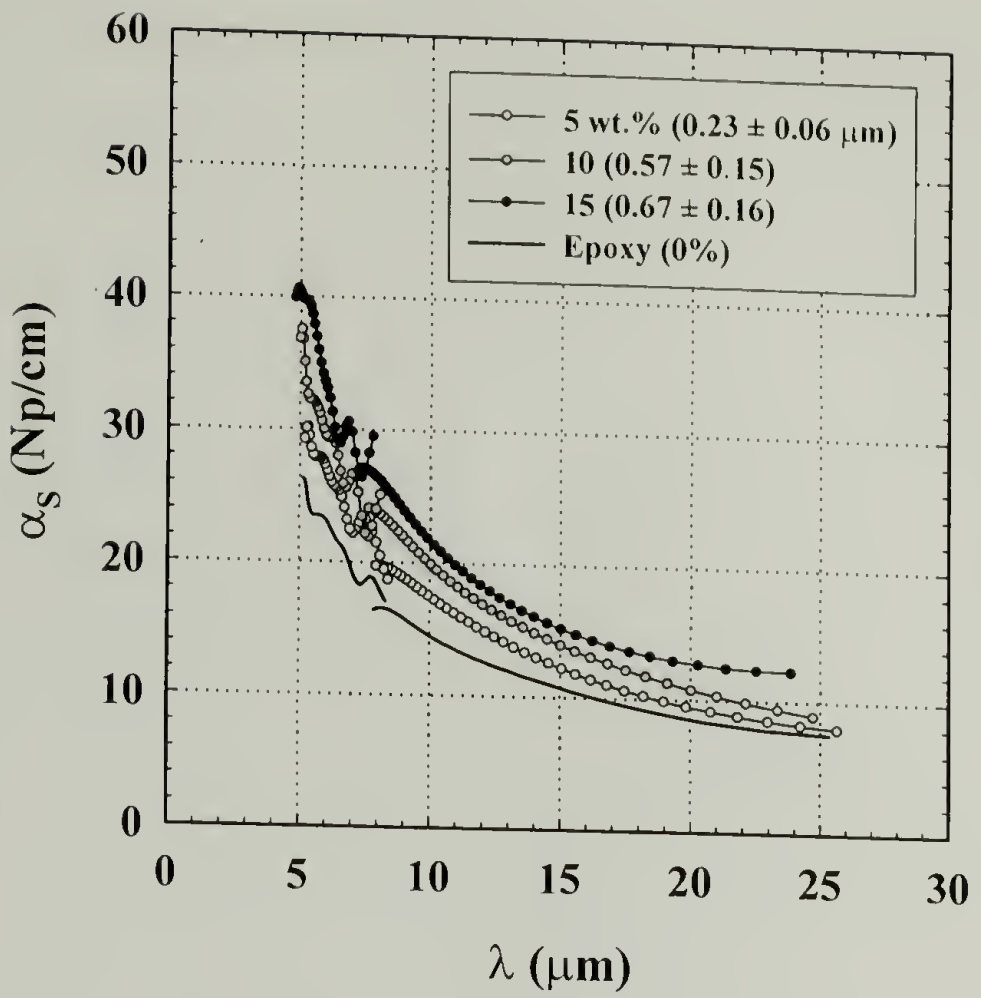

Figure 2.37: α_S versus λ over the 50 and 100 MHz bandwidth for 5,10, 15 wt.% CTBN – epoxy and epoxy gelled at 100 °C.

All of the CTBN specimen data in the 50 –100 MHz bandwidths show an increase in α_S with increasing *wt.*% CTBN and domain size. Several questions arise after examination of the data; 1) Is α_S dominated by changes in the overall amount of added CTBN or the size or number of domains?, and 2) What is the nature of the increasingly irregular data with increasing λ?

The second question is perhaps easier to address. When the α_S measurements are conducted with lower frequencies, i.e. longer λ, fewer and fewer compression and rarefaction cycles take place within the specimen. Thus, the sampling of material property and morphological changes decreases and the resultant resolution of the technique decreases. However, the longer λ are useful for characterizing large variations in morphology and/or material properties. This is illustrated in the PS foams of section

2.4.2 and latter in Chapter 4 where the 20 MHz bandwidth is employed to monitor the thermal degradation of graphite reinforced epoxy composites.

The first question is convoluted by the varying amount of rubber remaining dissolved within the epoxy matrix after cure. The question is addressed by comparing α_S versus λ data for specimens of similar $\overline{\mathbf{D}}$, $\mathbf{n_o}$, and *wt.*% CTBN. Also, the stress wave scattering theories of Truell *et al.* and Sayers will be applied to determine if they are applicable to this system. Figure 2.38 plots α_S versus λ for the 15 wt.% CTBN specimen gelled at 100 °C and the 5 wt.% CTBN specimen gelled at 150 °C. The 15% – 100 °C specimen has a $\overline{\mathbf{D}} = 1.02 \pm 0.29$ μm, $\mathbf{n_o} = 1.515 \times 10^{12}$ cm^{-3}, and a $T_g = 75$ °C. The 5% - 150 °C specimen has a $\overline{\mathbf{D}} = 0.23 \pm 0.06$ μm, $\mathbf{n_o} = 1.874 \times 10^{12}$ cm^{-3}, and a $T_g = 79$ °C. The $\mathbf{n_o}$ of the two specimens are similar yet their $\overline{\mathbf{D}}$ values are very different. Their T_gs differ by 4 °C indicating that the 15% – 100 °C specimen has more dissolved rubber within its epoxy matrix. Examining Figure 2.38 one clearly observes that α_S for the 15% – 100 °C specimen is significantly greater than that of the 10% – 150 °C specimen. Thus, the size of the domain more strongly influences α_S than the number. This observation is reinforced by Figure 2.39, where α_S versus λ is plotted for the10% - 100 °C and the 15% - 150 °C specimens. In this case the sizes are almost identical but the $\mathbf{n_o}$ for the 15% - 150 °C specimen is double that of the 10% - 100 °C specimen. The difference in α_S, Figure 2.39, is small with the 15% - 150 °C specimen having only slightly higher values than the 10% - 100 °C specimen.

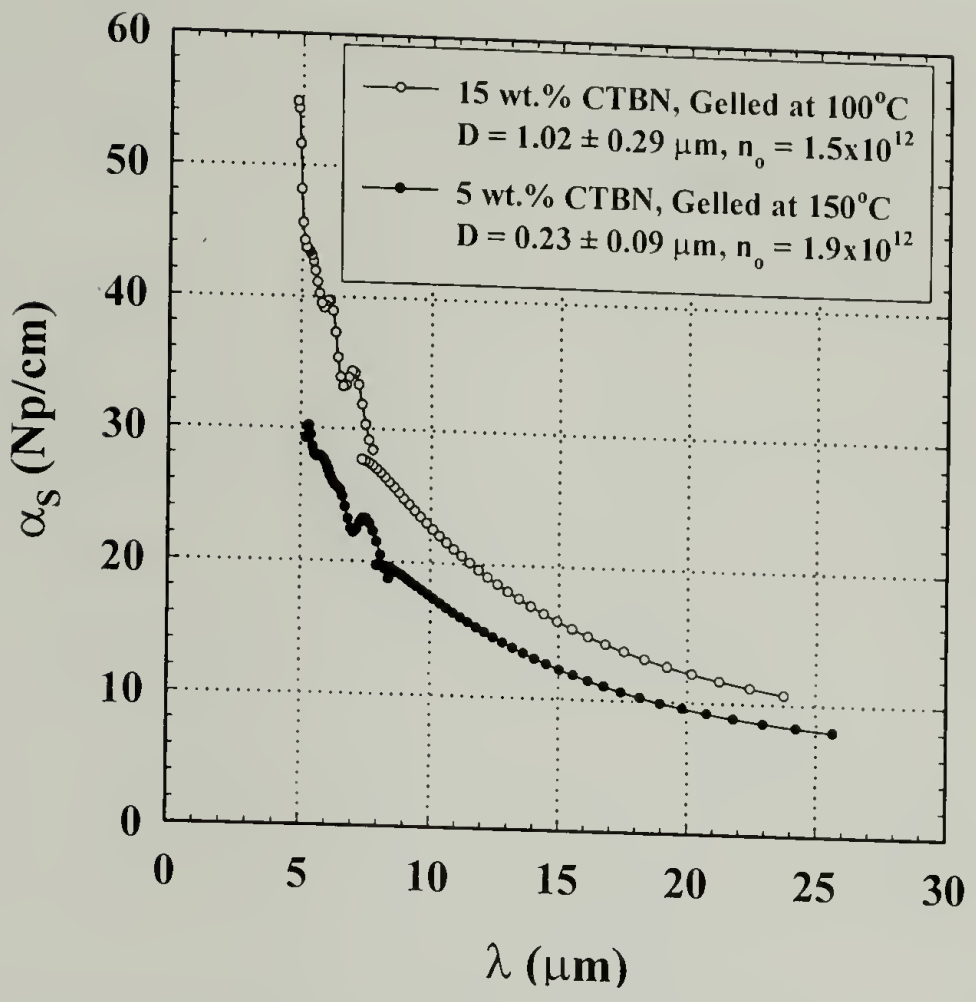

Figure 2.38: α_S versus λ comparison of 15 wt.% CTBN specimen gelled at 100 °C and 5 wt.% specimen gelled at 150 °C.

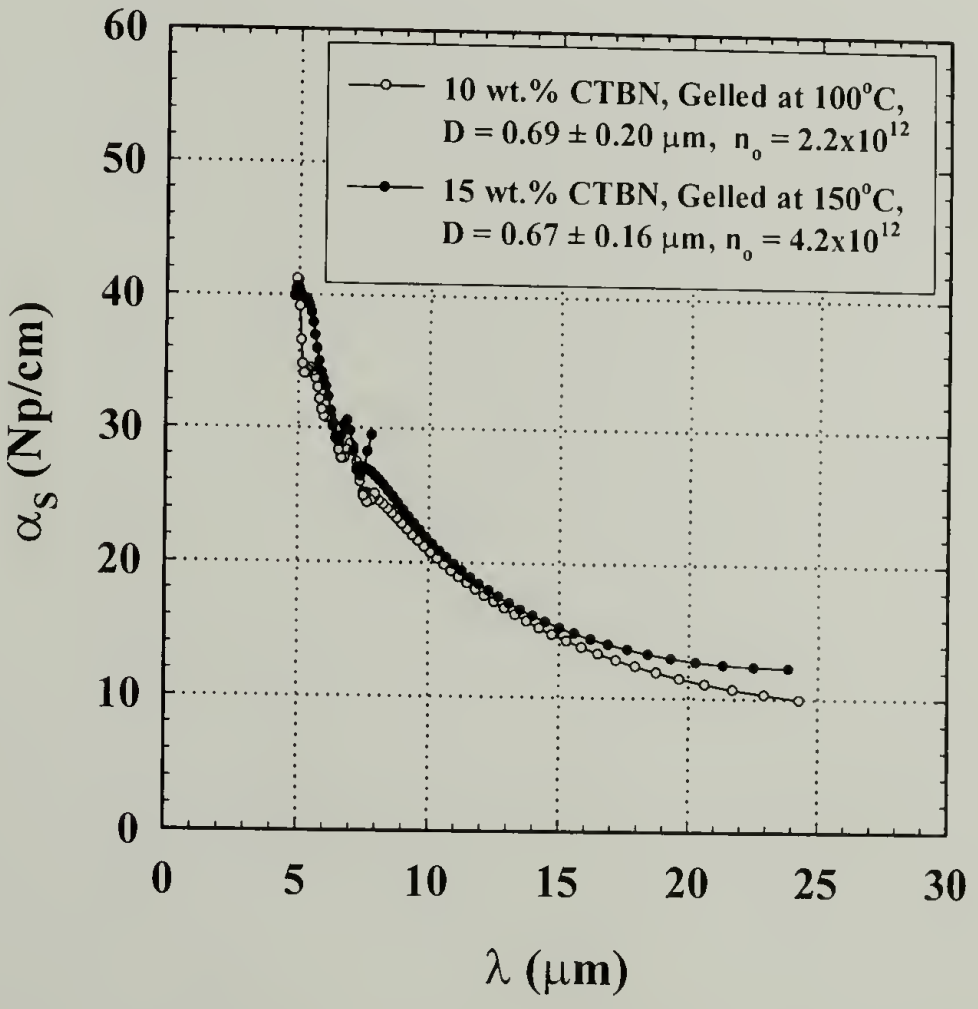

Figure 2.39: α_S versus λ comparison of 10 wt.% CTBN specimen gelled at 100 °C and 15 wt.% specimen gelled at 150 °C.

The effect of the quantity of added rubber on α_S is addressed by plotting the average α_S and associated standard deviation of all specimens with the same wt.% of added rubber. This plotted in Figure 2.40 versus frequency. The data is not plotted versus λ because each sample has a slightly different λ line and is does not make sense to average these quantities. Figure 2.40 clearly illustrates that increasing the amount of rubber increases α_S regardless of size or $\mathbf{n_o}$ of the domains. A caveat must be raised here in that the range of domain sizes is relatively narrow and further studies should be conducted to fully elucidate the α_S behavior over a couple of orders of magnitude. An interesting feature of Figure 2.40 is the jump in α_S between bandwidths. It is assumed that this is the result of different pulser/receiver settings such as attenuation or gain and not a real effect of the materials under examination.

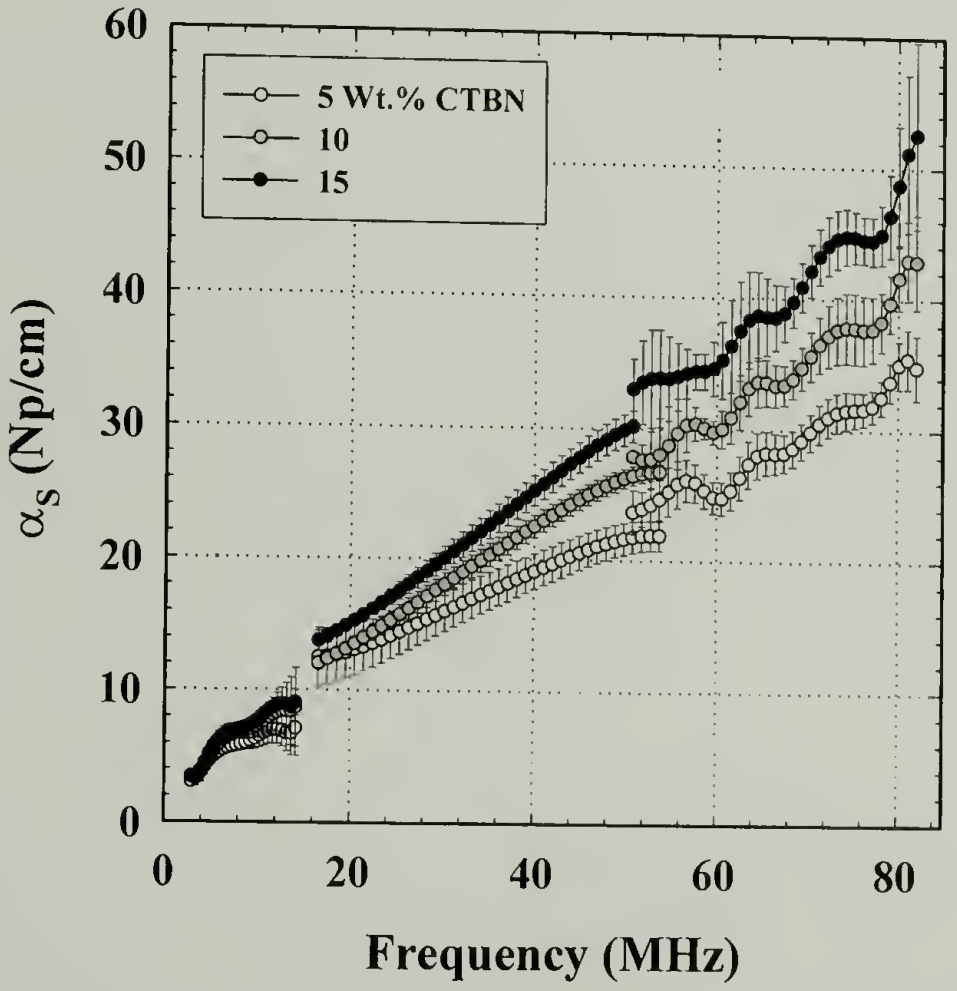

Figure 2.40: Average α_S versus frequency for all rubber modified specimens.

Truell *et al.* and Sayers *et al.*, as diseussed in the introduetion, have both derived relations that tie measure α_S values to the size, number, and properties of scattering eenters. A general form of their relationships is shown in equation 2.33.

$$\alpha_S = f(n_O, k_1^4, a^6, f(c_T, c_L, \rho)) \qquad (2.33)$$

Thus, α_S is a linear function of $\mathbf{n_o}$, a complex funetion of the matrix and heterogeneity material properties, and depends to the sixth power on the radius of the scattering domains. This relationship confirms the observations discussed in the previous seetion where α_S was observed to be dominated by ehanges in $\overline{\mathbf{D}}$ and only slightly by $\mathbf{n_o}$. Also, the strong dependence of α_S on the amount of added rubber is most likely a eombined result of the effeets of $\overline{\mathbf{D}}$, $\mathbf{n_o}$, and material properties.

The effieaey of these theories for predieting α_S from given $\overline{\mathbf{D}}$, $\mathbf{n_o}$, and material properties will be evaluated using the 5 wt.% speeimen gelled at 150 °C because it has a relatively uniform particle size distribution. Direct application of Truell's or Sayers' equations, 2.7 and 2.20 respeetively, to the measured α_S versus λ data for the 5% - 150 °C specimen yields α_S values that are off by several orders of magnitude. Franzblau and Kraft applied Truell's equations to longitudinal wave scattering in porous tungsten. They fitted Truell's equation to their data with an added a constant ($\mathbf{C_o}$) in order to aceount for the attenuation from mechanisms other than scattering, see equation 2.34. The result was a suecessful predietion of the size and a number density off by one order of magnitude.

$$\alpha_S = \frac{2\pi}{9} n_o k_1^4 a^6 g + C_O \qquad (2.34)$$

A similar approach is applied to the 5% - 150 °C specimen in the 50 MHz bandwidth. Figure 2.41 shows a least squares fit to the α_S data for this specimen. The intereept of

this equation is taken as $\mathbf{C_o}$ and the slope as the contribution due to Rayleigh scattering. Thus, the slope is set equal to α_S divided by the frequency, equations 2.35 for Truell and 2.36 for Sayers. Solving these equations for **a** and $\mathbf{n_o}$ yield the values shown in Table 2.14. Also, shown in Table 2.14 are the parameters not given in the preceding tables or discussion that are used in the calculations.

$$\frac{\alpha_S}{f} = \frac{4\pi^4 n_o k_1^3 a^6}{9c_L} \qquad (2.35) \qquad\qquad \frac{\alpha_S}{f} = \frac{4\pi^4 n_o k_1^3 a^6}{3c_L} \qquad (2.36)$$

Table 2.14: Calculated $\overline{\mathbf{D}}$ and $\mathbf{n_o}$ from scattering theory.

	Truell	**Sayers**
$\mathbf{n_o}$ **(#/cm^3)**	1.036×10^{25}	1.156×10^{24}
a (μm)	15.03	12.52
Parameters	$\mathbf{c_T}$(Epoxy) = 1236.6 m/s $\mathbf{c_L}$(CTBN) = 1698.2 m/s $\mathbf{g_f}$ = 2.443	$\mathbf{c_T}$ (5%-150 °C) = 1154.61 m/s **C** = 7.302

It is apparent that these numbers are far from those measured. The successful result of Franzblau and Kraft was obtained with a number density of 1.3×10^7 cm^{-3} and indicates that there cause of the large discrepancy may be the five orders of magnitude increase in the number of rubber domains for these samples. One possibility is that the liquid rubber domains are not acting as independent point scattering centers but as single or clusters of larger domains. Another possibility is that there is a considerable amount of rubber that has remained dissolved in the epoxy matrix after cure, as indicated by the depressed T_g, and may act to increase the overall attenuation of the matrix.

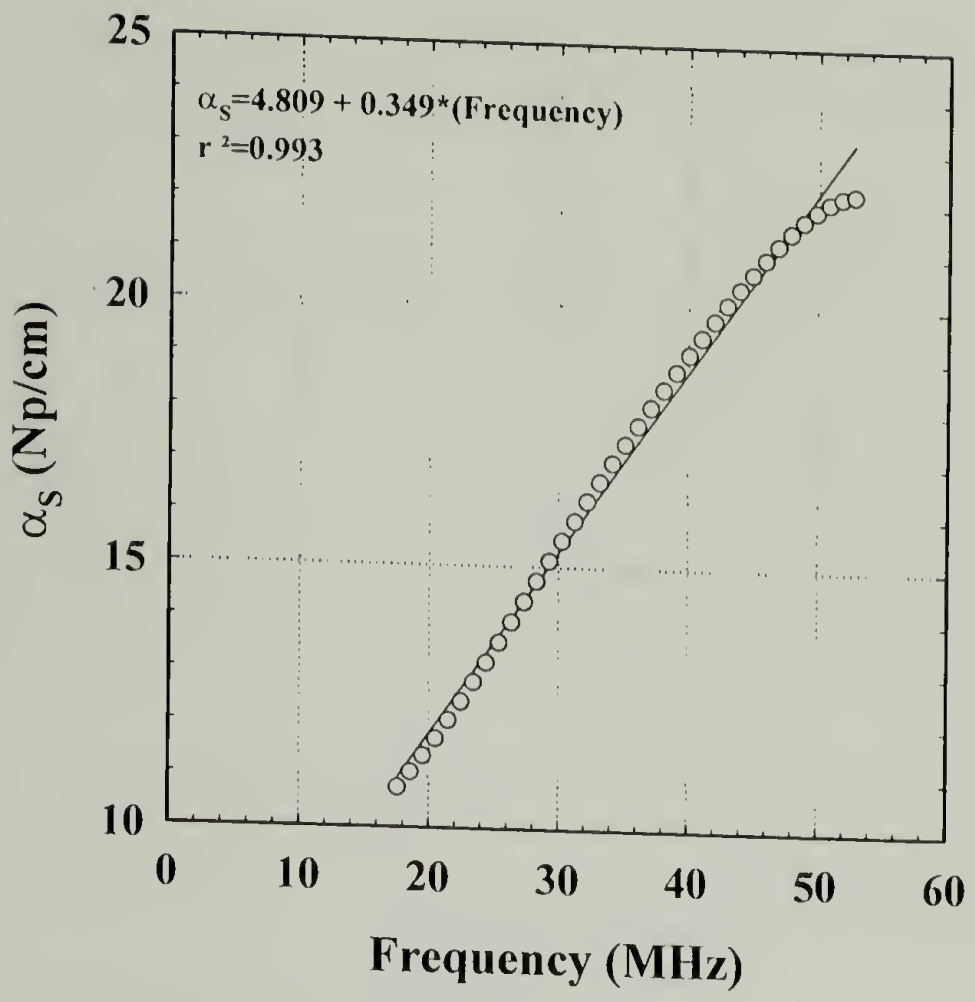

Figure 2.41: α_S versus λ for 5 wt.% CTBN specimen gelled at 150 °C with least squares fit.

2.5 Conclusions

Applying ultrasonic spectroscopy to a the morphological analysis of several different polymeric matrices containing spherical heterogeneities consisting of cavities, elastic solid, and fluid yielded a broad range of useful information. In the intermediate wavelength regime the average pore diameter was identified by strong attenuation of wavelengths of similar length scale. This was especially successful in the porous epoxy specimen with relatively uniform domain size. Surprisingly, the complex void shape and size, and high number density of the PS foams did not exclude them from study as sufficient signal amplitude was transmitted and favorable agreement was achieve in identifying the void size.

Analysis in the Rayleigh scattering regime did not yield information that related the size of the domains present. However, it did successfully identify responses believed to be effected by the phase transitions within the acrylic blends. The morphology of specimens is perhaps the most difficult to characterize by traditional means. Morphological information was only previously obtained by contrast developed through localized differences in crack propagation around domains of the dispersed phase.[34] Analysis of rubber modified epoxies with a range of added rubber content, domain size, and $\mathbf{n_o}$ revealed that ultrasonic spectroscopy could successfully differentiate between materials with different concentrations of added rubber and domain size. It was not as sensitive to changes in the number of domains present unless they tended to act collectively as larger domains. Application the stress wave scattering theories to the rubber modified epoxies was unsuccessful. Although, Sayers' approach takes into account scattering from multiple sites the number of rubber of domains within these specimens is perhaps too high for α_S versus λ to be discretely affected.

2.6 References

1) Stanley, R. K. *Special Nondestructive Testing Methods*; 2 ed.; Stanley, R. K., Ed.; American Society for Nondestructive Testing: Columbus, 1995; Vol. 9.

2) Cartz, L. *Nondestructive Testing Radiography, Ultrasonics, Liquid Penetrant, Magnitic Particle, Eddy Current*; AMS International: Materials Park, 1995.

3) Filipczynski, L.; Pawlowski, Z.; Wehr, J. *Ultrasonic Methods of Testing Materials*; 3rd ed.; Butterworth and Co.: London, 1966.

4) McClements *Langmuir* **1996**, *12*, 3454-3461.

5) Pollard, H. F. *Sound Waves in Solids*; Pion Limited: London, 1977.

6) Wada, Y.; Yamamoto, K. *Journal of the Physical Society of Japan* **1956**, *11*, 887-892.

7) Akker, S.; Arman, J. *Eur. Polym. J.* **1994**, *31*, 125-130.

8) Gilbert, A. S.; Pethrick, R. A.; Phillips, D. W. *J. Appl. Polym. Sci.* **1977**, *21*, 319-330.

9) Hull, J. B.; Langton, C. M.; Jones, A. R. *Macromolecular Reports* **1994**, *A31(Suppls. 6 & 7)*, 1191-1199.

10) Paladhi, R.; Singh, R. P. *European Polymer Journal* **1994**, *30*, 251-257.

11) Paladhi, R.; Singh, R. P. *J. Appl. Polym. Sci.* **1994**, *51*, 1559-1565.

12) Gupta, R. k.; Gaba, I. D.; Pande, C. D.; Singh, Y. P.; Singh, R. P. *Ultrasonic and Viscometric Investigation of Polymer-Polymer Compatibility in Solutions of Polyamic Acid Blends*; Plenum Press: New York, 1982; Vol. 1, pp 547-554.

13) Price, G. J.; West, P. J. *Polymer* **1996**, *37*, 3975-3978.

14) Somanthan, N.; Senthil, P.; Viswanathan, S.; Arumugam, V. *J. Appl. Polym. Sci* **1994**, *54*, 1537-1544.

15) Bear, R. S.; Brown, S. D. *Anal. Chem.* **1993**, *65*, 1169-1173.

16) Gendron, R.; Tatibouet, J.; Guevremont, J.; Dumoulin, M. M.; Piche, L. *Ultrasonic Behavior of Polymer Blends*; Society of Plastics Engineers, 1994, pp 2452-2456.

17) Gendron, R.; Tatibouet, J.; Guevremont, J.; Dumoulin, M. M.; Piche, L. *Poly. Eng. Sci* **1995**, *35*, 79-91.

18) Verdier, C.; Piau, M. *J. Phys. D: Appl. Phys.* **1996**, *29*, 1454-1461.

19) Patel, S. H.; Todd, D. B.; Xanthos, M. *Recent Developments in On-line Analytical Techniques Applicable to the Polymer Industry*; Society of Plastics Engineers, 1994, pp 2214-2219.

20) Matsushige, K.; Okabe, H.; Shichijyo, S.; Takemura, T. *Japanese J. Appl. Phys.* **1985**, *24*, 34-36.

21) Alder, L.; Rose, J. H.; Mobley, C. *J. Appl. Phys.* **1986**, *2*, 336.

22) Ying, C. F.; Truell, R. *J. Appl. Phys.* **1954**, *27*, 1086-1097.

23) Hertzfeld, K. F. *Philo. Mag. J. Sci* **1930**, *9*, 741-751.

24) Einspruch, N. G.; Truell, R. *J. Acoust. Soc. Am.* **1960**, *32*, 214-220.

25) Sayers, C. M. *J. Phys. D: Appl. Phys.* **1981**, *14*, 413-420.

26) Truell, R.; Elbaum, C.; Chick, B. B. *Ultrasonic Methods in Solid State Physics*; Academic Press: New York, 1969.

27) Underwood, E. E. *Quantitative stereology*; Addison-Wesley Pub. Co.: Reading, Mass., 1970.

28) Franzblau, M. C.; Kraft, D. W. *J. Appl. Phys.* **1971**, *42*, 5261-5262.

29) Waterman, P. C.; Truell, R. *J. Math. Phys.* **1961**, *2*, 512-537.

30) Foldy, L. L. *Phys. Rev.* **1945**, *67*, 107-119.

31) McClements, D. J.; Fairley, P. *Ultrasonics* **1992**, *30*, 43-45.

32) Crawford, E.; University of Massachusets: Amherst, 1999, pp 168.

33) Arora, K. ; Arora, K.; University of Massachusets: Amherst, 1999, pp 168.

34) Agarwal, N.; University of Massachusets: Amherst, 1998, pp 249.

35) Matsushige, K.; Hiramatsu, N.; Okabe, H. *Ultrasonic Spectroscopy for Polymeric Materials*; Springer Verlag: New York, 1995; Vol. 125, pp 147-186.

36) McClements, D. J. *Advances in Colloid and Interface Science* **1991**, *37*, 33-72.

37) Lee, C. C.; Lahham, M.; Martin, B. G. *IEEE Trans. Ultrasonics. Ferro. Freq. Control* **1990**, *37*, 286-294.

38) Sharpe, R. S. *Quality Technology Handbook*; 4 ed.; Butterworth: New York, 1949.

39) Kiefer, J.; Hilborn, J. G.; Hedrick, J. L. *Polymer* **1996**, *18*, 5715-5725.

40) Arends, C. B. *Polymer toughening*; Marcel Dekker: New York, 1996.

41) Martuscelli, E.; Musto, P.; Ragosta, G. *Advanced routes for polymer toughening*; Elsevier: Amsterdam ; New York, 1996.

42) Riew, C. K.; Kinloch, A. J.; American Chemical Society. Division of Polymeric Materials: Science and Engineering.; American Chemical Society. Meeting *Toughened plastics I : science and engineering*; American Chemical Society: Washington, DC, 1993.

43) Riew, C. K.; Kinloch, A. J.; American Chemical Society. Division of Polymeric Materials: Science and Engineering.; American Chemical Society. Meeting *Toughened plastics II : novel approaches in science and engineering*; American Chemical Society: Washington, DC, 1996.

44) Riew, C. K.; Gillham, J. K. *Rubber-modified thermoset resins : based on a symposium*; Riew, C. K.; Gillham, J. K., Ed.; American Chemical Society: Washingtgon, D.C., 1984, pp xi, 372.

45) Grillet, A. C.; Galy, J.; Pascault, J. P. *Polymer* **1992**, *33*, 34-43.

46) Kim, D. S.; Kim, S. C. *Polym. Eng. Sci.* **1994**, *34*, 1598-1604.

47) Verchere, D.; Pascault, J. P.; Sautereau, H.; Moschair, S. M.; Riccardi, C. C.; Williams, R. J. J. *J. Appl. Polym. Sci.* **1991**, *42*, 701-716.

48) Verchere, D.; Sautereau, H.; Pascault, J. P.; Moschiar, S. M.; Riccardi, C. C.; Williams, R. J. J. *Rubber-modified epoxies. Analysis of the phase separation process*; ACS, 1990; Vol. 63, pp 99-103.

49) Chen, J. P.; Lee, Y. D. *Polymer* **1995**, *36*, 55-65.

50) Pucciariello, R.; Villani, V.; Bianchi, N.; Braglia, R. *Polym. Int.* **1991**, *26*, 69-73.

51) Vallo, C. I.; Hu, L.; Frontini, P. M.; Williams, R. J. J. *J. Mater. Sci.* **1994**, *29*, 2481-2486.

52) Delides, C. G.; Hayward, D.; Pethrick, R. A.; Vatalis, A. S. *J. Appl. Polym. Sci.* **1993**, *47*, 2037-2051.

53) Nae, H. N. *J. Appl. Polym. Sci.* **1986**, *31*, 15-25.

54) Moschair, S. M.; Riccardi, C. C.; Williams, R. J. J.; Verchere, D.; Sautereau, H.; Pascault, J. P. *J. Appl. Polym. Sci.* **1991**, *42*, 717-735.

55) Chen, D.; Pascault, J. P.; Sautereau, H.; Ruseckaite, R. A.; Williams, R. J. J. *Polym. Int.* **1994**, *33*, 253-261.

56) Hsich, H. S. Y. *J. Mater. Sci.* **1991**, *25*, 1568-1584.

57) Chen, D.; Pascault, J. P.; Sautereau, H. *Polym. Int.* **1994**, *33*, 236-271.

58) Kim, S. C.; Ko, M. B.; Jo, W. H. *Polymer* **1995**, *36*, 2189-2195.

59) Griffth, A. A. *Phil. Trans. Roy. Soc.* **1921**, *A221*, 163-198.

60) Bucknell, C. B. *Toughened Plastics*; Applied Science: London, 1977.

61) Wu, S. *Polym. Int.* **192**, *29*, 229.

62) Dompas, D.; Groeninckx, G. *Polymer* **1994**, *35*, 4743-4759.

63) Nigam, V.; Setua, D. K.; Mathur, G. N. *J. Appl. Polym. Sci.* **1998**, *70*, 537-543.

64) Romano, A. M.; Garbassi, F.; Braglia, R. *J. Appl. Polym. Sci.* **1994**, *52*, 1775-1783.

65) Klug, J. H.; Seferis, J. C. *J. Appl. Polym. Sci.* **1997**, *66*, 1953-1963.

CHAPTER 3

IN SITU ULTRASONIC SPECTROSCOPY OF TRANSFORMING SYSTEMS

3.1 Introduction

As described in section 2.1 sound waves are mechanical vibrations that travel through materials by successive displacements. The efficiency of displacement transmission is a function of the material properties. Thus, ultrasonic waves are sensitive to variations in the density or modulus. This makes them ideal for probing material transformations. Also, the length scales of domains or heterogeneities can be monitored as the transformation takes place via scattering at their interfaces. Consequently, ultrasound has been used by many researchers as a non-invasive method to monitor transformations in real time. Recent contributions to the ultrasonic analysis of transforming systems has resulted from the examination of the effects due to the presence of a second phase and monitoring chemical reactions as they occur.

3.1.1 Transformation via a Second Phase

Maffezzoli *et al.* used changes in ultrasonic attenuation and velocity to monitor the water absorption kinetics of hydrogels.[1] A pulse echo technique was utilized to monitor the position of the swollen and unswollen fronts during water absorption by poly(2-hydroxyethyl methacrylate). Mikkonen and Savolainen made blends of low density polyethylene and plasticized poly(vinyl chloride) and monitored the ultrasonic velocity during extrusion via a two MHz transducer.[2] They found that ultrasonic velocity changes correlated with die swell and viscosity changes upon variation of the blend composition. Gendron *et al.* determined the residence time distribution for an extruder

using 4.75 MHz transducers in the through transmission mode operating inside an extruder.[3] Ultrasonic attenuation and velocity measurements were used to detect the passage of calcium carbonate filler used as a tracer. Shekarriz and Brenden developed a real-time ultrasonic imaging system as a method to detect heterogeneities flowing in a fluid.[4] This was accomplished using a 5 MHz transducer to measure the planar velocity of a longitudinal wave that is scattered by particles flowing in a fluid. D'Aprano *et al.* monitored the poly(vinyl pyrrolidone) – surfactant interactions via attenuation measurements as a function of frequency.[5,6] They were able to monitor micelle formation as a function of concentration.

3.1.2 Reacting Systems

Sladky *et al.* used 1 MHz longitudinal waves to monitor the suspension polymerization of poly(vinyl chloride).[7] Attenuation coefficients were recorded during set up of the suspension and during the course of polymerization. These measurements allowed them to monitor phase changes as the suspension stabilized and polymerization as it proceeded. Canegallo *et al.* used ultrasonic velocity changes to monitor the emulsion polymerization of methyl methacrylate and vinyl acetate.[8] A pair of 2 MHz transducers in the through transmission mode were used to determine the degree of conversion. The values obtained correlated well with off-line gravimetric measurements. Horvar *et al.* used a photoacoustic technique, ultrasonic pulses with optical detection, to monitor the curing reaction of polyester and epoxy resins.[9] The velocity of the ultrasonic pulse was used to track the kinetics of the curing reaction. The kinetic profiles thus obtained correlated with accepted models for the curing reaction. Matsukawa *et al.* used

ultrasonic velocity changes to monitor the sol-gel reaction of TEOS.[10] These measurements were used to accurately determine the gel point of the reaction.

The preceding discussion illustrates that ultrasound is a valuable method for analyzing systems as they transform. The majority of the research conducted to date has utilized the change in sound velocity to characterize transformation. However, as discussed in Chapter 2, a wealth of information is accessed by examining a broad band of ultrasonic frequencies and hence wavelengths. Specifically, the length scale over which transformation is occurring may be obtained by monitoring the wavelengths dependence of attenuation. The research presented in this chapter is conducted with a broad band transducer used to examine the length scale of transformation.

3.2 Experimental

3.2.1 Gelatin

Unflavored gelatin with a bloom count of 200 g (weight required to depress a 1.25 cm diameter plunger 4 mm into the gelled gelatin) was obtained from Hormel Foods Corporation. Gels were produced by dissolving 0.4 g of gelatin in 100 mL of 90 °C water. This was cooled to 50 °C and poured into an empty reaction chamber, Figure 3.1, prechilled to 5 °C. The reaction chamber is constructed entirely out of glass and is jacketed for cooling or heating with a circulating fluid. A Panametrics, Inc. model V390 50 MHz transducer with an element diameter of 0.635 cm and a focal point 1.3 cm from its face is sealed into the bottom of the chamber with a nylon bushing and rubber o-ring. The apparatus is conical in shape due to initial concerns of reflections from the chamber walls interfering with received waveforms. The same computer and digitizer board used

in Chapter 2 section 2.2.5 is employed here. However, the data was digitized at a rate of 500 MHz. The pulser/receiver used to drive the transducer and condition the signals returning from it is a Panametrics model 5601 TT. A pulse echo method was used to monitor the change in sound velocity and attenuation during gelation and melting. The pulse echo target was a steel cylinder. A macro was written by Martin Arnold of Panametrics within the Panametrics Multiscan software such that after collecting a waveform it caused the program to shell out to DOS and append the current computer time to a text file bearing the same name as the Panametrics scan file. Thus, waveforms were saved as a function of elapsed experimental time.

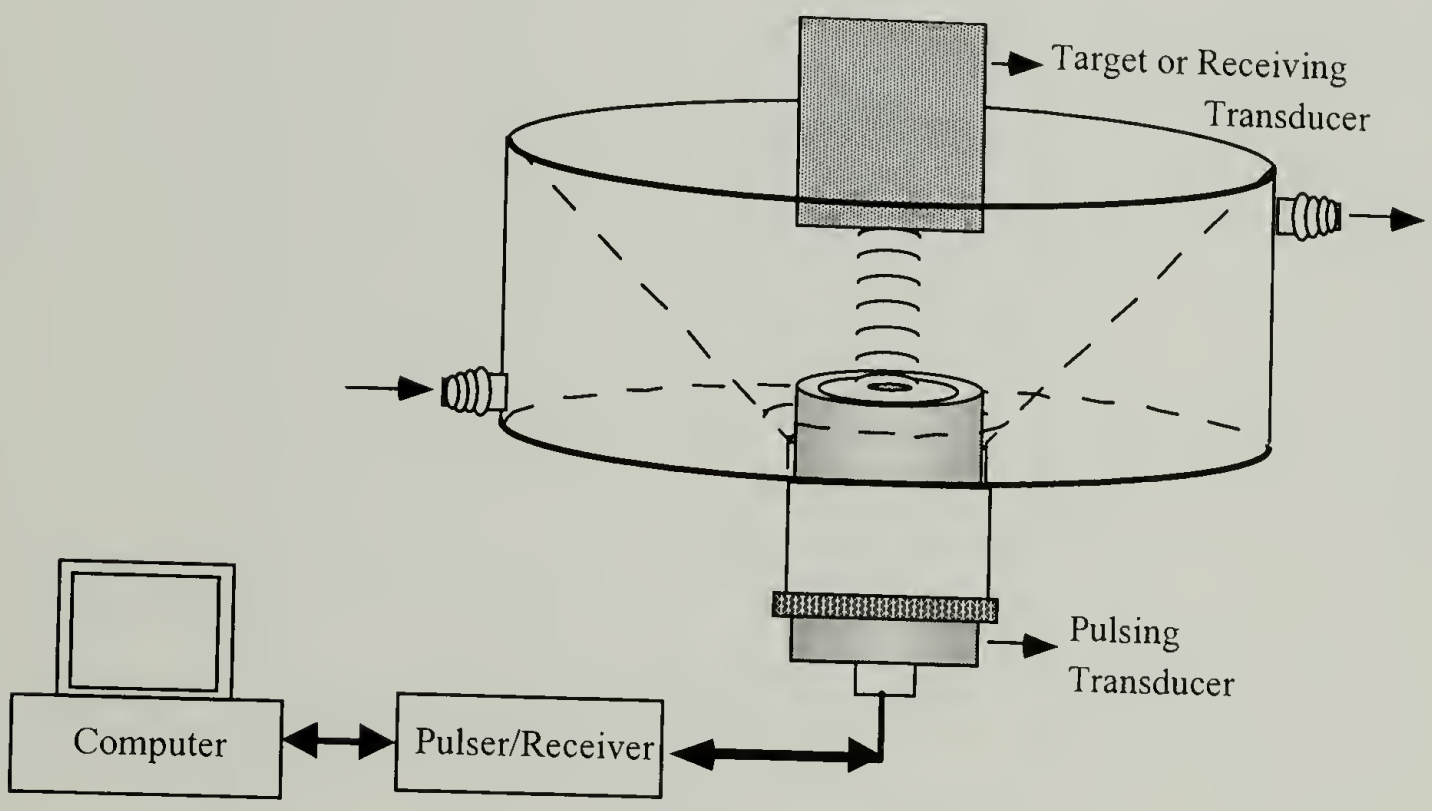

Figure 3.1: Instrument setup and apparatus for ultrasonic analysis of the gelation of gelatin.

3.2.2 Epoxy and rubber modified epoxy

3.2.2.1 Materials

Epon 828 (Shell Chemical Co.), a diglycidyl ether of bisphenol A, was stored under vacuum at 80 °C for 24 hr before being mixed with a stochiometric quantity of

Jeffamine D230 (Huntsman Chemical Co.), an aliphatic tertiary amine curing agent and a desired weight percent, of carboxyl terminated butadiene-co- acrylonitrile (CTBN) rubber modifier (BFGoodrich Performance Materials, Inc.). Five weight percent of the CTBN was added for rubber modification. The CTBN utilized here was the 1300x31 grade with 10% AN. It is important to note that this CTBN is less compatible with epoxy and produces rubber domains that are an order of magnitude larger than those of the CTBN studied in Chapter 2 section 3.3.4.

3.2.2.2 Reaction chamber

A new chamber for through transmission measurements was designed and again constructed entirely out of glass with a jacket for heating and cooling, Figure 3.2a. Nylon bushings and rubber o-rings are used to seal two transducer into the chamber such that they are squarely facing each other. The opening on the chamber top allows the insertion of a small cell containing the desired reactant. The use of a separate reaction cell eliminates possible damage to the transducer faces by chemical agents and greatly expands the possible reactants that can be studied. The reaction cell, shown in Figure 3.2b, is constructed of five layers of Mylar glued together to form the desired U – shaped thickness (~0.5 mm). The front and back faces of the cell were covered with thin layers (0.035 mm) of polyimide This cell effectively contained the reactants while allowing efficient sound transmission. The epoxy/curing agent and epoxy/curing agent/CTBN mixtures were allowed to degas at 50 °C for 25 minutes before being pipetted into the reaction cell. The cell inserted into the reaction chamber which was filled with 50 °C water, and then monitored ultrasonically as described below.

Two Panametries. 50 MHz transdueers were used for through transmission measurements of the reaetion eell. The pulsing transdueer was a Panametries model V390 with an element diameter of 0.635 em and a foeal point 1.3 em from its faee and the reeeiving transdueer was a Panametries model 3409 with a 0.635 cm element diameter and foeal point 4.45 em from its face. The eomputer, digitizer board, and pulser/reeeiver were identieal to those used in seetion 2.2.5 in Chapter 2.

The temperature was eontrolled by a VWR Seientifie model 1157 programmable eireulating bath set to hold a eonstant temperature of 54 °C. Setting the bath at this temperature produeed a stable temperature of 50 °C in the reaetion ehamber. The programmable bath has an external temperature probe that was not used due to the bulkiness of the fixture holding the reaetion eell in plaee. The maero used in the gelatin experiments deseribed above was modified sueh that upon shelling out to DOS it exeeuted a eompiled program written in BASIC that interfaeed with the eireulating bath via an RS232 port and retrieved the eurrent temperature. The temperature was stored along with the eurrent eomputer time in a text file bearing the same name as the Panametries sean file. The eompiled BASIC program used portions of uneompiled eode provided along with the eireulating bath from Polyseienees, the original manufaeturer of the bath. The instrument eonfigured in this way is able to eolleet data over periods of days or perhaps longer. Also, a second BASIC program was written sueh that it eaused the bath to eycle between predetermined set points until the sean is eomplete. One of the most diffieult hurdles that was overeome during the development of this apparatus and interfaee was the unexplained halting of the ultrasonie sean at random times during the experiment. It was determined that the stepper motors used to control the XY position of

the transducer were over heating during the scan. The transducers used in the experiments were not moving but the Multiscan software is configured such that the motors must move in order for data to be recorded. Once this problem was diagnosed it was easily solved by inserting a "motion stop" statement into the macro.

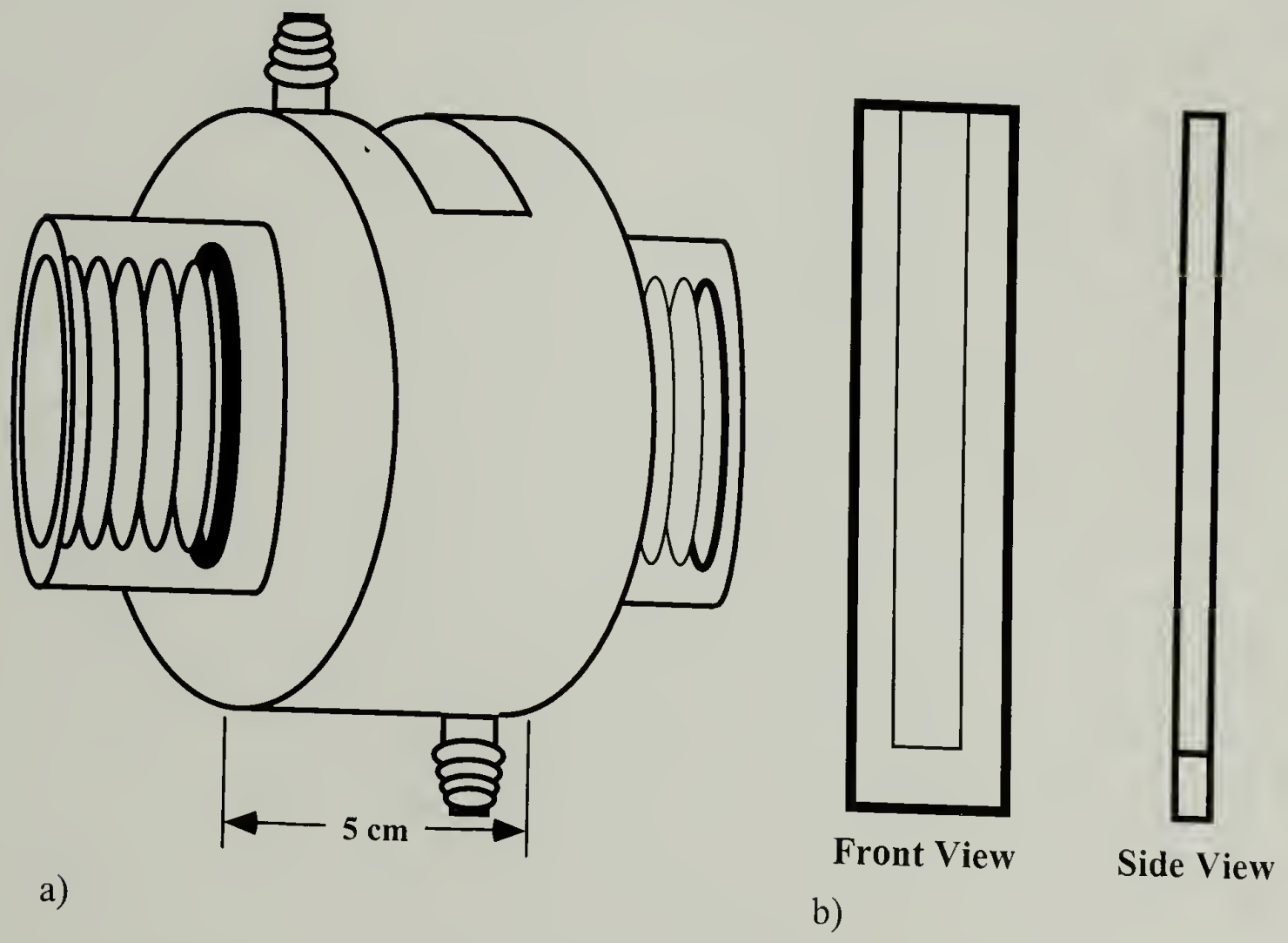

a) b)

Figure 3.2: Reaction chamber (a) and cell (b) used for ultrasonic analysis of curing epoxy and rubber modified epoxy.

3.3 Results and Discussion

3.3.1 Gelatin

Gelatin is utilized as a nonhazardous model system that reversibly gels over a moderate temperature range. Elevated temperature is a major concern because the poled ceramic piezoelectric elements used in the transducers revert to a nonpiezoelectric state once heated above a critical temperature, 110 °C for a common barium titanate

composition.[11] However, this critical temperature varies greatly with composition. This limits the experimental range of the technique. The time for the ultrasonic signal to travel through the gelatin, reflect off the steel target, back through the gelatin, and into the transducer, transit time, is plotted for gelatin during gelation at 5 °C in Figure 3.3. Typical gelation times are about 30 minutes in this apparatus as detected by the gel becoming resistant to penetration. Figure 3.3 indicates that $\mathbf{c}_L$ decreases as the gelatin gels. Velocities are greater generally in solids than liquids, however for gelatin the increase in modulus is not sufficient to overcome the increase in density upon gelation. However, the shift in $\mathbf{c}_L$ may be the result of the overall decrease in temperature of the gelatin instead of the gelation process.

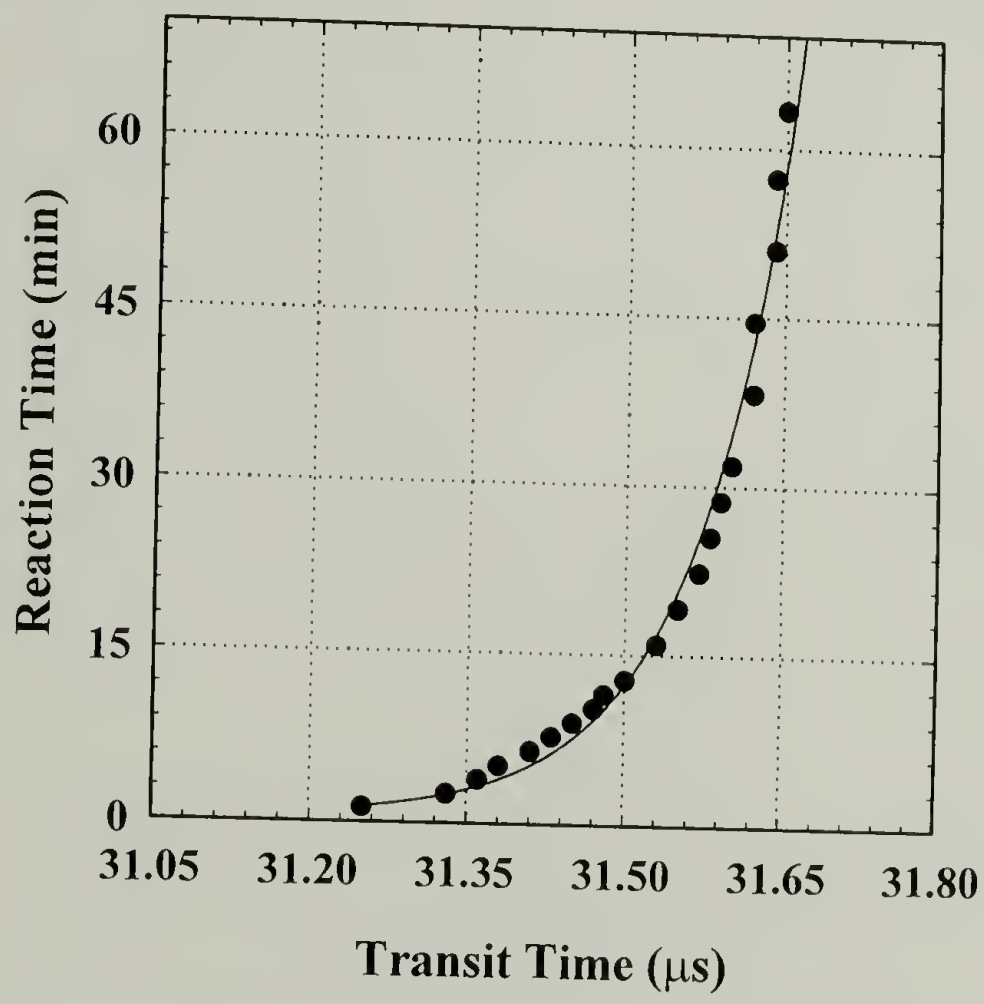

Figure 3.3: Transit time of ultrasonic waveforms collected during gelation of gelatin at 5 °C.

The frequency spectra obtained via fast Fourier transformation of the received waveforms are shown in Figure 3.4. There is an initial sharp drop in amplitude followed by a gradual decrease during gelation. The scatter in Figure 3.4 is most likely the result of the original ultrasonic signals being digitized at 500 MHz resulting in waveforms with fewer data points and hence more scatter. This does not significantly effect the overall waveform shape but does change the peak values. The low data resolution did not effect the transit time measurements because the first peak in the wave form was taken as the transit time regardless of its intensity. In Figure 3.4 the shape of the spectra does not change, but are incrementally depressed during gelation. These observation are more clearly displayed in Figure 3.5, where the peak amplitude and frequency are plotted versus reaction time.

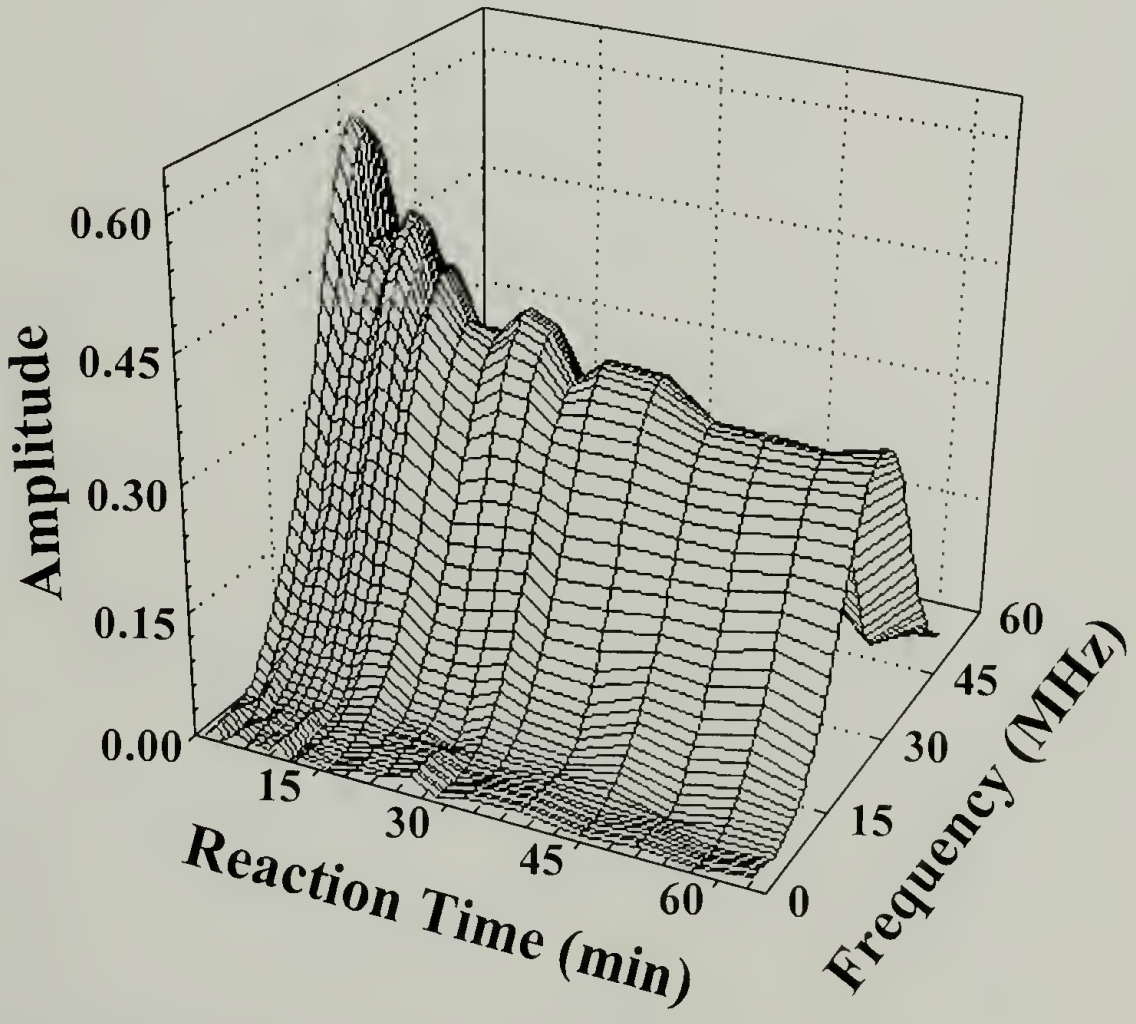

Figure 3.4: Frequency spectra during gelation of gelatin.

Figure 3.5 indicates that a linear drop in peak frequency occurs during gelation which is relatively minor in nature (~ 1 MHz). The amplitude decreases in a similar manner as the velocity. This is observed as an exponential decay of the amplitude and growth of the transit time (hence decay of velocity) during gelation. These results show that both the spectrum amplitude and ultrasonic velocity undergo similar transitions during gelation. Similarity between observed attenuation and velocity changes is expected since it has been shown by several researchers that Kramers – Kronig relations[12,13] exist for sound waves as they do for electromagnetic radiation.[14-18]

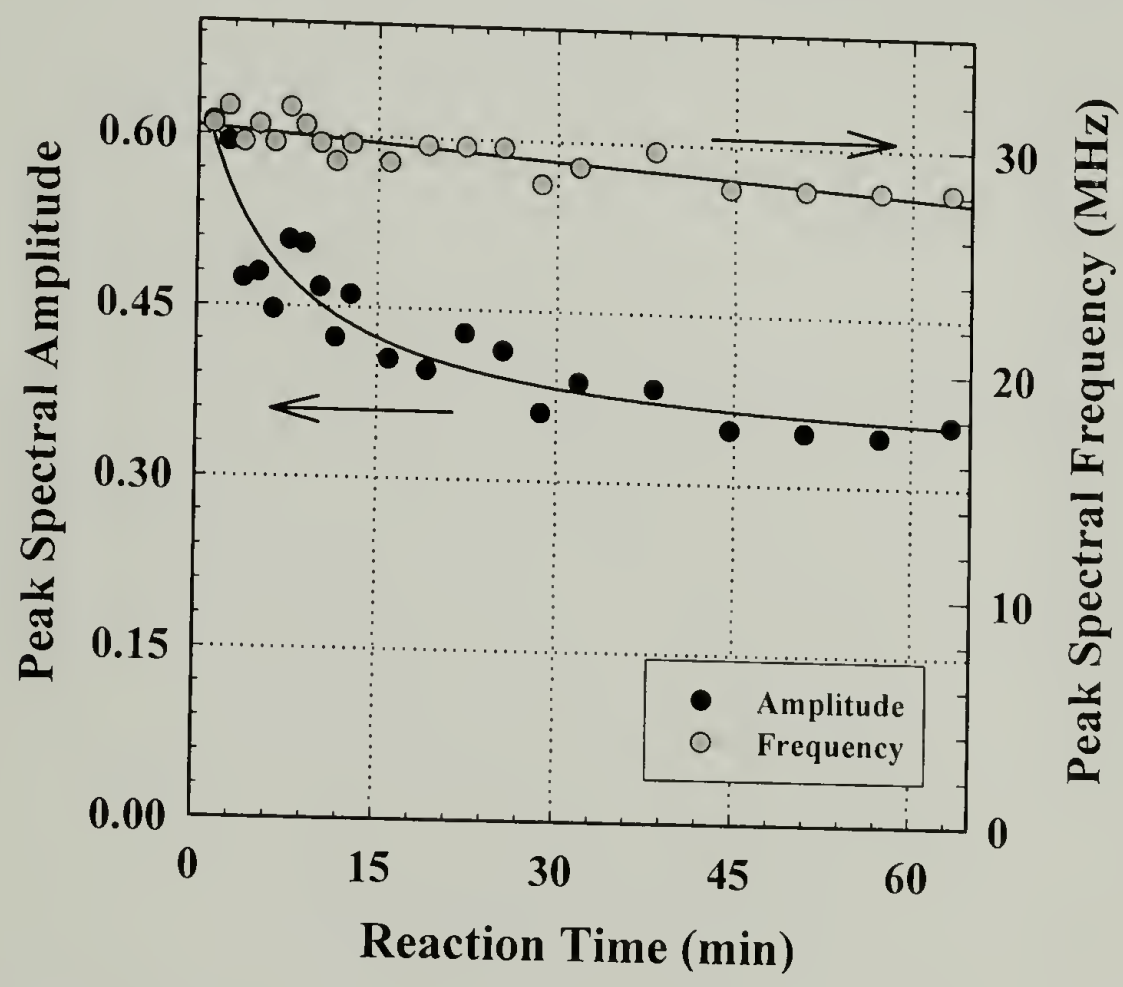

Figure 3.5: Peak amplitude and frequency during gelation of gelatin.

3.3.2 Epoxy and rubber modified epoxy

Epoxy and rubber modified epoxy were studied as model reacting systems to develop the apparatus and techniques for ultrasonic analysis of hazardous and more complex reacting systems. Thus, an epoxy and rubber modified epoxy of formulations

described in section 3.2.2 are placed in cells (Figure 3.1b) and cured in the chamber shown in Figure 3.1a at 50 °C. The transit time is plotted for epoxy and rubber modified epoxy in Figure 3.6. This figure indicates that during cure there is a sharp increase in ultrasonic velocity and hence a sharp increase in the modulus relative to the change in density of the curing epoxies. Both specimens begin with similar transit times then increase rapidly after two hours. The shift to lower transit times, higher velocities, plateaus at 39.78 μs and 38.72 μs for the rubber modified epoxy and the epoxy specimens respectively. The reaction cell thickness is 0.66 mm and 0.85 mm for the rubber modified epoxy and the epoxy specimens respectively. Since the overall transit time is a linear combination of the time spent (thickness) of each component traversed (i.e. water ⇒ polyimide ⇒ specimen ⇒ polyimide ⇒ water for this case) the transit time decreases as the thickness of components with a higher $\mathbf{c_L}$ increases. This partially explains the discrepancy in the transit time plateau values for the rubber modified epoxy and epoxy specimens. Also, the $\mathbf{c_L}$ of fully cured epoxy (2707.5 m/s) is greater than that of the specimen with 5 wt.% CTBNx31 (2607.2 m/s) at 50 °C.

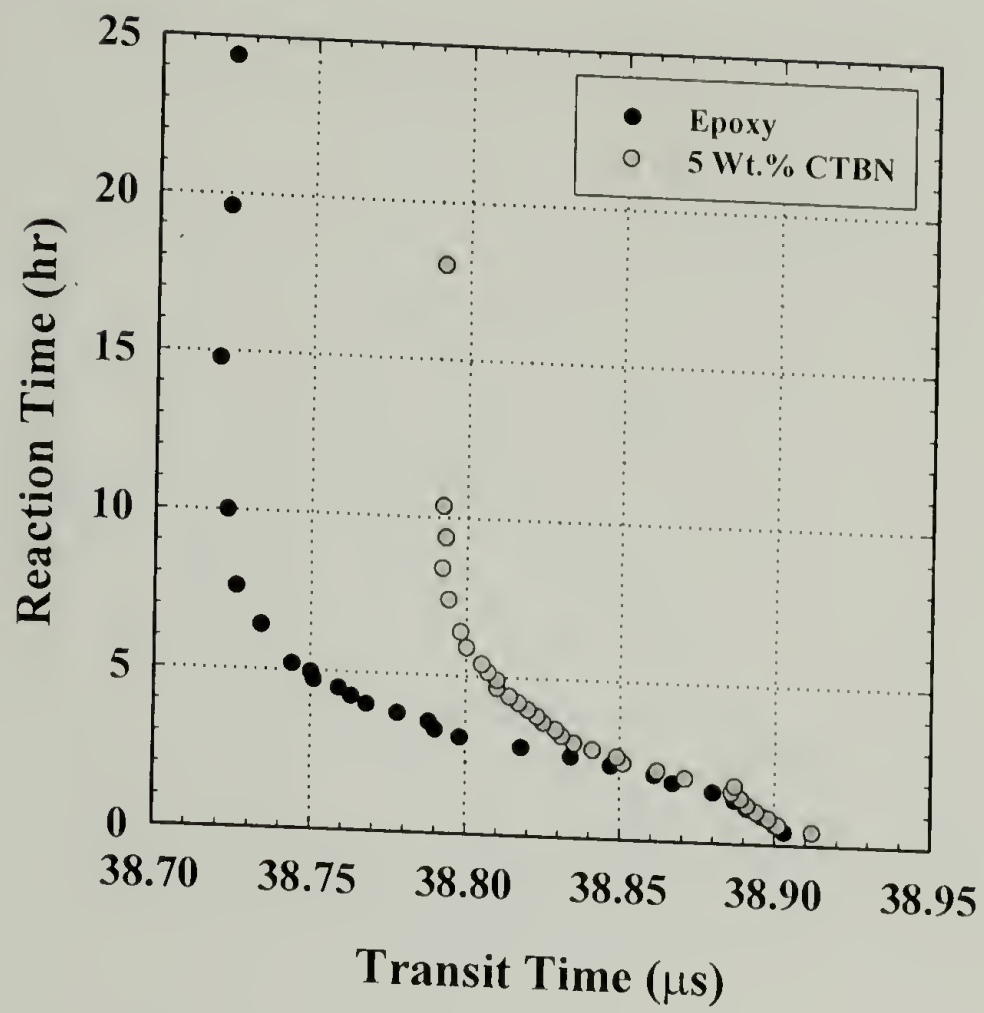

Figure 3.6: Transit time of ultrasonic waveforms collected during cure of epoxy and rubber modified epoxy.

Frequency spectra were obtained via fast Fourier transformation of the receivcd time domain waveforms. These are shown in Figures 3.7 for epoxy and 3.8 for rubber modified epoxy versus the reaction time. It is apparent how much more uniform the plots are than those from gelatin. This results from the higher digitization rate (1 GHz) and the resulting uniform waveforms. Both Figures show that in the beginning when unreacted epoxy and curing agent are the primarily components the amplitude is high and the entire frequency band is efficiently transmitting through the reaction cell. As the reaction progresses the amplitude decreases and the peak frequency shifts to lower and lower frequencies until a minimum is reached, after which the amplitude begins to regrow and shift to higher frequencies.

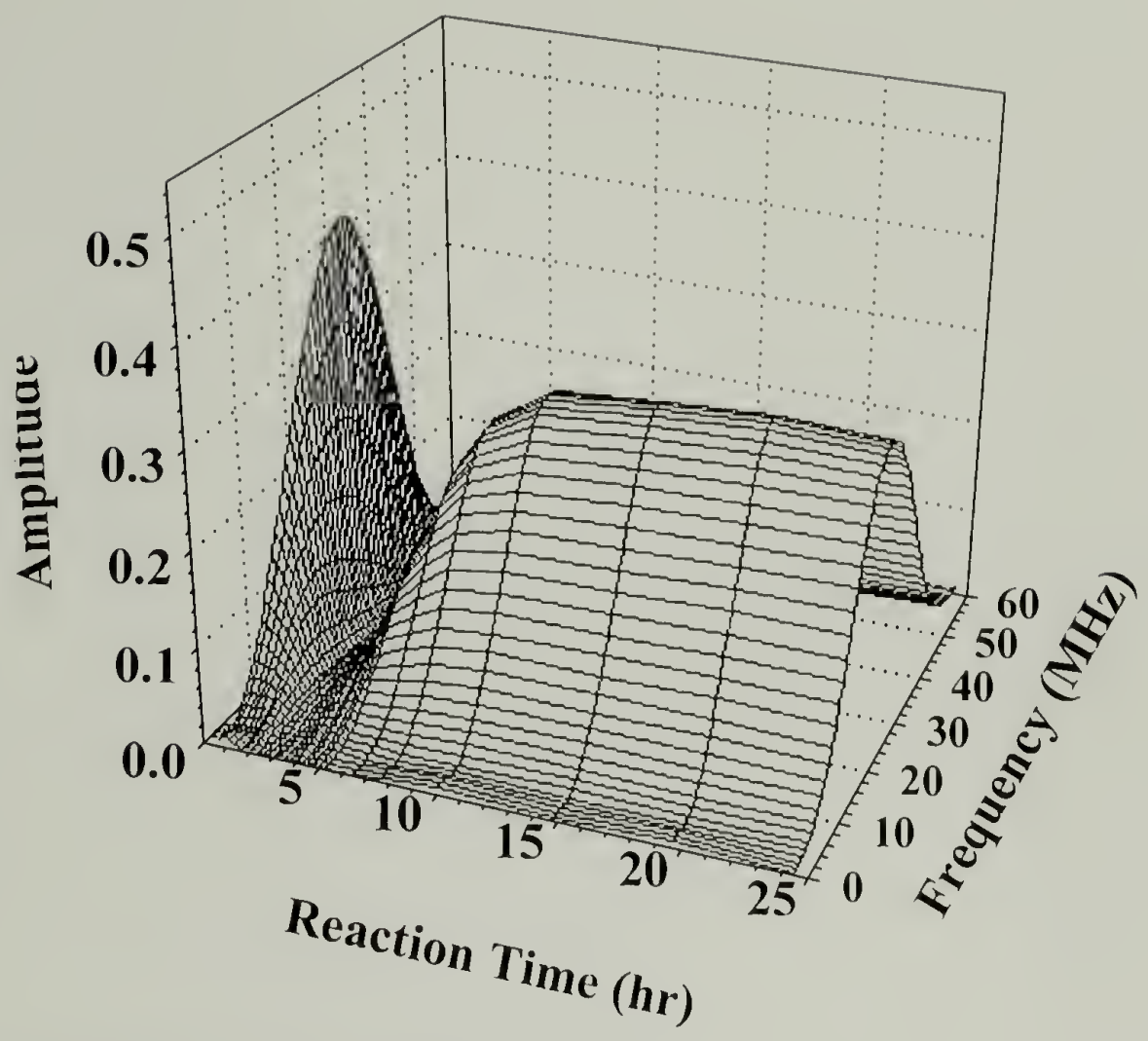

Figure 3.7: Frequency spectra of curing epoxy.

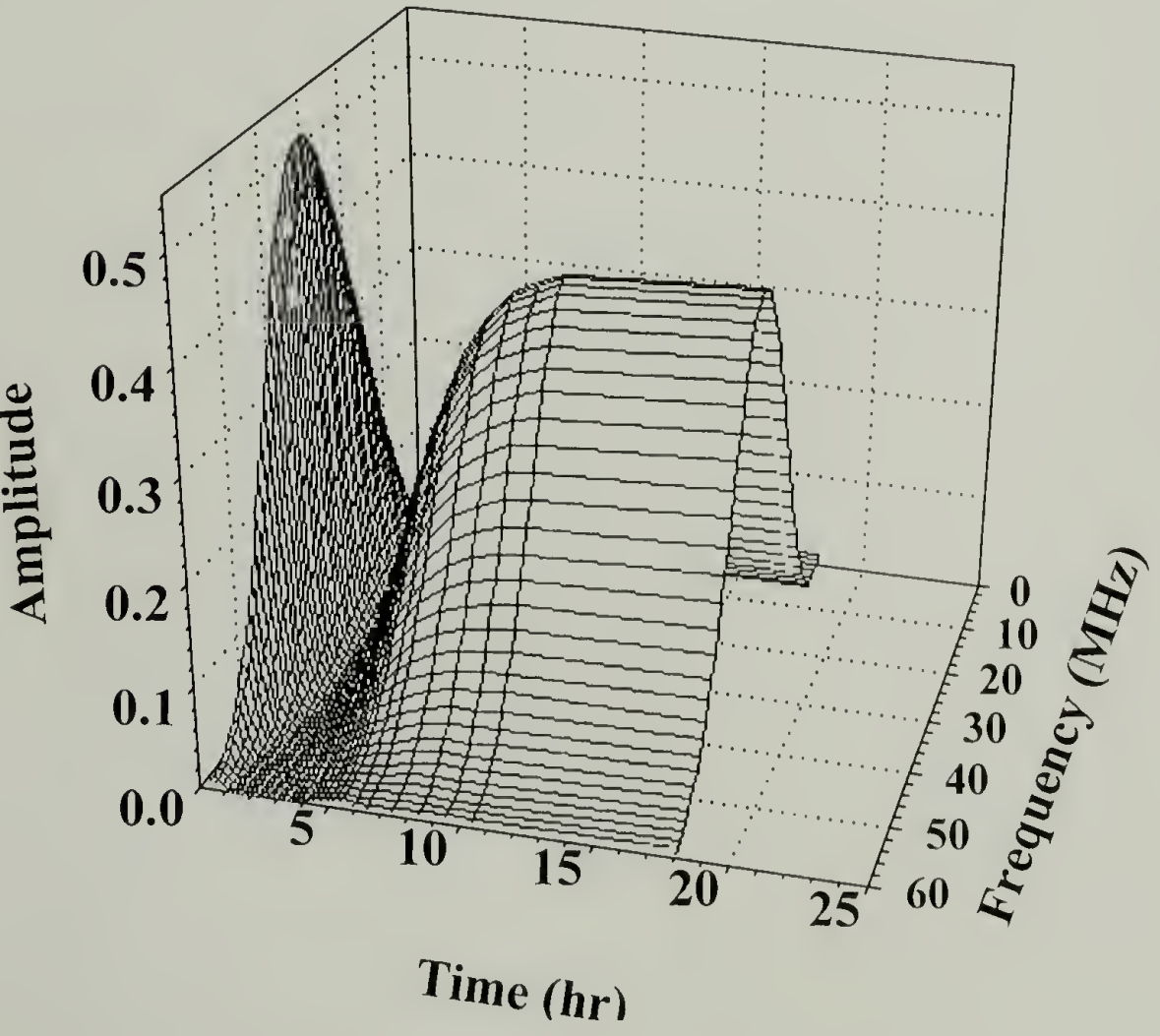

Figure 3.8: Frequency spectra of curing rubber modified epoxy.

Figures 3.7 and 3.8 are summarized by plotting the peak amplitude and frequency as a function of reaction time in Figures 3.9 and 3.10 for epoxy and rubber modified epoxy respectively. The peak amplitude reaches a minimum at 2.8 hr and 2.4 hr for epoxy and rubber modified epoxy respectively. The frequency at peak amplitude obtains a minimum value (20.5 MHz) at the same time at the peak amplitude for rubber modified epoxy (2.4 hr), but for epoxy the frequency minimum (11.7 MHz) is reached at 2.3 hrs which is about half an hour earlier than its amplitude minimum. This is intriguing because the amplitude is related to the specimens overall efficiency of sound transmission while the frequency of transmitted sound is indicative of a length scale within the material that transmits sound.

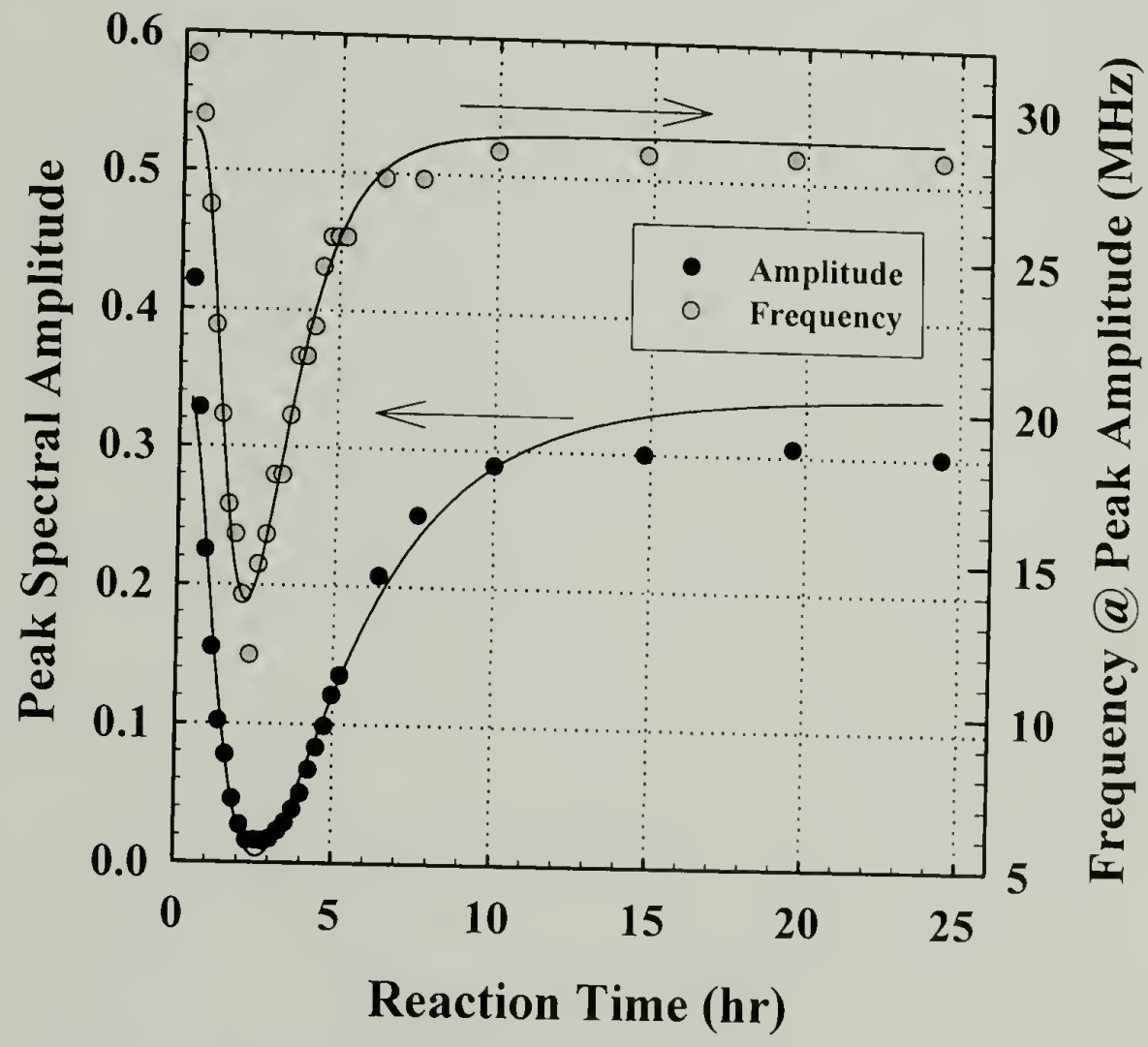

Figure 3.9: Peak amplitude and frequency during cure of epoxy.

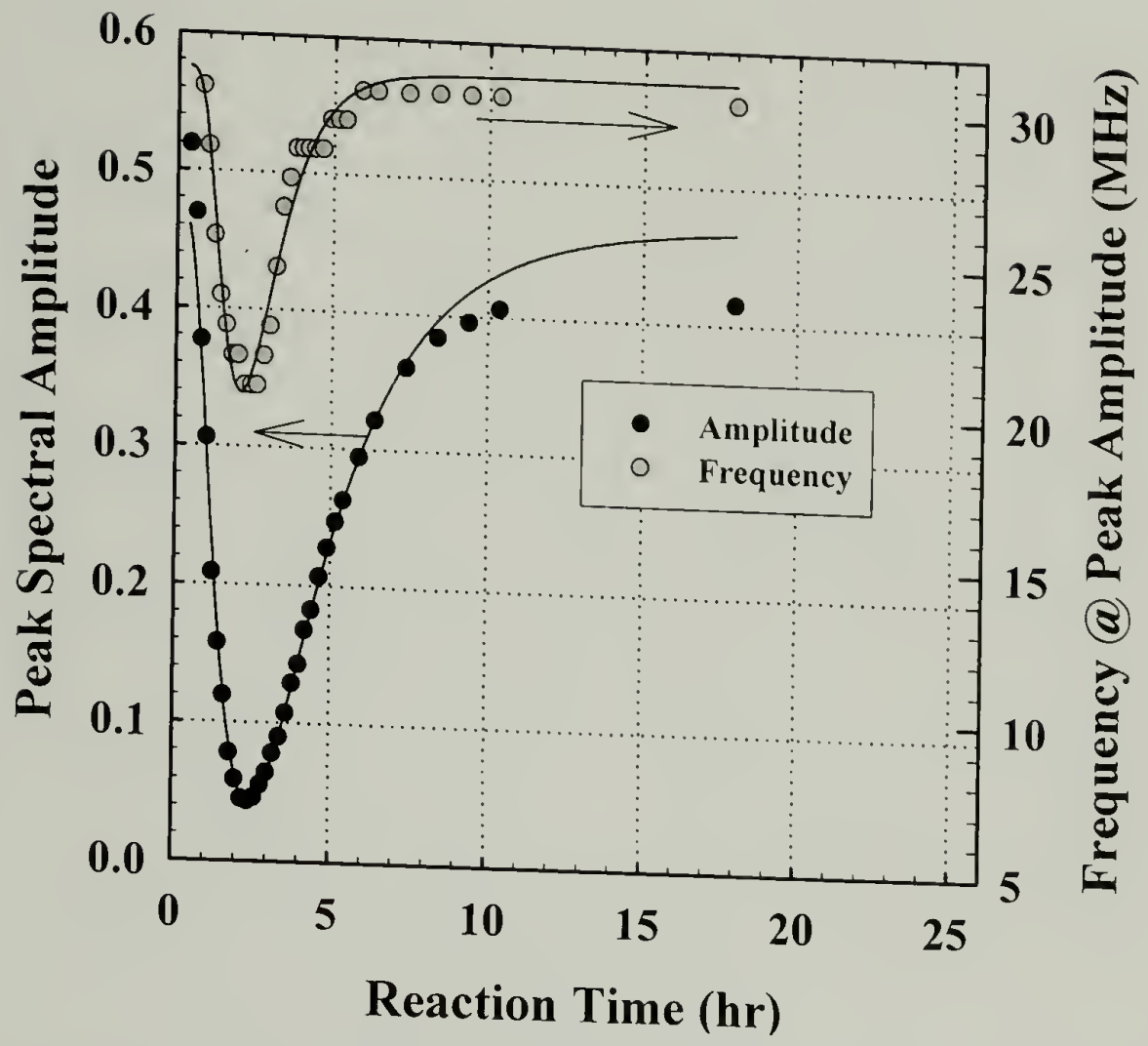

Figure 3.10: Peak amplitude and frequency during cure of rubber modified epoxy.

The rubber modified epoxy does not undergo the large frequency shift (22 MHz) that epoxy exhibits, but shift only about 10 MHz at its minimum peak frequency. After reaching a minimum, the peak frequency rapidly shift back to higher frequencies and the amplitude gradually increases. These observation will be examined in detail after calculation of the attenuation coefficients and the wavelengths as a function of reaction time.

Attenuation coefficients were calculated using a modified version of equation 2.31, equation 3.1.

$$\alpha = -\frac{1}{x}\mathrm{Ln}\left(\frac{Y(\omega)}{Y_W(\omega)}\right) \qquad (3.1)$$

This is used because the density is known as a function of reaction time and hence the reflection coefficients could not be determined. Thus, the attenuation coefficient values

calculated are relative in nature (α). $\mathbf{Y_W(\omega)}$ was taken as the frequency spectrum obtained via trough transmission of the respective reaction cells filled with water and inserted into the reaction chamber at 50 °C. The attenuation coefficients at the peak amplitude are plotted in Figure 3.11 for epoxy and rubber modified epoxy. The attenuation coefficient a peak amplitude is plotted because the spectra are symmetric in shape and thus Figure 3.11 is indicative of the depression of each entire spectrum. Equation 3.1 corrects the observed change in amplitude for cell thickness and the resulting values are very similar to each with only a slight shift in α values for the rubber modified epoxy specimen. α values start relatively low (8 Np/cm) and then jump to a maximum of 34 Np/cm after 2.4 hr and 33 Np/cm after 3.0 hr for the rubber modified epoxy and epoxy specimens respectively. After reaching these peak values, α decreases rapidly and obtains a constant value of approximately 11 Np/cm for both specimens. The shift, although slight, may indicate the beginning of rubber phase separation. Incorporation of the reflection coefficient into equation 3.1 would increase the α values for rubber modified epoxy relative to that of pure epoxy.

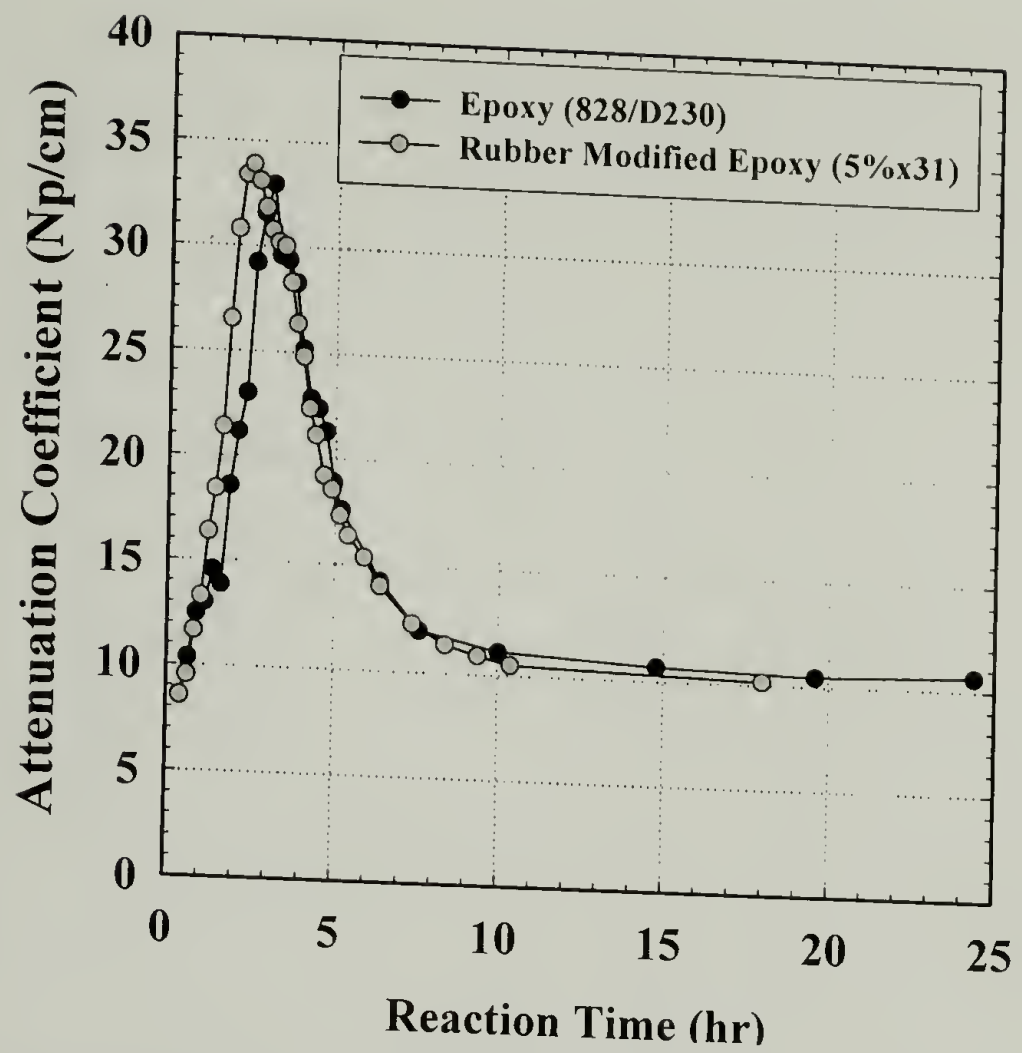

Figure 3.11: Attenuation coefficient at peak amplitude versus reaction time for epoxy and rubber modified epoxy.

Direct observation of an epoxy of identical formulation curing at 50 °C indicates that it is still fluid at 2 hr, non-flowing yet drawable at 3 hr, soft and easily deformable at 4 hr, hard yet sticky at 5 hr, and hard and non sticky at 6 hr. Thus, direct observations indicate that gelation does begin in the 2- to 3 hr time frame. Then why does the gelation process cause such a strong attenuation of sound waves? Similar attenuation and velocity phenomena were observed by McClements and coworkers while studying the melting and crystallization of a 3 wt.% n-hexadecane – water emulsion.[19] They found that the velocity rapidly shifted to a lower value and the attenuation suddenly rose to a peak value during melting. The phenomena was attributed to the temperature and pressure fluctuations associated with the transmission of ultrasonic waves disturbed the solid ⇔ liquid equilibrium present during melting. This caused the relative fractions of solid and

liquid to oscillate around the equilibrium value. Thus, absorbing ultrasonic energy and producing the sharp rise in attenuation coefficient. This effect increased as the ultrasonic frequency increased. Also, the shape of the attenuation peak was found to be dependent upon size of the emulsion droplets.

As discussed in the introduction Hovart and coworkers monitored the curing of polyester and epoxy resins via a photoacoustic technique.[9] They found that ultrasonic velocity underwent a step increase similar to that shown for these studies in Figure 3.6. They did not calculate attenuation coefficients, but from the waveforms shown in their paper as a function of time it is clear that strong attenuation did occur during the sharp increase in velocity. Ultrasonic peaks in attenuation and shifts in velocity during the cure of epoxies have recently been observed by several authors.[20-22] Alig *et al.* used ultrasonic longitudinal waves and dynamic light scattering to show that the reaction time at which the attenuation peak and velocity shift occurred is frequency dependent.[21] They state that the attenuation peak is associated with the primary glass transition of the epoxy and that is correlates with gelation of the epoxy net work as measure by viscosity. The peak and shift were shown to occur sooner during the reaction as the frequency was increased. Figures 3.12 and 3.13 plot the attenuation coefficient at various frequencies for epoxy and rubber modified epoxy during cure. These figures indicate that the peak in attenuation increases in intensity as the frequency increases, but do not show a distinct shift in peak position with frequency. However, the peaks do begin to rise at shorter times as the frequency is increased.

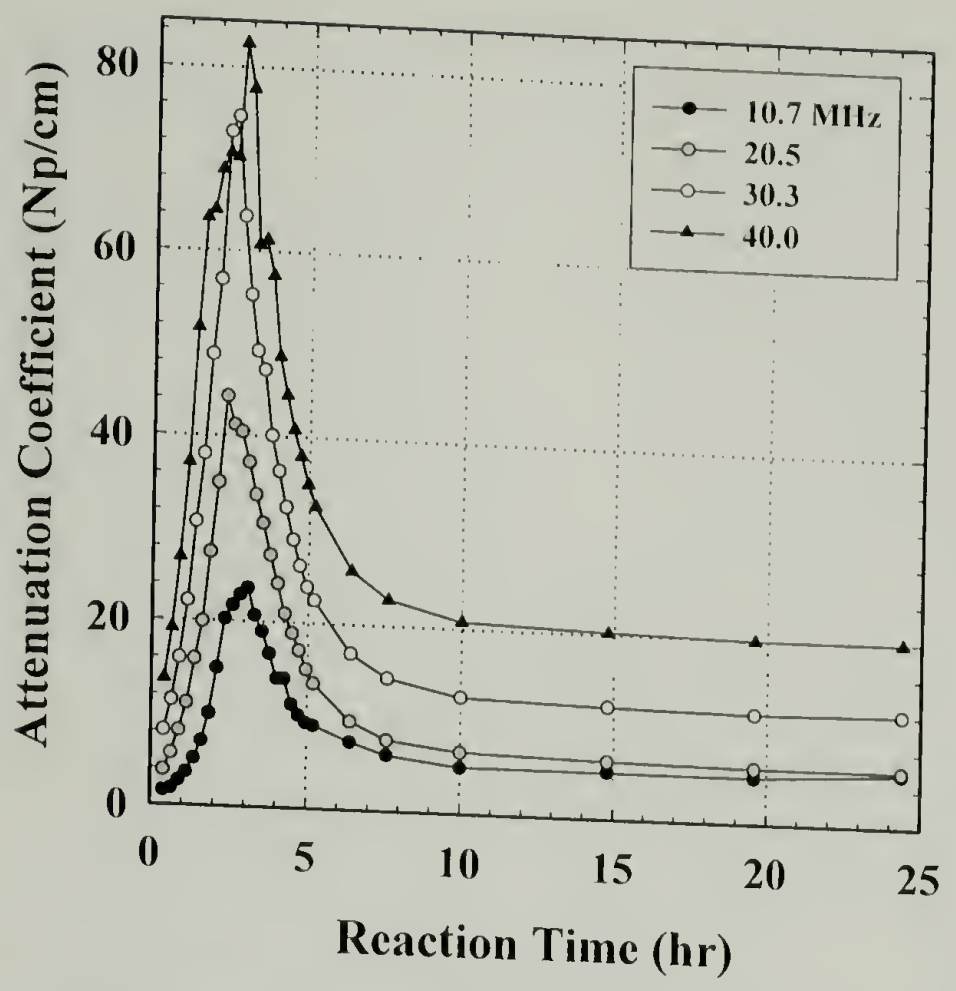

Figure 3.12: Attenuation coefficient at various frequencies versus reaction time during the cure of epoxy.

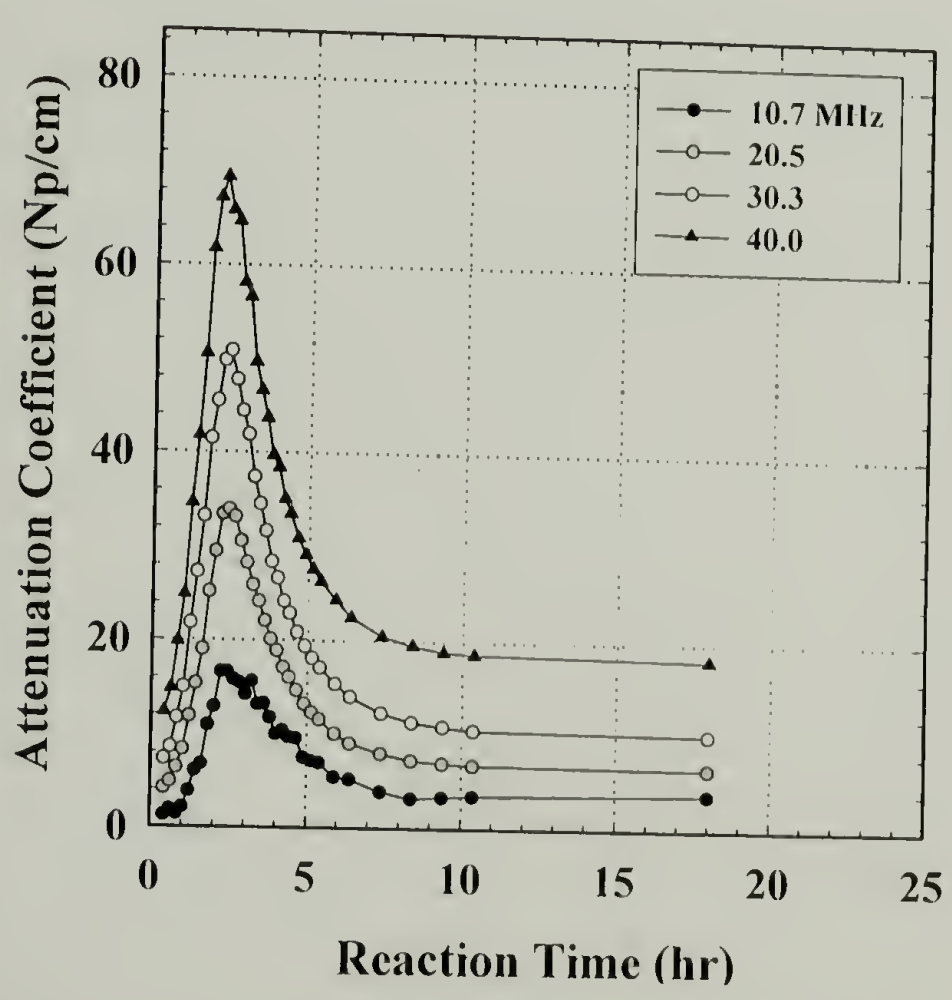

Figure 3.13: Attenuation coefficient at various frequencies versus reaction time during the cure of rubber modified epoxy.

Freemantle and Challis studied the curing of several commercial epoxy adhesive via ultrasonic longitudinal and shear waves.[20] They found that the position (with respect to reaction time) and width of the peak are related to the rate of polymerization and cross-linking reactions of the adhesive. Generally, the peak occurred at shorter reaction times and was narrower as the rate increased. Also, shear waves began to transmit through the reacting epoxy on the down slope of the attenuation peak. Although, not stated in their paper this result indicates that the peak is associated with the formation of a critical amount of solid material as liquids do not transmit shear waves. This result is confirmed by the work of Younes *et al.* who monitored the epoxy curing reaction via FT-Raman spectroscopy, torque measurements, and ultrasonic longitudinal waves. They found via torque and FT Raman measurements that the shift in velocity and the peak in attenuation directly correlated with the vitrification of the epoxy network and not the gel point. This distinction can be better understood base upon the definitions of the vitrification and gelation points. Vitrification is solidification of the reactants causing further chemical reactions to be diffusion controlled. Thus, the reactants undergo a glass transition at vitrification. If the polymer is not heated further after vitrification then the T_g will equal the cure temperature.[23] Gelation is generally defined as the point at which a three dimensional network is formed and when the cross links are covalent bonds the material is insoluble.[24]

The above discussion illustrates that ultrasound can become coupled with transformations occurring within the medium it travels in. In epoxy curing reactions the peak in attenuation is related to percent conversion necessary for the T_g to equal the reaction temperature. Ultrasonic energy is most likely absorbed by the molecular

motions associated with the transition from a viscous liquid to a rubbery solid. Further studies are warranted to see if the frequency dependence follows a William - Landel - Ferry[25] type of relationship where the T_g is shown to increase with increasing frequency (i.e. rate of probing).

Knowledge of the velocity as a function of reaction time allows the wavelength of the transmitted frequencies to be calculated assuming that the thickness of the reaction cell does not significantly change during cure. The velocity of sound within the reactants is determined using this time shift assuming that the velocity of the epoxy and rubber modified epoxy at long reaction times is identical with that measured at 50 °C in specimens confirmed to be fully cured by DSC measurements. Thus, the wavelength of the frequency at peak amplitude is plotted in Figure 3.14.

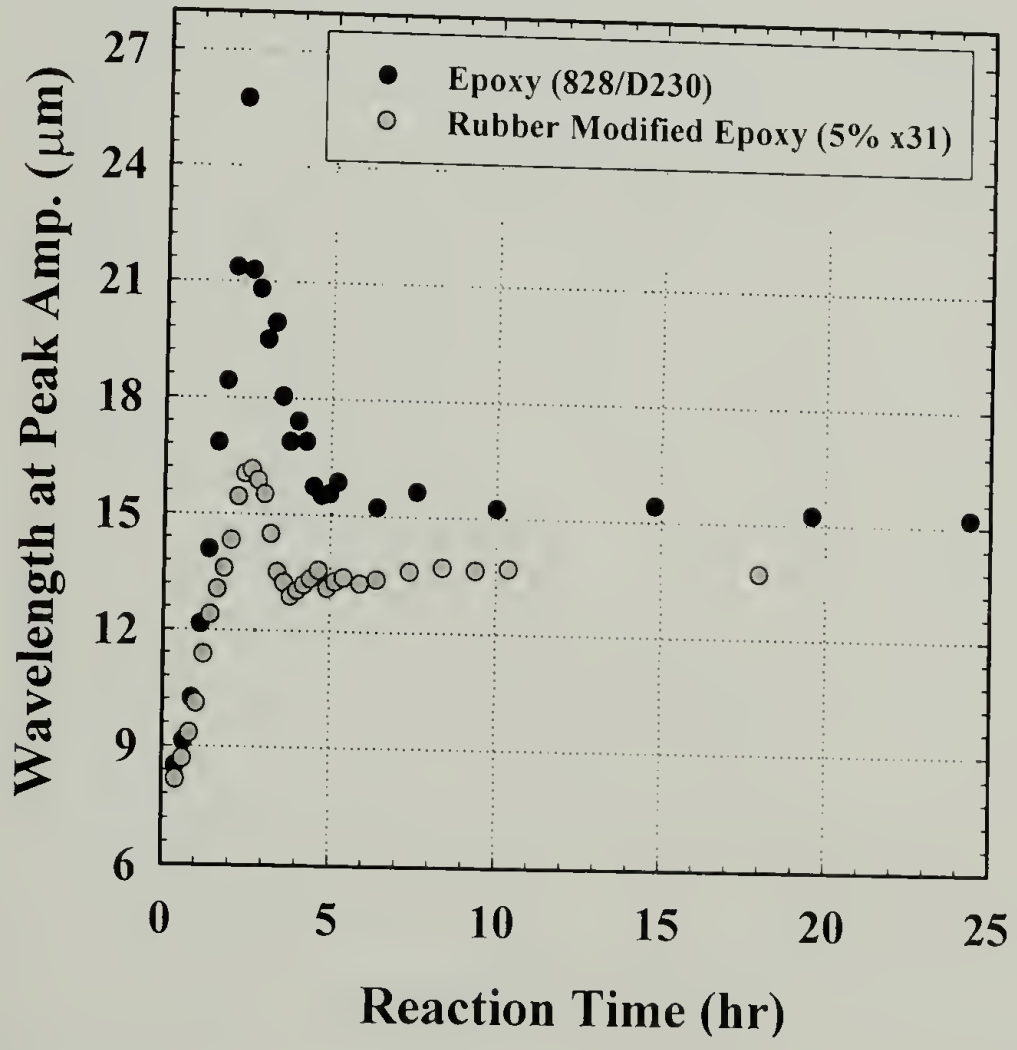

Figure 3.14: Wavelength peak amplitude for epoxy and rubber modified epoxy during cure.

The results of this calculation are for comparison purposes only because as stated above the epoxy and rubber modified epoxy were not heated above the cure temperature and thus the resultant T_g is equal to the cure temperature (50 °C). The T_g of fully cured epoxy of this formulation is 90 °C and a T_g of 50 °C is clear evidence of an incomplete cure. Keeping this in mind Figure 3.14 will be used only to compare epoxy and rubber modified epoxy which are at relatively equal stages of cure. Thus, Figure 3.14 shows that the peak frequency is shifted to a maximum wavelength of 25.8 and 16.2 μm for epoxy and rubber modified epoxy respectively. This indicates that the absorption of sound energy is occurring in different length scales within these two specimens. Figure 3.15 is an SEM image of the surface of freeze fracture rubber modified epoxy. The image clearly shows the specimen's high degree of inhomogeneity. Rubber domains of roughly 15, 5, and 1 μm appear dispersed throughout the specimen. The domains are clearly having a strong effect on the ultrasonic characteristics of the specimen. Certainly, this is expected from the discussions of section 2.3.5. The nature of the length scale effect will need to be elucidated with further studies.

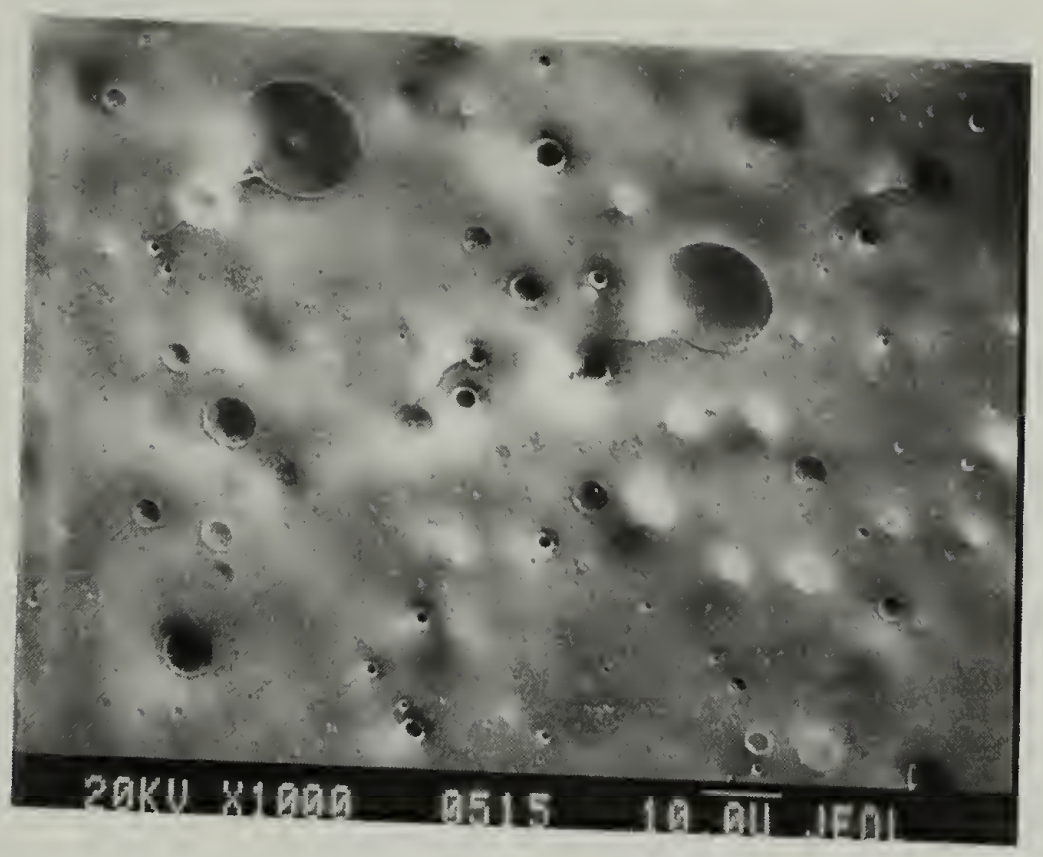

Figure 3.15: SEM image of the surface of rubber modified epoxy specimen after freeze fracture.

3.4 Conclusions

In situ ultrasonic spectroscopy analysis methods have been successfully developed and employed in the study of model reacting systems. The gelation of gelatin was evidenced by an initial sharp decrease in ultrasonic velocity followed by a gradual decrease. A similar trend was observed the amplitude of the frequency spectra. However, only a minor change in peak spectra frequency was observed upon gelation. These observations indicate that the mechanical properties change during gelation in a manner such that the increase in modulus is out weighted by the increase in density. Also, the minor change in peak frequency and absence of spectrum shape change indicates that gelation occurs over large length scales such that no discrete attenuation in the transmitted waves results.

The cure of epoxy and rubber modified epoxy (5 wt.% CTBN) were monitored via a through transmission method. Ultrasonic velocity under went a sharp step increase and

attenuation simultaneously obtained a peak value during the cure reaction. This phenomena was observed by several other researchers and is attributed to the absorption of ultrasonic energy by molecular motions associated with the glass transition. The time at which the shift and peak occur correlates with the vitrification of the epoxy networks, where the T_g becomes equal to the cure temperature. The time at which vitrification is observed to occur is dependent upon the time and length scale at which the reaction is probed. Thus, the observed vitrification time decreases as the frequency increases and the wavelength consequently decreases. This was observed to occur in both epoxy and the rubber modified epoxy. Estimates of the wavelength of the peak spectral frequency were made based on the observed time shift and the velocity of sound in fully cured epoxy and rubber modified epoxy at 50 °C. This indicated a distinct difference in the change in attenuated wavelength during cure for epoxy and rubber modified epoxy. This is most likely related to the morphology of the phase separated rubber modifier. However, because these experiments have just recently become successful there is little data available to allow such conclusions to be drawn. The potential for further detailed studies is very promising.

3.5 References

1) Maffezzoli, A.; Luprano, A. M.; Montagna, G.; Nicolais, L. *J. Appl. Polym. Sci.* **1998**, *67*, 823-831.

2) Mikkonen, R.; Savolainen, A. *J. Appl. Polym. Sci.* **1990**, *39*, 1709-1725.

3) Gendron, R.; Daigneault, L. E.; Tatibouet, J.; Dumoulin, M. M. *Advan. Polym. Tech.* **1996**, *15*, 111-125.

4) Shekarriz, A.; Brenden, B. B. *J. Fluids Eng.* **1995**, *117*, 317-319.

5) D'Aprano, A.; Mesa, C. L.; Persi, L. *Langmuir* **1997**, *13*, 5876-5880.

6) Persi, L.; Mesa, C. L.; D'Aprano, A. *Phys. Chem.* **1992**, *101*, 1949-1956.

7) Sladky, P.; Parma, L.; Zdrazil, J. *Polym. Bull.* **1982**, *7*, 401-408.

8) Canegallo, S.; Apostolo, M.; Storti, G.; Morbidelli, M. *J. Appl. Polym. Sci.* **1995**, *57*, 1333-1346.

9) Horvat, D.; Mozina, J.; Diaci, J. *J. De Physique* **1994**, *4*, C7-249 - C7-252.

10) Matsukawa, M.; Nagai, I.; Tanaka, Y. *Jpn. J. Appl. Phys.* **1995**, *34*, 2575-2578.

11) Carlin, B. *Ultrasonics*; 2d ed.; McGraw-Hill: New York, 1960.

12) Kronig, R. L.; Kramers, H. A. *Zeits f. Phys.* **1928**, *48*, 174-179.

13) Kronig, R. L. *J. Opt. Soc. Am.* **1926**, *12*, 547-557.

14) Lee, C. C.; Lahham, M.; Martin, B. G. *IEEE Trans. Ultrasonics. Ferro. Freq. Control* **1990**, *37*, 286-294.

15) Hughes, M. S.; Handley, S. M.; Miller, J. G. *IEEE Ultrasonics Symposium* **1987**, *9*, 1041-1045.

16) Zellouf, D.; Jayet, Y.; Saint-Pierre, N.; Tatibouet, J.; Barboux, J. C. *J. Appl. Phys.* **1996**, *80*, 2728-2732.

17) O'Donnell, M.; Jaynes, E. T.; Miller, J. M. *J. Acoust. Soc. Am.* **1981**, *69*, 696-701.

18) Arfken, G. *Mathematical Methods for Physicists*; 3 ed.; Academic Press: New York, 1985.

19) McClements, D. J.; Povey, M. J. W.; Dickinson, E. *Ultrasonics* **1993**, *31*, 433-437.

20) Freemantle, R. J.; Challis, R. E. *Meas. Sci. Technol.* **1998**, *9*, 1291-1302.

21) Alig, I.; Lellinger, D.; Nancke, K.; Rizos, A.; Fytas, G. *J. Appl. Polym. Sci.* **1992**, *44*, 829-835.

22) Younes, M.; Wartewig, S.; Lellinger, D.; Strehmel, B.; Strehmel, V. *Polymer* **1994**, *35*, 5269-5278.

23) Gillham, J. K. *Polym. Eng. Sci.* **1979**, *19*, 676.

24) Flory, P. J. *Principles of Polymer Chemistry*; Cornell University Press: Ithaca, 1953.

25) Williams, M. L.; Landel, R. F.; Ferry, J. D. *J. Amer. Chem. Soc.* **1955**, *77*, 3701.

CHAPTER 4

EVALUATION OF THE THERMAL DEGRADATION OF POLYMER MATRIX COMPOSITES VIA ULTRASONIC SPECTROSCOPY AND FRACTURE TOUGHNESS

4.1 Introduction

Polymer matrix composites (PMCs) are commonplace materials in many industries including commercial aircraft, marine, offshore oil platforms, and automotive applications. Over recent years, a safety concern has been raised regarding the use of these materials in situations where fire could erupt due to their general susceptibility PMCs may degrade, decompose, or even combust. In certain fire situations, a structural or load-bearing PMC may be exposed to excessive thermal loads that only char the surface of the material, yet thermally degrades the matrix below the surface. This thermal degradation may, in turn, dramatically affect the mechanical integrity long before combustion of the matrix occurs. Also, in controlled fire situations, structural or load-bearing components may be exposed to excessive temperatures for short periods of time and show little or no apparent signs of degradation. In these situations, questions arise with regard to what the residual strength is and what non-destructive methods are available today to assess residual strength. In this chapter, the utility of ultrasonic nondestructive analysis as a means of assessing the residual characteristics of PMCs exposed to thermal loads is presented.

Nondestructive testing (NDT) methods are commonly used for quality control and safety certification.[1-3] Methods of investigating materials with ultrasound are being rapidly developed and utilized. Common methods are to examine the velocity

(dispersion) and attenuation of ultrasonic waves and to correlate these with specific material property, condition or morphology. Researchers' efforts in the area of composites have been in the development of the following methodologies; image analysis, ultrasonic measurements of modulus changes, and observation of the frequency spectrum (ultrasonic spectroscopy). Ultrasonic spectroscopy is a relatively new technique and has been increasingly applied to composite materials analysis. Scott and Gordon developed a model for describing the interactions of ultrasonic waves with multi – laminate structures. Frequency spectra obtained by fast Fourier transforming the portion of the time domain associated with the layers were found to be sensitive to changes in thickness and modulus.[4] Stiffler et al utilized the frequency dependence of ultrasonic transmission to characterize the fatigue damage of carbon fiber - epoxy composites.[5] They found that different damage states yielded unique frequency spectra. Ourak *et al.*[6] and Raju *et al.*[7] correlated the frequency dependence of ultrasonic absorption to a composite's structure and periodicity. The spectral amplitudes at anti-resonance (or resonance) frequencies of the normalized amplitude have been utilized to determined the attenuation coefficients of glass, epoxy, and laminate composites.[8] Jayet *et al.* imbedded transducers in a composite and monitored the evolution of surrounding media during cure. Post cure the transducers monitored the hydrolytic degradation in polyester-based composites. After 30 days immersed in water at room temperature, there was an increase in longitudinal velocity and a decrease in the amplitude of the peak transmitted frequency and an increase in lower frequencies.[9] Kazys *et al.* compared the ultrasonic spectra from a flawless sample to that of one under investigation and were able to determine in which layer a delamination had taken place.[10] These resent applications

of ultrasonic spectroscopy to composite analysis illustrates the versatility and sensitivity of this technique. However, direct correlation of changes in ultrasonic frequency spectra with transformations due to discrete damage or chemical modification is lacking. One area where such evidence should be pronounced is thermal degradation.

Ultrasonic characterization of thermal transformations in metal and ceramic composites has resulted in mixed results. Webb *et al.* used ultrasonic image analysis to examine the effects of thermal shock upon continuous fiber ceramic composites.[11] They found that thermal shock resulted in a loss in ultrasonic image detail but did not consistently change the signal intensity. Huang *et al.* used ultrasonic velocities to study thermal cycling effects upon the modulus of Haynes 214 metal matrix composites reinforced with sapphire fibers.[12] The velocity was unchanged for all but one specimen which was markedly lower than the others. They state that this specimen may have undergone interfacial failure. Rokhlin *et al.* examined the thermal – oxidative degradation of a ceramic/ceramic composite exposed to flowing oxygen at elevated temperatures using ultrasonic velocities to characterize changes in modulus.[13] The modulus along the fiber was found to be dependent upon exposure temperature while that in the transverse direction was independent. A critical oxidation temperature was identified from this work. The inconsistency of ultrasonic characterization of thermal effects in ceramic and metal composites is not completely surprising since these materials are not greatly effected by elevated temperatures and thus the effects in question may be subtle.

Polymers and PMCs undergo significant mechanical behavior and chemical transformations upon thermal exposure. Tse *et al.* studied the transition from smoldering to flaming of polyurethane foam.[14] Ultrasonic image analysis was used to monitor the

evolution of the char permeability during burning. They found that the char layer continued to react and increased in permeability for long times after the primary smoldering front had passed. Armstrong-Carroll *et al.* investigated the thermal degradation of PMCs and found reductions in hardness and flexural strength only in specimens that had delaminations detected via ultrasonic image analysis.[15] Also, they found no evidence of incipient damage prior to delamination. However, the results of research presented here and published elsewhere[16-18] confirm that transformations which effect PMC mechanical behavior can be detected via ultrasound in non delaminated regions.

Unidirectional laminates were exposed to excessive thermal loads in a manner that produced a gradient in temperatures along the length of the sample and thus a gradient in thermal degradation. The thermal programs consisted of long term – low intensity and short term – high intensity regimes. Ultrasonic power spectra from these laminates are then compared with Mode I fracture toughness tests, TGA/DSC analysis, and FTIR analysis of the specimens before and after thermal exposure. The results are utilized to characterize the residual properties of the composites after exposure to excessive thermal loads. It is important to mention before continuing, that this research was conducted in collaboration with Terry R. Hobbs and maybe further discussed in his future Ph.D. dissertation.

4.2 Experimental

4.2.1 Laminate fabrication

Laminates were fabricated from 3501-6 and R922 prepreg were obtained from Hexeel Corporation. The 3501-6 prepreg eonsists of IM6G graphitc fiber and partially aminc curcd cpoxy. R922 prcpreg is made with G30-500 graphite fiber and a partially amine eured epoxy. Unidireetional pancls of 30 plies wcrc fabricatcd in a hand lay-up fashion with a 0.02 mm spacer (aluminum foil for 3501-6 and PTFE tapc for R922) inserted midway through thc lay-up scquencc along one edgc of the panel. The panels werc cured in an autoelave according to manufacture's specifications. Double cantilever bcam (DCB) tests speeimens were thcn maehined from cach panel to a total lcngth of 20 cm and a width of 2.5 em. The notch produced from the spaecr measured approximatcly 12 mm.

4.2.2 Ultrasonic speetroscopy

Sclcctcd DCB specimens werc submergcd in water and seanned in a baek scatter (pulse/echo) mode with a Panametries Ine. model V316 20 MHz focused transduecr. The transdueer used had a 3 mm diamcter elemcnt and a focal point 19 mm from its facc. A Panametries Ine. model 5601A/TT pulser/rcccivcr was uscd to drive thc transducer. Thc signal from the pulscr/receiver was digitizcd at a ratc of 1 GHz with a Sonix STR81G PC based digitizer. Panametries Ine. Multisean softwarc was uscd to set the trigger thrcshold and gate the eehoes returning from thc sample. Thc softwarc controllcd two stcpper motors that rastered the transdueer in thc X - Y plane via a Panametries Inc. P1399 position mateh generator and MEI motion controller. A sehematie of the apparatus is

shown in Figure 4.1. Specimens were held by a aluminum fixture designed such that they could repeatably be placed in the same location before and after thermal exposure. The height of the transducer above the sample was calibrated for each sample by recording a waveform from a rectangular piece of epoxy of known composition. The height of the transducer was adjusted to obtain the same time of flight of a reflection from the top surface of the epoxy. Five A-scans were collected and averaged every 0.25 mm along the length of the sample and digitally stored as a B-scan. B-scans were collected every 2.5 mm along the width of the sample. The B-scans were collected to form a three-dimensional data array for each DCB specimen. The 3D array could be separated into A-scans at selected points in the specimen, B-scans along the length or width of the specimen, and C-scans to map specific depths across the entire sample.

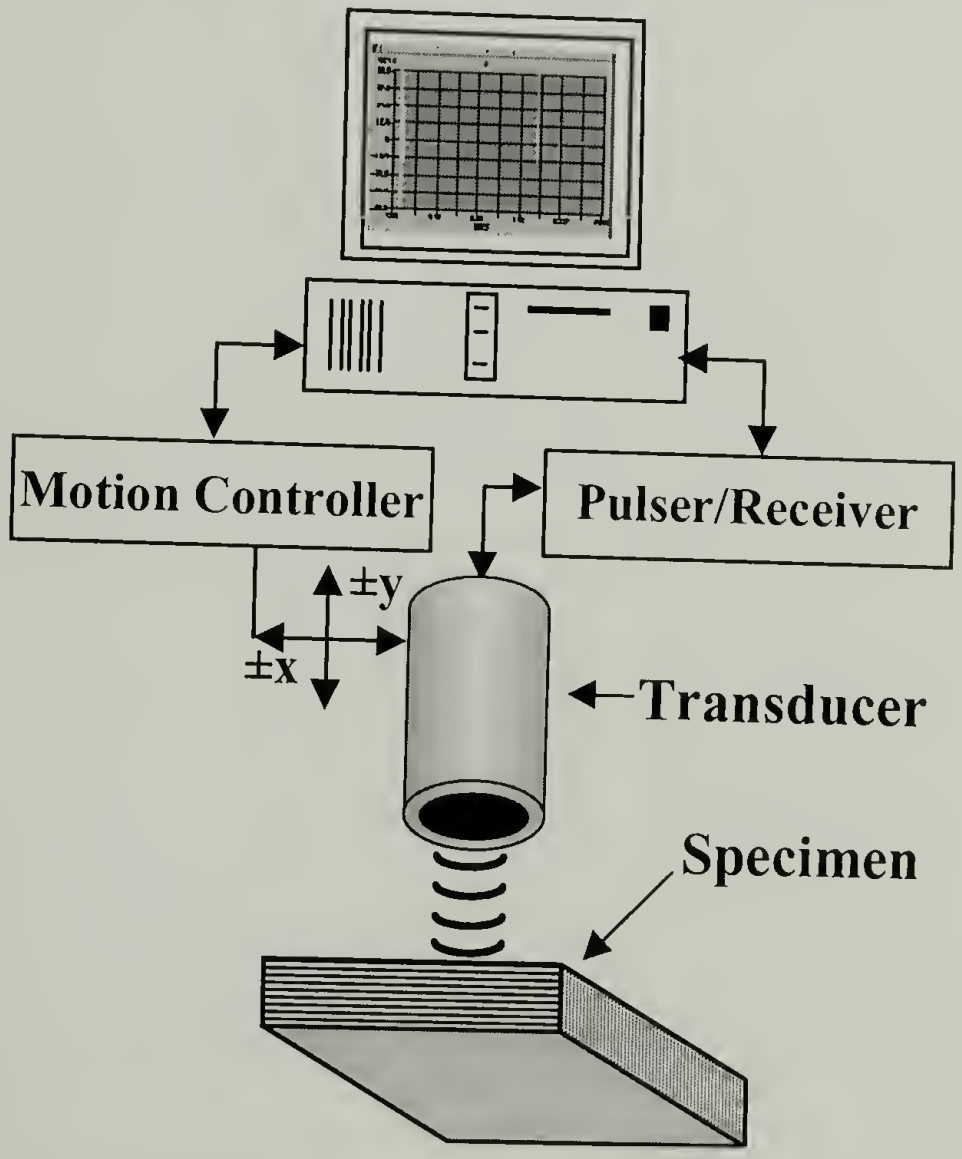

Figure 4.1: Ultrasonic scanning apparatus.

4.2.3 Thermal exposure

Thermogravimetric analyses (TGA) were conducted on samples of the laminates to determine an approximate decomposition temperature. A 10 mg sample was heated at a rate of 10 °C/min in a nitrogen atmosphere. This test indicated the onset of degradation for this material to be in the range of 320 – 330 °C. Thus, long term – low intensity exposures were conducted below this temperature and short term – high intensity exposures were at temperatures above it. Only one end of the specimen was exposed to the heat source to induce a gradient of temperature along the length of the specimen. Consequently, it was anticipated that a single specimen exposed in this fashion would contain a similar gradient of resin and fiber-resin interfacial degradation that could be compared with ultrasonic and fracture toughness measurements.

4.2.3.1 Short term – high intensity exposure

The untabbed ends of the DCB specimens fabricated from 3501-6 were exposed to extreme temperatures (350, 400, and 450 °C) for 1 hr. Here the untabbed ends were used to avoid sever damage to the tabbed region. The short term exposure apparatus consisted of a steel two liter beaker containing about 100 mL of sand. This was placed on a hot plate and wrapped with glass wool for insulation. Thermocouples were placed on the ends and at 5 cm increments along the length of each sample. Samples were inserted into the apparatus such that 12 mm of the untabbed ends were immersed in the sand. The thermal gradient induced in the specimen exposed to 450 °C for 1 hr is shown in Figure 4.2a. In Figure 4.2b, the average thermal gradients after 20 minutes of

exposure are plotted for specimen exposed at 350, 400, and 450 °C. 4.2.3.2 Long term – low intensity exposure

The prenotched end of DCB specimens constructed from the R922 prepreg were polished and then thermocouples were placed at the polished end, the opposing end and midway along the length of each specimen. The polished tips of the specimens were then submerged 12 mm into a silicone oil bath. The oil bath was maintained at a temperature of 205 °C and the specimens were exposed for a period of 28 days. The steady-state temperature measured at the mid-point averaged 130 °C and the temperature at the opposing end averaged approximately 90 °C. The thermal gradient is shown in Figure 4.2b.

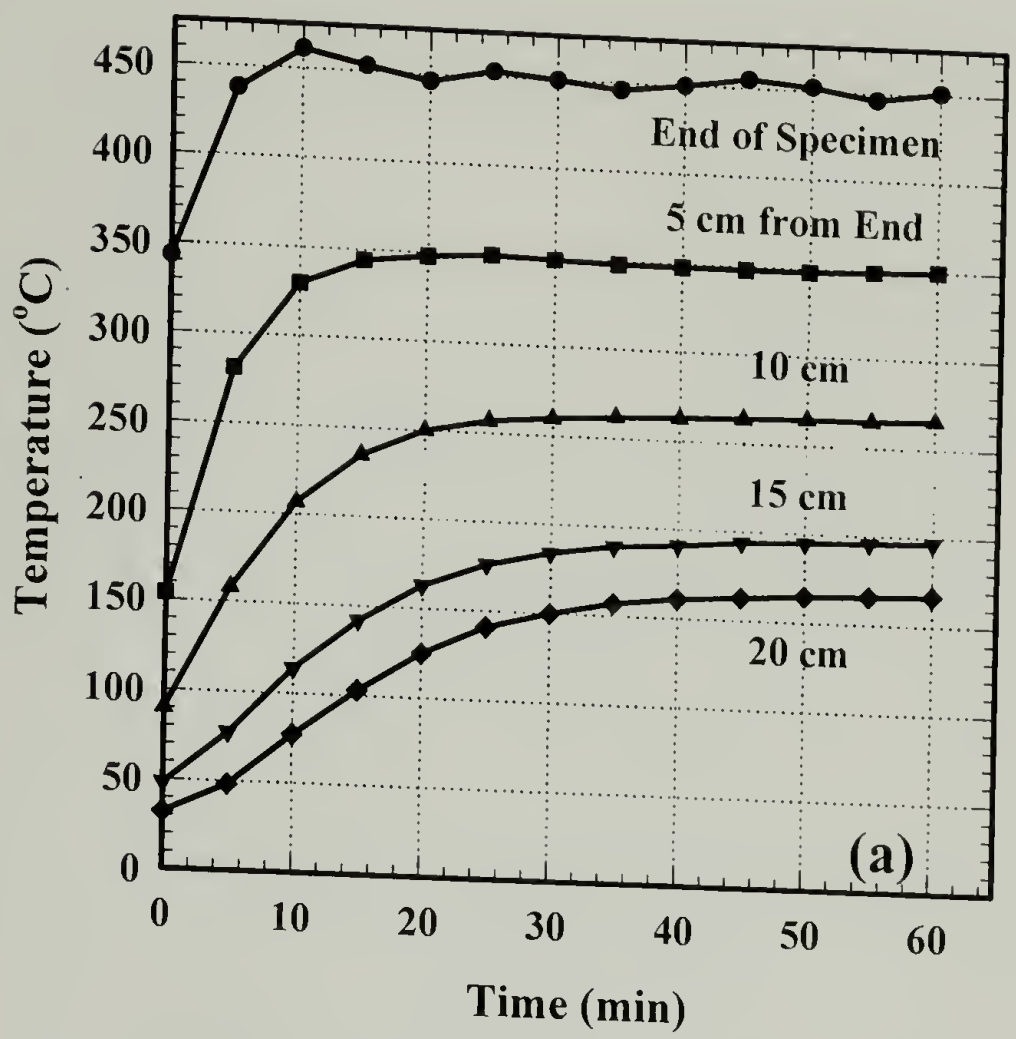

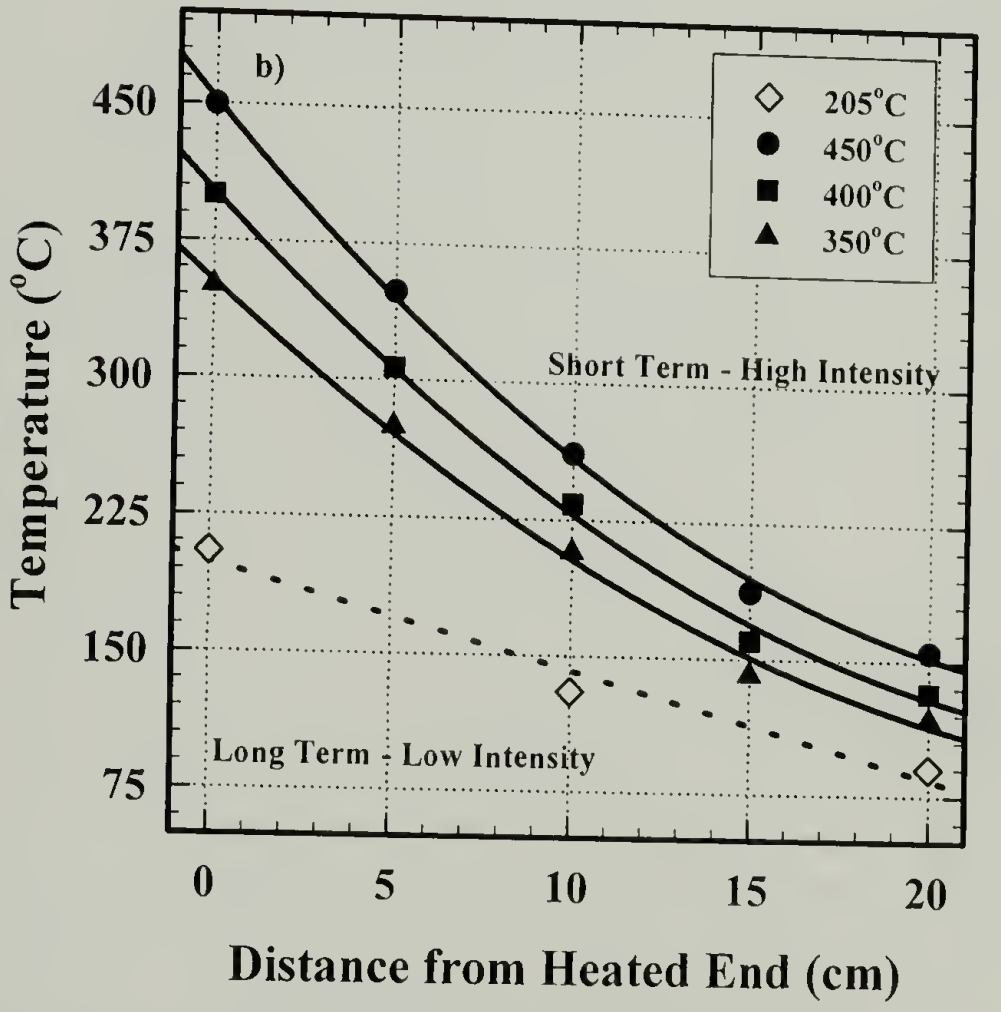

Figure 4.2: Thermal gradient induced in composite specimens exposed to 450 °C for 1 hr (a). Thermal gradients induced in DCB specimens during thermal exposure (b).

4.2.4 Mode I energy release rate measurement

The Mode I tests were conducted at a cross head speed of 2 mm/min. Crack lengths were measured optically during the testing and verified/corrected via inspection of the fracture surfaces after the testing was complete. The energy release rates were determined using the compliance method.[19] This method utilizes measured values of critical load per crack length together with the specimen's compliance at the specified crack lengths. The result is a series of load displacement curves where the compliance of a specimen gradually increases as the crack is incrementally propagated. This is shown in Figure 4.3a for an unaged sample constructed from 3501-6 prepreg. In this approach, the measured compliance is used to calculate the energy release rates using equation 4.1.

$$G_{IC} = \frac{P^2}{2b}\frac{\partial C}{\partial a} \qquad (4.1)$$

where $\mathbf{G_{IC}}$ is the energy release rate (fracture toughness), **P** is the applied load, **C** is the specimen compliance, **a** is the crack length, and **b** is the specimen width. Figure 4.3b is a plot of the measured compliance versus crack length curves for unaged DCB test specimens. The curve fit is a third order polynomial with a Pearson's correlation coefficient of 0.990.

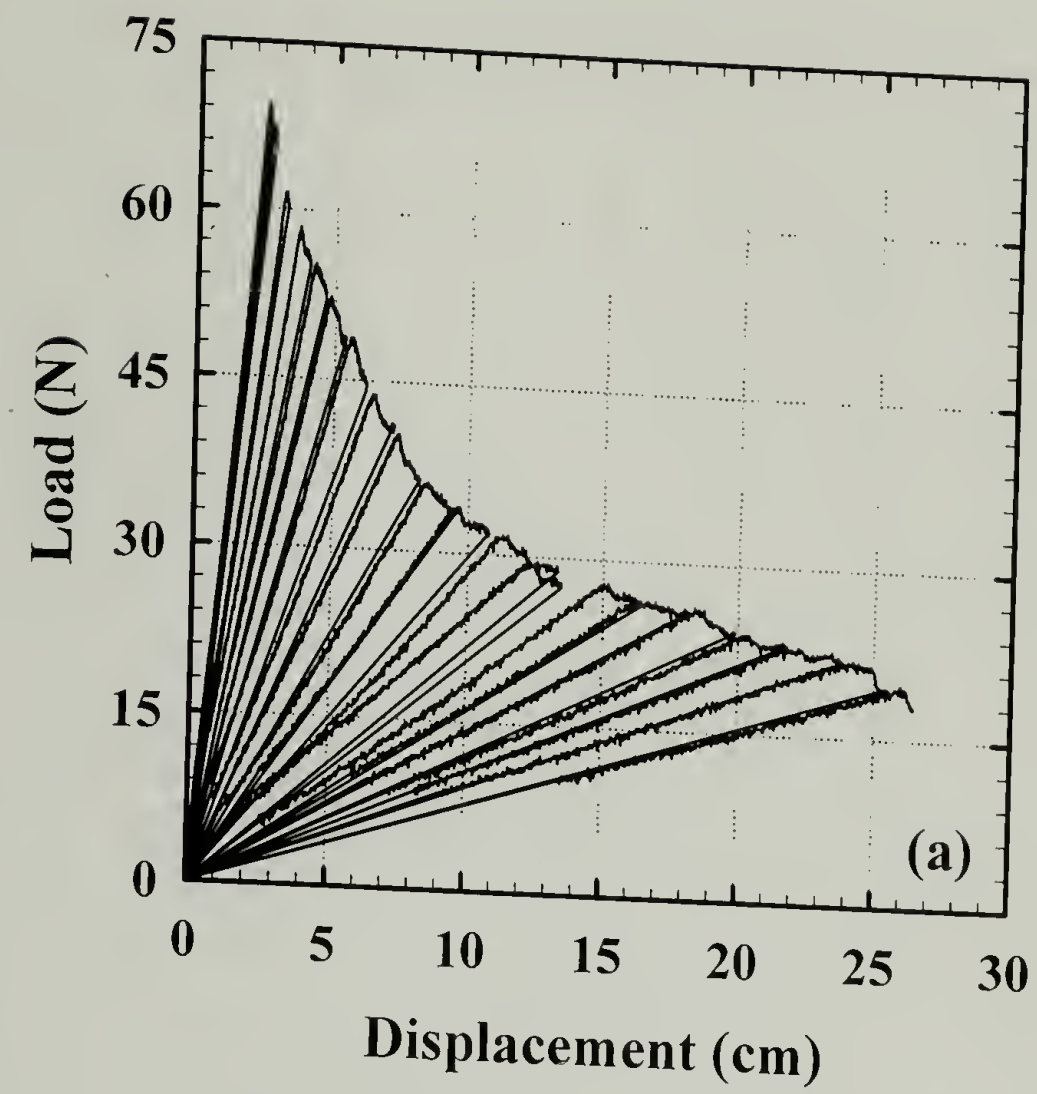

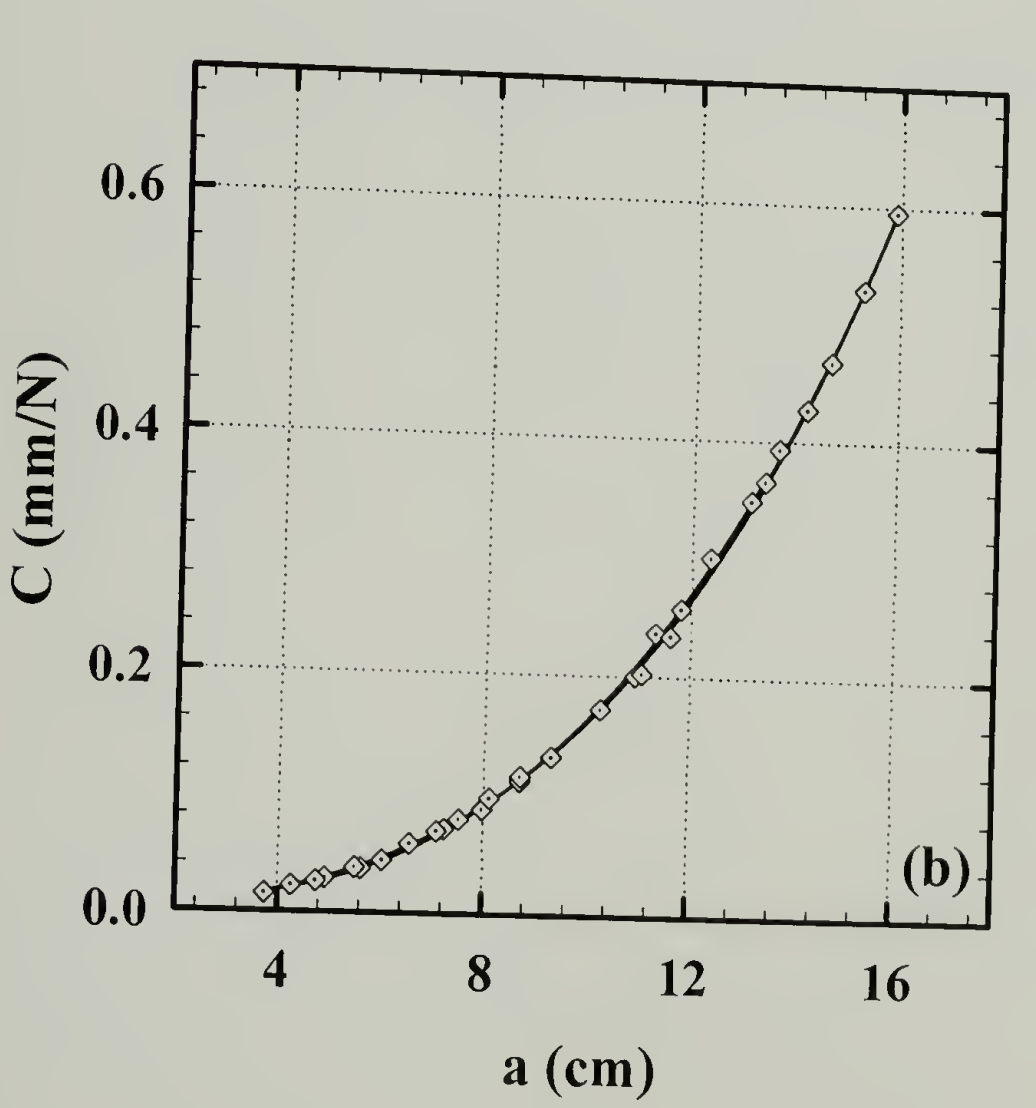

Figure 4.3: Load displacement curves for unaged DCB specimen (a). Plot of measured compliance curves for Mode I energy release rate experiments on unaged DCB specimens (b).

4.2.5 Fourier transform infrared spectroscopy (FTIR)

FTIR spectra were collected at 2.5 cm intervals along the length of the fracture surfaces of the short term – high intensity specimens. These measurements were conducted by Cristiane Rodriguez of Nicolet using a Nicolet Magna 760 spectrometer interfaced to an InspectIR microsampling accessory with a silicon ATR (attenuated total reflectance) crystal producing an IR sampling spot size of approximately 70 μm. A total of 200 scans were collected and averaged per spectrum.

4.2.6 Simultaneous thermogravimetric analysis and differential scanning calorimetry (DSC/TGA)

After fracture toughness was measured, a lengthwise section of each short term – high intensity specimen was removed and samples, approximately 10 mg each, were cut from this section at 2.5 cm intervals. Each sample was heated at a rate of 10 °C/min in nitrogen (flow rate = 50 mL/min) using a Rheometrics STA Model 1500 TGA/DSC. Weight loss and heat flow were recorded for each sample from 30 to 900 °C.

4.2.7 Scanning electron microscopy (SEM) Analysis

SEM was conducted using a Joel 35 CF. The products were placed on carbon tape affixed to a one inch diameter aluminum disk and coated with gold using a Polaron Instruments Inc. SEM Unit, model E51000. All images were taken in the secondary electron imaging mode.

4.3 Results and Discussion

4.3.1 Ultrasonie spectroseopy

After thermal exposure, all samples were reseanned using ultrasonic radiation. Figure 4.4 shows a typical pulse-echo waveform reeorded from an unaged speeimen. The waveform consists of three parts; 1) the most intense refleetion near t=0 μs is from the front face of the sample, 2) the middle portion of the waveform consists of refleetions from individual layers and reverberations within these layers, and 3) the strong signal at the end of the waveform is the reflection from the baek wall of the speeimen. Spectroscopic analysis was condueted on the baek wall refleetion. This was ehosen because it represents sound that had traveled through the sample twiee and should be the most affected by material changes. The reflection from the baek wall was isolated, its baseline eorrected, and then transformed into the frequeney domain via fast Fourier transformation. This process was repeated along the length of all speeimens before and after thermal exposure.

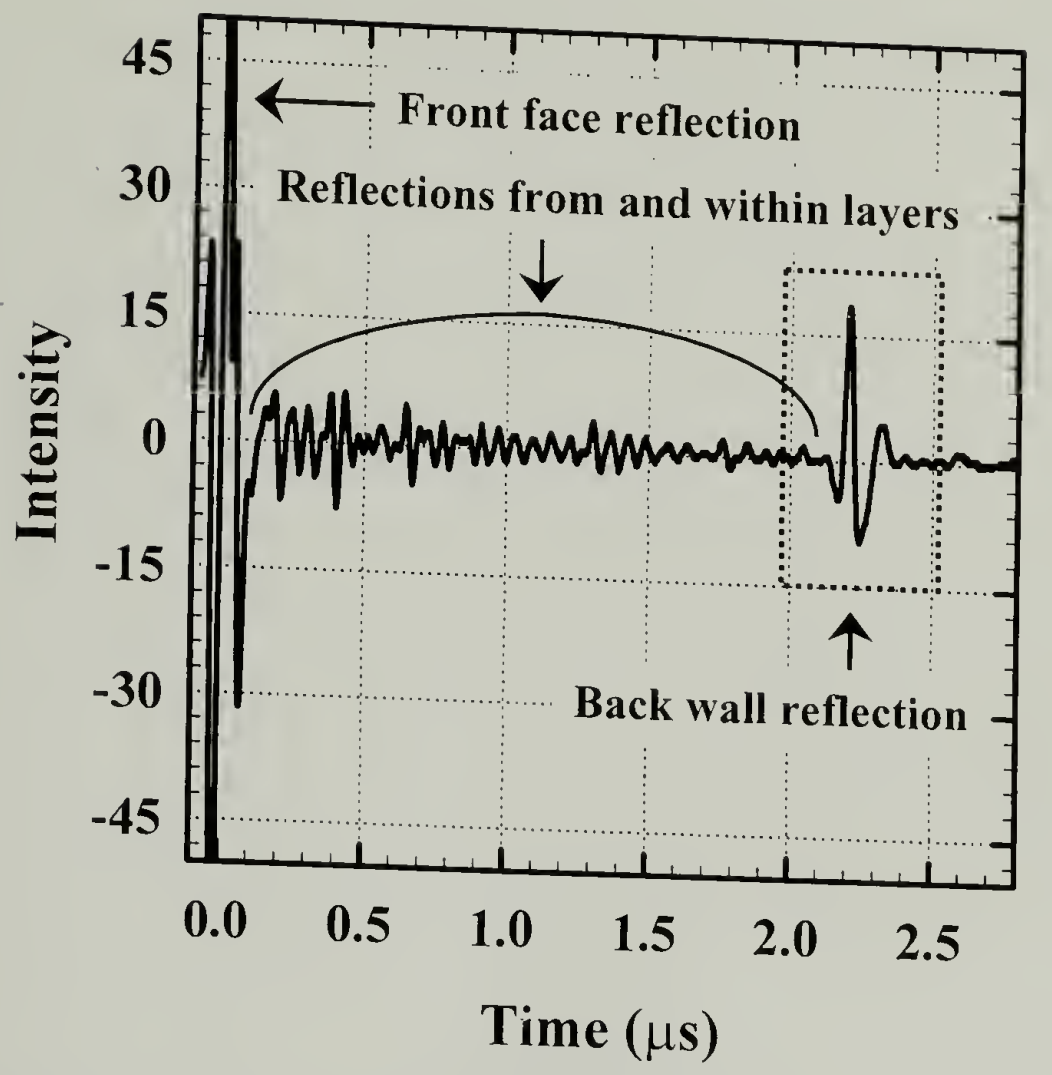

Figure 4.4: Pulse echo waveform from unaged composite specimen.

4.3.1.1 Short Term – High Intensity

Figure 4.5a shows the frequency spectra collected along the length a specimen prior to its exposure to 450 °C for 1 hr. The spectra are not completely uniform due to the presence of discrete variations within the composite. Note that there are no spectra near the end of the specimen. The back wall reflection is not present in this area due to strong reflections at the aluminum prenotch. Figure 4.5b shows the frequency spectra from the same specimen after exposure to 450 °C for 1 hr. After thermal exposure the amplitude of the frequency spectra are increased with a distinct increase occurring just before the amplitude drops off sharply. The location of the sharp drop off is adjacent to areas of delaminated layers. In this area and beyond (moving closer to the heated end) no back

wall reflections were detected. Similar behavior was observed for the specimens exposed to 400 and 350 °C for 1 hr. The peak spectral amplitude in Figure 4.5 and for those for the 400 and 350 °C specimens is plotted versus the distance from the heated end in Figures 4.6 –4.8. Plotting the data in this manner makes it clear that the amplitude has increased with a sharp increase occurring just before a sharp drop. The magnitude of this behavior decreases with exposure temperature. This evidence clearly illustrates a direct correlation between the severity of thermal exposure/damage and the ultrasonic frequency spectrum. The transmission and reflection efficiency of ultrasound is dependent upon the material properties of the medium. Thus, these results indicate that short term – high intensity thermal exposure transformed the composites making them more efficient at propagating sound. Possible causes of this are a localized increase in stiffness and/or decrease in density due to chemical transformation of the matrix.

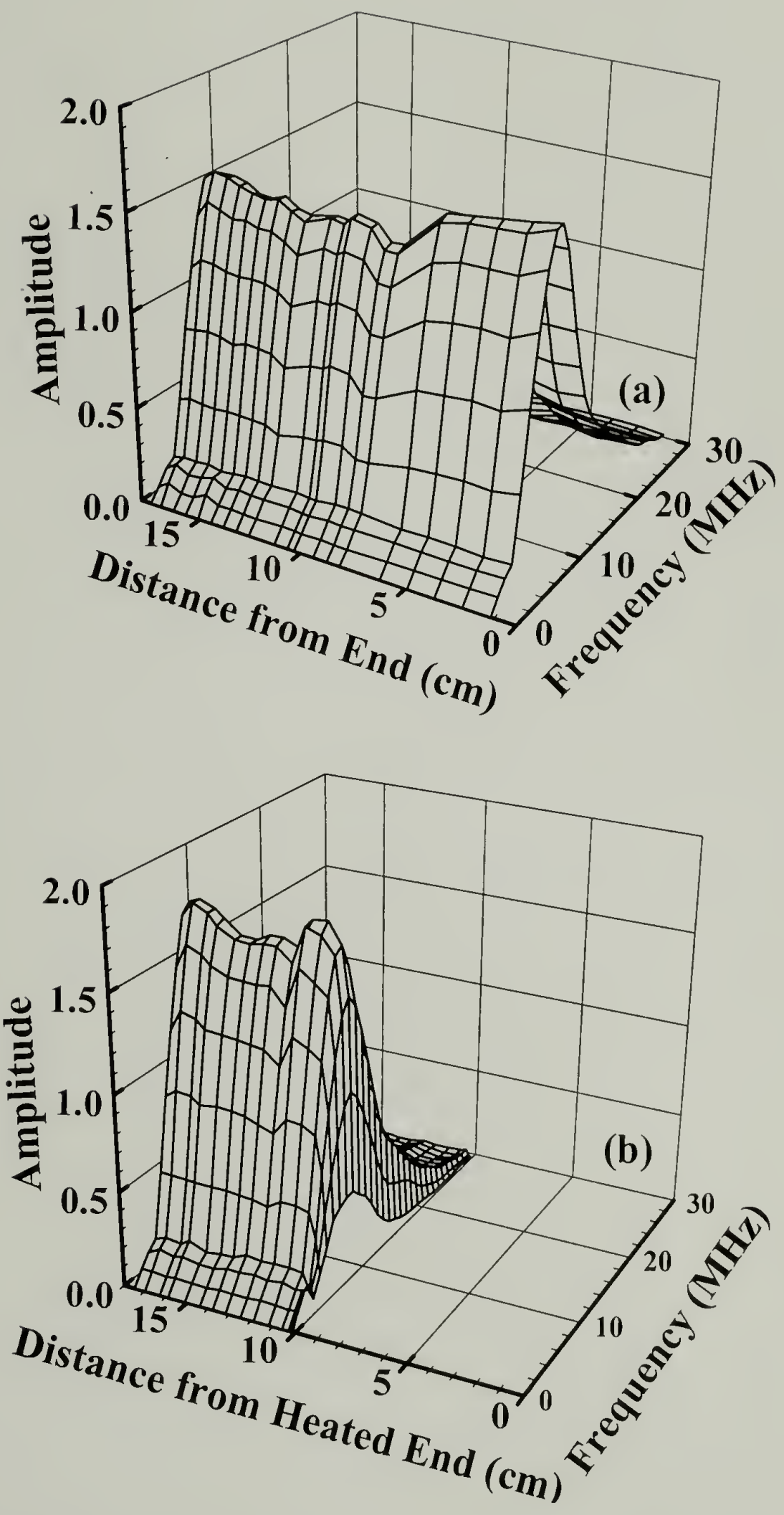

Figure 4.5: Frequency spectra along the length of a specimen prior to its exposure to 450 °C for 1 hr (a). Frequency spectra along the length of a specimen after exposure to 450 °C for 1 hr (b).

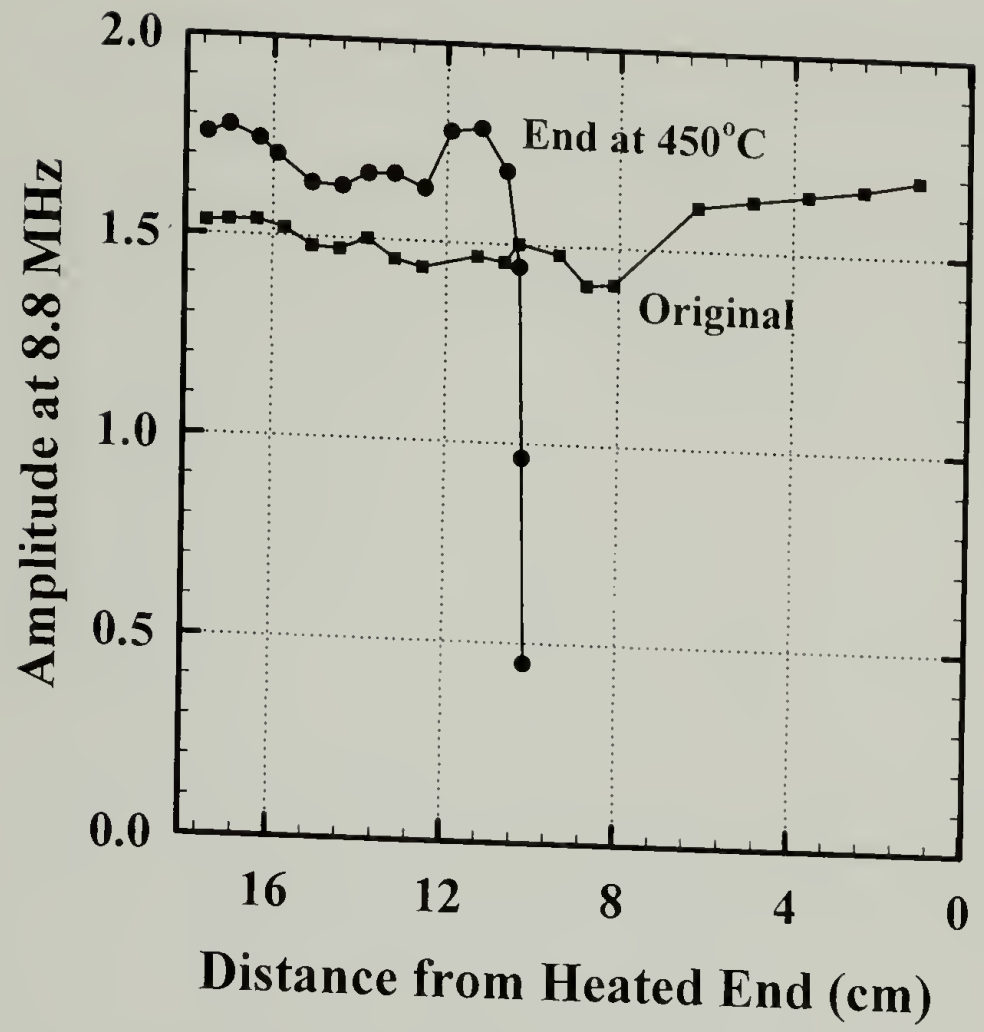

Figure 4.6: Amplitude of frequency spectra at 8.8 MHz before and after exposure to 450 °C.

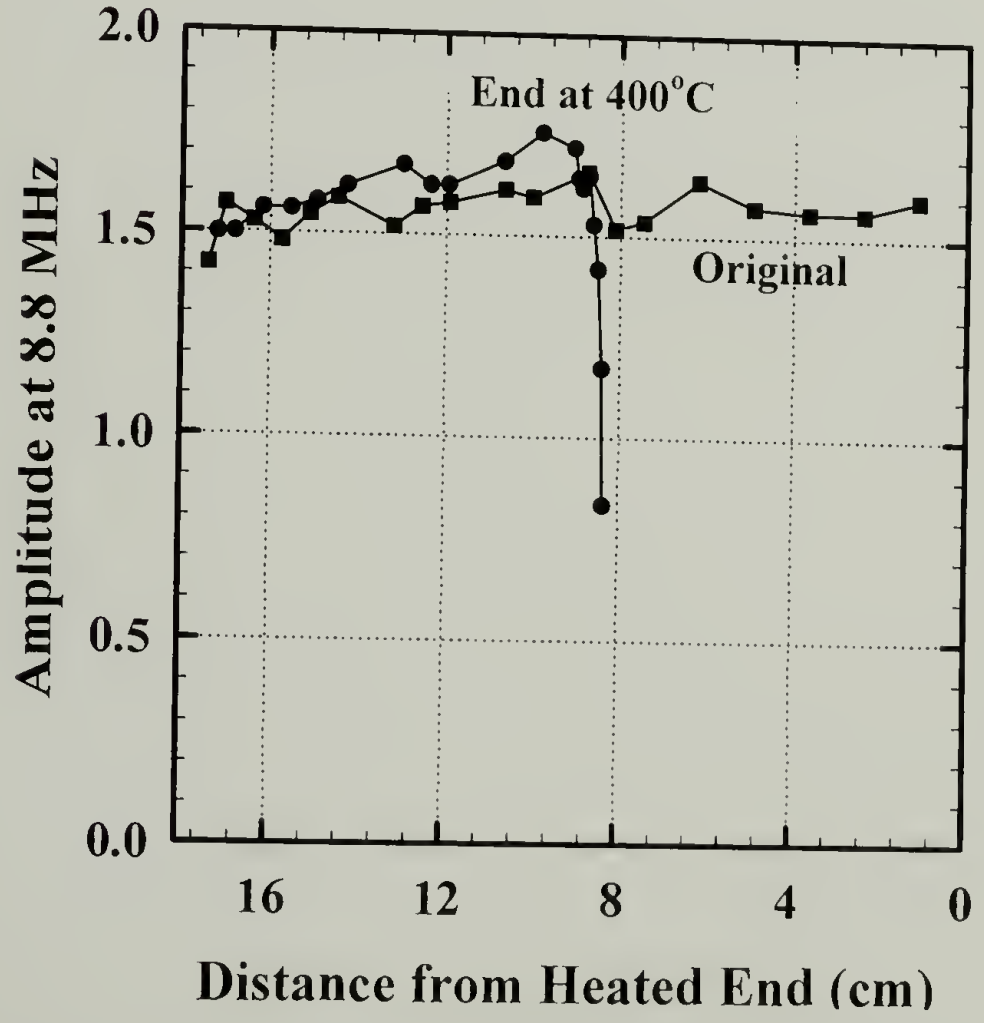

Figure 4.7: Amplitude of frequency spectra at 8.8 MHz before and after exposure to 400 °C.

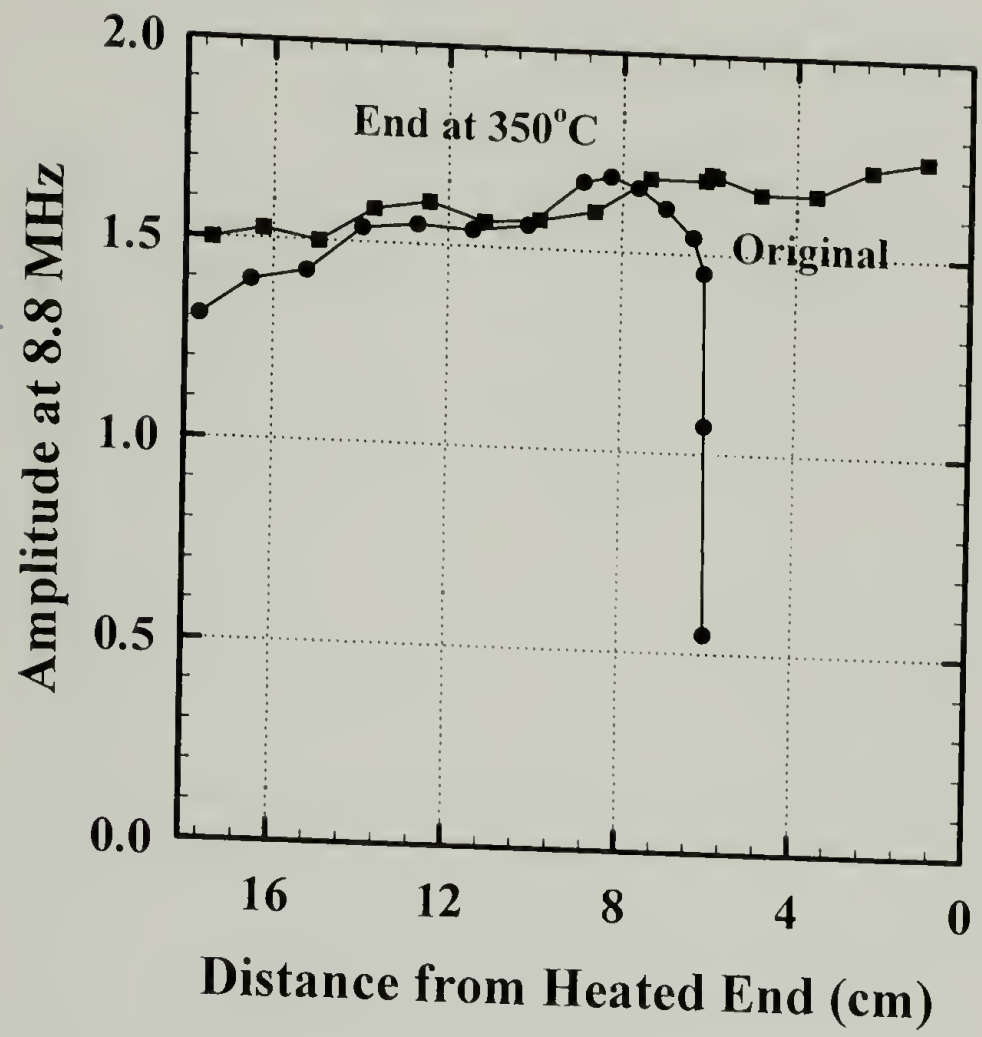

Figure 4.8: Amplitude of frequency spectra at 8.8 MHz before and after exposure to 350 °C.

4.3.1.2 Long term – low intensity

The frequency spectra are shown for the test specimens exposed to 205 °C for 28 days in Figure 4.9. The plots in Figure 4.9 are labeled with numbers that denote the measurement distance away from the heat source. Figure 4.9 shows that there is a clear reduction in the frequency spectral amplitude that becomes more pronounced as the measurements are taken nearer the heat source. This indicates that additional attenuation occurs in the composite as a consequence of the heat exposure. Since the ultrasonic frequency spectra decrease, the excess attenuation coefficient (α_{ex}) due to the thermal treatment of the DCB specimen can be calculated using equation 4.2.

$$\alpha_{ex} = \alpha_W - \frac{1}{x} Ln\left(\frac{A_T}{A_O}\right) \qquad (4.2)$$

In equation 4.2 α_W is the attenuation coefficient of water (0.025 Np/cm), **x** is the thickness of the specimen, $\mathbf{A_T}$ is the frequency spectra of the exposed specimen and $\mathbf{A_O}$ is the average frequency spectrum from the unaged specimen (see Figure 4.10). The thickness of the specimen did not change after exposure and was ascribed a value of one. The excess attenuation coefficients versus frequency are plotted in Figure 4.11 and clearly illustrate that the loss in signal intensity begins with the highest frequencies and then progressed to the lower frequencies as damage increases. It is intriguing that long term – low intensity exposure produces the opposite effect on ultrasonic signal amplitude than that of short term – high intensity exposure. The cause is investigated in the following sections.

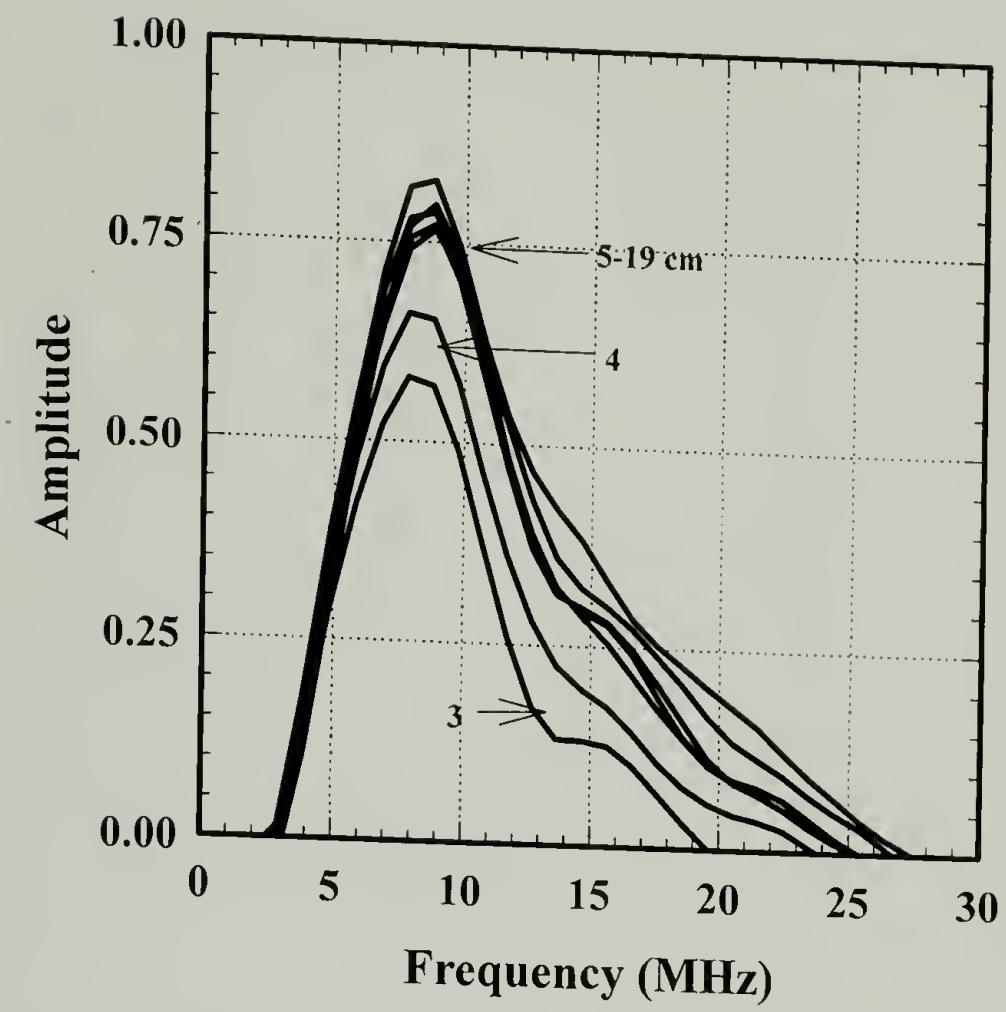

Figure 4.9: Frequency spectra for a DCB specimen exposed to 205 °C heat source.

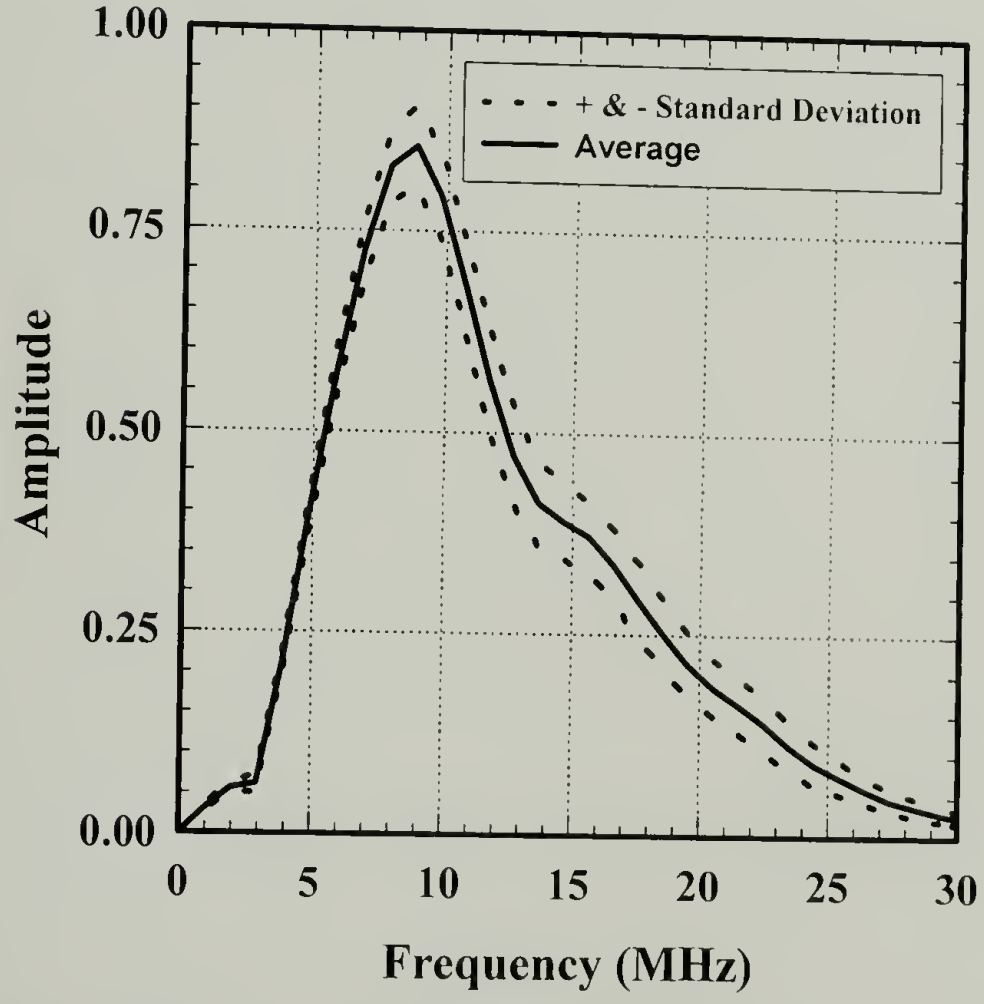

Figure 4.10: Average frequency spectra and ± standard deviation from unaged specimen.

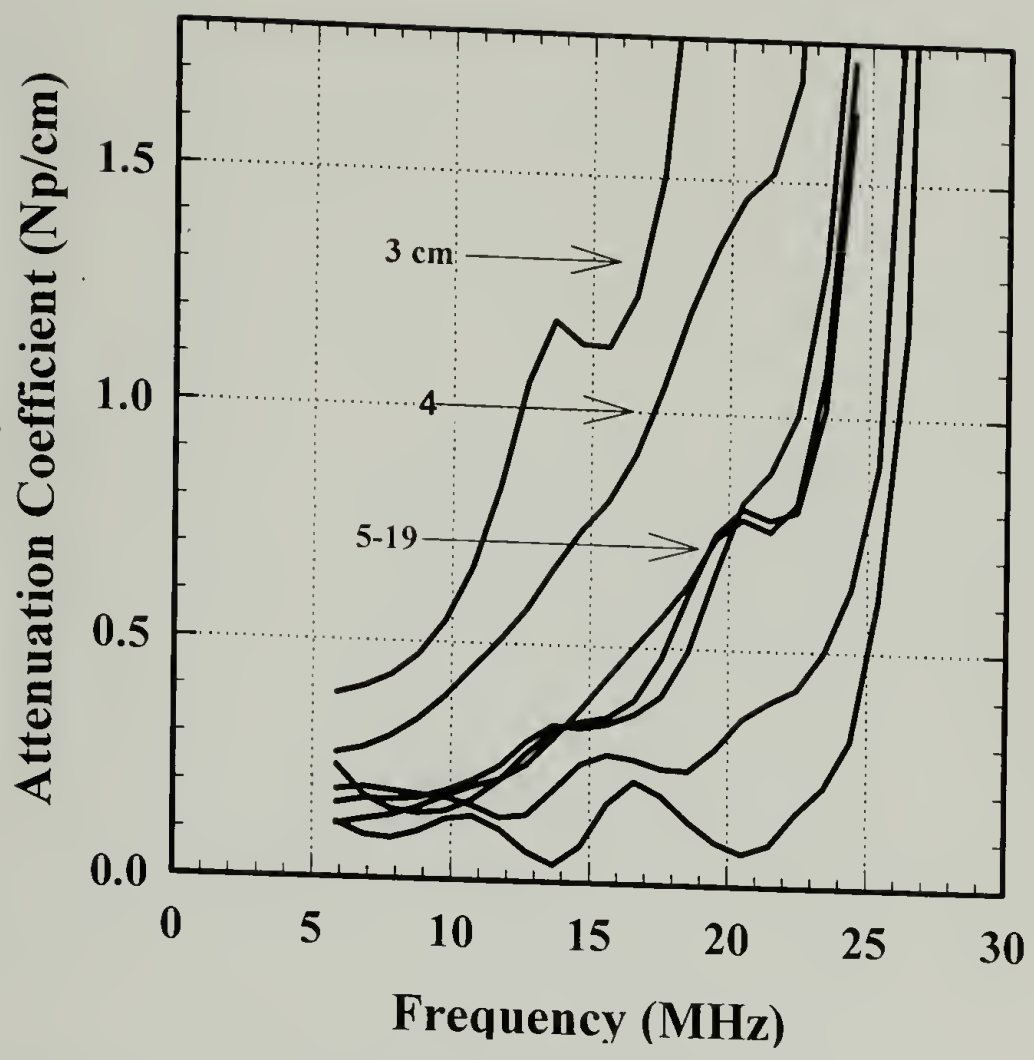

Figure 4.11: Ultrasonic attenuation for sample heat aged at 205 °C for 28 days.

4.3.2 Fracture toughness

Mode I critical energy release tests (G_{IC}) were conducted on the DCB test specimens to evaluate if any degradation in the resin or resin/fiber interface occurred as a consequence of the thermal loading. Under normal conditions, the critical energy release rate is independent of crack length and is ascribed a value of G_{IC}. As a result, a typical test on DCB specimens reaches a steady state condition corresponding to the G_{IC} value. However, if the fracture energy changes along the specimen's length, as we might expect for the heat treated samples, then a steady state value will not be obtained.

4.3.2.1 Short Term – High Intensity

Figure 4.12a shows the compliance curves generated from successive load displacement measurements for aged and unaged DCB specimens. The compliance of the thermally loaded specimens incrementally decreases as the temperature of exposure increases. Thus, the specimens were significantly stiffened as the result of thermal exposure. The increase in stiffness with exposure temperature may explain the increase in ultrasonic intensity as the composite is becoming more efficient at propagating of sound upon thermal exposure. Figure 4.12b shows the G_{IC} values obtained using the compliance curves in Figure 4.12a. Note that the control specimens have G_{IC} values of 240 J/m^2. The specimen exposed to 450 °C has greater toughness values than the control and there is a jump in toughness prior to failure near the heated end. Again similar effects are seen for the specimens exposed to 400 and 350 °C specimens except the toughness is only slightly greater or similar to the control specimens prior to a jump in toughness just before failure. Other researchers have also seen increase fracture toughness with short term thermal exposure. Yuan and Hutapea studied effects of temperature, loading rate, and thermal aging on the Mode I fracture toughness of unidirectional composites fabricated from IM7 fibers and LaRC-RP46 a polyimide resin.[20] They found that DCB specimens exposed to 232, 288, and 316 °C for 1 hr and tested at these temperatures exhibited significantly increased G_{IC} values.

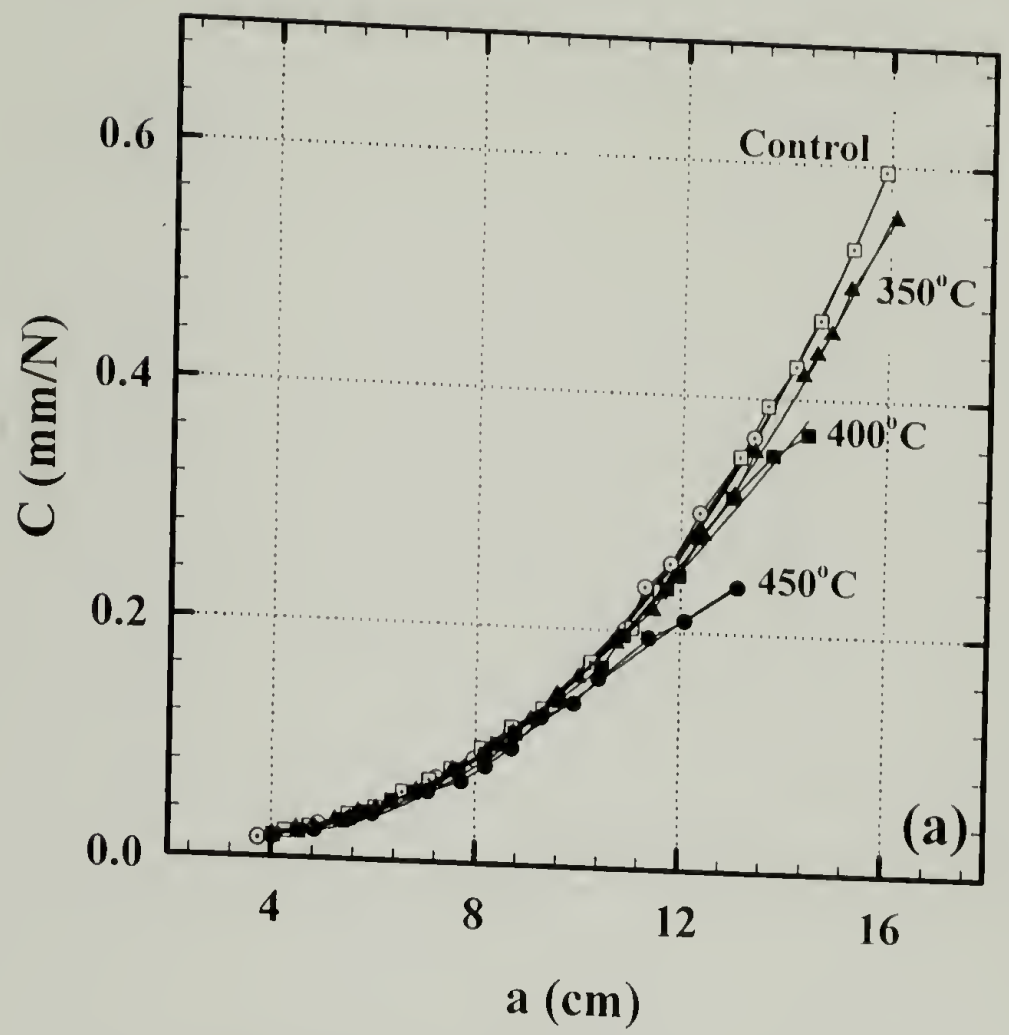

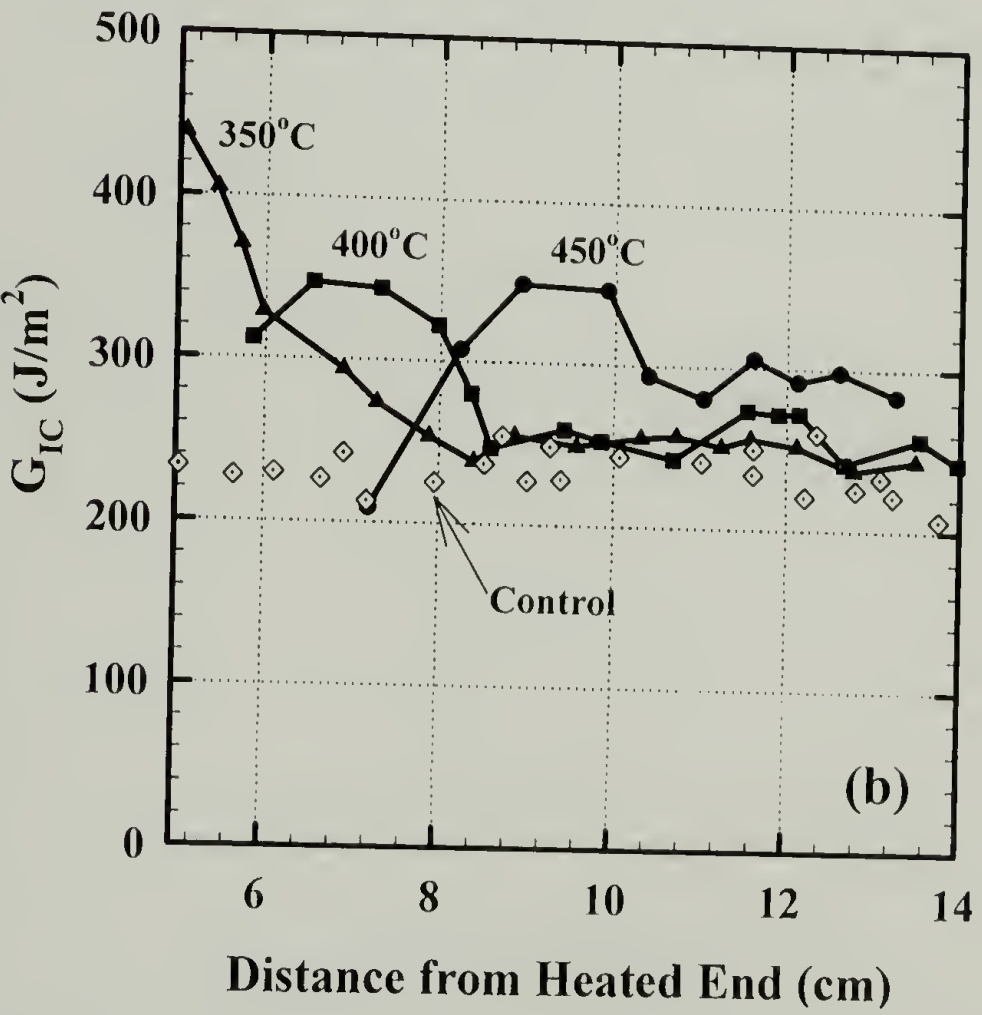

Figure 4.12: Compliance curves from exposed and unexposed (control) specimens (a). Fracture toughness of exposed and unexposed specimens (b).

Comparing Figures 4.6 and 4.12b for the specimen exposed to 450 °C a remarkable similarity is noted in the shape of the curves. Both figures show an increase in magnitude over the unaged specimen with a sharp increase occurring just before delamination and failure. This is more clearly illustrated in Figures 4.13 where the amplitude of the frequency spectra at 8.8 MHz for the unaged and aged specimens are plotted with the fracture toughness of the aged specimen versus the distance from the heated end. Plotting the data in this matter illustrates the following consistent trends; 1) the sharp drop in amplitude occurs just before the sharp increase in toughness, 2) the location of these sharp changes shifts to the right (closer to the heated end) with decreasing exposure temperature, and 3) the intensity of the amplitude jump sequentially decreases as the severity of the thermal gradient was reduced. Thus, there is a strong correlation between the ultrasonic spectra and fracture toughness responses to thermal degradation.

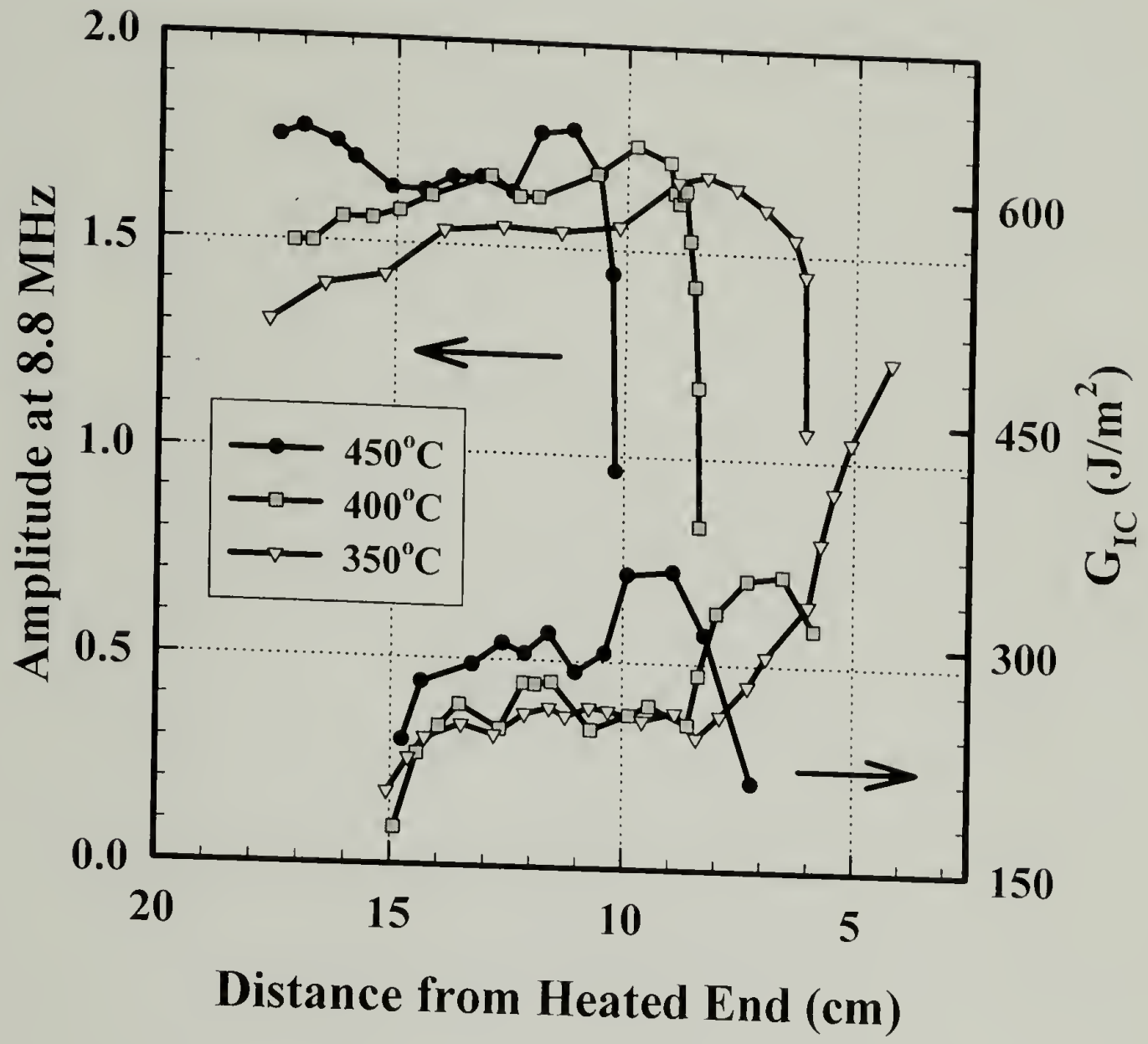

Figure 4.13: Peak ultrasonic amplitude and fracture toughness versus the distance from the heated end.

Plotting the data in Figure 4.13 versus the positional exposure temperature, Figure 4.14, collapses all of the data together with the sharp drop off in frequency spectra and sharp rise in fracture toughness occurring at 250 °C. This clearly indicates evidence of a critical temperature at which sever thermal degradation and/or composite delamination takes place.

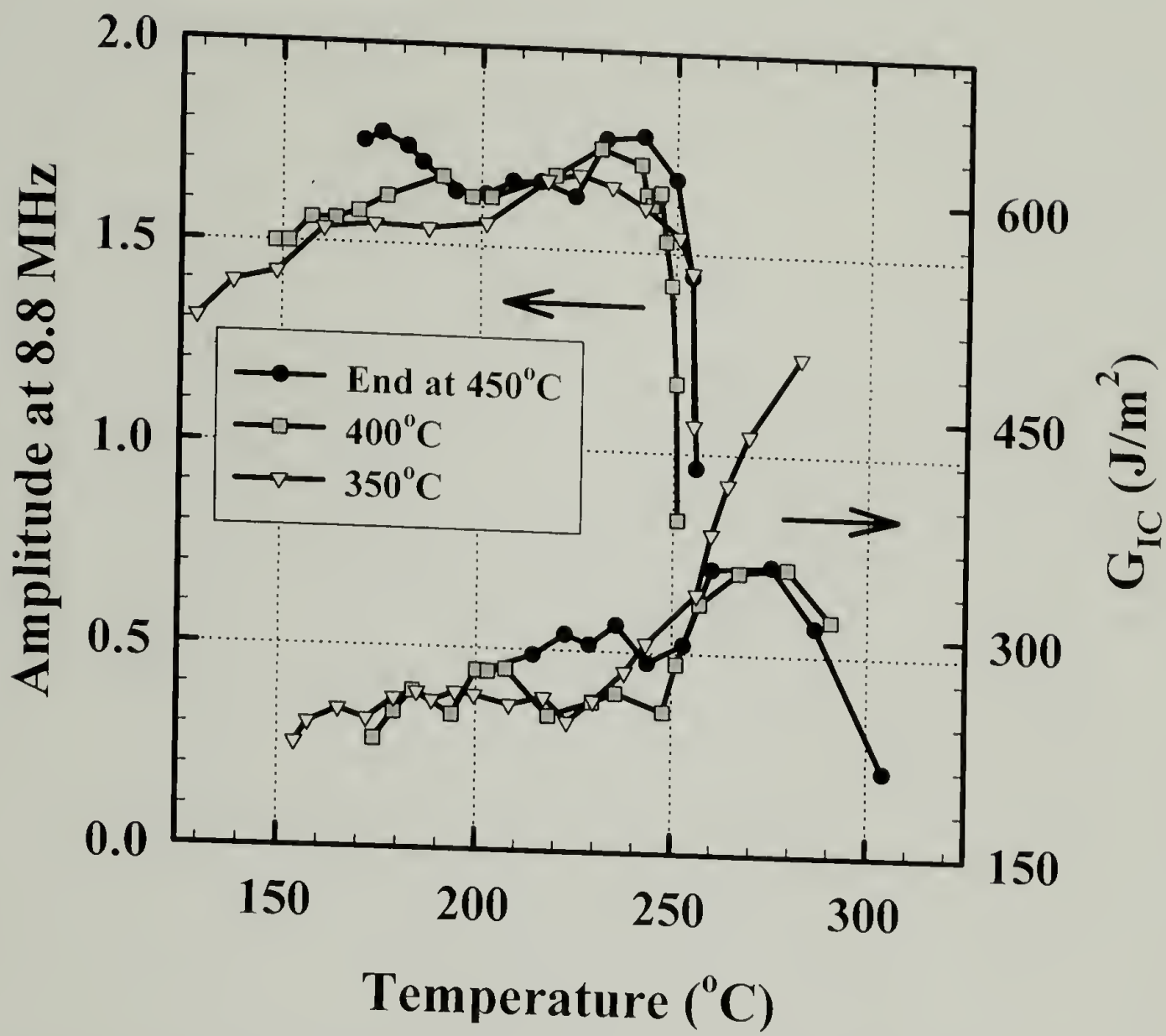

Figure 4.14: Peak ultrasonic amplitude and fracture toughness versus exposurc temperature.

Searching for evidence of toughening mechanisms, the fracture surface are examined via SEM. Figure 4.15 is an electron micrograph of the specimcn exposed to 450 °C for 1 hr. The micrograph was taken 16 cm from the heated end and indicates that fracture proceeded uniformly between layers of carbon fiber. The fracturc surfacc of the same specimen in the region of increased toughness, 9 cm from thc heated end, (Figurc 4.16) is no longer uniform indicating that the crack does not propagatc uniformly between layers but now must break fibers to grow. Thus, thc mcchanisms of incrcascd toughening may include fiber bridging in the regime just prior to the rapid decrease in fracture toughness. In this region, the matrix has been sufficiently degraded such that the

crack no longer propagates discretely between layers. Thus, crack growth requires increased energy to propagate. The sharp increase in ultrasonic amplitude preceding this region maybe evidence of incipient damage prior to delamination. Note that the specimen temperatures at 16 and 9 cm from the heat source were 185 °C and 290 °C.

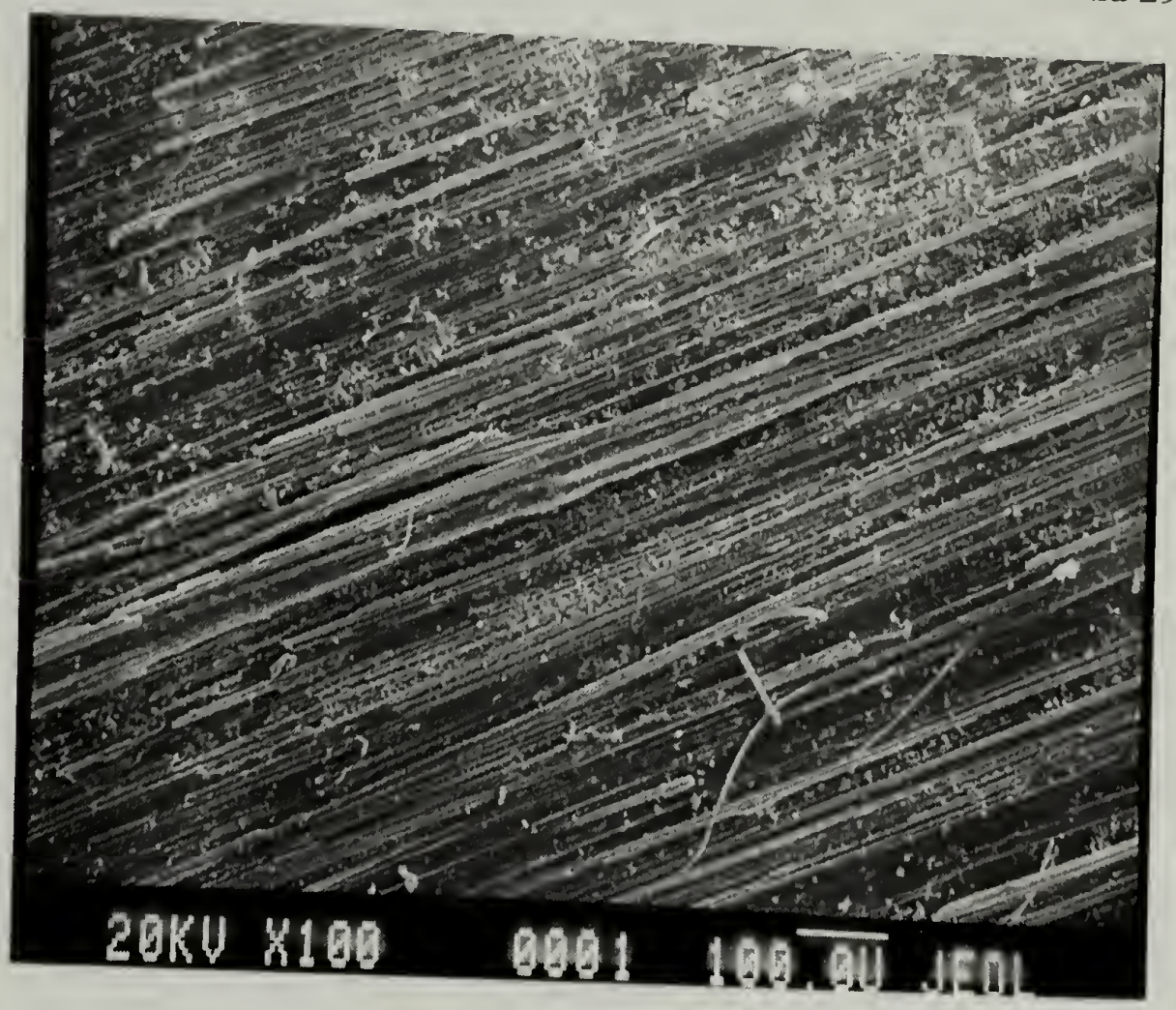

Figure 4.15: SEM image of 450 °C specimen's fracture surface 16.0 cm from heat source.

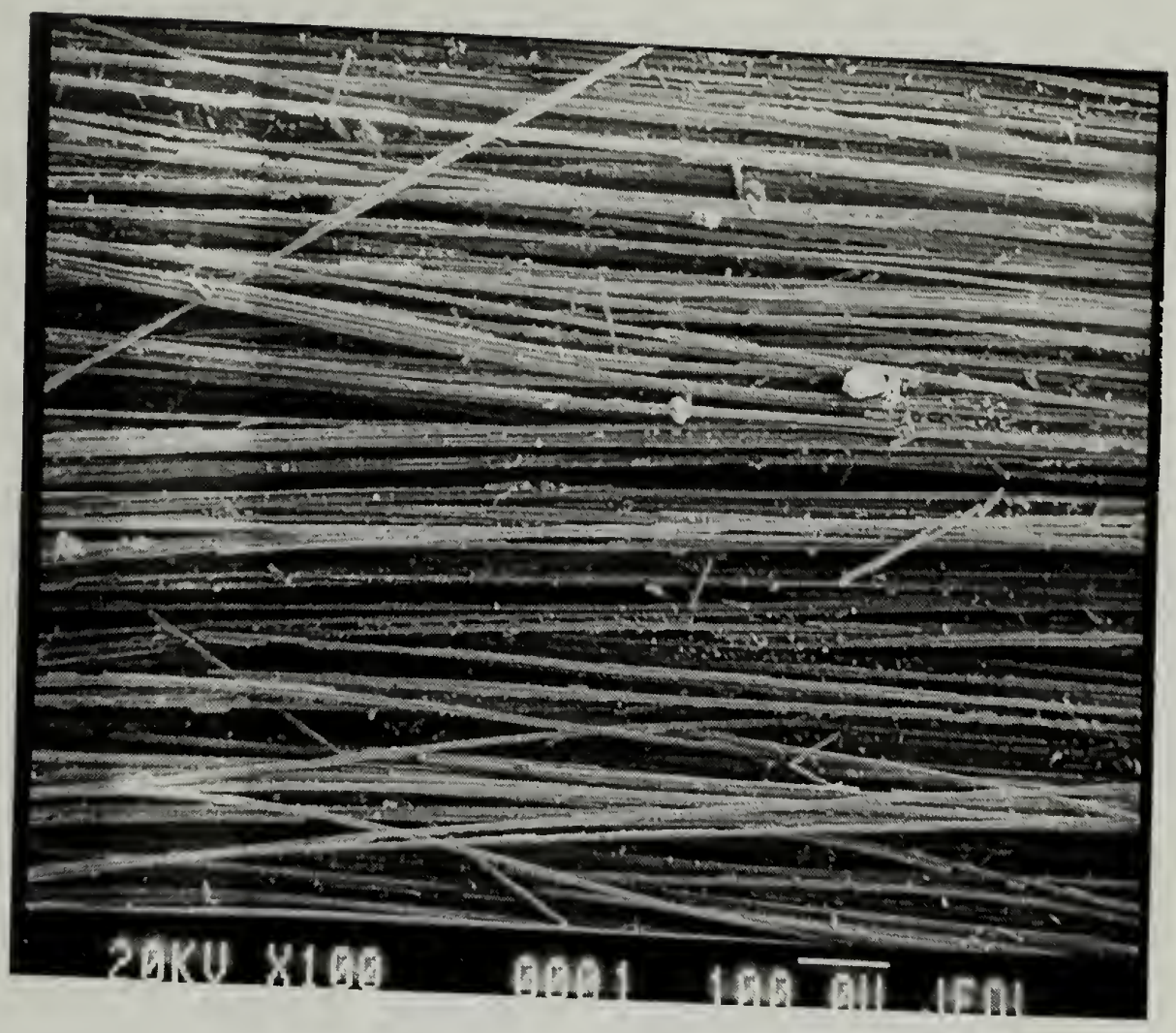

Figure 4.16: SEM image of 450 °C specimen's fracture surface 9.0 cm from heat source.

4.3.2.2 Long term – low intensity

Compliance curves from a control specimen and one aged at 205 °C for 28 days are plotted in Figure 4.17. Figure 4.18 shows the G_{IC} results for a control specimen and one exposed to the heat treatment. Unlike the short term – high intensity specimens the compliance of the exposed specimen increases indicating that the stiffness is decreased and the fracture toughness decreased after exposure. The decrease in stiffness with exposure temperature may explain the decrease in ultrasonic signal amplitude as the composite is now less efficient at propagating sound after thermal exposure. The unexposed specimens had a G_{IC} value of 260 J/mm^2. The exposed specimens incurred a significant decrease in G_{IC} to a value of 120 J/mm^2 near the heated end. As the crack propagated away from the heated end a gradual increase in toughness occurred obtaining

a value of 160 J/mm^2 14 cm from the heated end. This behavior correlates with that observed in Figure 4.9 showing a gradual erosion of the ultrasonic signal amplitude. Again we observed a correlation between the ultrasonic frequency spectrum and the fracture toughness.

SEM micrographs were also taken of the surface to identify if any evidence of interfacial failure was responsible for the decrease in the measured fracture energy and increase in acoustic attenuation of the test specimens. No direct evidence was obvious and the fracture surfaces resembled that shown in Figure 4.15.

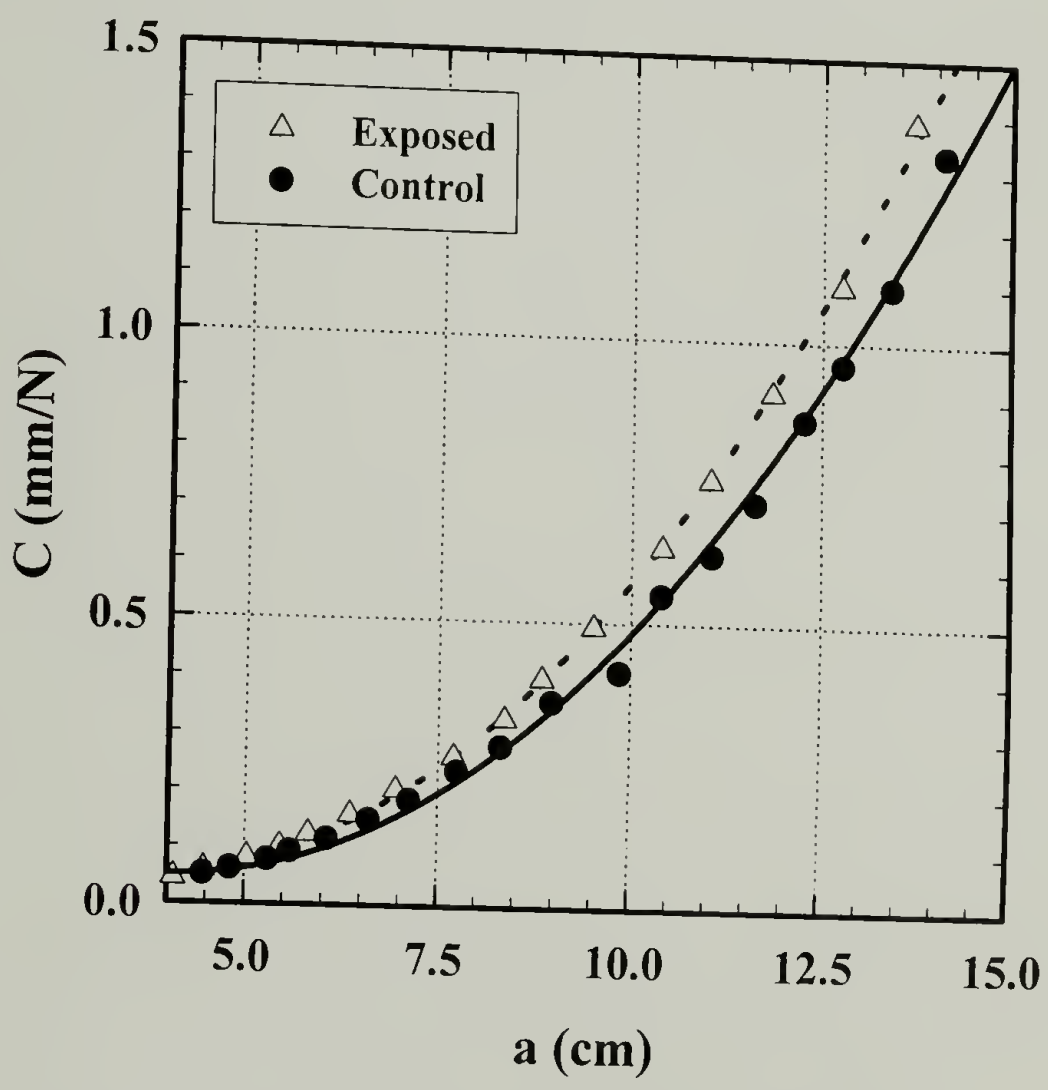

Figure 4.17: Compliance curves for control and heat-treated DCB.

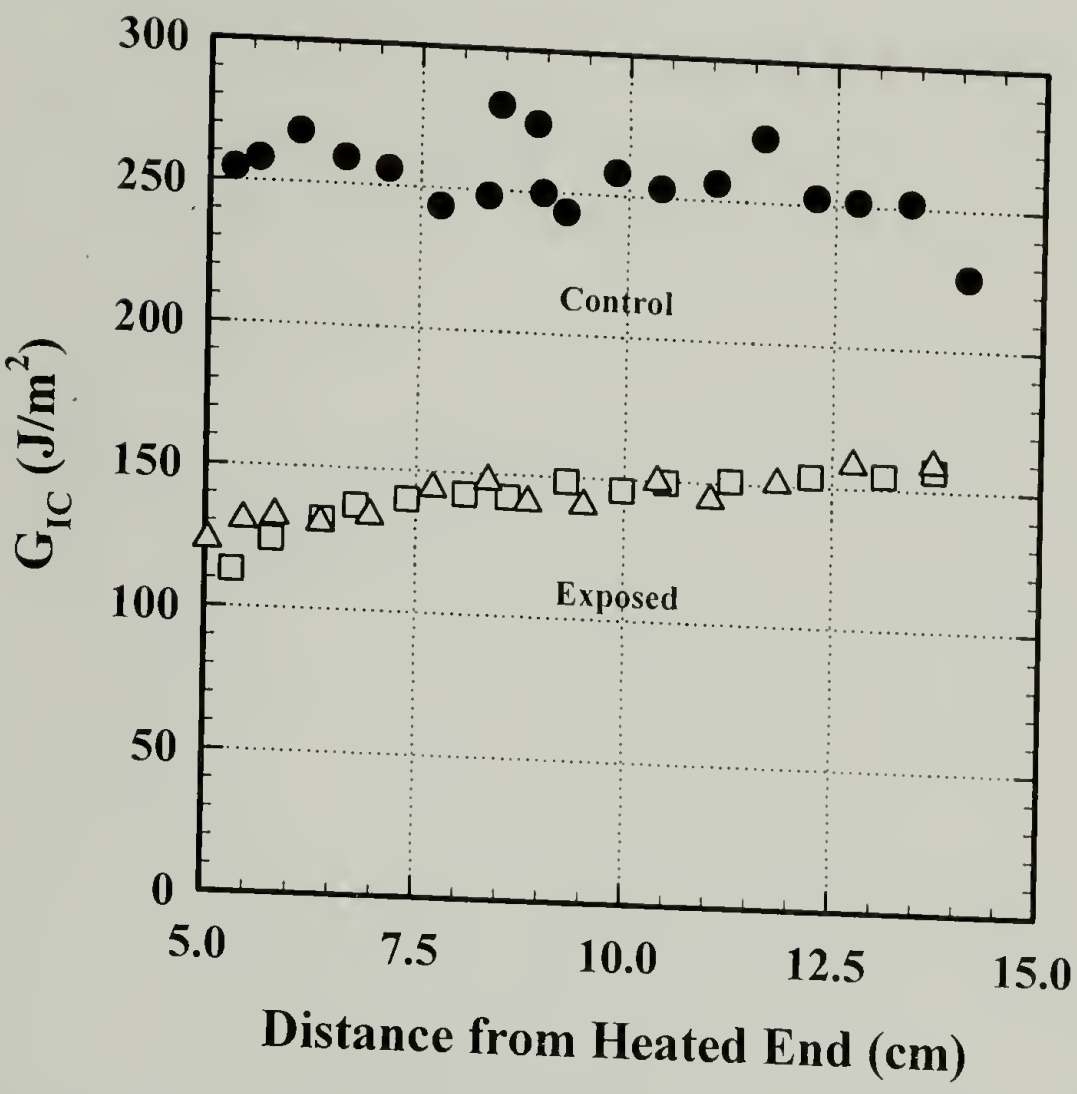

Figure 4.18: G_{Ic} fracture energy measurements on DCB control and heat-treated.

4.3.3 Fourier transform infrared spectroscopy (FTIR)

FTIR analysis of the fracture surfaces was conducted to obtain an understanding of the degree and chemical nature of degradation induced by short term – high intensity thermal loads. Specifically, we sought to understand what chemical degradation processes had occurred and how they related to observed changes in ultrasound and fracture toughness. The thermal degradation of epoxies has been studied by many researchers.[21-29] FTIR has been applied to the analysis of epoxy degradation.[26,28,29] Lin *et al.* studied the thermal stability of a variety of epoxy resins cured with trimethoxyboroxine via FTIR.[28] They ranked the order of functional group stability as; methyl group ~ benzene ring > methylene > p-phenylene > ether linkage > isopropylidene.[28] Grassie *et al.* examined the thermal degradation of the diglycidyl ether

of bisphenol-A cured with ethylene diamine via chromatography and FTIR.[26] They described the degradation mechanism to proceed by first dehydration of backbone alcohols yielding conjugation and imparting stiffness to the chain, second scission of the ether linkage yielding phenolic hydroxyl groups, third scission of carbon – nitrogen bonds yielding primary and secondary amines and ammonia, and finally a small amount of decomposition of bisphenol A via scission of the carbon – phenyl bond. Dyakonov *et al.* studied the thermal degradation of several epoxy resins cured with a variety of aromatic amine curing agents via TGA, nuclear magnetic resonance (NMR) spectroscopy, and FTIR.[29] They found similar changes in the FTIR spectra for all thermally degraded resin systems tested. Thermal degradation at 300 °C for 1 hr in nitrogen resulted in a reduction in the intensity of the phenyl ester absorbance. This absorbance was decreased further upon exposure to 350 °C for 1 hr in nitrogen. This literature review is by no means exhaustive, however, it clearly illustrates that the degradation mechanisms of epoxies are well documented and understood. Thus, during degradation the chemical nature and physical structure of the carbon fiber epoxy composites are dramatically changing.

The FTIR spectrum obtained from the fracture surface of the unexposed specimen is shown in Figure 4.19. The peak assignments are taken directly from the literature discussed above. FTIR spectra taken from the specimen exposed to 350 °C for 1 hr are shown in Figure 4.20. The severity of the thermal degradation induced in the specimens exposed at 400 and 450 °C resulted in surfaces too rough to obtain consistent spectra. Upon thermal exposure the most notable change in the spectra is the height of the phenyl ether stretch (1100 cm^{-1}) versus that of the aliphatic carbon - carbon stretch (1137cm^{-1}).

FTIR analysis of the fracture surfaces is convoluted by variations in surface roughness and the absence of a calibration peak. A qualitative measurement of degradation was made by taking the ratio of the phenyl ether stretch to that of the aliphatic carbon stretch. This assumes that the aliphatic content remains relatively constant during degradation. This is a reasonable assumption based upon the accepted degradation route presented above. A plot of phenyl ether to aliphatic absorbance peak ratio versus distance from the heated end and the exposure temperature is shown in Figure 4.21.

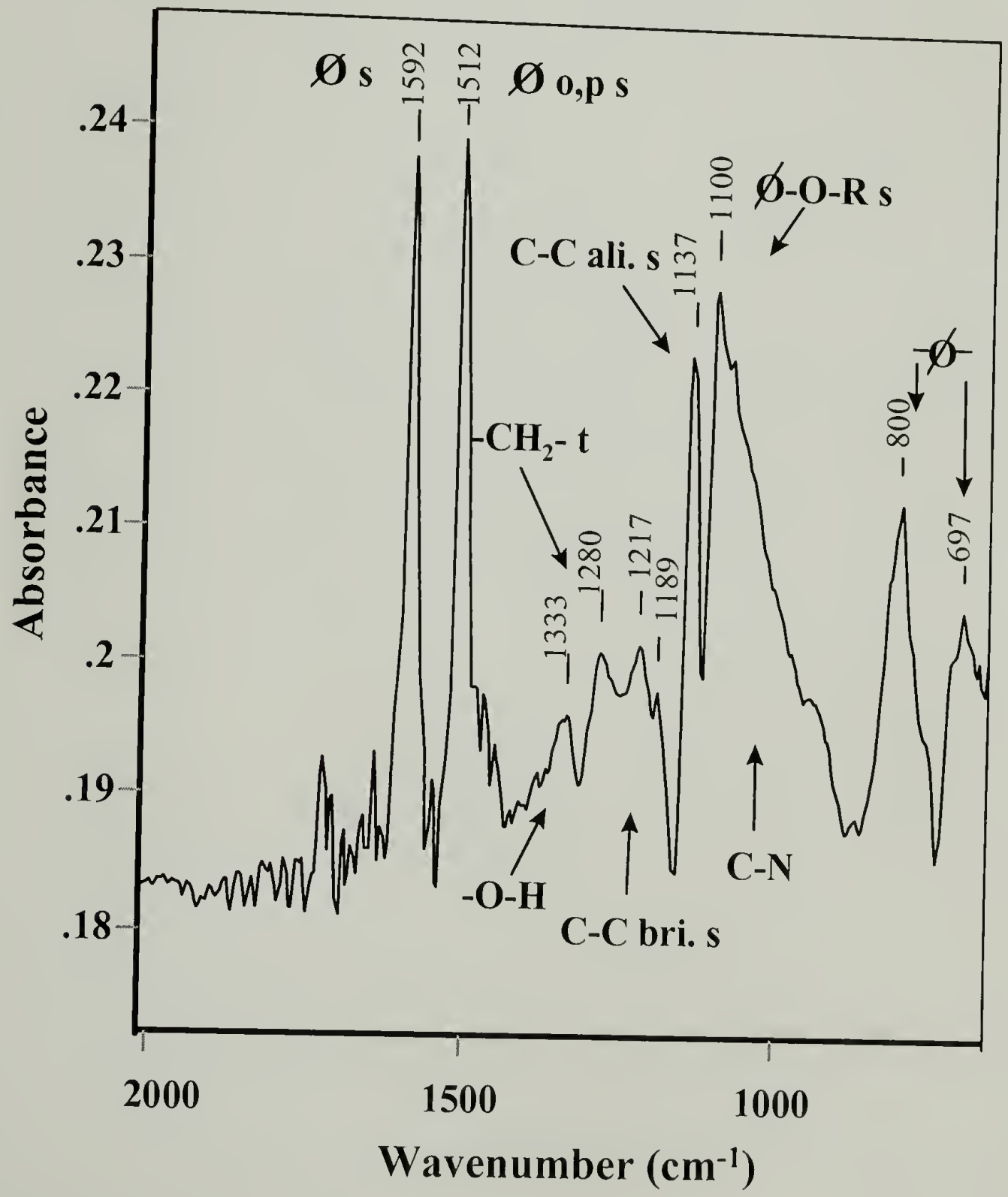

Figure 4.19: FTIR spectrum taken from the fracture surface of an unexposed specimen.

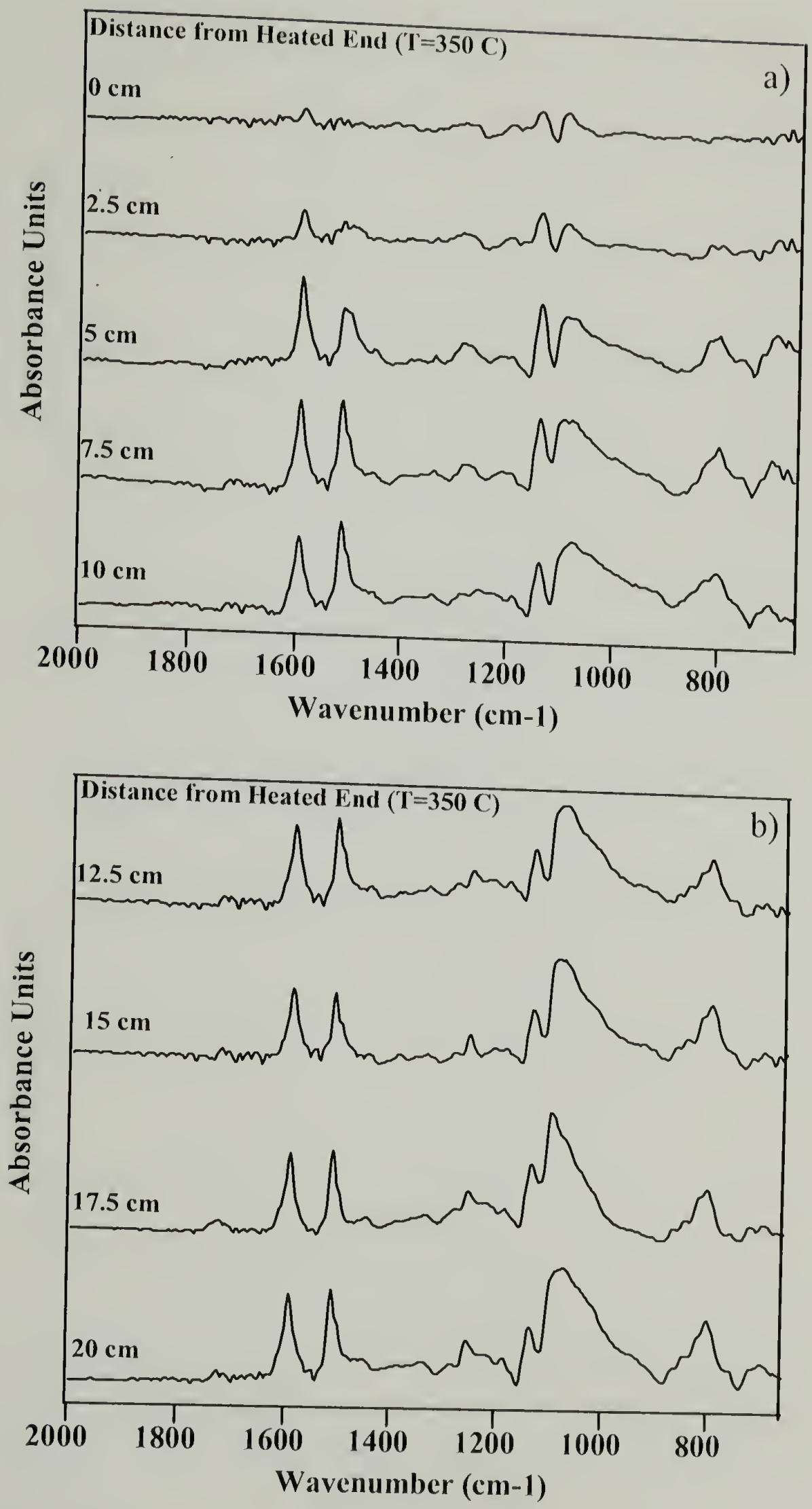

Figure 4.20: FTIR Spectra taken from specimen exposed to 350 °C. a) 10 to 0 cm from the heated end. b) 20 to 12.5 cm from the heated end.

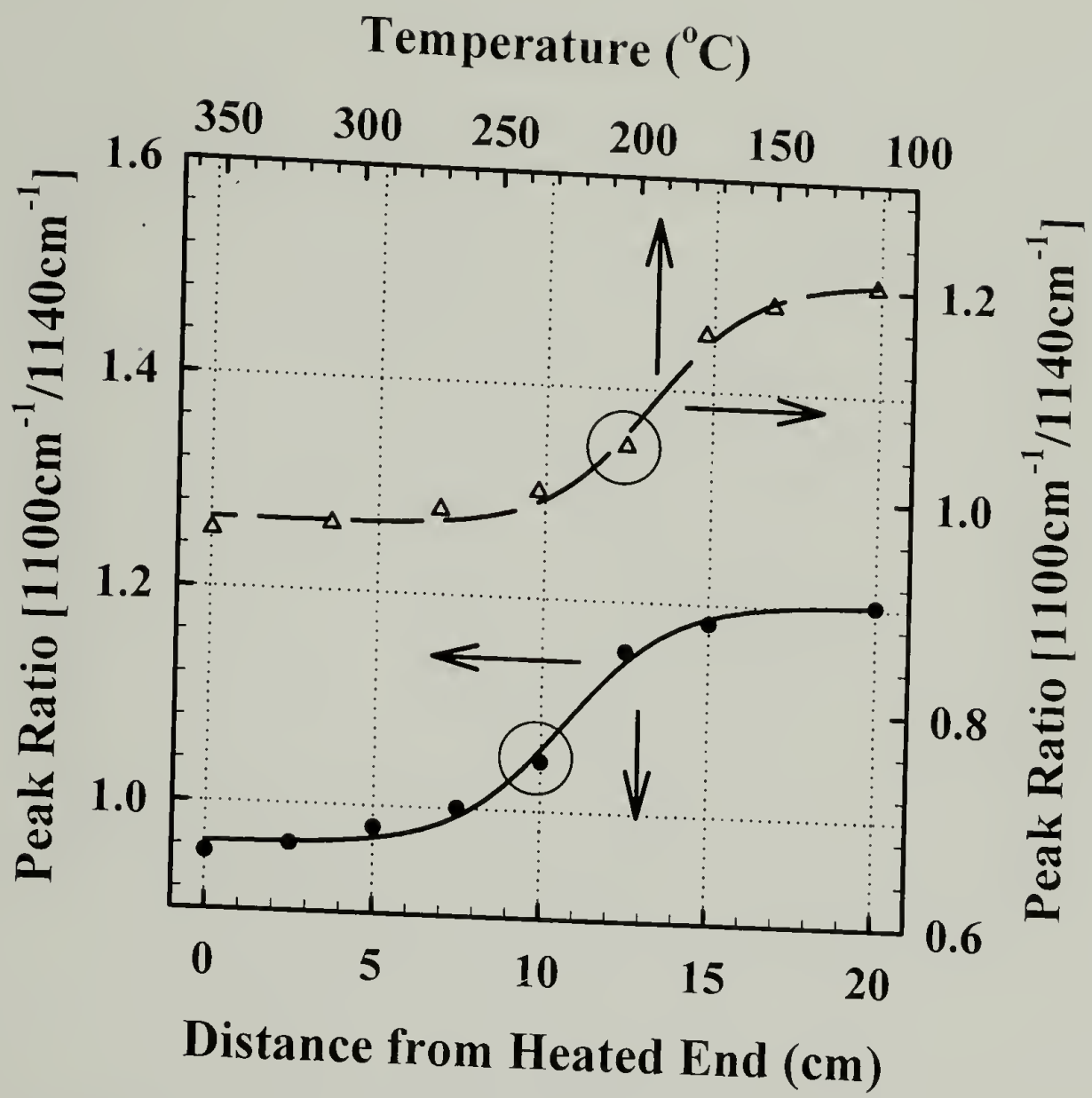

Figure 4.21: FTIR peak ratios versus distance from the heated end and the exposure temperature for the specimen exposed to 350 °C.

Figure 4.21 indicates a sigmoidal increase in the peak ratio with increasing distance from heated end and hence decreasing exposure temperature. The sigmoidal curve fits excluded the ratio obtained at 17.5 cm from the heated end. This area corresponds with the end of the aluminum spacer. Significantly more resin was observed on this surface greatly changing the observed spectrum. The circled points in Figure 4.21 correspond to the inflection points of the curves and are from spectra collected 10 cm from the heated end where the specimen was exposed to 205 °C. The inflection points mark transitions in the specimen from more degraded to less degraded regions. The relative degree degradation is relatively constant within these regions. The region more

degradation begins at 7.5 cm from the heated end and at a temperature of 240 °C. Comparing this result with that shown in Figure 4.13 illustrates that 240-250 °C is a critical temperature regime at which sever degradation takes place. This transition from less to more degradation was seen via ultrasonic spectroscopy, fracture toughness and FTIR. Thus ultrasonic spectroscopy correlates with changes in mechanical behavior and chemical transformation.

4.3.4 Simultaneous thermogravimetric analysis and differential scanning calorimetry (DSC/TGA)

TGA/DSC analysis is utilized to gauge the amount of overall thermal degradation that has taken place in specimens exposed to short term – high intensity thermal loads. This method allows the measurement of thermal degradation regardless of surface roughness. TGA thermograms for the unexposed composite and epoxy matrix are shown in Figure 4.22. TGA thermograms obtained from samples of the 350 °C specimen taken at 2.5 cm increments are shown in Figure 4.23. Similar thermograms were obtained for the 400 and 450 °C specimens. All of the TGA results are summarized in Figures 4.24 and 4.25, where the total weight fraction of volatile components is plotted versus distance from the heated end (4.24) and versus the exposure temperature (4.25). Here exposure temperature means the temperature each individual 10 mg sample experienced during thermal treatment. The volatile weight fraction was calculated from the total weight loss after heating to 900 °C. Figure 4.24 shows similar volatile fractions for all aged specimens 20 to 7.5 cm from the heated end. These values are similar to the volatile fraction of the unexposed composite. This indicates that the degree degradation is not markedly different in this region. However, we have seen via ultrasonic spectra analysis

and fracture toughness that significant changes in properties did occur in this region. At 7.5 cm, there is a deviation from this trend by the specimen exposed to 350 °C to higher volatile fractions which is expected due to its lower exposure temperature. Plotting this same date versus the exposure temperature (Figure 4.25) collapses it illustrating that the volatile weight fraction remaining after thermal treatment corresponds with the exposure temperature. This graph also has a sigmoidal shape with a rapid drop in volatile fraction (increase in prior degradation) for those regions exposed to 250 °C and greater. This temperature corresponds with the region of sharp signal loss in ultrasound, sharp increase in fracture toughness and the marked decrease in FTIR absorbance ratio.

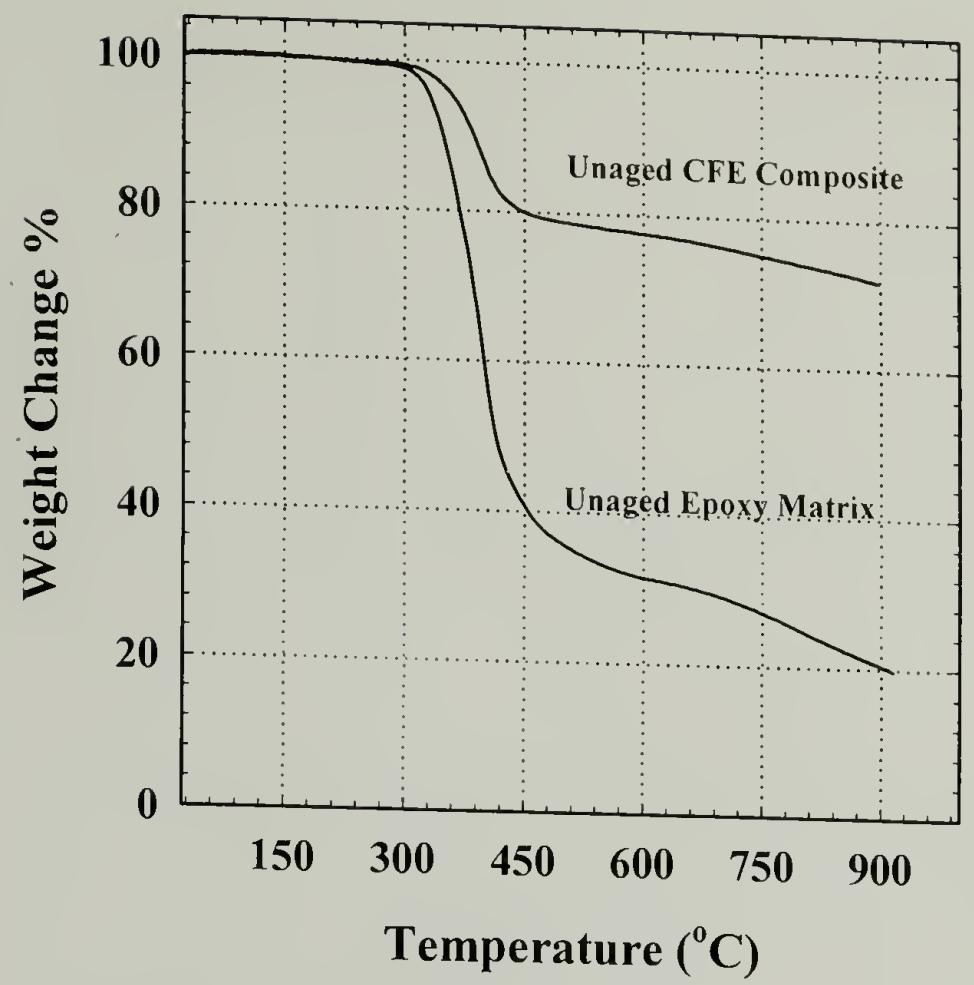

Figure 4.22: TGA of unaged composite and epoxy matrix.

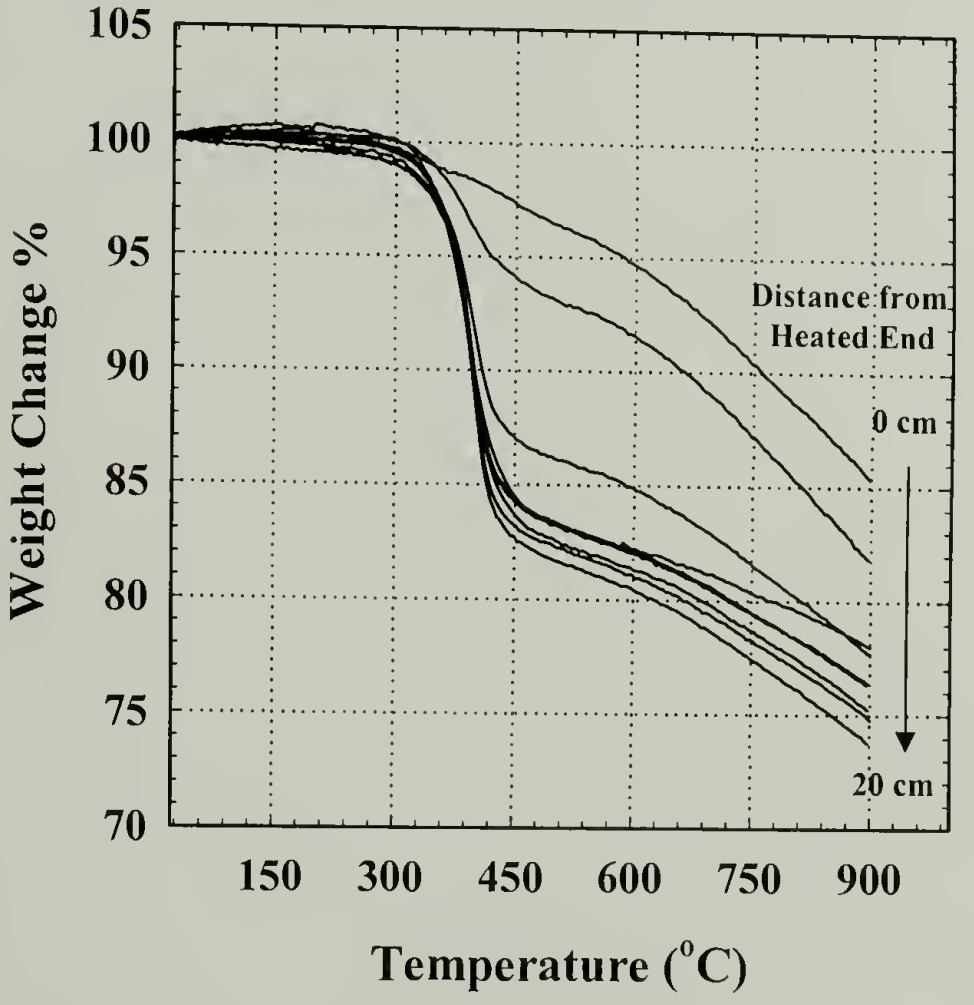

Figure 4.23: TGA data from incremental samples of 350 °C specimen.

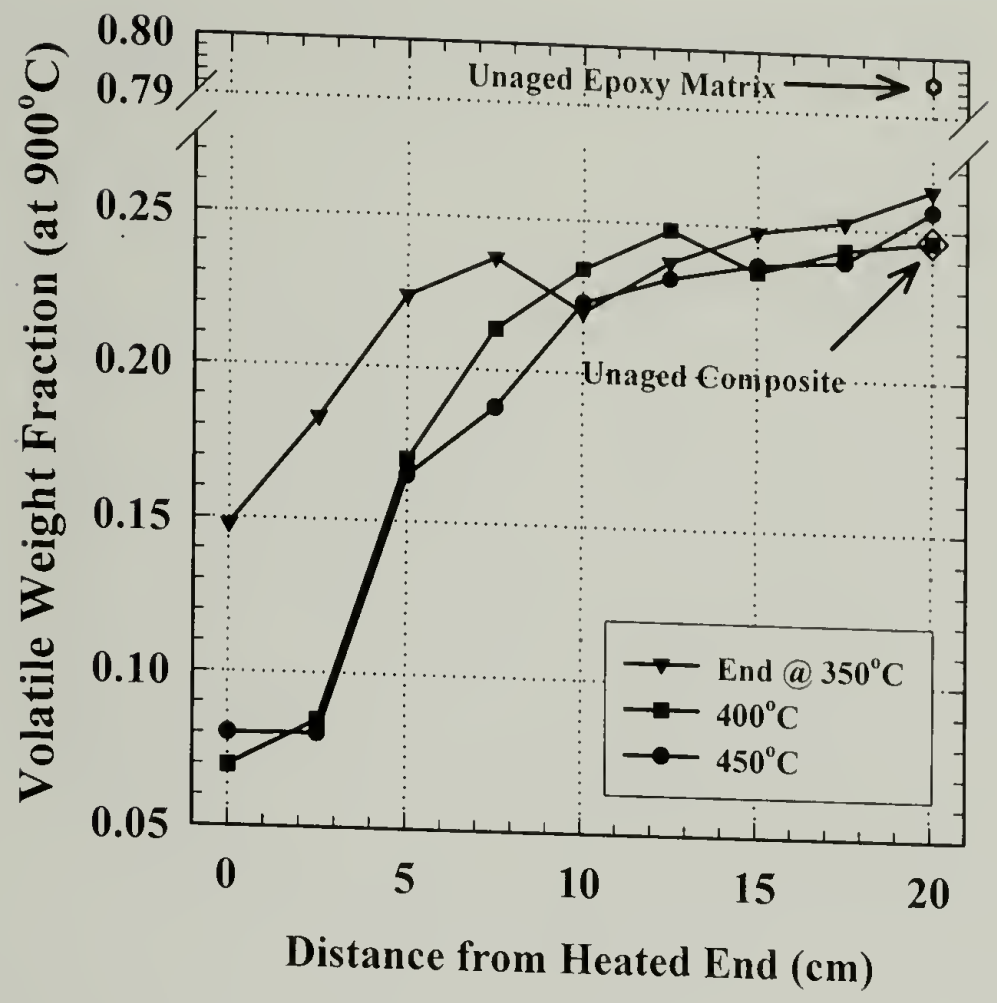

Figure 4.24: Volatile weight fraction of exposed and unexposed specimens versus distance from heated end.

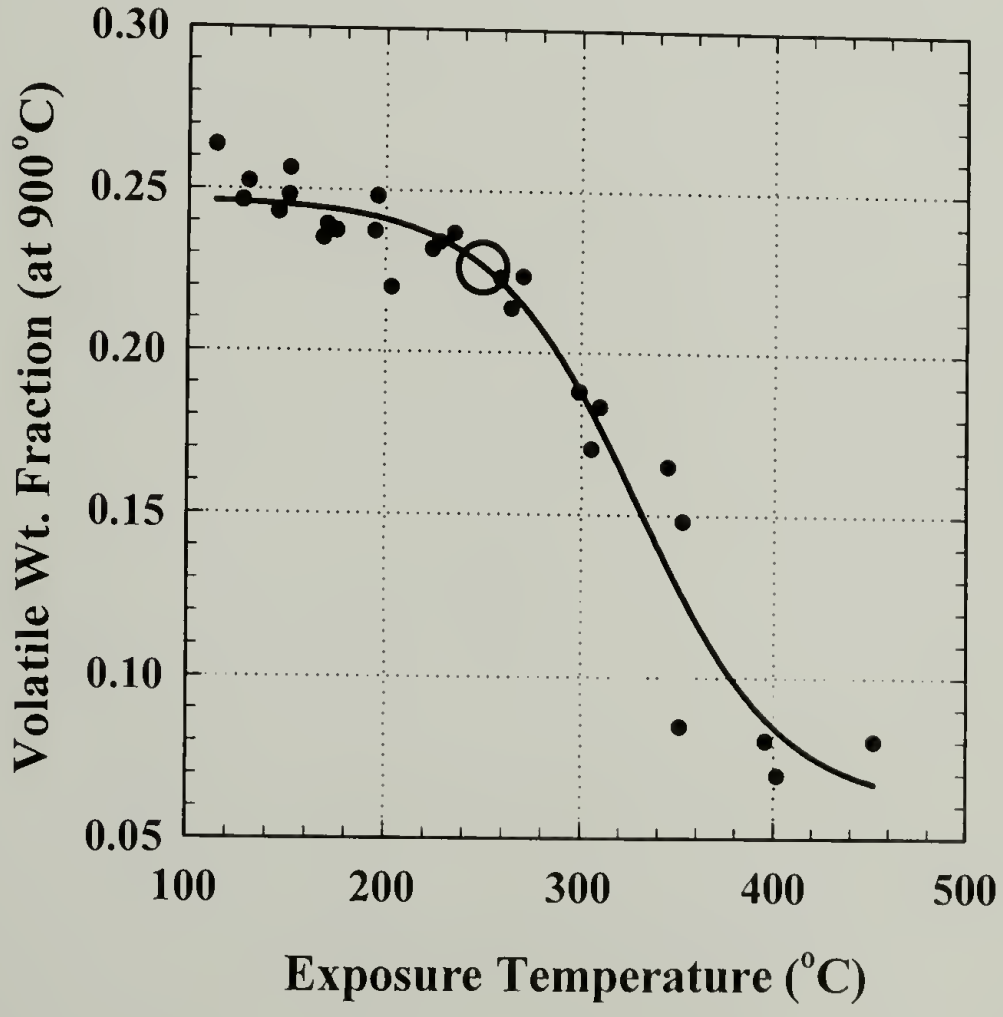

Figure 4.25: Volatile weight fraction of exposed specimens versus exposure temperature.

DSC thermograms for the unexposed composite and epoxy matrix are shown in Figure 4.26. DSC thermograms obtained from samples of the 350 °C specimen taken at 2.5 cm increments are shown in Figure 4.27. Similar thermograms were obtained for the 400 and 450 °C specimens. All of the DSC results are summarized in Figures 4.28 and 4.29 where the enthalpy of the primary degradation endotherm is plotted versus distance from the heated end (4.28) and exposure temperature (4.29) for all specimens. Examining Figure 4.28 one observes little to no measurable endotherm close to the heated end. Moving away from the end the three curves separate and an expected trend is seen with greater endotherms for specimens and areas with less heat exposure. This continues until 10 cm from the end of the specimen where a break in the data to lower endotherm values occurs (greater damage) for the specimen exposed to 350 °C. The 400 and 450 °C specimens continue their respective trends of increasing enthalpy with increasing distance from the heated end. Observing that the unaged composite and the 350 °C specimen at 20 cm have similar enthalpies it is reasonable to conclude that the 350 °C specimen did not incur greater damage than the 400 and 450 °C specimens. The endothermic peaks observed for the 350 °C and the unaged specimens were narrow and sharp while the peaks for the 400 and 450 °C specimens were broad and flat. The observed increase in degradation enthalpy for the 400 and 450 °C specimens are most likely the result of a different degradation mechanism or combination of mechanisms than that observed for the 350 °C and unaged specimens.

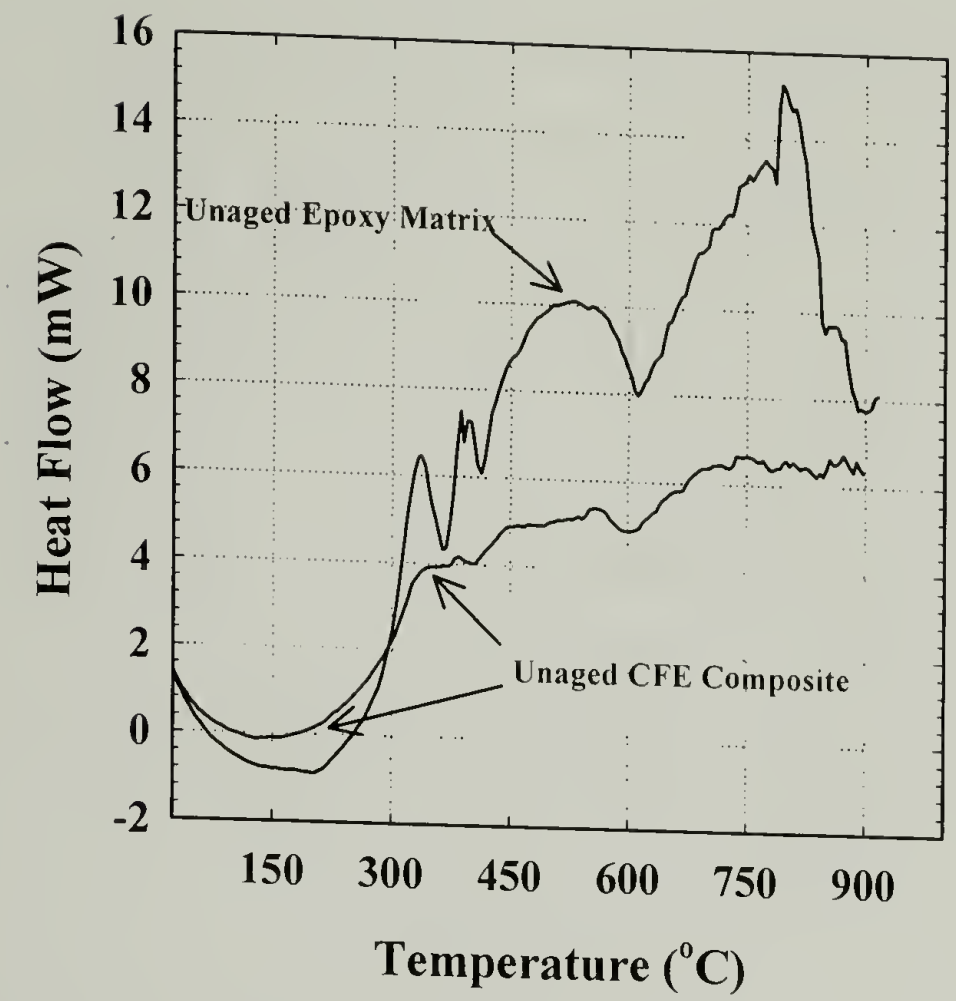

Figure 4.26: DSC of unaged composite and epoxy matrix.

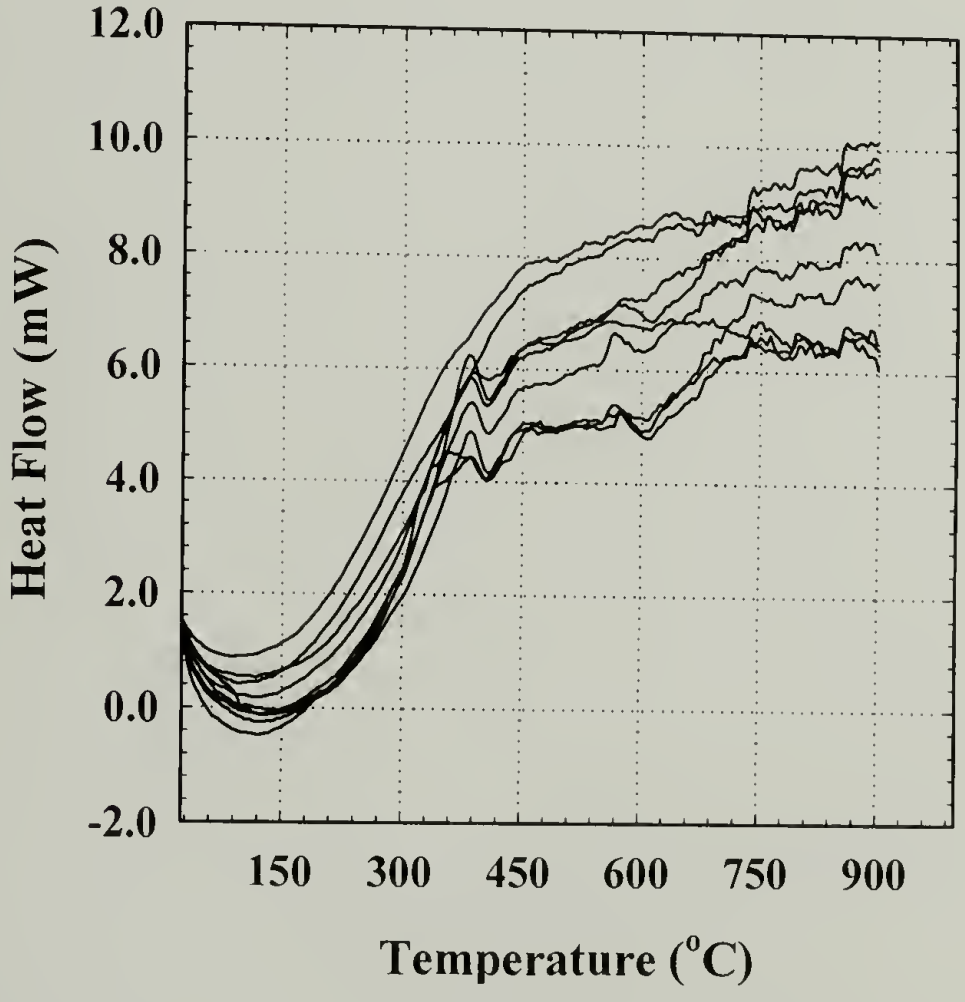

Figure 4.27: TGA data from incremental samples of 350 °C specimen.

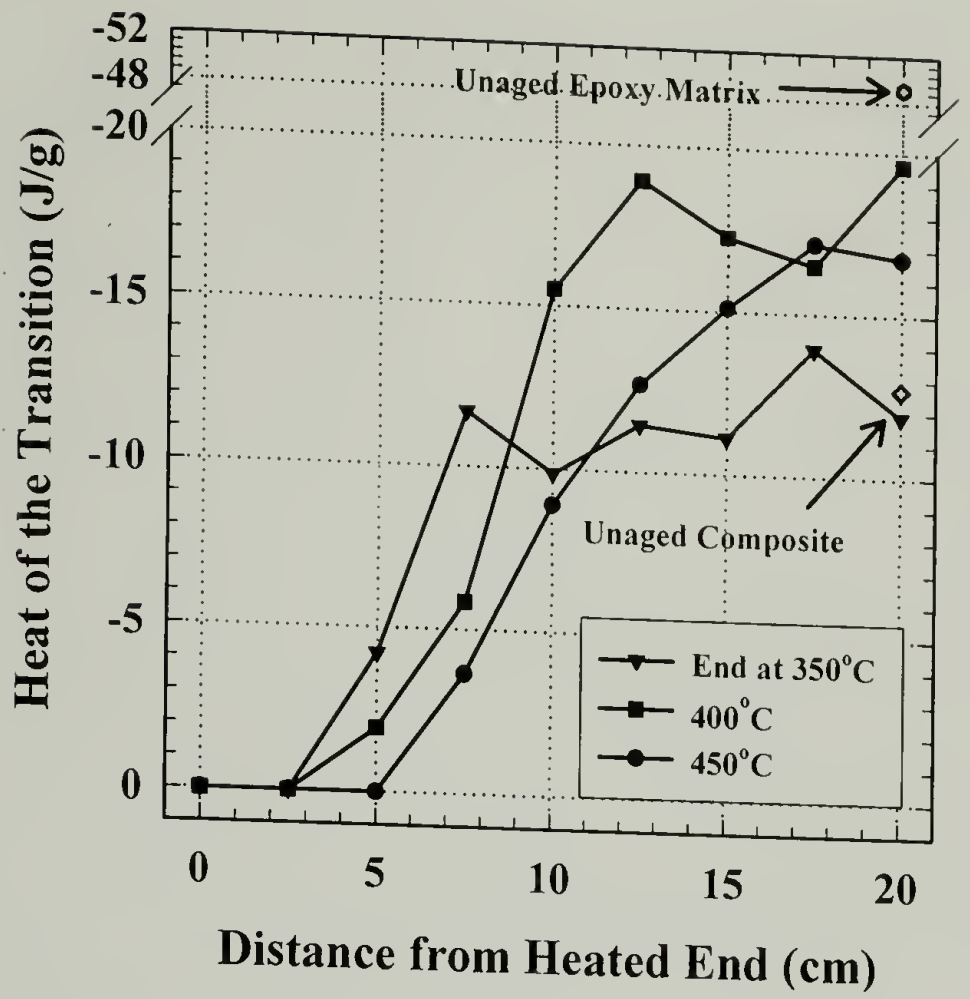

Figure 4.28: Heat of primary degradation transition of exposed and unexposed specimens versus distance from heated end.

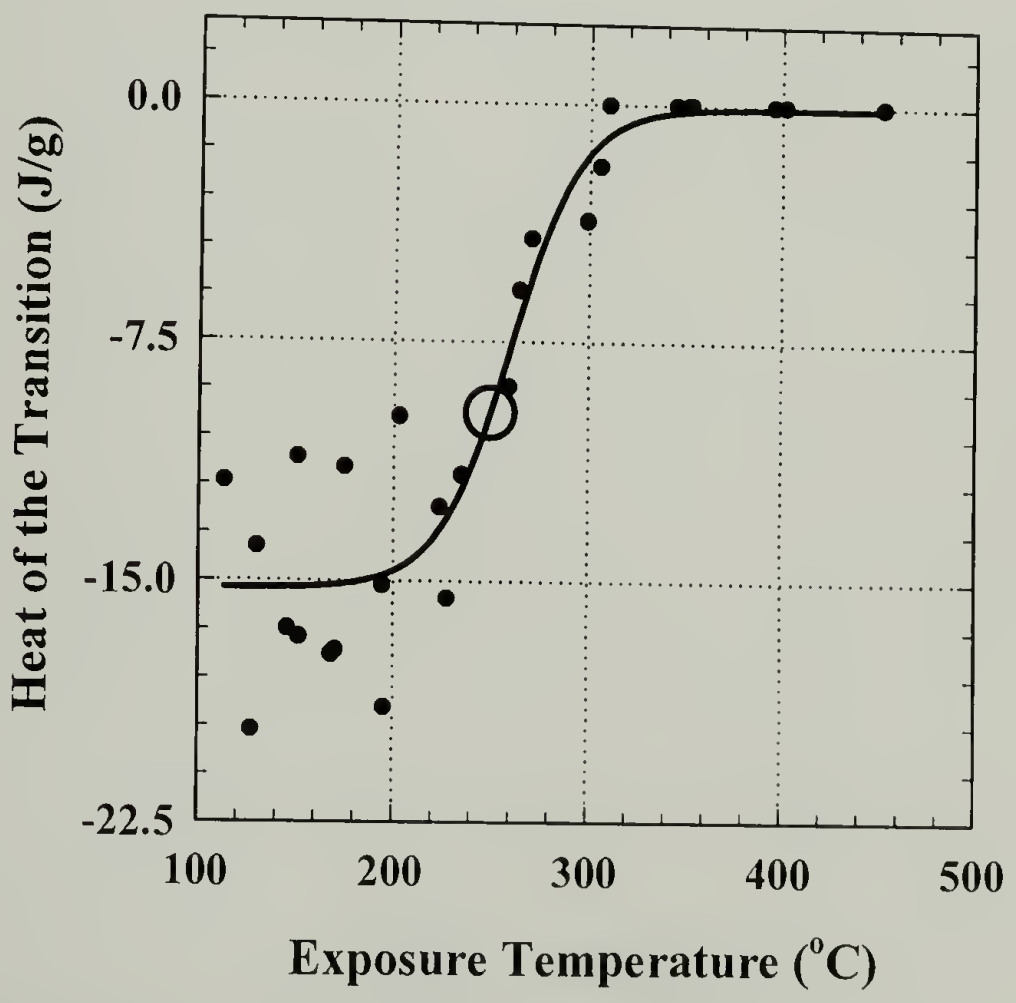

Figure 4.29: Heat of primary degradation endotherm versus exposure temperature.

Plotting the enthalpies versus exposure temperature (Figure 4.29) collapses all of the data to trends consistent with the exposure temperature except for the 350 °C specimen in the 220 – 110 °C region where scatter in the data is seen. Again, a sharp transition from less to more degradation occurs near 250 °C.

4.4 Conclusions

Short term – high intensity thermal loads induced an increase in Mode I fracture toughness with a sharp increase occurring prior to catastrophic failure. Observation of the fracture surfaces indicated that one mechanism of increased toughening may include fiber bridging in the regime just prior to the rapid decrease in fracture toughness. The dependence of the ultrasonic spectral amplitude on thermal degradation correlated with the observed changes in Mode I fracture toughness. A sharp rise in amplitude occurred just prior to the location of the sharp rise in toughness. This behavior was most pronounced for the specimen exposed to 450 °C and incrementally decreased in magnitude for the specimens exposed to 400 and 350 °C. FTIR, TGA/DSC, and fracture toughness correlated with ultrasound indicating that 250 °C is a critical temperature at which thermally induced damage greatly increases. A similar correlation between changes in the frequency spectrum and Mode I fracture toughness upon exposure of PMC to long term – low intensity thermal loads. The correlation is remarkable and clearly illustrates the efficacy of ultrasonic spectroscopy as a nondestructive method for characterizing the thermal degradation of PMC. This research illustrates that ultrasonic spectroscopy is remarkably sensitive to changes in material properties and chemical transformation upon thermal degradation. Thus, ultrasonic spectroscopy may be useful

as a means of detecting incipient damage prior to the formation of delaminations and the detection and monitoring of thermal degradation of PMCs.

4.5 References

1) Stanley, R. K. *Special Nondestructive Testing Methods*; 2 ed.; Stanley, R. K., Ed.; American Society for Nondestructive Testing: Columbus, 1995; Vol. 9.

2) Cartz, L. *Nondestructive Testing Radiography, Ultrasonics, Liquid Penetrant, Magnitic Particle, Eddy Current*; AMS International: Materials Park, 1995.

3) Filipczynski, L.; Pawlowski, Z.; Wehr, J. *Ultrasonic Methods of Testing Materials*; 3rd ed.; Butterworth and Co.: London, 1966.

4) Scott, W. R.; Gordon, P. F. *J. Acoust. Soc. Am.* **1977**, *62*, 108-116.

5) Stiffler, R.; Henneke, E.; Duke, J. *Application of ultrasonic spectrum analysis for determining the damage state in advanced composite materials undergoing cyclic loading.*; ASNT: boston, 1982, pp 95-99.

6) Ourak, M.; Nongaillard, B.; Rouvaen, J. M.; Ouafrouh, M. *NDT International* **1991**, *24*, 21-28.

7) Raju, P. K.; Vaidya, U. K. *Polym. Compo.* **1996**, *17*, 275-287.

8) Guo, N.; Lim, M. K.; Pialucha, T. *J. Nondestructive Evaluation* **1995**, *14*, 9-19.

9) Jayet, Y.; Saint-Pierre, N.; Tatibouet, J.; Zellouf, D. *Ultrasonics* **1996**, *34*, 397-400.

10) Kazys, R.; Svilainis, L. *Ultrasonics* **1997**, *35*, 367-383.

11) Webb, J. E.; Singh, R. N.; Nagy, P. B.; Lowden, R. A. *Ceramics Eng. Sci. Proc.* **1997**, *18*, 237-244.

12) Huang, W.; Chu, Y. C.; Rokhlin, S. I.; Wright, P. K. *Journal of Testing and Evaluation* **1997**, *25*, 1-14.

13) Rokhlin, S. I.; Chu, Y. C.; Lavrentyev, A. I.; Baaklini, G. Y.; Bhatt, R. R. *Ceramic Eng. Sci. Proc.* **1994**, *15*, 1164-1173.

14) Tse, S. D.; Fernandez-Pello, A. C.; Miyasaka, K. *Controlling Mechanisms in the Transition from Smoldering to Flaming of Flexible Polyurethane Foam*; Rheinhold Pub. Corp.: Napoli, Italy, 1996; Vol. 1, pp 1505-1513.

15) Armstrong-Carroll, E.; Mehrkam, P. A.; Cochran, R. *Characterization of Heat Damage in Graphite/Epoxy Composites*; Armstrong-Carroll, E.; ASTM: Montreal, Can, 1996; Vol. 12, pp 37-55.

16) Schueneman, G. T.; Lesser, A. J.; Hobbs, T.; Novak, B. M. *J. Polym. Sci. Part B: Polym. Phys.* **1999**, *In press*.

17) Schueneman, G. T.; Lesser, A. J.; Hobbs, T.; Novak, B. M. *Evaluation of the thermal degradation of polymer matrix composites via ultrasonic spectroscopy and fracture toughness*; SPE: New York, 1999.

18) Lesser, A. J.; Schueneman, G. T.; Hobbs, T. R. *Evaluation of Thermal Degradation of the Resin-Fiber Interface in Graphite Fiber Reinforced Laminates Using Ultrasonic Spectroscopy*; SAMPE: Anaheim, CA, 1998; Vol. 1, pp 1042-1052.

19) Williams, J. G.; Kinloch, A. J. *J. Mater. Sci. Letters* **1989**, *8*, 125-129.

20) Yuan, F. G.; Hutapea, P. *Mode-I fracture toughness of IM7/LaRC-RP46 composites under thermal aging*; AIAA: Long Beach, CA, 1998; Vol. 3, pp 2122-2131.

21) Rose, N.; Bras, M. L.; Bourbigot, S.; Delobel, R. *Polym. Deg. Stab.* **1984**, *45*, 387-397.

22) Ciuacu, S.; Budrugeac, P.; Niculae, I. *Polym. Deg. Stab.* **1991**, *31*, 365-372.

23) Venger, A. E.; Fraiman, Y. E.; Yurevich, F. B. *J. Therm. Anal.* **1983**, *27*, 325-332.

24) Grassie, N.; Guy, M. I. *Polym. Deg. Stab.* **1985**, *12*, 65-91.

25) Grassie, N.; Guy, M. I. *Polym. Deg. Stab.* **1985**, *13*, 11-20.

26) Grassie, N.; Guy, M. I. *Polym. Deg. Stab.* **1986**, *14*, 125-137.

27) Farquharson, S.; Bassilakis, R.; DiTaranto, M. B.; Haigis, J. R.; Smith, W. W.; Solomon, P. R. *Measurement of Thermal Degradation in Epoxy Composites by Fourier Transform Raman Spectroscopy*; SPIE International: Boston, MA, 1994; Vol. 2072, pp 319-331.

28) Lin, S. C.; Bulkin, B. J.; Pearce, E. M. *J. Polym. Sci.: Polym. Chem. Ed.* **1979**, *17*, 3121-3148.

29) Dyakonov, T.; Mann, P. J.; Chen, Y.; Stevenson, W. T. K. *Polym. Deg. Stab.* **1996**, *54*, 67-83.

BIBLIOGRAPHY

Achenbach, J. D. *Wave Propagation in Elastic Solids*; Elsevier: New York, 1973.

Bhatia, A. B. *Ultrasonic Absorption: An Introduction to the Theory of Sound Absorption and Dispersion in Gases, Liquids and Solids*; Clarendon Press: Oxford, 1967.

Blitz, J. *Fundamentals of Ultrasonics*; Butterworths: London, 1963.

Cartz, L. *Nondestructive Testing Radiography, Ultrasonics, Liquid Penetrant, Magnitic Particle, Eddy Current*; AMS International: Materials Park, 1995.

Colby, M. Y. *A College Course in Sound Waves and Acoustics*; H. Holt and Company: New York, 1938.

Filipczynski, L., Z. Pawlowski, and J. Wehr. *Ultrasonic Methods of Testing Materials*; Butterworth and Co.: London, 1966.

Gooberman, G. L. *Ultrasonics Theory and Application*; Hart Publishing Co.: New York, 1968.

Herzfeld, K. F. and T. A. Litovitz *Absorption and dispersion of ultrasonic waves*; Academic Press: New York, 1959.

Kino, G. S. *Acoustic Waves : Devices, Imaging, and Analog Signal Processing*; Prentice-Hall: Englewood Cliffs, N.J., 1987.

Krautkrämer, J. and H. Krautkrämer *Ultrasonic testing of materials*; Springer-Verlag: Berlin, New York, 1969.

Lamb, H. *The Dynamical Theory of Sound*; Dover: New York, 1960.

Pollard, H. F. *Sound Waves in Solids*; Pion Limited: London, 1977.

Rayleigh, J. W. S. *The Theory of Sound*; Macmillan: London, 1894.

Richardson, E. G. *Ultrasonic Physics*; Elsevier Publishing Co., New York, 1962.

Rzhevkin, S. N. *A Course of Lectures on the Theory of Sound*; Macmillan Co.: New York, 1963.

Stewart, G. W. and R. B. Lindsay *Acoustics; a text on theory and applications*; D. Van Nostrand company inc.: New York, 1930.

Truell, R., C. Elbaum, and B. B. Chick. *Ultrasonic Methods in Solid State Physics*; Academic Press: New York, 1969.